Technische Universität München
TUM School of Engineering and Design

# Aerodynamic Analysis of Coupled Technologies for Hybrid Laminar Flow Wings

Mauricio Manuel Jentys

Vollständiger Abdruck der von der TUM School of Engineering and Design der Technischen Universität München zur Erlangung eines

Doktors der Ingenieurwissenschaften (Dr.-Ing.)

genehmigten Dissertation.

Vorsitz: Prof. Dr.-Ing. Sabine Ardey

Prüfende der Dissertation:
1. apl. Prof. Dr.-Ing. Christian W. M. Breitsamter
2. Prof. Dr.-Ing. Eike Stumpf
3. Prof. Dr.-Ing. Claus Wagner

Die Dissertation wurde am 11.10.2024 bei der Technischen Universität München eingereicht und durch die TUM School of Engineering and Design am 26.03.2025 angenommen.

Typesetting: LaTeX

# Vorwort

Die vorliegende Dissertation entstand während meiner Zeit als wissenschaftlicher Mitarbeiter am Lehrstuhl für Aerodynamik und Strömungsmechanik der Technischen Universität München. An dieser Stelle möchte ich mich bei den Personen bedanken, die maßgeblich zum Erfolg meines Promotionsvorhabens beigetragen haben.

Als erstes will ich meinem Doktorvater Prof. Dr.-Ing. Christian Breitsamter meinen Dank aussprechen. Sie haben mir ermöglicht, mich im Rahmen meiner Dissertation mit einem extrem spannenden, hochaktuellen und herausfordernden Thema zu beschäftigen und mich dabei jederzeit unterstützt. Sowohl auf fachlicher, als auch auf persönlicher Ebene war die Zeit am Lehrstuhl extrem lehrreich.

Auch bei Prof. Dr.-Ing Sabine Ardey, Prof. Dr.-Ing Eike Stumpf und Prof. Dr.-Ing. Claus Wagner möchte ich mich für das Übernehmen der Arbeiten in der Prüfungskommission bedanken. Besonders hervorheben möchte ich nochmals die Zusammenarbeit mit Prof. Stumpf und dem Institut für Luft- und Raumfahrtsysteme der RWTH Aachen im LuFo Projekt CATeW, aus dem diese Arbeit entstanden ist.

Der Erfolg des Projekts beruht zu großen Teilen auch auf der herausragenden Leistung von Dr.-Ing. Tim Effing. Es hat mich sehr gefreut, mit dir HLFC und VC aus verschiedenen Blickwinkeln zu beleuchten. Vor allem gemeinsame Konferenzen, wie der ICAS Kongress in Stockholm oder die AEC in Lausanne, waren sehr einprägsame Erlebnisse.

Ausschlaggebend waren auch alle Kollegen, mit denen ich das Glück hatte, am Lehrstuhl zusammenzuarbeiten. Vielen Dank an Euch alle! Besonders in Erinnerung bleiben werden mir mit Sicherheit entspannte Zone 1 Rennradausfahrten mit dem Rasenden Rudel (und Erweiterungen) Ulrich Hartmann, Dominik Sedlacek, Christopher Reinbold und Moritz Zieher, teils intensive Matches mit den AEC All-Stars Julius Stegmüller, Jonathan Pflüger, Stefan Hayböck und Andreas Kümmel und natürlich Training und Teilnahme an renommierten Laufrennen mit den NACA Alpacas Catharina Moreira und Paloma Garcia Guillén.

Den größten Beitrag zum erfolgreichen Abschluss meiner Promotion haben sicherlich Freunde und Familie geleistet. Besonders Fabian Oestereich und Leonie Müller haben dabei eine zentrale Rolle gespielt und mir stets mit Rat und Tat beiseite gestanden. Meine Eltern, Cristina Garcia de Jentys und Andreas Jentys, die mir alles gegeben haben und mich immer bedingungslos unterstützt haben. Am wichtigsten war aber mit Sicherheit die Unterstützung meiner Partnerin Leslie Müller. Ich bin überglücklich mit dir diese aufregende Zeit verbracht zu haben und hoffe noch viele weitere Erinnerungen mit dir zu sammeln.

Hallbergmoos, April 2025 Mauricio Manuel Jentys

# Abstract

Hybrid Laminar Flow Control (HLFC) and Variable Camber (VC) are two promising techniques for reducing the aerodynamic drag of future transport aircraft. While the individual benefits of these technologies have been extensively studied, their synergistic potential to further reduce drag when operated simultaneously remains an open research question. The synergy between these technologies arises from the impact of VC not only on the spanwise loading of the wing but also on the chordwise pressure distribution, a critical factor influencing the laminar performance of an HLFC system.

The present thesis investigates these effects on wing level of a representative reference configuration. The analyses employs linear stability theory together with a two-$N$-factor method, and the local-correlation-based $\gamma - Re_\theta$+CF transition model to account for boundary layer transition in the numerical simulations. Through comprehensive parameter variations, the technology coupling is shown to achieve an aerodynamic drag reduction due to synergy effects.

The analysis is subsequently extended to a higher integration level, incorporating the fuselage and horizontal tailplane alongside the wing of the reference configuration. Analyses of the trimmed aircraft throughout its operational envelope reflect the synergistic potential of the technology coupling for drag reduction considering off-design operation.

The thesis concludes by proposing methods for data exploitation, focusing on the development of surrogate and reduced order models. These models enable efficient and highly accurate exploration of the design space and subsequent optimization of configurations that integrate such coupled technology approaches for future aircraft designs.

# Zusammenfassung

Hybride Laminarhaltung (HLFC - "*Hybrid Laminar Flow Control*") und die Integration variabler Wölbung (VC - "*variable camber*") am Tragflügel zukünftiger transonischer Transportflugzeuge gehören zu vielversprechenden Technologien zur Reduktion aerodynamischen Widerstands. Während das Potential beider Technologien in isolierter Betrachtung bereits gründlich untersucht wurde, ist das Synergiepotential zur weiteren Widerstandsreduktion bei gleichzeitiger Anwendung eine offene Forschungsfrage. Die synergetische Überschneidung ergibt sich aus dem Einfluss von VC Integration auf die Druckverteilung am Flügel, welche nicht nur in spannweitiger, sondern auch in Tiefenrichtung effektiv gesteuert werden kann. Die Druckverteilung in Tiefenrichtung stellt dabei eine zentrale Stellgröße für die durch HLFC erreichbare laminare Lauflänge dar.

Die Arbeit befasst sich zunächst mit Untersuchungen am Flügel einer repräsentativen Referenzkonfiguration. Zur Transitionslagenvorhersage in den numerischen Analysen kommen sowohl lineare Stabilitätstheorie zusammen mit einer zwei-$N$-Faktor Methode, als auch das auf lokalen Korrelationen basierte $\gamma - Re_\theta$+CF Transitionsturbulenzmodell zur Anwendung. Durch umfassenden Parametervariationen kann das Synergiepotential der Technologiekopplung zur Widerstandsreduktion gezeigt werden.

In einem nächsten Schritt werden die Analysen auf eine höhere Integrationsstufe erweitert, indem zusätzlich zum Tragflügel auch der Rumpf und das Höhenleitwerk berücksichtigt werden. Die Analysen der Referenzkonfiguration in einem getrimmten Flugzustand bestätigen das Synergiepotenzial der Technologiekopplung zur Widerstandsreduktion für den Betrieb außerhalb des Auslegungspunkts.

Auf Grundlage der umfangreichen Datensätzen der numerischen Simulationen, schließt die Arbeit mit der Ableitung von Ersatzmodellen und Modellen reduzierter Ordnung. Diese Modelle ermöglichen eine effiziente und präzise Darstellung der gesamten Betriebsenveloppe und ermöglichen somit eine Optimierung künftiger Flugzeugkonfigurationen mit gekoppelten Technologieanwendungen.

# Contents

# List of Figures

# List of Tables

# Nomenclature

| Roman Symbols | Denotation |
|---|---|
| $b$ | Wing span |
| $c$ | Chord length |
| $C_D$ | Drag coefficient |
| $C_{D,p}$ | Pressure drag coefficient |
| $C_{D,f}$ | Friction drag coefficient |
| $c_f$ | Skin-friction coefficient |
| $C_L$ | Lift coefficient |
| $C_M$ | Pitching moment coefficient |
| $c_p$ | Pressure coefficient |
| $C_q$ | Suction coefficient |
| $D$ | Drag force |
| $H$ | Flight altitude |
| $H_{12}$ | Shape factor |
| $k$ | Covariance function |
| $K$ | Covariance matrix |
| $l$ | Length |
| $L$ | Lift force |
| $Ma$ | Mach number |
| $N$ | N-factor |
| $N_{CF}$ | N-Factor for cross-flow instabilities |
| $N_{TS}$ | N-Factor for Tollmien-Schlichting instabilities |
| $p$ | Static pressure |
| $\boldsymbol{p}$ | Parameter vector |
| $\boldsymbol{p}^*$ | Prediction parameter vector |
| $P$ | Matrix of parameter vectors |
| $P^*$ | Matrix of prediction parameter vectors |
| $q$ | Dynamic pressure |
| $R$ | Range |
| $Re$ | Reynolds number |
| $Re_\theta$ | Momentum thickness Reynolds number |
| $Re_{\theta c}$ | Critical momentum thickness Reynolds number |
| $\widehat{Re}_{\theta t}$ | Critical momentum thickness Reynolds number at transition onset |
| $Re_{He}$ | Helicity Reynolds number |
| $Re^+_{He,t}$ | Critical helicity Reynolds number at |

| | |
|---|---|
| | transition onset |
| $Re_\nu$ | Vorticity Reynolds number |
| $T$ | Temperature |
| $Tu$ | Turbulence intensity |
| $u$,$v$,$w$ | Velocity vector components |
| $V$ | Flight velocity |
| $x$,$y$,$z$ | Cartesian coordinate components |

| **Greek Symbols** | **Denotation** |
|---|---|
| $\alpha$ | Angle of attack, wave number |
| $\beta$ | Flow direction angle, wave number |
| $\gamma$ | Intermittency |
| $\delta_{ADHF}$ | Adaptive Dropped Hinge Flap deflection angle |
| $\delta_1$ | Displacement thickness |
| $\delta_{99}$ | 99% $u_\infty$ boundary layer thickness |
| $\epsilon$ | Error |
| $\eta$ | Non-dimensional spanwise coordinate |
| $\theta$ | Momentum thickness |
| $\kappa$ | Heat capacity ratio |
| $\lambda$ | Wing taper ratio |
| $\mu$ | Dynamic viscosity |
| $\mu_T$ | Eddy-viscosity |
| $\nu$ | Kinematic viscosity, vorticity |
| $\rho$ | Density |
| $\sigma$ | Standard deviation, singular value |
| $\tau$ | Shear stress |
| $\varphi$ | Wing sweep angle |
| $\omega$ | Frequency |

| **Subscripts** | **Denotation** |
|---|---|
| $c$ | Cross-wise |
| $e$ | Edge |
| $i$ | Inviscid |
| $lam$ | Laminar |
| $loc$ | Local |
| $max$ | Maximum |
| $min$ | Minimum |
| $N$ | Normal |
| $ref$ | Reference |

| | |
|---|---|
| $T$ | Tangential |
| $tr$ | Transition |
| $turb$ | Turbulent |
| $w$ | Wall |
| $\infty$ | Freestream |

# Abbreviations and Acronyms

| | |
|---|---|
| ADHF | Adaptive dropped hinge flap |
| ALT | Attachment line transition |
| BL | Boundary layer |
| CATeW | Coupled Aerodynamic Technologies for Aircraft Wings |
| CFD | Computational fluid dynamics |
| CFI | Cross-flow instability |
| CG | Center of gravity |
| DLR | German Aerospace Center (Deutsches Zentrum für Luft- und Raumfahrt) |
| GPR | Gaussian process regression |
| HiFi | High-fidelity |
| HLFC | Hybrid laminar flow control |
| HTP | Horizontal tailplane |
| ICA | Initial cruise altitude |
| LCTM | Local-corrrelation based transition model |
| LFC | Laminar flow control |
| LowFi | Low-fidelity |
| LRZ | Leibniz Supercomputing Center (Leibniz Rechenzentrum) |
| LST | Linear stability theory |
| MICADO | Multidisciplinary Integrated Conceptual Aircraft Design and Optimization environment |
| NLF | Natural laminar flow |
| OAD | Overall aircraft design |
| POD | Proper orthogonal decomposition |
| RBF | Radial basis function |
| ROM | Reduced order model |
| SG | Surrogate |
| SOB | Side-of-body |
| TSI | Tollmien-Schlichting instability |
| TUM | Technical University of Munich |
| (U)RANS | (Unsteady) Reynolds-averaged Navier-Stokes |
| VC | Variable camber |
| VTP | Vertical tail plane |

# 1 Introduction

Next-generation transport aircraft are required to be substantially more fuel-efficient than today's products. Apart from economic aspects, this requirement is primarily founded in environmental aspects, as fuel burn directly translates to $CO_2$ emissions of the aircraft, which need to be significantly reduced within the time frame to 2030 and entirely mitigated until 2050 to meet the requirements formulated by the Advisory Council for Aviation Research and Innovation in Europe [30].
While mid- to long-term developments aim to replace fossil energy carriers with synthetic drop-in kerosene or hydrogen, the requirement for efficiency increase still prevails. This can be attributed to energy carriers remaining a limited resource, next to increasing energy costs and market competitiveness. Furthermore, within the short-term transition phase to novel energy carriers, future aircraft will still be operating on fossil fuels and thus will need to be significantly more efficient in comparison to current products [94].
When determining the key factors driving the performance of an aircraft, the Breguet range equation indicates three key levers, namely aerodynamic and engine efficiency, next to structural weight:

$$R = \frac{1}{g} \overbrace{V \frac{L}{D}}^{\text{Aero}} \underbrace{\frac{1}{SFC}}_{\text{Engine}} \ln \overbrace{\left(\frac{W_i}{W_f}\right)}^{\text{Structure}} \tag{1.1}$$

Each of the associated sub-disciplines of aeronautics has majorly advanced, converging into the latest aircraft designs. Nevertheless, technological disruption in all of them is still required to meet the above-introduced environmental goals [90].

## 1.1 Motivation

For increasing aerodynamic efficiency, two of the most promising techniques consist of hybrid laminar flow control (HLFC) and the introduction of variable camber (VC) capabilities to the wing of an aircraft. The goal of HLFC is to maintain a laminar boundary layer for large areas of the wing through a downstream shift in the transition location of the boundary layer, which is achieved by combining boundary layer suction (LFC: laminar flow control), with a suitable pressure distribution downstream of the suction panel (NLF: Natural Laminar Flow). This reduces the associated skin friction drag, which forms up to 50% of the total drag of an aircraft during cruise flight [110], see Fig. 1.1 (left panel) for a typical drag breakdown.
The application area of HLFC focuses mainly on wing, nacelle and empennage regions of modern configurations. Whilst the fuselage is also connected to a large portion of friction drag, the associated Reynolds numbers are typically excessive concerning HLFC,

next to surface irregularities (e.g. windows, door gaps, sensors), resulting in prohibitive boundary conditions for maintaining large-scale laminar flow.

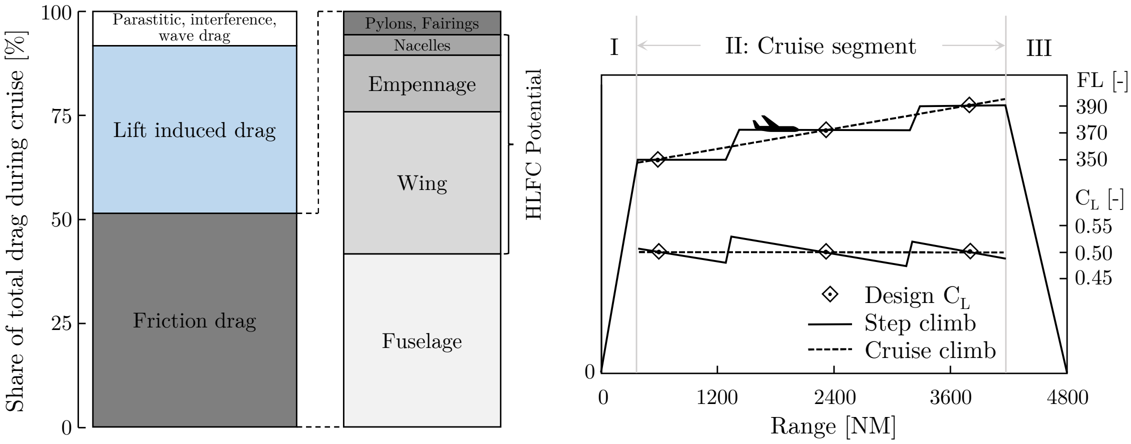


Figure 1.1: Left panel: Typical aircraft drag breakdown during cruise. Right panel: Typical cruise mission profile with associated cruise or step climb procedure between different flight levels (FL). Segments I and III refer to take-off/climb and descent/landing, respectively. Overviews adapted from [101, 110].

The integration of VC capabilities into aircraft wings provides a tool to actively control the pressure and, thus, load distribution of the wing. This is especially targeted at $L/D$ optimization when an aircraft is not operated in its design point, forming a substantial part of a typical mission profile (see Fig. 1.1). To be concise, maximizing the range specified by the Breguet range equation 1.1, given the aircraft's design point through its lift coefficient $C_L$ and flight velocity $V$, results in a so-called cruise climb when considering the optimal flight path [92]. Due to operational restrictions, however, such a flight path is hardly possible in a real application, leading to aircraft typically performing step climbs during the cruise segment. Therefore, keeping the flight velocity fixed, the aircraft faces variations in its required lift coefficient, i.e. it is being operated out of its design point for large parts of the cruise flight duration. This is where the integration of variable camber capabilities to the wing possesses its greatest potential, actively adapting the shape of the wing to the requirements of the current mission segment.

The above-mentioned aspects of VC integration primarily aim to control the spanwise load distribution of the wing, which is directly connected to the lift-induced drag component of the aircraft. Nevertheless, adapting the airfoil through VC integration simultaneously has comparable implications on the streamwise pressure distribution. As will be discussed in Sec. 2.1.2, the latter is a key component of an HLFC system, i.e. to suppress boundary layer transition, an HLFC wing requires an adequate streamwise pressure distribution downstream of the suction panel. Therefore, the possibility arises to exploit a synergistic overlap between both technologies, where synergy refers to the efficiency increase of the coupled technology application exceeding the benefit of individually applying the components. This forms the primary framework for the analyses presented within this thesis, an overview is given in Fig. 1.2.

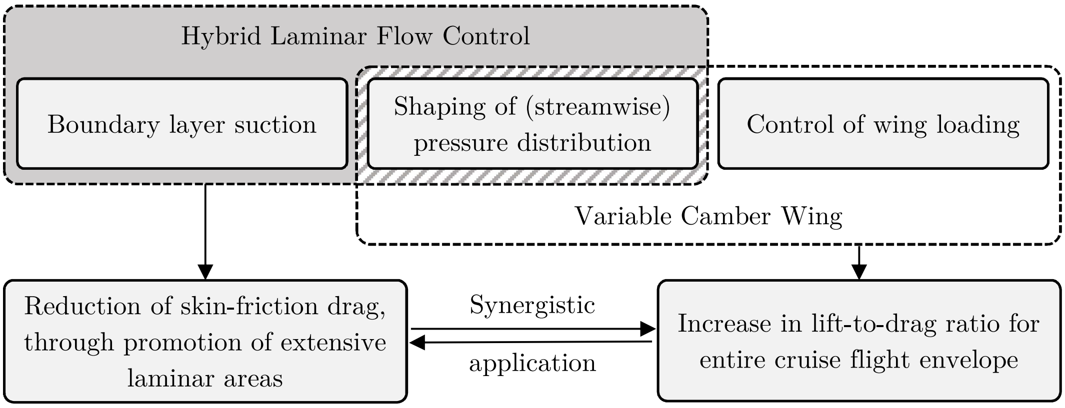


Figure 1.2: Schematic diagram of primary flow control mechanisms, alongside synergistic coupling potential between HLFC and VC for drag reduction.

## 1.2 State of the Art

To build a foundation for the assessments conducted within this thesis, a short overview of work related to both technology bricks is presented below. Furthermore, literature concerning the coupled application of VC and HLFC is introduced, to which the objectives of this thesis are connected. The content of the section closely follows a previously published paper by the author in the journal of *Aerospace Science and Technology* [54][1].

**Hybrid Laminar Flow Control.** The earliest activities concerning laminar flow control (LFC) were conducted within the time frame from the late 1930s to the late 1960s. This first era of LFC research was concluded by a shift in priorities, primarily concerning the United States allocating resources to military programs connected to the Vietnam War. Nevertheless, interest in research and development activities re-emerged after the oil embargo in 1973, with the main goal of reducing fuel burn associated with aircraft operation. This led to numerous research projects in the United States, shortly after which research in Europe was resumed in the time frame starting from the 1980s to today [13, 139].

Concerning European research activities[2], one of the first programs that underwent flight tests was an HLFC system applied on the fin, and later in the inboard section of the wing of a Dassault Aviation Falcon 50 business jet [15]. The experiments primarily

[1] All authors consented to publication in this thesis. 1270-9638/© 2023 Elsevier Masson SAS.

[2] The overview presented in the following focuses on European research programs, for comprehensive overviews of US activities the reader may refer to Refs. [13, 53, 60]

showed the feasibility of controlling boundary layer transition by means of HLFC, even in the highly three-dimensional flow close to an aircraft fuselage. Furthermore, the experiments revealed driving parameters for the suppression of attachment line transition, using boundary layer suction and application of a Gaster bump [37], next to systems for prevention of insect or ice contamination.
Following these investigations, a series of large-scale European research projects were initiated, for a comprehensive overview the reader may refer to Refs. [53] and [139]. Within the projects, numerous wind tunnel and flight tests were performed, both on wings, e.g. by retrofitting a NLF glove on the mid-wing section of a Fokker F100 aircraft [134], and on the vertical tailplanes of transonic transport aircraft.
One of the most prominent examples for the latter is the application of HLFC to the vertical tail plane (VTP) of an Airbus A320. First flight tests were conducted in 1998 [47], underlining the potential for drag reduction and transition control through HLFC. Due to the complexity of the applied suction system, Horstmann et al. [48] introduced a simplified suction system, which was further developed by Schrauf and von Geyr [113], undergoing wind-tunnel tests in 2014. Flight tests with the simplified suction system design were again conducted on the VTP of the ATRA Airbus A320 in the course of the AFLoNext project in 2018. These worked as a proof-of-concept for the simplified suction system and showed the corresponding shift in transition location on the VTP through HLFC integration. An overview of aerodynamic modeling and design techniques via computational fluid dynamics (CFD) and linear stability theory (LST) are described by Schrauf and von Geyr [114], alongside sample results from the flight tests.
Based upon the above-mentioned research results, the latest activities are tailored towards integration and manufacturing aspects of HLFC systems. Within Ref. [10], the authors summarize different efforts for increasing the technology readiness level of a HLFC system, performed within the scope of the European CleanSky 2 project HLFC-WIN. A key result is the ground-based demonstrator of an HLFC wing section, featuring necessary sub-systems for operation and aspects considering maintenance and economic impact of the HLFC system [61].
Up to the present day, the number of aircraft possessing an HLFC system certified for commercial operation is limited. After the above-mentioned flight tests on the Dassault Falcon 50, Dassault certified a Falcon 900 business jet with a HLFC system applied to the inboard station of the wing, accumulating 1000 flight hours from 1995 - 97 with the HLFC system in operation [139]. The latest example of an HLFC system active in operation is on the empennage of the Boeings 787-9 and -10 aircraft, using a passively driven suction system [53]. Nevertheless, details apart from news articles have not been published so far.

**Variable Camber Wing.** Variable Camber (VC) technology has been incorporated as a means of active flow control since the dawn of aviation, e.g. already the

Wright Flyer incorporated a wing that could be seamlessly warped in its twist for controlling the aircraft about its roll axis [5].
While the latter example reflects a deformation of a primary flight structure, i.e. the wing, the way in which roll control or high-lift is achieved on modern airliners has not fundamentally changed. Control surfaces or high-lift devices effectively alter the wing geometry and thus the airfoil camber, adapting the pressure distribution on the wing to achieve the desired behavior of the aircraft.
The above-mentioned use cases of VC may be classified as "conventional" application scenarios. Nevertheless, as introduced above and relevant for this thesis, VC might as well be used to actively adapt the geometry of the aircraft wing to the current operational point during the cruise segment of the aircraft[3]. Thereby, an additional geometrical degree of freedom to the otherwise fixed outer mold line of the wing is added, opening the opportunity for optimization of the aircraft not only to multiple (fixed) operating points, but also to intermediate operating conditions (cf. Sec. 1.1) [85].
The realization of VC can be structured into three main streams, namely adaptation of the entire airfoil shape, adaptation of nose- and trailing edge geometry, or adjustments of the trailing edge geometry solely [125]. Stemming from the first domain, modern materials and processes allow for seamless adaptation of the outer mold line of an airfoil or wing, one of the latest examples being presented by Joo et al. [59]. The concept is termed "Variable Camber Compliant Wing" (VCCW), where numerical studies and wind tunnel tests of a demonstrator segment using composite materials alongside compliant mechanisms indicate the potential for lift-to-drag ratio optimization for an expanded operating parameter range.
The VCCW builds upon earlier studies, one of them being reflected by the "Mission Adaptive Wing" (MAW). The MAW was not only used for analyses considering the possibility of increasing the lift-to-drag ratio [124] through VC, but also for its potential considering maneuver load control [128]. Variable camber integration was achieved by locally adapting the wing shape in the leading and trailing edge regions of an F-111A Fighter Aircraft, using flexible fiberglass elements in connection with sliding panels. Following these analyses, a lot of effort has been directed especially to the structural realization of VC integration, using seamlessly deformable leading and trailing devices. For instance, the so-called "Smart wing model" [65] used shape memory alloys alongside a torque-tube actuation to achieve VC integration, next to twist adaptation of a demonstrator. Nevertheless, while reflecting the corresponding potential in wind-tunnel experiments, upscaling the demonstrator to aircraft level proved impossible due to the power requirements of the system, especially when targeting operation in transonic flight regimes.
A concept designed for transonic flight and especially operation in conjunction with a

[3] Further potential of VC lies, e.g. in maneuver or gust load, shock and buffet control.

laminar wing was developed within the research program ADIF [125]. Variable camber integration in the trailing edge region of the wing was achieved using the so-called "finger concept" [79], which consists in flexible ribs made up of several moveable plates, next to a flexible skin sliding along the deformed ribs of the wing. Furthermore, VC was coupled with shock control bumps within the project, where numerical analysis of such a coupled system approach applied to the wing of an Airbus A340 [20] showed a possible aerodynamic benefit of approx. 4% drag reduction when applying the coupled system. Next to the system consisting in VC and adaptive shock control bumps, the analysis presented in [20] considered HLFC in the aircraft polars by assuming a suitable HLFC system being able to maintain laminar flow on 60% of the wing area.

Latest developments towards VC integration at the trailing edge are for instance presented by Nguyen et al. in Refs. [81, 82]. The system is termed "Variable Camber Continuous Trailing Edge Flap", featuring a VC trailing edge device with multiple segments in chord- and spanwise direction. While the system primarily targets the aspect of aeroelastic tailoring, the numerous degrees of freedom connected to the device assessed a potential benefit of 6% in lift-to-drag ratio when compared to a single-element trailing edge device in wind tunnel tests.

The above-mentioned concepts are all primarily developed for VC integration to aircraft wings, i.e. the primary design goal is to achieve the highest possible geometrical degrees of freedom with the lowest possible system complexity. This typically leads to such systems requiring the usage of mechanisms and materials that do not possess a sufficiently high technology readiness level for the short- to mid-term time frame envisaged within this thesis. Furthermore, VC application is subject to operational constraints in a realistic scenario. That means, integrating VC due to deformation of the entire airfoil will not be possible in the near future, due to the installation space of the deformation mechanisms being blocked by the fuel tanks within the wings. Integrating VC in trailing and leading edge regions of the wing is primarily subject to high-lift requirements of the aircraft during take-off and landing, further limiting the above-mentioned design freedom by this requirement.

Nevertheless, the latter aspect not only limits but also opens an attractive method for VC integration in terms of the multi-functional usage of modern high-lift devices. Such integration is presented by Strüber and Reckzeh in Refs. [127] and [93], respectively, where VC capabilities are implemented to the wing of the Airbus A350 XWB via deflections of the "Adaptive Dropped Hinge Flap" (ADHF). The design philosophy of the high-lift system is tailored towards the multi-functional character as a VC system. Multi-functionality is achieved through the Fowler motion of the dropped hinge flap being accompanied by a spoiler droop, and a simplified kinematics system allowing for streamwise deflection of the flap, leading to a completely sealed flap gap for deflection angles between $\delta_{ADHF} = [-2°; 4°]$.

A similar approach is used on the wing of Boeing's 787 aircraft family [72, 80]. Again a Fowler-type flap is applied alongside a spoiler droop, leading to the desired multi-functionality of the high-lift system for VC integration. Both approaches are operative in the latest products of the two biggest airframers and, therefore, represent the latest state of operative VC integration applicable to the analyses performed within this thesis.

**HLFC - VC Coupled Application.** In the paragraph above, constraints and limitations towards the application of VC for the analyses within this thesis were formulated, leading to the most promising concept being the multi-functional usage of high-lift devices for VC integration. Nevertheless, further considerations have to be made when aiming for a HLFC/VC system coupling. These aspects primarily target VC integration in the leading edge region of the wing, where the HLFC suction system is situated.
At first, a major concern for the operation of an HLFC system is imposed by the prevention of wing contamination. On one hand, this refers to insects or ice accumulating in the leading edge region of the wing during take-off and climb, ultimately tripping the boundary layer to premature transition in the same region. On the other hand, insects as well as ice might block the holes of the HLFC suction panel, for which the system is not able to provide a sufficient suction mass flow to suppress boundary layer transition. Secondly, VC integration in the leading edge region of the wing is limited to contour deformations of the lower side of the airfoil. Suction is typically applied only to the upper side of the wing, while the suction panel is fabricated from a perforated titanium sheet and may not be deformed. Furthermore, the upper surface of the wing incorporating the HLFC system needs to be smooth, which prohibits the usage of any leading edge device requiring a gap on the upper surface of the wing.
The "go-to solution" used to provide for contamination shielding, alongside sufficient high-lift performance of the wing, is the application of a Krueger flap at the leading edge of the wing [50]. This approach is, for instance, also realized in the HLFC ground-based demonstrator introduced above in Ref. [10]. While satisfying the above-mentioned requirements, this limits the application region of VC to the trailing edge region of the wing, at least considering the technology status presumed within this thesis.
Different studies already indicate the potential of coupling both technologies synergistically. Greff formulated VC incorporation being a "prerequisite for a HLFC wing to control the pressure gradients and the off-design behaviour" [41], while formulating different aerodynamic design constraints and interplays with aeroelasticity, aircraft weight and performance. Later, Edi [27] and Edi and Fielding [28] developed a design methodology and applied a simplified drag prediction methodology to assess the technology coupling, showing a potential drag reduction of 10%.
Further aspects considering the effects of camber variations on off-design operations of an HLFC system are included for instance in [89], where in the course of airfoil design for Boeing's HLFC flight tests on the wing of a Boeing 757 [139], optimal trailing edge flap deflection angles for extensions of the HLFC envelope are studied.
The above-mentioned references present a baseline from which this work initiates. While

the potential is indicated, there is a lack of systematic assessments on full-scale realistic configurations, especially envisaging three-dimensional aerodynamic effects at flight Mach and Reynolds numbers. Modern, high-fidelity computational tools open the possibility for further analyses, from which the main objectives of the present thesis are derived.

## 1.3 Objectives and Thesis Outline

The goal of the present thesis is to analyze the above-introduced technology coupling using high-fidelity numerical tools and to assess the possible synergistic potential and trade-off effects from the viewpoint of configurational aerodynamics. The focus lies on the potential to reduce aerodynamic drag during the cruise segment of a typical transonic transport mission, especially considering the operation of the aircraft for variable operating conditions. The assessments are performed on a set of realistic configurations, extending the current state-of-the-art in different aspects.

A key element of the analyses is the prediction of transition position on swept, tapered aircraft wings. As substantial variations characterize the parameter space for the herein-presented observations, this poses constraints on the applicable numerical simulation tools. Reynolds-averaged Navier-Stokes simulations offer the best trade-off between accuracy and computational cost, for which they present the core element for flow simulation within this thesis. The go-to solution in an engineering or industrial context for transition prediction is linear stability theory coupled to an $e^N$-Method. While the method is not free of empiricism (in the choice of critical $N$-factors) and a set of modeling assumptions used in the context of the two-$N$-factor method introduced later in this thesis (see Sec. 2.2.2.2). Next to its maturity, it offers the advantage of being directly calibratable through experimental data and possessing a high level of compatibility to the workflow of a typical CFD simulation. The systematic coupling within the context of combination with a VC-system has not been documented so far in this context.

More recent approaches for transition prediction, in the framework of turbulence modeling, are also applied and analyzed within this thesis. A toolchain for modeling the influence of an active boundary layer suction system is presented within this thesis (see Sec. 2.3.1), and the influence on driving relations of one of the most widely spread local-correlation based transition transport models (LCTM), the $\gamma - Re_\theta$+CF model, are assessed.

Results with both transition prediction approaches, on isolated wing level are presented in chapter 3, while the analysis is extended to configuration level in chapter 4, both for design as well as off-design conditions.

This work originated from the joint research project CATeW[4] (Coupled Aerodynamic

[4] Funded within the scope of the German national civil aviation research programme (LuFo VI-1) of the Federal Ministry for Economic and Affairs and Climate Action (BMWK), FKZ: 20E1917B

Technologies for Aircraft Wings) between the author's institution, the chair of Aerodynamics and Fluid Mechanics of the Technical University of Munich, and the Institute of Aerospace Systems of RWTH Aachen University. A dedicated goal of the project was not only the aerodynamic assessment of the technology coupling introduced above but also consisted of the formulation of reduced order models based on the comprehensive aerodynamic data sets. This allows for an efficient data flow of high-fidelity simulation data into low-fidelity toolchains, such as those used by the project partner for analysis on system level and in the context of overall aircraft design. Therefore, chapter 5 of the thesis is dedicated to the application and formulation of different methodologies for model order reduction, suitable for direct integration into low-fidelity aerodynamic toolchains. This aspect builds an indispensable building block to assess the aerodynamic benefits introduced by the technology coupling on the overall aircraft level. A general overview of the thesis structure can be extracted from Fig. 1.3.

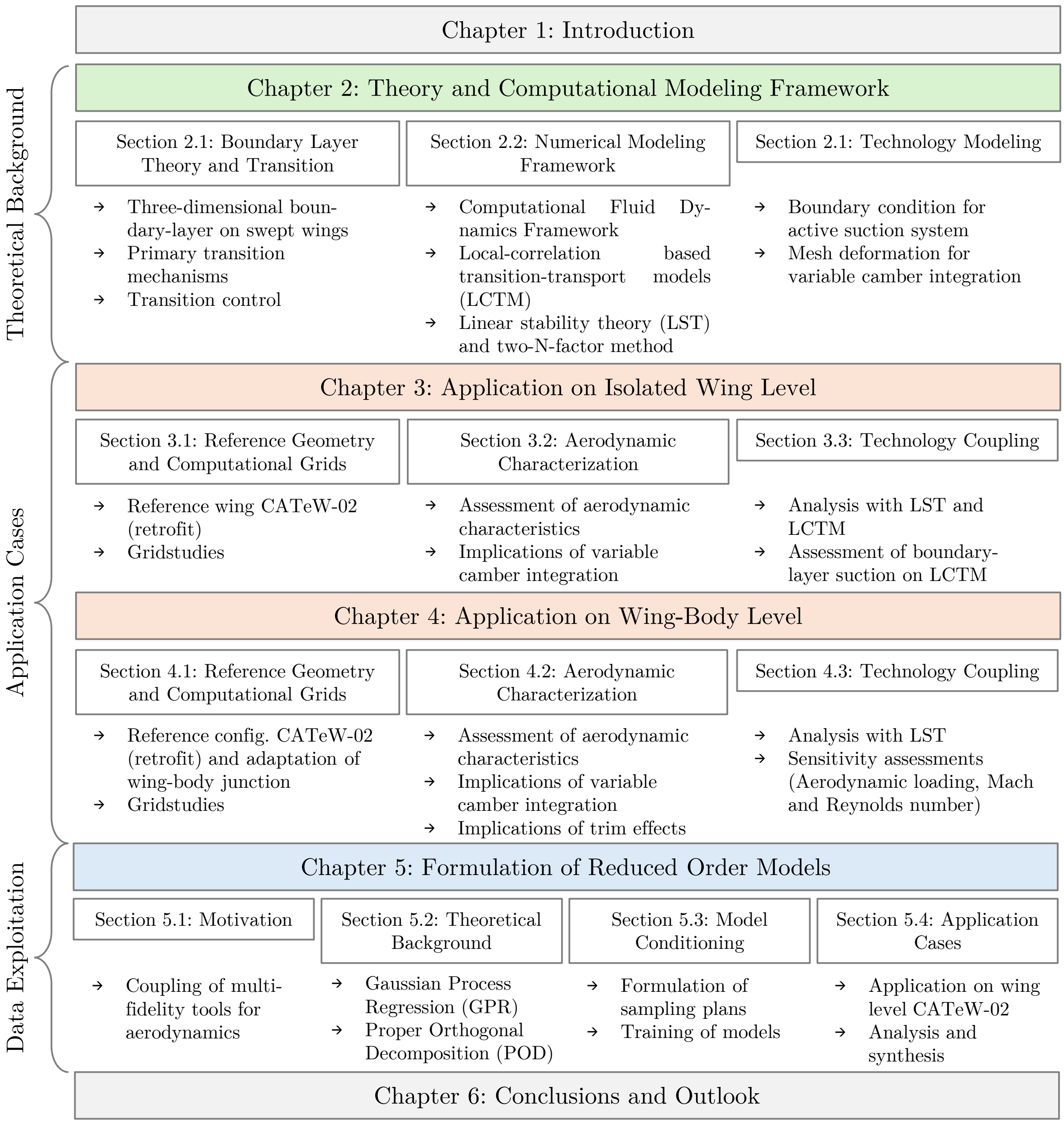


Figure 1.3: Overview of the thesis structure.

# 2 Theory and Computational Modeling Framework

The following chapter gives an overview of relevant theoretical and methodical aspects for the herein presented analyses. Within Sec. 2.1, an introduction to boundary layer theory with a special focus on the mechanism of laminar-turbulent transition and transition control is presented, see Secs. 2.1.1 and 2.1.2, respectively.
The numerical framework for the analyses in terms of Reynolds-averaged Navier-Stokes (RANS) simulations is presented in Sec. 2.2.1, while later applied tools for transition prediction in terms of local correlation-based transition turbulence models (Sec. 2.2.2.1) and linear stability theory (Sec. 2.2.2.2) are introduced.
The implemented framework for modeling an active suction system within a numerical simulation is presented in Sec. 2.3.1, followed by details considering the modeling approach for variable camber integration in Sec. 2.3.2, with a brief overview of the modeling methods integration into an automated software framework in Sec. 2.3.3 concluding the chapter.

## 2.1 Boundary Layer Theory and Transition

Before Prandtl introduced the concept of the boundary layer in his conference contribution *"Über die Flüssigkeitsbewegung bei sehr kleiner Reibung"* [88], (analytical) solution of the governing flow equations was only possible assuming inviscid flows, i.e. observing the limiting case of the Reynolds number [107]:

$$Re = \frac{u_\infty l_{ref}}{\nu} \tag{2.1}$$

approaching $Re \to \infty$.
Nevertheless, examples such as D'Alembert's paradox[1] underline the importance of incorporating viscous effects into the analysis of wall-bounded flows characterized by high, but finite Reynolds numbers.
Prandtl, therefore, proposed dividing the flow field around bodies into two regions - an inviscid or potential outer flow region and a thin, viscous boundary layer, fulfilling the no-slip condition directly at the wall and matching the outer potential flow conditions at the boundary layer edge. Confining viscous effects to the boundary layer leads to significant simplifications of the governing equations, enabling the theoretical study of wall-bounded flows and forming the backbone of modern computational methods for the

[1] Assuming inviscid, subsonic incompressible flow, closed objects moving through a fluid experience only normal or pressure forces. Neglecting viscous shear forces leads to the contributions of the pressure forces mutually neutralizing, for which the theory predicts no drag force being exerted onto the object - a clear contradiction with real-world observations [107].

solution of the Navier-Stokes equations, cf. Sec. 2.2.
Since there is no sharp interface between the boundary layer and the "inviscid" outer flow, the boundary layer thickness $\delta$ is typically defined as the wall-normal distance $y$, at which the $x$-velocity component $u$ within the boundary layer reaches 99% of the inviscid outer flow velocity $u_\infty$. Further key metrics for the description of a boundary layer's effect on the outer flow are the displacement thickness $\delta_1$ [126]:

$$\delta_1 = \lim_{\zeta \to \infty} \int_0^\zeta \left(1 - \frac{\rho(x,y)u(x,y)}{\rho_\infty u_\infty}\right) dy \tag{2.2}$$

characterizing the displacement of the inviscid outer flow streamlines due to the existence of the boundary layer[2] and the momentum thickness $\theta$:

$$\theta = \lim_{\zeta \to \infty} \int_0^\zeta \frac{\rho(x,y)u(x,y)}{\rho_\infty u_\infty} \left(1 - \frac{u(x,y)}{u_\infty}\right) dy \tag{2.3}$$

which correspondingly characterizes the momentum flux deficit imposed by the boundary layer [107]. The ratio of displacement thickness to momentum thickness is referred to as the shape factor $H_{12}$:

$$H_{12} = \frac{\delta_1}{\theta} \tag{2.4}$$

Phenomenologically, the shape factor is associated with the "fullness" of a boundary layer velocity profile, where a lower shape factor is characteristic of a fuller velocity profile, see the left panel of Fig. 2.1.
Referring to Sec. 2.2.2.2 for a further overview of the mathematical description of the boundary layer, another decisive distinction for the thesis at hand concerns the boundary layer state. One generally speaks of a boundary layer being either laminar, transitional or turbulent, referring to characteristics of the fluid flow constituting the boundary layer. Reynolds first documented this distinction after his well-known dye experiments in 1883 [99]. Depending on the flow Reynolds number, he observed the fluid particles either orderly following their streamlines (laminar flow) or, after reaching a critical Reynolds number, transitioning to an irregular flow pattern (turbulent flow). This pattern is characterized by the formation of coherent eddies and, thus, an increased momentum exchange between different fluid layers. The critical Reynolds number for which such pipe flows undergo transition from laminar to turbulent is $Re \approx 2300$. Considering the formulation of the Reynolds number introduced in Eq. 2.1 raises the physical intuition, that laminar flows are rather the exception than the rule. That is, laminar flows are connected to either small length scales and low velocities or high viscosity, rendering most technically relevant external aerodynamic flow scenarios turbulent [18]. The state of the boundary layer is connected to different implications for wall-bounded

[2] In other words, the necessary thickening of the body contour line when considering purely inviscid flow to match the displacement effect imposed by the wall-normal mass flux defect of the boundary layer.

as well as free-shear flows. In the context of this thesis, the most important metric is connected to the shear stress $\tau$ and the skin friction coefficient $c_f$, correspondingly imposed by the shear stress at the wall station $\tau_w$ onto a body [107]:

$$\tau = (\mu + \mu_T)\frac{du}{dy} \tag{2.5}$$

$$c_f = \frac{\tau_w}{q_\infty} = \frac{\tau_w}{\frac{1}{2}\rho u_\infty^2} \tag{2.6}$$

The term $\mu_T$ constitutes the eddy-viscosity, which, in the context of the Reynolds-averaged Navier-Stokes (RANS) equations alongside the eddy-viscosity hypothesis, is used as an auxiliary variable to reflect the effects of turbulent mixing on the boundary layer velocity profile, i.e. model turbulent shear stresses or Reynolds-stresses (see Sec. 2.2.1).

As apparent from Eq. 2.5, a central characteristic of a laminar boundary layer is lower skin friction in comparison to its turbulent counterpart, as $\mu_T \approx 0$ for a laminar boundary layer, which in turn directly influences the $u$ velocity profile and its wall-normal gradient, see Fig. 2.1. The additional eddy-viscosity tends to make the turbulent velocity profile fuller, as indicated by the associated shape factors $H_{12}$. A characteristic of a turbulent boundary layer is its turbulent "knee", arising due to the eddy-viscosity distribution in wall-normal direction, and leading to a sharp flow deceleration in the wall layer[3] (up to $y \approx 0.2\delta$) of the turbulent boundary layer.

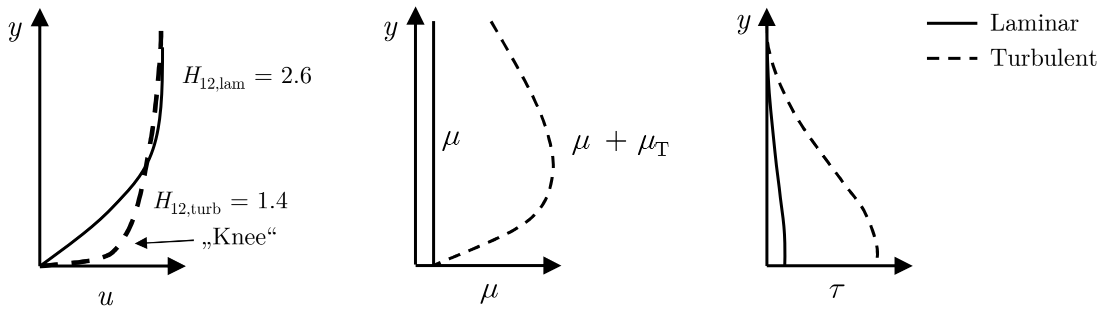


Figure 2.1: Sketch of characteristic streamwise velocity profiles (left panel), viscosity (mid panel) and shear stress (right panel) distributions throughout laminar and turbulent boundary layers, adapted from [23].

On the other hand, a turbulent boundary layer is associated with greater resistance to adverse pressure gradients and thus flow separation, when compared to a laminar one.

[3] Referring to the near-wall layer of a turbulent boundary layer, consisting of the viscous sublayer and the buffer layer. The presence of the wall tends to dampen turbulent fluctuations, for which the wall layer is dominated by viscous effects [68].

Using the two-dimensional $x$-momentum equation with $y$ defining the wall-normal direction and $x$ the (locally) streamwise-oriented direction, a change in fluid velocity $\Delta u$ over an increment $\Delta x$ can be expressed as [23]:

$$\Delta u \simeq \frac{\partial u}{\partial x}\Delta x = \frac{\rho_\infty u_\infty}{\rho u}\Delta u_e + \frac{1}{\rho u}\frac{\partial \tau}{\partial y}\Delta x \tag{2.7}$$

The velocity increment $\Delta u_e$ is directly connected to the streamwise pressure gradient $dp/dx$ and is constant throughout the boundary layer, i.e. it is typically assumed that $dp/dy \approx 0$ throughout the boundary layer. One speaks of the inviscid flow pressure distributions being impressed onto the boundary layer. Therefore, the term $\rho_\infty u_\infty/\rho u$ linearly scales the corresponding $\Delta u_e$ throughout the boundary layer, for which an adverse pressure gradient $dp/dx > 0$ leads to less deceleration over a streamwise increment $\Delta x$ considering the higher momentum associated with a turbulent boundary layer compared to a laminar one. Taking into account the point of flow separation being connected to flow reversal at the wall station of the boundary layer, i.e. $(\partial u/\partial y)_\mathrm{w} = 0$, gives the turbulent boundary layer its higher separation resistance, which is of primary concern when it comes to avoiding excessively high form drag on a body.

Following the main characteristics introduced above, two primary scenarios can be deducted considering whether a laminar or a turbulent boundary layer is advantageous for the technical application at hand. When the primary concern is to reduce skin friction drag, the boundary layer should be maintained laminar as far downstream as possible. In contrast, if the boundary layer is exposed to strong adverse pressure gradients, a turbulent boundary layer is beneficial, due to its higher resistance to flow separation.

As the Reynolds number associated with a transonic transport aircraft during cruise is typically in the orders of magnitude of $\mathcal{O}(10^7)$, and thus connected to a turbulent boundary layer, critical transition mechanisms need to be suppressed to exploit the potential to minimize the friction drag component (cf. Fig. 1.1), e.g., by employing hybrid laminar flow control.

### 2.1.1 Dominant Transition Mechanisms

The change of state of a boundary layer from laminar to turbulent is called boundary layer transition. From a phenomenological viewpoint, transition initiates from a laminar boundary layer experiencing a disturbance. These disturbances amplify and lead to the development of instabilities within the boundary layer, ultimately triggering the transition to a turbulent state at some point further downstream.

A widespread overview of the different possible transition paths is adapted from [105] in Fig. 2.2. As indicated above, a disturbance originating from, e.g., freestream turbulence, sound waves, or surface irregularities is transferred into the initially laminar boundary layer by the process of receptivity. Depending on the amplitude of the disturbance, two core scenarios for transition can be identified. In the case of small disturbance amplitudes (Path I, Fig. 2.2), the growth of the so-called primary modes developing within the laminar boundary layer is relatively slow and of small amplitude, thus can be described using a linearized form of the boundary layer equations and performing a corresponding stability analysis (cf. Sec. 2.2.2.2). Considering the low turbulence environment an aircraft faces during the cruise segment, this path is crucial when it comes to transition on transport aircraft wings, for which path I reflects what is referred to as natural transition.

Since the incurring disturbances associated with primary instability modes are weak, their growth is subject to and thus can be controlled by pressure gradients, surface mass transfer (suction) and temperature distributions, see Sec. 2.1.2. Nevertheless, once the disturbances reach a specific amplitude, the linearized ansatz is no longer applicable, as three-dimensional and nonlinear interactions lead to the development of secondary mechanisms, for which rapid disturbance growth ultimately provokes the breakdown of the laminar flow into turbulence.

The second critical scenario for transition is denoted as path V in Fig. 2.2. For large environmental disturbances, the growth of primary modes and subsequent development of secondary mechanisms are bypassed and transition is caused immediately, for which this mechanism is termed Bypass-Transition.

Paths II - IV in Fig. 2.2 refer to what is known as transient growth, which results from the interaction of two stable boundary layer modes. Depending on the disturbance amplitude, this process triggers any of the critical mechanisms described above [105].

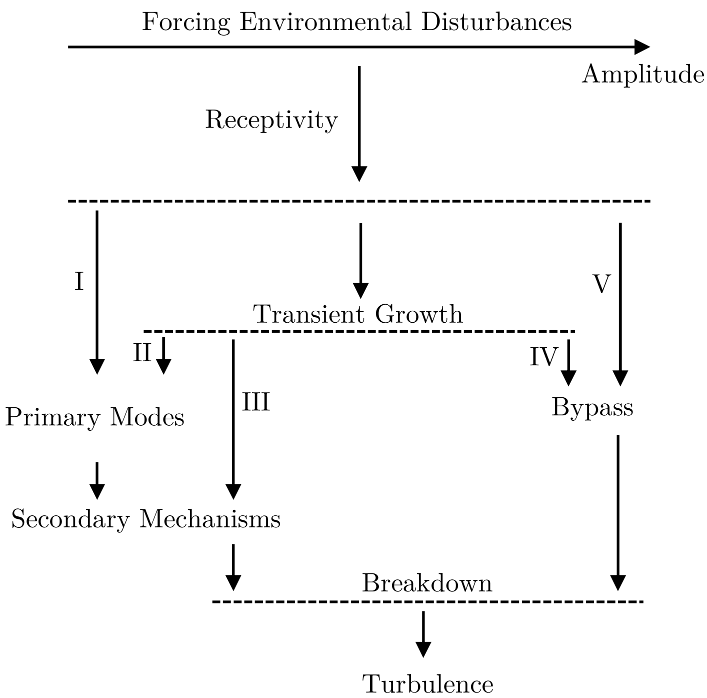


Figure 2.2: Overview of different mechanisms characterizing the transition process, adapted from [105].

Considering the application case of the thesis at hand, the main focus is upon the boundary layer developing for attached, wall-bounded flows around swept, high aspect ratio aircraft wings, as schematically presented in Fig. 2.3. When considering a laminar wing, the critical path to transition is reflected by primary instability modes, i.e. path I in Fig. 2.2 needs to be suppressed. From this group, a series of different primary transition modes are of central importance when it comes to maintaining laminar flow through HLFC application, namely attachment line transition (ALT), cross-flow instabilities (CFI) and Tollmien-Schlichting instabilities (TSI). Each of these transition mechanisms is connected to a critical region on an aircraft wing (see Fig. 2.3) and will be presented in more detail in the following.

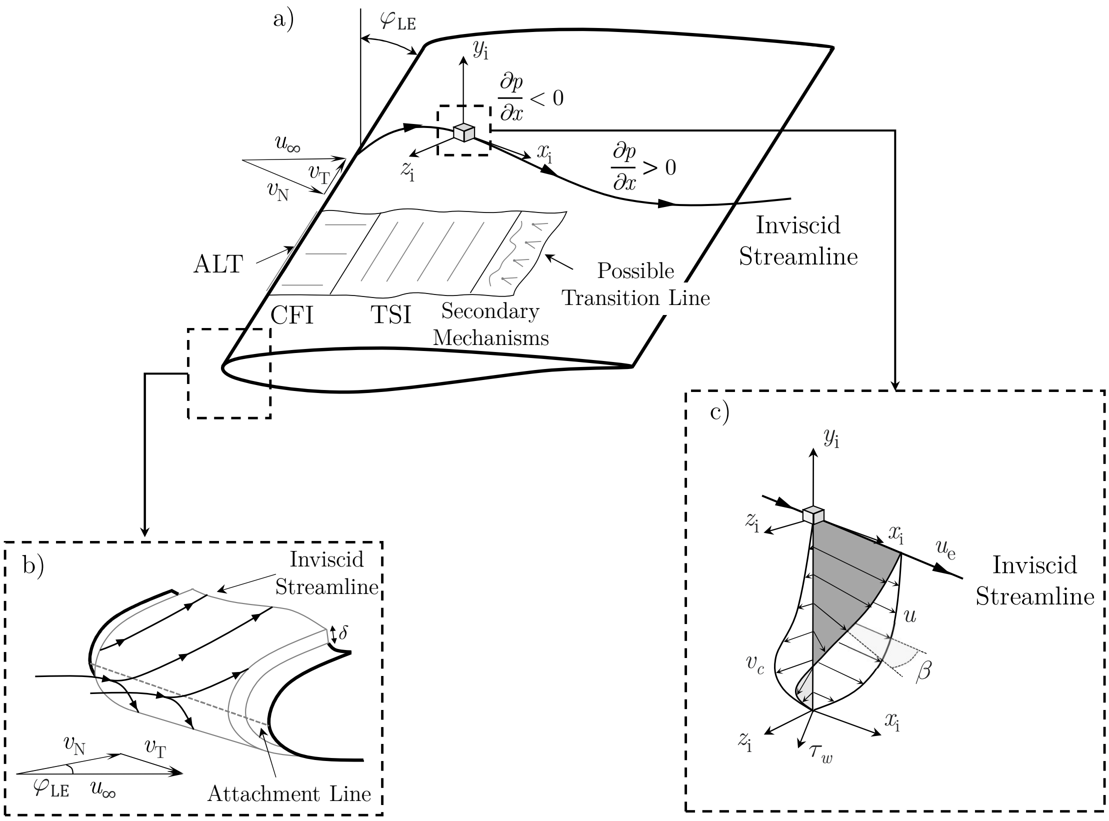


Figure 2.3: Panel a): Overview of three-dimensional inviscid streamline development on swept aircraft wings, alongside an indication of critical regions for different primary transition mechanisms. Panel b): Detailed view of attachment line flow. Panel c): Detailed view of three-dimensional boundary layer velocity profile. Adapted from [9, 60, 107].

**Attachment Line Transition.** The flow around the attachment line of a swept wing is schematically depicted in Fig. 2.3 b). In contrast to a purely two-dimensional flow, no designated stagnation point develops, but the flow attaches along a so-called attachment line. As shown in Fig. 2.3 b), the freestream velocity vector $u_\infty$ can be split into a leading edge normal velocity component $v_N$, and a tangential velocity component $v_T$, where the latter, spanwise velocity component is dominant concerning the development of the attachment line boundary layer. Over a series of bifurcations, the chordwise velocity component of the inviscid outer streamline increases, therefore curving the streamlines in the direction of the freestream [38].

The attachment line boundary layer might undergo transition from laminar to turbulent flow due to two different effects. First, as a type of bypass transition, disturbances from, e.g., the turbulent fuselage boundary layer might propagate into the attachment line boundary layer along the wing-body junction, rendering the attachment line completely turbulent along the entire wing span. This phenomenon is termed leading edge contamination (LEC) and must be suppressed in the context of a laminar wing, e.g. through utilization of a Gaster bump [37], as the initial state of the attachment line boundary layer dictates the boundary layer state of the entire wing.

Additionally, due to the structure of the attachment line boundary layer being primarily two-dimensional in spanwise direction, it might undergo natural transition due to Tollmien-Schlichting type instabilities (see paragraph below) [8].

Quantitatively, two different criteria are typically applied to assess whether the attachment line boundary layer is laminar or turbulent. These criteria are based on the attachment line momentum thickness Reynolds number $Re_{\theta,AL}$ [31]:

$$Re_{\theta,AL} = \frac{v_T \theta_{AL}}{\nu} \tag{2.8}$$

where $Re_{\theta,AL}$ is typically expressed as $Re_{\theta,AL} = 0.4044\overline{R}$, with $\overline{R}$ denoting a velocity gradient based Reynolds number stemming from the analytical solution of a swept Hiemenz flow[4], i.e. the attachment line flow about an infinitely long swept cylinder [38].

Following theoretical [43] and experimental investigations by Pfenninger [86] and Poll [87], the Pfenninger-Poll criterion builds upon the critical momentum thickness Reynolds numbers $Re_{\theta,AL,nat} = 230$ and $Re_{\theta,AL,LEC} = 100$, typically applied in the cases of natural transition of the attachment line boundary layer or leading edge contamination, respectively [60].

**Cross-Flow Instability.** Downstream of the wing leading edge region, the swept-wing boundary layer possesses a marked three-dimensional structure. This is a result of the spanwise pressure gradient arising due to the geometric sweep of the wing, typically manifesting itself in an s-shaped inviscid streamline shape (see Fig. 2.3 a). As exemplarily sketched in Fig 2.3 c), the three-dimensional boundary layer velocity profile consists of a cross-flow velocity component $v_c$ and a streamwise (local flow direction) velocity component $u$, the superposition of which leads to the skewed three-dimensional velocity profile. As indicated above, the cross-flow velocity component develops due to the

[4] Thus being a function of the leading edge or cylinder radius, the leading edge sweep angle and the unit Reynolds number [101]

(constant) spanwise pressure gradient acting upon portions with different momentum throughout the boundary layer. Low momentum portions of the boundary layer, close to the wall, face a more pronounced acceleration due to the spanwise pressure gradient, whereas approaching the boundary layer edge, centrifugal forces balance the pressure forces exerted onto the fluid particles.

As the cross-flow velocity components are zero both at the wall station and the edge of the boundary layer, a cross-flow velocity profile inherently possesses an inflection point, which according to the criterion initially introduced by Rayleigh [69] and later further developed by Tollmien [130], presents a sufficient criterion for the existence of inviscid instability [107].

Transition due to cross-flow instability is critical for geometric sweep angles $\varphi_{LE} > 25°$, especially in the leading edge region of the wing where high flow acceleration leads to the development of strong cross-flow profiles. Cross-flow instabilities manifest themselves as a set of stationary, co-rotating vortices, where the corresponding vortex axes are aligned with the inviscid streamline direction $x_i$ [107].

**Tollmien-Schlichting Instability.** Tollmien-Schlichting instabilities are the primary transition mechanism when considering quasi two-dimensional boundary layers, and are therefore critical for unswept wings, or, provided neither ALT nor CFI causes premature transition, in the mid-chord region of a swept wing, typically in the adverse pressure gradient region downstream of the point of minimum pressure. This is due to an adverse pressure gradient highly destabilizing a laminar boundary layer towards primary instability modes. As discussed in the last part of Sec. 2.1, this is connected to an adverse pressure gradient leading to a strong flow deceleration throughout the laminar boundary layer and, thus, as for CFI, promoting the development of an inflected boundary layer velocity profile. On the other hand, a negative (or proverse) pressure gradient $dp/dx < 0$ leads to the opposite effect, namely a stabilization of the streamwise boundary layer profile as it acts in making the profile fuller, i.e., decreasing its shape factor $H_{12}$.

Tollmien-Schlichting instabilities, named after the theoretical foundations of Tollmien [129] and Schlichting [106], are disturbance waves propagating in the streamwise direction of the boundary layer. As depicted in Fig. 2.4, the transition process due to TSI possesses several distinct stages.

The process of receptivity initially transfers external disturbances into the laminar boundary layer. These disturbances are initially damped within the laminar boundary layer (I) up to a specific location characterized by the indifference Reynolds number $Re_{ind}$, which determines the first point within the boundary layer at which disturbances are amplified and form Tollmien-Schlichting waves (II). The growth of these waves can be described by linear stability theory (see Sec. 2.2.2.2). As presented in Fig. 2.2, at a point further downstream secondary instabilities develop, ultimately leading to the formation of so-called $\Lambda$-vortices (III), which decay (IV) and promote the development of turbulent spots (V), representing the seed points for fully turbulent flow at the critical Reynolds number $Re_{crit}$ (VI) [107].

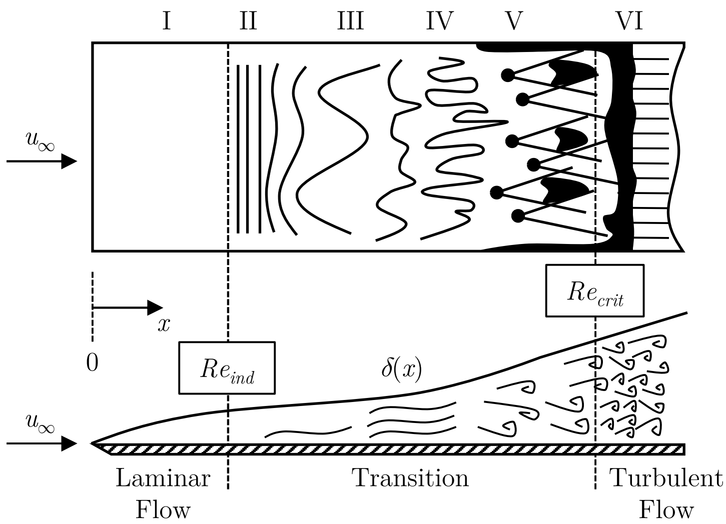


Figure 2.4: Characteristic stages of the transition process driven by Tollmien-Schlichting instabilities, adapted from [107].

**Other Transition Mechanisms.** The previously discussed transition mechanisms are central when it comes to HLFC. Nevertheless, a series of further transition mechanisms exist, possibly arising on aircraft wings, described in the following paragraph.
One of them is separated-flow transition, where a laminar boundary layer separates, for instance, due to a pronounced adverse pressure gradient or from a sharp geometrical edge, with the transition process subsequently taking place in the free-shear layer. Depending on the strength of the adverse pressure gradient, the turbulent shear layer either reattaches, forming what is known as a laminar separation bubble, or stays completely separated. The transition mechanism is attributed to a combination of Tollmien-Schlichting waves in the attached laminar boundary layer, leading to the amplification of Kelvin-Helmholtz instabilities in the free-shear layer [42, 126].
Another transition mechanism is reflected through the formation of (Taylor-)Görtler instabilities. These instabilities manifest themselves as counter-rotating vortex pairs, which form due to centrifugal forces in concave parts of the airfoil, e.g. as present in the trailing edge region of the lower airfoil side [107]. Nevertheless, in the context of a transonic swept wing, Görtler instabilities are typically not critical, as the boundary layer will undergo transition upstream of the above-mentioned region.

### 2.1.2 Transition Control

Each critical transition mechanism presented in Sec. 2.1.1 is influenced by a series of parameters and, thus, can be controlled by adequately setting them. From a purely aerodynamic viewpoint, one can define a set of "external" parameters, such as the freestream turbulence intensity [107]:

$$Tu = \sqrt{\frac{\frac{1}{3}(\overline{u'}^2 + \overline{v'}^2 + \overline{w'}^2)}{u_\infty}} \tag{2.9}$$

where prime denotes fluctuating velocity components in a turbulent velocity field, acoustic disturbances, e.g. stemming from engine noise, or the surface quality of the aircraft wing. External refers to these parameters not being primarily connected to the aerodynamic design of an aircraft. Parameters influenced by mission planning include the flight Mach and Reynolds numbers, the latter connecting the aircraft's operating point to its wing shape through the corresponding planform. Connected to the planform, key parameters from an aerodynamic viewpoint are correspondingly the three-dimensional wing and airfoil shapes. These transfer to one of the central levers for passive transition control, namely achieving an adequate pressure distribution and gradient on the wing surface, promoting a laminar boundary layer. Finally, arising from the domain of active transition control, the inclusion of boundary layer suction and control of the wall temperature reflect central parameters affecting the transition development on a wing [31, 107].
Following the differentiation in terms of external, passive, or active parameters influencing transition, different technological solutions emerged for controlling and delaying transition on swept aircraft wings, an overview of which is presented in Fig. 2.5.

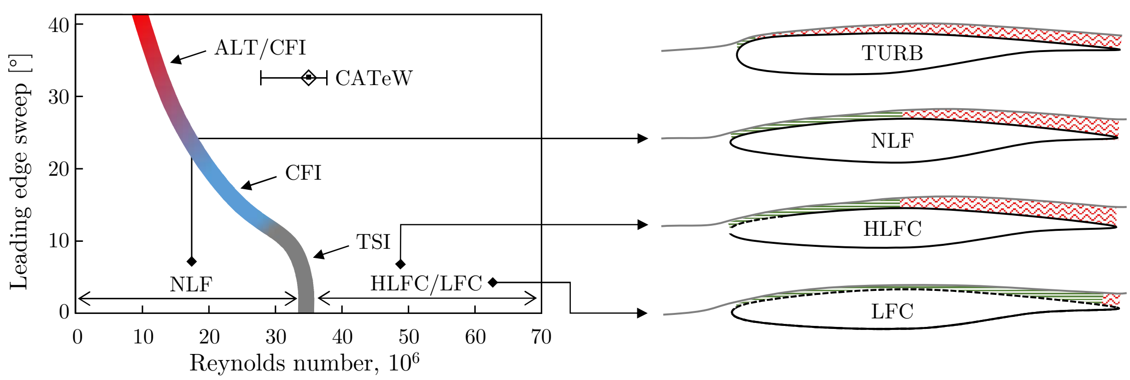


Figure 2.5: Characteristic transition mechanisms in dependence of wing sweep angle and cruise Reynolds number, with additional indication and schematic representation of applicable techniques (NLF, LFC, HLFC) for maintaining laminar flow. Adapted from [53, 101, 110]

The first technique is denoted as natural laminar flow (NLF), where boundary layer transition is delayed solely by passive means. This is realized by choosing an adequate planform (unswept or marginally swept wings) and airfoil geometry, which achieves the desired pressure distribution on the wing surface. So-called laminar airfoils implement small leading edge-radii, while the point of maximum thickness is shifted downstream in comparison to, e.g., classical supercritical airfoil as the one sketched on the top right of Fig. 2.5. This design promotes the development of a pressure distribution characterized by an extensive region of negative pressure gradient flow, which, as mentioned in Sec. 2.1.1, stabilizes the laminar boundary layer concerning Tollmien-Schlichting instabilities. The transonic flight regime of transport aircraft necessitates a leading edge sweep angle that exceeds the range of applicability of NLF, making it technically advantageous to resort to what is known as laminar flow control (LFC). This is connected to the critical transition mechanisms switching from TSI to ALT and CFI for $\varphi > 20°$ [98], where especially the latter cannot be controlled effectively by shaping the pressure distribution, as any pressure gradient acts in a destabilizing way upon the cross-flow velocity profile [121].

Laminar flow control refers to applying suction on the entire chord length of the airfoil. Boundary layer suction is the most effective way of suppressing transition due to CFI. Suction stabilizes the boundary layer velocity profile by reducing the boundary layer thickness, therefore making the velocity profile "fuller". From a flow physical viewpoint, the stability increase of a thinner boundary layer is associated with vortical disturbances being drawn closer to the wall, where higher dissipation reduces the associated amplification rates of instability modes [19]. Consequently, suction is not only applicable for the stabilization of the flow concerning CFI but also enhances the stability of a laminar boundary layer with respect to TSI and ALT. Wall cooling has shown a similar effect in stabilizing TSI but, apart from the technical challenge connected to the provision of a sufficient temperature gradient towards the wall, is much less effective for controlling CFI compared to suction [60].

The combination of NLF and LFC is known as hybrid laminar flow control (HLFC). As introduced above, suction is applied in the front region of the airfoil, typically up to the front spar of the wing, to avoid premature transition due to CFI and ALT (cf. Fig. 2.3 a). Downstream of the suction panel, the dominant transition mechanism is TSI, for which it suffices to naturally stabilize the flow by assuring a large extent of negative pressure gradient flow. Requirements towards the pressure distribution for an HLFC airfoil will be discussed in the context of the isolated wing results in Sec. 3.2.2.

## 2.2 Numerical Modeling Framework

The assessments of the VC-HLFC technology coupling presented within this thesis are performed in the context of a RANS framework, where the DLR TAU Code [119] is employed as flow solver. Therefore, an overview of the governing flow equations in their Reynolds-averaged form is provided in Sec. 2.2.1, with an additional focus on the aspect of turbulence modeling. One central requirement of the computational framework concerns the incorporation of boundary-layer transition due to the above-introduced mechanisms into the simulations, more precisely in an automatic prediction of the transition location, which is subsequently imposed onto the CFD solution during run time. To achieve this goal, two different philosophies are presented in Secs. 2.2.2.1 and 2.2.2.2, one employing the $\gamma - Re_\theta$+CF model, stemming from the domain of local-correlation based transition turbulence-models (LCTM), and on the other hand linear stability theory (LST) using the two-$N$-factor method, coupled to a conical boundary layer code and the flow solver.

### 2.2.1 Computational Fluid Dynamics

The full set of (Favre- and) Reynolds-averaged Navier-Stokes equations, solved in the framework of computational fluid dynamics, reads [11]:

$$\frac{\partial \bar{\rho}}{\partial t} + \frac{\partial}{\partial x_i}\bar{\rho}\tilde{u}_i = 0 \tag{2.10}$$

$$\frac{\partial}{\partial t}(\bar{\rho}\tilde{u}_i) + \frac{\partial}{\partial x_j}(\bar{\rho}\tilde{u}_j\tilde{u}_i) = -\frac{\partial \bar{p}}{\partial x_i} + \frac{\partial}{\partial x_j}(\bar{\sigma}_{ij} - \overline{\rho u_i'' u_j''}) \tag{2.11}$$

$$\begin{aligned}\frac{\partial}{\partial t}(\bar{\rho}\widetilde{E}) + \frac{\partial}{\partial x_j}(\bar{\rho}\tilde{u}_j\widetilde{H}) = \frac{\partial}{\partial x_j}&\left(-\bar{q}_j - \overline{\rho u_j'' h''} + \overline{\sigma_{ij} u_i''} - \overline{\rho u_j'' k}\right)\\ &+ \frac{\partial}{\partial x_j}\left[\widetilde{u}_i\left(\bar{\sigma}_{ij} - \overline{\rho u_i'' u_j''}\right)\right]\end{aligned} \tag{2.12}$$

$$\bar{p} = \bar{\rho}R\widetilde{T} \tag{2.13}$$

where bar relates to the Reynolds-average, tilde to the Favre-average[5], and double-prime to the fluctuating part of the Favre-average, i.e. $u_i'' = u_i - \tilde{u}_i$ [136]. Based on [136] and [104], additional relationships constituting the terms arising in the momentum 2.11 and energy equation 2.12 read as:

$$\overline{\sigma}_{ij} = 2\tilde{\mu}\left(\tilde{S}_{ij} - \frac{1}{3}\frac{\partial \tilde{u}_k}{\partial x_k}\delta_{ij}\right) \tag{2.14}$$

for the viscous stress tensor $\overline{\sigma}_{ij}$, where the molecular viscosity $\mu$ is typically expressed through the temperature $T$ following Sutherland's law:

$$\mu = \mu_0 \left(\frac{T}{T_0}\right)^{\frac{3}{2}} \frac{T_0 + Su}{T + Su} \tag{2.15}$$

where $\mu_0 = 1.716 \cdot 10^-5\ kg/(ms)$, $T_0 = 273.15\ K$ and $Su = 110.4\ K$.
The reader may refer to, e.g., [136] or [4] for a detailed description and the physical interpretation of the remaining terms in the RANS equations, such as total and specific

[5] The Favre-average generally represents a mass-weighted average of a quantity $\phi$, i.e. $\tilde{\phi} = \overline{\rho\phi}/\bar{\rho}$.

energy $E$, $e$ and enthalpy $H$ and $h$, respectively, or the molecular heat flux $q$. The central remaining term considered in turbulence modeling and thus the framework applied within this thesis is the term $\overline{\rho u_i'' u_j''} = \tau_{ij}$, which constitutes the Reynolds-stress tensor. Half of the Reynolds-stress tensor trace is denoted as the turbulent kinetic energy $k$:

$$\bar{\rho}\tilde{k} = \frac{1}{2}\bar{\rho}\tau_{kk} \tag{2.16}$$

Employing the eddy-viscosity hypothesis introduced by Boussinesq, the components of the Reynolds-stress tensor can be expressed as [11]:

$$\tau_{ij} = 2\mu_T \tilde{S}_{ij} - \left(\frac{2\mu_T}{3}\right)\frac{\partial \tilde{u}_k}{\partial x_k}\delta_{ij} - \frac{2}{3}\bar{\rho}\tilde{k}\delta_{ij} \tag{2.17}$$

Comparison with Eq. 2.14 for the viscous stress tensor reflects the main modeling assumption Boussinesq introduced for turbulent stresses, namely the momentum transfer due to the process of turbulent mixing being similar to momentum transfer imposed by viscosity onto a laminar flow, introducing the eddy-viscosity $\mu_T$ as the linear scaling factor. As both terms are connected to the strain rate $S_{ij}$, molecular or, as frequently termed, laminar viscosity and eddy- or turbulent viscosity are typically lumped together to the effective viscosity $\mu_{eff} = \mu + \mu_T$ (cf. Eq. 2.5) when solving the RANS equations. For the numerical flow simulations presented within this thesis, the $k-\omega$ Shear Stress Transport (SST) turbulence model derived by Menter [77] is used. The model is based on two additional transport equations for the turbulent kinetic energy $k$ and the specific turbulent dissipation rate $\omega$ [11]:

$$\frac{\partial \rho k}{\partial t} + \frac{\partial \rho u_j k}{\partial x_j} = \frac{\partial}{\partial x_j}\left[(\mu + \sigma_k \mu_T)\frac{\partial k}{\partial x_j}\right] + \overbrace{\tau_{ij}S_{ij}}^{P_k} - \overbrace{\beta^* \rho \omega k}^{D_k} \tag{2.18}$$

$$\begin{aligned}\frac{\partial \rho \omega}{\partial t} + \frac{\partial \rho u_j \omega}{\partial x_j} = \frac{\partial}{\partial x_j}\left[(\mu + \sigma_\omega \mu_T)\frac{\partial \omega}{\partial x_j}\right] + \frac{C_\omega \rho}{\mu_T}\tau_{ij}S_{ij} - \beta\rho\omega^2 \\ + 2(1-F_1)\frac{\rho\sigma_{\omega 2}}{\omega}\frac{\partial k}{\partial x_j}\frac{\partial \omega}{\partial x_j}\end{aligned} \tag{2.19}$$

which need to be solved numerically alongside the RANS Eqs. 2.10 - 2.13. Through $k$ and $\omega$, the eddy-viscosity $\mu_T$ arising in the corresponding equations is expressed as [11]:

$$\mu_T = \frac{\rho a_1 k}{\max(a_1\omega, \Omega F_2)} \tag{2.20}$$

The $k-\omega$ SST model is one of the most widespread models for external aerodynamic applications. The model combines the $k-\omega$ model of Wilcox [135] with a high Reynolds number formulation of the $k-\epsilon$ model by the usage of a model blending function $F_1$. The blending function activates and smoothly blends the closure coefficients $\sigma_k$, $\sigma_\omega$, $C_\omega$, $\beta$, of the respective models depending on the distance to the nearest wall. The rationale

Table 2.1: Numerical settings and schemes employed for the flow simulations.

| | |
|---|---|
| Spatial Discretization | Central scheme |
| Temporal Discretizaion | Backward Euler scheme |
| Multigrid Scheme | 3W |
| Convergence Criterion | Cauchy criterion with $\Delta C_{L/D/M} < 1 \cdot 10^{-5}$ for 500 iterations |

is to activate the turbulence models in their correspondingly advantageous regions, that is, the $k-\omega$ model in near-wall regions and the $k-\epsilon$ model in freestream and free-shear layer regions of the flow field. This is targeted at the $k-\omega$ model being superior due to the formulation of its dissipation term when it comes to low Reynolds numbers flows, where $k \rightarrow 0$, such as in the near-wall portions of the boundary layer. In contrast, the $k-\epsilon$ model is less sensitive to the freestream and inflow boundary conditions imposed on $\omega$ when compared to the $k-\omega$ turbulence model, for which the above-mentioned regions of the flow field offer themselves for corresponding activation [11, 40]. For a comprehensive overview of all model closure coefficients and details on the models, the reader may refer to any of the previously indicated references [11, 68, 136].
The DLR TAU code [119] is used as a flow solver throughout this thesis. The TAU code constitutes an extensive software system for high-fidelity computational fluid dynamics simulations. Different modules of the code are applied within this thesis for pre- and post-processing tasks, modeling of the coupled technology system (cf. Sec 2.3), as well as the solution of the above-introduced governing flow and turbulence equations. When not indicated differently, a series of central numerical settings and methods have been consistently applied within the thesis and are summarized in Tab. 2.1. Hybrid grids predominantly consisting of prisms and tetrahedra were generated using the commercial CENTAUR grid generator by Centaursoft [16]. As the simulations target the cruise flight regime of the airplane, typically no transient effects need to be taken into account for the flow simulations. Partially, local flow separation with transient flow structures emerges at the boundaries of the simulation envelope, i.e., at high lift coefficients $C_L$ or Mach numbers the development of aerodynamic buffet can be observed. In these cases, an unsteady (URANS) approach has been adopted.

### 2.2.2 Transition Prediction

When solving the above-introduced flow equations, one inherently imposes the entire flow field being turbulent. Therefore, the effect of boundary layer transition is not included in the solution of the RANS equations for wall-bounded flows. When considering the Reynolds number regime of an aircraft during cruise flight, the assumption of a completely turbulent boundary layer is justified, especially in conjunction with wing sweep angles on transonic transport aircraft favoring boundary layer transition due to CFI or ALT in direct vicinity of the leading edge.

Naturally, for the assessment of an HLFC system, the effect of transition needs to be considered within the flow simulations. To reach this goal, a series of different approaches exist, characterized by their trade-off between fidelity level and computational expense. From the viewpoint of configurational aerodynamics, the main requirement consists of automated prediction of the transition position in dependence on driving parameters (cf. Sec. 2.1.2), i.e. modeling of the transition process itself is not the central necessity. Next to empirical or semi-empirical criteria, e.g. the correlations of Abu-Ghannam and Shaw [1] or Drela and Giles [24], two approaches satisfying these requirements have been applied within this thesis and are briefly introduced in the following. First, the $\gamma - Re_\theta$+CF model, stemming from the regime of local correlation-based transition transport (LCTM) models, has been used in the numerical simulations. Furthermore, linear stability theory with a two-$N$-factor approach for transition prediction is applied, reflecting the standard method in industrial applications.

#### 2.2.2.1 Local Correlation-Based Transition Models

Local correlation-based transition models are a subtype of turbulence models, where additional transport equations are solved to reflect the process of boundary layer transition. Within this thesis, the $\gamma - Re_\theta$+CF model is applied, which builds upon the $\gamma - Re_\theta$ model formulated by Langtry and Menter [67] and possesses additional correlations to model transition due to CFI [39].
The additional transport equations for the $\gamma - Re_\theta$ model read [67]:

$$\frac{\partial \rho \widehat{Re}_{\theta t}}{\partial t} + \frac{\partial \rho u_j \widehat{Re}_{\theta t}}{\partial x_j} = P_{\theta t} + \frac{\partial}{\partial x_j}\left[\sigma_{\theta t}(\mu + \mu_T)\frac{\partial \widehat{Re}_{\theta t}}{\partial x_j}\right] \tag{2.21}$$

$$\frac{\partial \rho \gamma}{\partial t} + \frac{\partial \rho u_j \gamma}{\partial x_j} = P_\gamma - E_\gamma + \frac{\partial}{\partial x_j}\left[\left(\mu + \frac{\mu_T}{\sigma_f}\right)\frac{\partial \gamma}{\partial x_j}\right] \tag{2.22}$$

where $\widehat{Re}_{\theta t}$ reflects a transported momentum thickness Reynolds number at transition onset and $\gamma$ denotes the intermittency.
The transport equations for $\widehat{Re}_{\theta t}$ and $\gamma$ can be readily implemented into any present turbulence modeling framework, however, they pose additional complexity when it comes to parallelization and execution of the numerical flow simulation. Coupling to the $k - \omega$ SST model is achieved by altering the turbulent kinetic energy production $P_k$ and destruction $D_k$ terms of the turbulent kinetic energy transport equation (cf. Eq. 2.18) to read [67]:

$$\widehat{P}_k = \gamma_{eff} P_k \tag{2.23}$$

$$\widehat{D}_k = \min(\max(\gamma_{eff}, 0.1), 1) D_k \tag{2.24}$$

Following from the equations above, the intermittency [6] $\gamma_{eff}$ is used to effectively suppress the production of turbulent kinetic energy in laminar regions of the boundary layer ($\gamma_{eff} \approx 0$) while smoothly blending into the standard turbulence model terms for fully turbulent flow regions ($\gamma_{eff} = 1$).
Given the above-introduced LCTM framework, a set of different empirical transition criteria is evaluated in a grid point local manner during the numerical flow simulation to detect and model the transition process. Considering streamwise transition mechanisms, e.g. transition due to TSI, Langtry and Menter [67] formulated a local transition criterion, based upon a critical momentum thickness Reynolds number $Re_{\theta c} = f(\widehat{Re}_{\theta t})$:

$$F_{onset,1} = \frac{Re_\theta}{Re_{\theta c}} = \frac{Re_\nu}{\zeta Re_{\theta c}} > 1 \tag{2.25}$$

The onset of transition is thus detected when the momentum thickness Reynolds number $Re_\theta$ surpasses the critical value $Re_{\theta c}$. As denoted in Eq. 2.25, $Re_\theta$ is not directly used but substituted by $Re_\nu/\zeta$, as computation of the momentum thickness would require wall-normal integration of the boundary layer velocity profile, thus violating the requirement for exclusively local operations. Therefore, the vorticity Reynolds number $Re_\nu$ in conjunction with the scale parameter $\zeta = 2.193$ (see [67]) is used, based on the observation that the maximum of the vorticity Reynolds number, which according to van Driest and Blumer [25] lies at the point of emergence of turbulent structures within the boundary layer, is proportional to the momentum thickness Reynolds number $Re_\theta$. The scale factor $\zeta = 2.193$ is assumed to be constant, which is generally only valid for a Blasius boundary layer and differs with altering pressure gradient. The effect of the pressure gradient, through the pressure gradient parameter $\lambda_\theta$, as well as the external turbulence level, is imposed onto $Re_{\theta t} = f(\lambda_\theta, Tu)$ employing an empirical transition criterion [67], similar to the above-mentioned empirical criterion by Abu-Ghannam and Shaw [1]. As the correlation for $Re_{\theta t}$ is only valid outside of the boundary layer, the production term $P_{\theta t}$ within Eq. 2.21 is employed to achieve $Re_{\theta t} = \widehat{Re}_{\theta t}$ at the boundary layer edge, while $\widehat{Re}_{\theta t}$ is subsequently diffused into and convected within the boundary layer by the transport equation 2.21.
Grabe et al. [39] extended the model by a series of correlations to additionally account for transition due to CFI. The variant employed within this thesis builds upon a critical ratio of the helicity Reynolds number:

$$F_{onset,1,CF} = \frac{Re_{He}}{CRe^{+}_{He,t}} > 1 \tag{2.26}$$

where again $Re_{He}$, only depends on grid point local quantities, while $Re^{+}_{He,t}$ denotes an approximated helicity Reynolds number at transition onset, correlated as a function of a newly approximated pressure gradient parameter $\lambda^{+}$ on the basis of experimental

[6] The intermittency $\gamma_{eff}$ includes a formulation for separation induced transition $\gamma_{eff} = \max(\gamma, \gamma_{sep})$

results. The proportionality factor $C$ is set to $C = 0.7$ (see [39]) in the original model variant.
Based upon the detection of transition onset by Eq. 2.25 or 2.26, the central onset functions $F_{onset,1}$ and $F_{onset,1,CF}$ are abstracted with a series of further terms to the final onset functions $F_{onset}$ and $F_{onset,CF}$. Along with the transition length function $F_{length}$, these onset functions activate the production term in the intermittency transport equation 2.22 [39]:

$$P_\gamma = (F_{length}[\gamma F_{onset}]^{1/2} + F_{length,CF}[\gamma F_{onset,CF}]^{1/2}) c_{a1} \rho S (1 - c_{e1}\gamma) \tag{2.27}$$

thus gradually increasing the intermittency $\gamma$ over the extent of the transition onset location to the fully turbulent boundary layer.

#### 2.2.2.2 Linear Stability Theory

Whilst LCTMs are a current topic of research and development activities, the usage of linear stability analysis coupled to an $e^N$-Method for transition prediction is highly mature, and typically used in an industrial context when it comes to transition prediction. As indicated in Sec. 2.1.1, when dealing with boundary layer transition on transport aircraft wings and HLFC application, primary instability modes, the growth of which can be described by linear theory, are of central interest. Following a small disturbance ansatz, the flow variables $\phi = [\boldsymbol{u},p,\rho,T]$ characterizing the laminar base flow are decomposed into a steady mean-flow term $\Phi$ and a fluctuating component $\psi$ [71]:

$$\phi(x,y,z,t) = \Phi(x,y,z) + \psi(x,y,z,t) \tag{2.28}$$

Inserting the decomposition into the Navier-Stokes Equations, while neglecting all higher-order terms (greater than $\mathcal{O}(1)$) and applying the parallel flow assumption, i.e. locally the growth of the boundary layer is neglected, leads to a set of linearized equations for the disturbance metrics $\psi(x,y,z,t)$. The derivation is documented, for instance, in [71]. Important for the application case at hand is the set of equations allowing for normal mode solutions for the disturbance waves $\psi$:

$$\psi(x,y,z,t) = \varphi(y) e^{i(\alpha x + \beta z - \omega t)} \tag{2.29}$$

Equation 2.29 thus specifies a set of complex eigenfunctions or disturbance mode shapes $\varphi(y)$, while $\alpha$ and $\beta$ specify the components of the wavenumber vector $\boldsymbol{k}$ and $\omega$ the corresponding frequency. Inserting Eq. 2.29 into the linearized Navier-Stokes equations leads to the stability equations, a system of ordinary differential equations for the disturbance modes $\varphi(y)$, which can be solved as an eigenvalue problem for different combinations of $\alpha$, $\beta$, and $\omega$. The system of equations depends on Reynolds and Mach numbers, the local (laminar) boundary layer velocity and temperature profiles, alongside their first

and second derivatives [108].
More precisely, the focus of linear stability theory given the local velocity and temperature profiles is evaluating the dispersion relation:

$$\omega = \Omega(\alpha,\beta) \tag{2.30}$$

which specifies the combinations of the six unknown components of the complex eigenvalues $\alpha$, $\beta$, and $\omega$ leading to non-trivial solutions of the stability equations. To do so, four of the six unknown components need to be prescribed, while the other two components are solved for. One distinguishes between the spatial and the temporal formulation of the stability problem. In the spatial formulation, $\omega$ is considered purely real, while the spatial amplification of the disturbance wave is described by the imaginary parts of $\alpha$ and $\beta$. The temporal theory uses real wave numbers $\alpha$ and $\beta$, with $\omega$ comprising the temporal amplification rate of the disturbance mode [71].
The solutions of either of the two approaches can be graphically represented using a stability diagram. A schematic representation is presented in Fig. 2.6 a), when considering solutions to the spatial formulation of the eigenvalue problem. Depending on the streamwise position $x$, that is, the local Reynolds number $Re_x$, and the (real) wave frequency $\omega$, the imaginary part of $\alpha$ (here considering a two-dimensional flow) is either positive, negative or zero. When $\alpha_i > 0$, disturbance waves of frequency $\omega$ are damped, whereas a negative imaginary part of $\alpha$ leads to amplification of the disturbances. The isoline $\alpha_i = 0$ is termed the neutral-stability curve, where the furthest upstream Reynolds number connected to $\alpha_i = 0$ reflects the indifference Reynolds number addressed in Fig. 2.4 [71].
Using linear stability theory for transition prediction requires coupling to a suitable transition criterion. While solving the above-mentioned stability equations leads to a set of local amplification rates downstream of the indifference point, the criterion is needed to quantify the magnitude of disturbance amplification required for the transition process to take place. The connection is achieved through the $e^N$-method, as introduced by Smith and Gamberoni [123] and van Ingen [51].
The $e^N$-method builds upon critical $N$-factors, which quantify the ratio between the disturbance amplitude $A$ of the most unstable mode, i.e. the envelope of different amplification rates, and an initial disturbance amplitude $A_0$ (see Fig. 2.6 b). Considering spatial theory, for a two-dimensional boundary layer the $N$-factor is computed as [126]:

$$N = \max_{f_i}[N_i(f_i)] = \max_{f_i}\left[\ln\left(\frac{A}{A_0}\right)\right] \tag{2.31}$$

where

$$\ln\left(\frac{A}{A_0}\right) = \int_{x_0}^{x} -\alpha_i dx \tag{2.32}$$

The $N$-factor envelope is now compared to a critical $N$-factor, where the onset of transition is predicted at the point $N > N_{crit}$.
For the computations conducted in the following, the linear stability solver LILO [111] is used. Furthermore, a two-$N$-factor transition criterion is applied, which follows from a series of assumptions proposed by Schrauf for the efficient aerodynamic design of swept HLFC wings [115].
As the name implies, the two-$N$-factor integration strategy uses two dedicated $N$-factors, for respective growth rate integration of TS-waves $N_{TS}$ and CF-waves $N_{CF}$. The method is connected to several assumptions, on the one hand when prescribing the conditions on the above-mentioned eigenvalue problem, as well as the growth rates to be integrated yielding the corresponding $N$-factors. Considering a purely two-dimensional flow, the direction of the highest wave amplification coincides with the inviscid edge streamline, leading to the previously mentioned Tollmien-Schlichting waves. Considering the three-dimensional case, this analogy is used for the computation of $N_{TS}$-factors, i.e. the analysis and subsequent $N$-factor integration is performed for waves propagating in the direction of the inviscid boundary layer edge streamline [108].
For the determination of $N_{CF}$, Schrauf [108] proposes to prescribe the wavelength while limiting the observations to stationary cross-flow waves, i.e. $\omega = 0$. This simplification is based on experimental evidence, suggesting the dominant waves leading to CFI are of constant length and stationary.
The strategies are implemented in LILO, alongside a series of schemes for estimating relevant frequencies and wavelengths for the computation of $N_{TS}$ and $N_{CF}$, respectively. The $N$-factor envelopes are then compared to a critical $N$-factor curve. As the critical $N$-factor curves are typically derived using experimental data, the method can be classified as semi-empiric, opening the opportunity to connect experimental data to numerical analysis. It has to be noted, however, that the critical $N$-factor correlation strongly depends on the experimental setting used for its determination, as transition prediction based on the $e^N$-method combines the initial disturbance amplitude $A_0$, as well as the non-linear processes leading to the conclusion of the transition process (see Fig. 2.2) into a single critical factor. The first is highly susceptible to the process of receptivity and thus sensitive to the experimental testing environment (e.g. wind tunnel, free-flight experiment) used to correlate critical $N$-factors, while the latter cannot be modeled by linear theory. The correlation curve used within this thesis has been derived from HLFC free-flight experiments and is used in HLFC-related design activities, for instance, at the DLR or Airbus [101]. The curve is depicted in Fig. 2.6, alongside an exemplary representation of an $N_{TS}$-$N_{CF}$-factor envelope assessed at a representative spanwise station of the reference wing.
Integration of LST into the RANS workflow is carried out through the automatic transition prediction framework implemented in TAU by Krumbein et. al in [64]. The workflow builds around the aforementioned LST solver LILO, while including the compressible

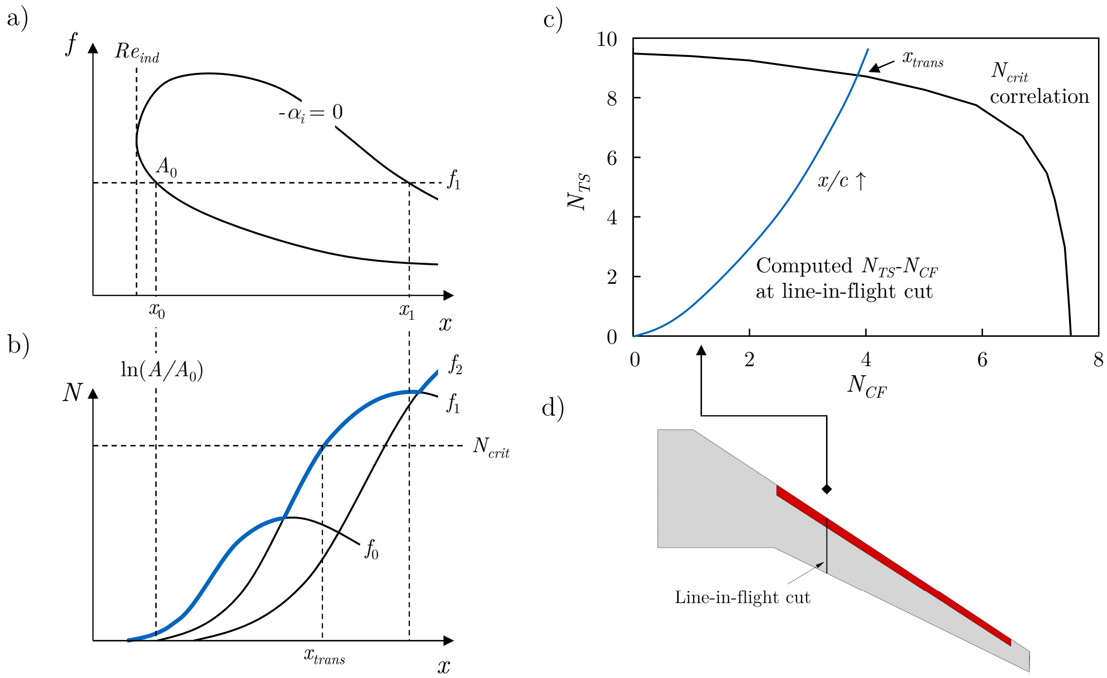


Figure 2.6: Schematic representation of an LST workflow alongside an $e^N$-method for transition prediction. Panel a: Stability diagram with $\alpha_i = 0$ isoline, leading to $N$ factors and corresponding $N$-factor envelope for the highest amplification rate (blue), depending on the chordwise station $x$, depicted in panel b) (adapted from [7]). Panel c) shows the critical $N_{TS}$-$N_{CF}$ correlation curve used for transition prediction within the present thesis [101], alongside a representative $N_{TS}$-$N_{CF}$ factor envelope extracted at a line-in-flight cut along the wing span, shown in panel d).

conical boundary layer solver COCO [109] for the determination of highly accurate laminar boundary layer velocity and temperature profiles. COCO uses a set of planform and operating parameters from the RANS simulation and computes the boundary layer profiles based on the pressure distribution resulting from the latter. The pressure distribution is extracted from the RANS simulation along line-in-flight cuts, i.e. at a set of user-specified spanwise stations along the wing (see Fig. 2.6 d). The corresponding boundary layer profiles undergo stability analysis, resulting in a predicted transition position $x_{tr}$ at the corresponding line-in-flight cuts, which is communicated back to the RANS solver. If neither transition criterion is fulfilled, the transition position is assumed to coincide with the point of laminar boundary layer separation predicted by COCO. It should be noted, however, that this does not necessarily imply the flow completely separating off the wing surface at this point, as the transition to turbulent flow generally tends to stabilize the boundary layer towards separation at the corresponding streamwise position.

The transition positions at the different spanwise stations, that is line-in-flight cuts, are connected through a polygon line, upstream of which wall adjacent cells are flagged laminar. The turbulence model in the RANS simulation is turned off in the corresponding

cells, resulting in a laminar solution upstream of the transition point. Downstream of the polygon line the conventional formulation of the turbulence model is employed.
A central advantage of using the boundary layer code COCO consists of a wall-normal velocity (distribution) being directly prescribable as a boundary condition during the calculation of the boundary layer velocity profile. Whilst connection to the later described suction mass flux boundary condition is also possible[7] by extracting the boundary layer profiles directly from the RANS solution, the latter requires a high boundary layer resolution within the numerical grid [64]. This is additionally aggravated by the fact, that this thesis deals with full-scale, three-dimensional configurations alongside an ample parameter space for assessment of the technology coupling, rendering the numerical costs connected with the required grid resolutions excessively high. Therefore, the boundary layer code is employed in calculations connected to LST.

## 2.3 Technology Modeling

Different software frameworks have been implemented in the course of this thesis to include both the influence of an active suction system and the integration effects of variable camber. While the effect of a wall-normal velocity can be directly included in the boundary layer profiles computed by COCO, a non-zero wall mass flux boundary condition has been used in the context of LCTM calculations, see Sec. 2.3.1. Furthermore, a framework for variable camber integration through mesh deformation has been implemented (see Sec. 2.3.2), where both tools have been embedded into an automated software chain (see Sec. 2.3.3). The latter is targeted to form an interface between geometrical data formats used in overall aircraft design, such as CPACS [3] or the Aircraft Exchange (AiX) [102] format, and high-fidelity RANS workflows in the context of high-performance computing environments. This is especially important for the automated data set generation used for the derivation of reduced order models, as treated in Chap. 5 of this thesis.

### 2.3.1 Modeling of the Active Suction System

To model the effect of boundary layer suction on the boundary layer development underlying the solution of the RANS equations, the effusion mass flux boundary condition [75], implemented in the TAU code, has been utilized. The boundary condition allows for the application of a non-zero momentum flux on viscous wall boundary conditions of

[7] Thus directly modeling the effect of suction on the boundary layer profiles within the CFD run, see Sec. 2.3.1. When using the boundary layer code, e.g. thinning of the boundary layer due to suction is not reflected in the RANS results.

the computational grid, in this case, the HLFC suction panel of the wing by pointwise specification of the effusion mass flux $j$ [6]:

$$j = \frac{\dot{m}}{A} = \rho v_n \tag{2.33}$$

While the boundary condition does not alter the underlying turbulence model, Meerts [75] showed that boundary layer velocity profiles and skin-friction coefficient distributions extracted from RANS computations, including the boundary condition, match well to the law of the wall and theoretical solutions. In the context of HLFC, Krimmelbein and Krumbein [63] used the effusion mass flux boundary condition within the context of linear stability theory for transition prediction (cf. Sec. 2.2.2.2), where the boundary layer profiles undergoing stability analysis where correspondingly extracted from the RANS solution. Within their validation study, high agreement with a comprehensive series of two- and three-dimensional experimental test cases is achieved.
Fehrs [32] demonstrated that the flat plate laminar boundary layer computed by the RANS solver under the application of the effusion mass flux boundary condition shows excellent agreement with the analytical solution. Furthermore, the aspect of transition prediction in the context of LCTM is included in the latter publication, also showing high agreement when compared to experimentally determined transition positions on airfoils. Further experimental and numerical studies are presented by Helm [46], specifically focusing on the comparison of transition prediction using LCTM and LST with experimental results. While the LCTM shows the expected behavior concerning a downstream shift in transition position with increasing suction mass flow rates, quantitative discrepancies arise in the absolute position, necessitating further investigation. The discussions presented in Sec. 3.3.2.2 seek to contribute to this goal.
The usage of the effusion mass flux boundary condition in the present case is tailored towards the specification of a suction coefficient distribution:

$$C_q(x/c, \eta) = \frac{v_n(x/c, \eta)}{u_\infty} = \frac{j(x/c, \eta)}{\rho(x/c, \eta) u_\infty} \tag{2.34}$$

An overview of the particular steps implemented to obtain the desired distribution during the run time of a CFD computation is presented in Fig. 2.7.
Based on the geometrical representation derived by the automated toolchain (see Build-Wing - Module, Sec. 2.3.3), user-specified wall-normal velocities $v_{n,BW-Grid}$ are specified on a set of three-dimensional control points lying on the surface of the suction panel. As indicated in Eq. 2.34, these points are parameterized by their chord- and spanwise coordinates $x/c$ and $\eta$, respectively, allowing for the prescription of variable suction distributions in terms of these coordinates (see Fig. 2.8).
Using radial basis function interpolation, the scattered data is transferred to the boundary part specifying the HLFC panel in the numerical grid, therefore allowing the prescription of a variable suction coefficient distribution on the boundary part of a mesh

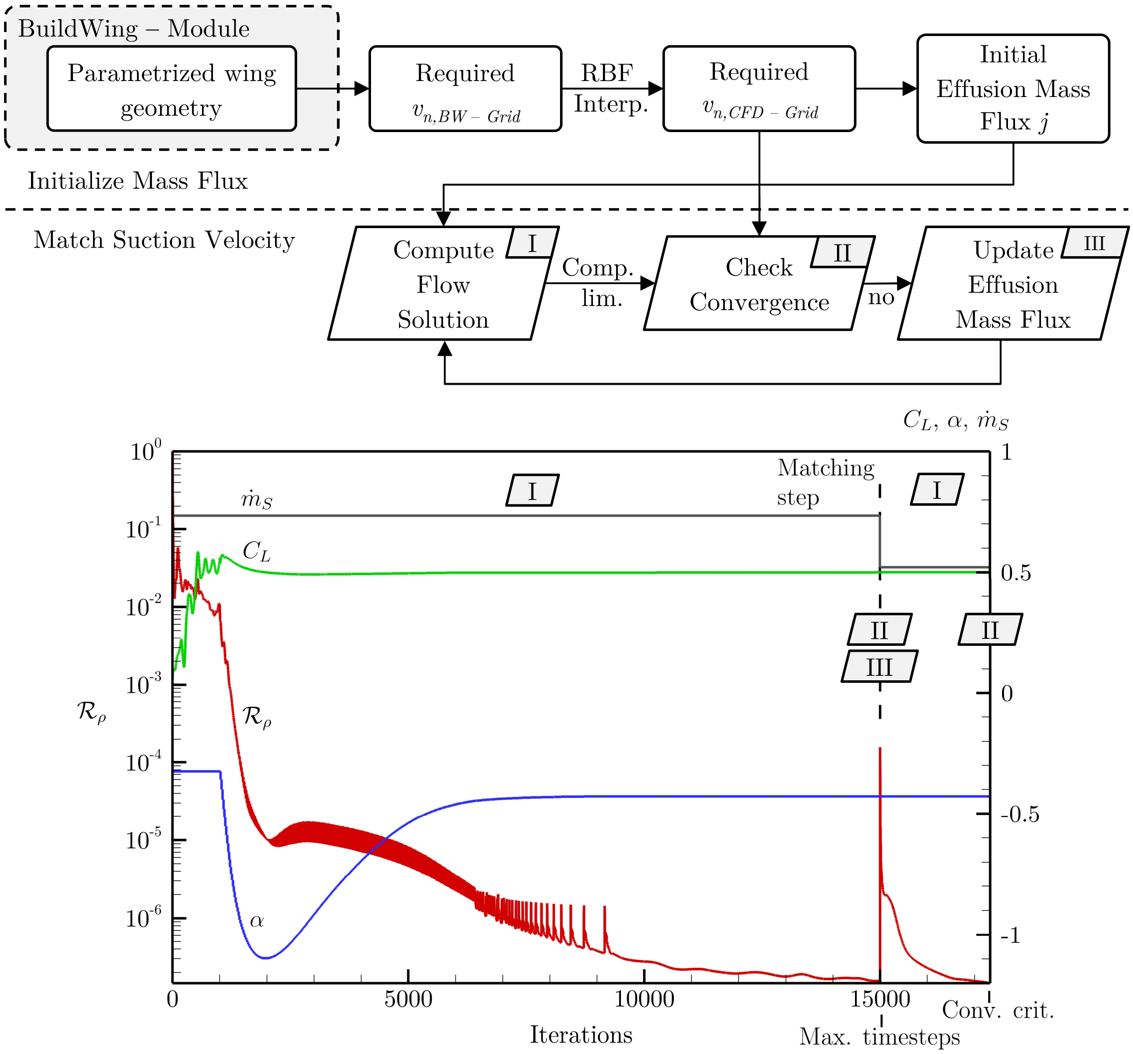


Figure 2.7: Overview of the iterative process to prescribe a suction coefficient (distribution) $C_q$ on the CFD surface grid, alongside a representative convergence history for a computation employing the chain.

specified by a single marker. As per Eq. 2.34 the suction coefficient is not directly prescribed, but rather, the effusion mass flux $j$ is used. The resulting wall-normal velocity distribution still depends on the density distribution $\rho$ on the suction panel. This distribution is not known a priori, for which an iterative matching scheme is implemented. The scheme updates the prescribed effusion mass flux $j$ with the computed density distribution after a certain number of solver iterations, until reaching a convergence criterion defined through the absolute difference of prescribed and actual wall-normal velocity, evaluated at each grid point of the CFD surface grid.

The computational expense added by the second loop is very small, as it is not required to run the computation until reaching the numerical convergence criterion imposed upon the numerical simulation. Instead, the density distribution can be extracted during the run time of the simulation to update the effusion mass flux distribution. This is complemented by an adequate initial mass flux distribution, e.g. stemming from an earlier computation, typically requiring a limited number of one to three update iterations to

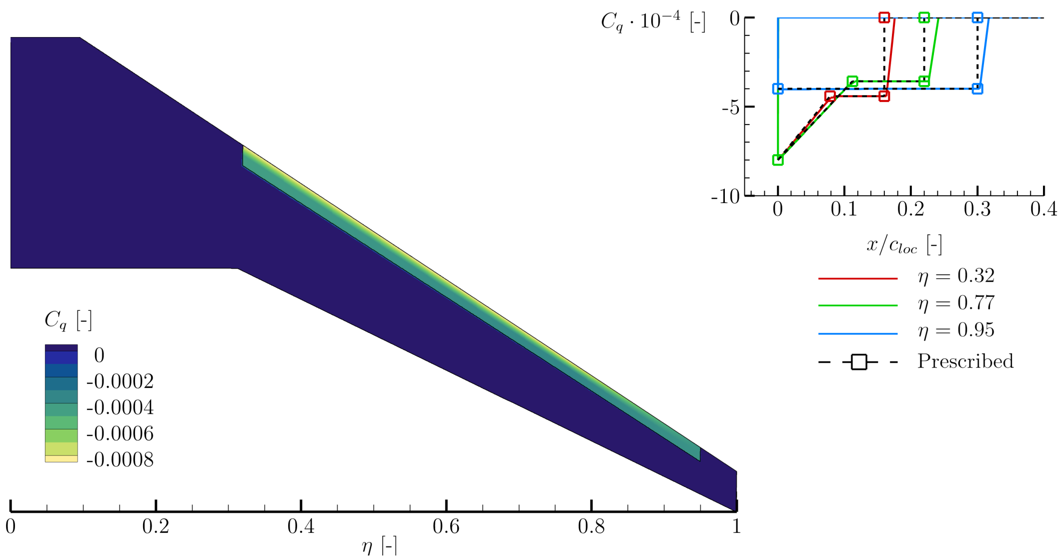


Figure 2.8: Example of a varying suction coefficient distribution $C_q$, set according to the optimization studies presented in [29].

reach the specified convergence criterion, in the present case set to $\epsilon < 0.01m/s$ with $\epsilon = |v_{n,actual} - v_{n,prescirbed}|$ for all suction panel grid points. This criterion can be further tightened, as typically $\epsilon = \mathcal{O}(10^{-4})$, resulting in an error below 1% error, depending on the prescribed value of $C_q$ for the converged solution. A representative convergence history, simultaneously applying a target lift coefficient algorithm implemented in the DLR TAU code, is depicted in the bottom panel of Fig. 2.7.

### 2.3.2 Modeling of Variable Camber Integration

As discussed in the last paragraph of Sec. 1.2, variable camber integration in this thesis is performed through the deflection of wing trailing edge devices. As for the suction boundary condition described in Sec. 2.3.1, a dedicated process chain has been implemented to include these capabilities, see Fig. 2.9 for an overview.

The process chain is centered around the radial basis function (RBF) mesh deformation tool implemented within the TAU code, which, as presented for instance by Alcaraz Capsada and Heinrich in [2], is a highly efficient tool for modeling of control surface deflections. The usage of RBF for mesh deformation builds upon a set of scattered base points alongside their corresponding deflection field, which again is computed based on the parameterized geometry representation derived in the software environment embedding the deformation process chain, see Sec. 2.3.3. These scattered data points are transferred to the surface grid of the undeformed computational mesh, followed by a corresponding deformation of the volume mesh based on the prescribed deflection fields.

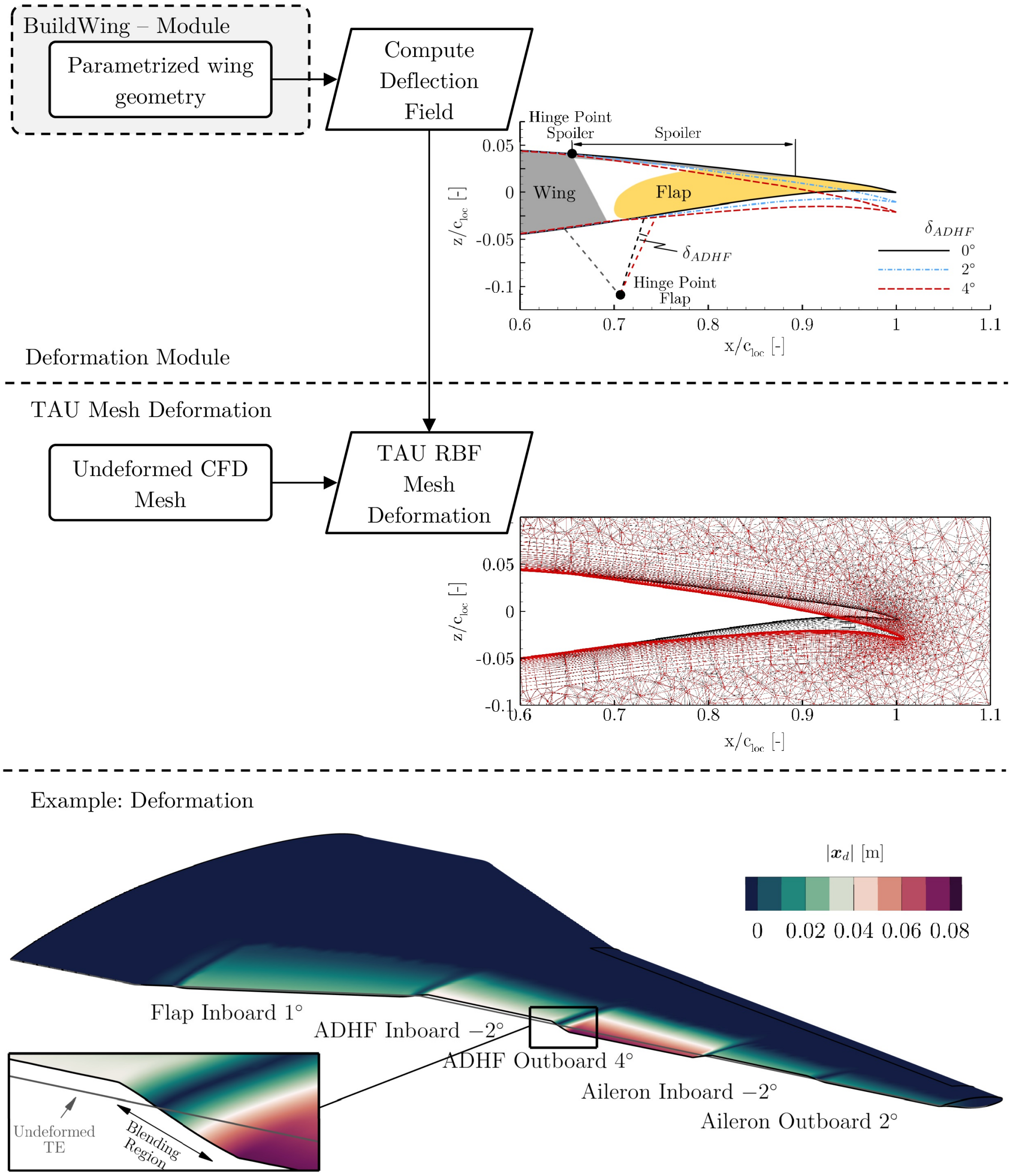


Figure 2.9: Overview of the VC integration process chain, along with an exemplary representation of a deformed surface mesh.

The software framework embeds different computational routines for conventional flaps as well as dropped hinge flaps, such as the ADHF (see top right of Fig. 2.9), as presented on the bottom of Fig. 2.9 for a series of arbitrarily chosen flap deflection angles. The main limitation of using RBF mesh deformation for modeling of VC integration is connected to its mathematical formulation, not allowing for discontinuous deformations or changes in the connectivity of the computational grid. Therefore, incorporating flap gaps into the model typically leads to an unacceptable mesh quality deterioration within the gaps. If gaps need to be incorporated to the numerical model, typically overset grid methods or sliding interface boundary conditions are standard methods [2].

Therefore, the resulting gaps are considered sealed, where the numerical framework reflects the sealing by smoothly blending the deflection fields of different trailing edge devices in spanwise direction, see bottom of Fig. 2.9. This approach aligns with commonly employed numerical frameworks, e.g. as used by Reist et al. [97].

### 2.3.3 Automation and Solver Integration

The methodologies for modeling the suction system and the VC integration are embedded into a toolchain for automatic numerical analysis of the technology coupling, see Fig. 2.10. The toolchain consists of a series of Python modules, containing the corresponding routines within the ApplySuctionDist and the Deformation-modules.

The toolchain is built about two central capabilities. First, it is designed for usage as an interface for coupling low-fidelity aerodynamic analyses to a high-fidelity CFD workflow. This is achieved through the toolchain, and especially the BuildWing-module, representing an interface to commonly used geometry specifications in overall aircraft design (OAD). For instance, all geometries investigated within this thesis emerged from the research project CATeW, and were designed and analyzed using MICADO[8] at the Institute of Aerospace Systems of RWTH Aachen. Amongst other data, geometrical specifications of the reference aircraft are stored in a MICADO-specific xml-file, the so-called Aircraft Exchange (AiX) file. The BuildWing-module extracts the corresponding information and computes three-dimensional surface point coordinates, required by the subsequent ApplySuctionDist - and Deformation - modules, or usable for CAD and mesh generation.

The second central design philosophy of the toolchain consists of automation and modularity. In addition to generating the required numerical setup for calculations incorporating the technology coupling, either using LCTM or LST for transition prediction, the toolchain embeds all routines required to automatically execute the simulation and create the desired output file structure for subsequent post-processing. As indicated by the differentiation in pre-, post-, and solver-related activities in Fig. 2.10, the software required to ultimately conduct the simulations is external to the toolchain, i.e. it can be modularly replaced by adding the required interfaces to the different modules comprising the toolchain.

[8] Multidisciplinary Integrated Conceptual Aircraft Design and Optimization environment [102, 116]; MICADO is an ILR internal specialization of UNICADO [118] providing conceptual design methods with increased fidelity.

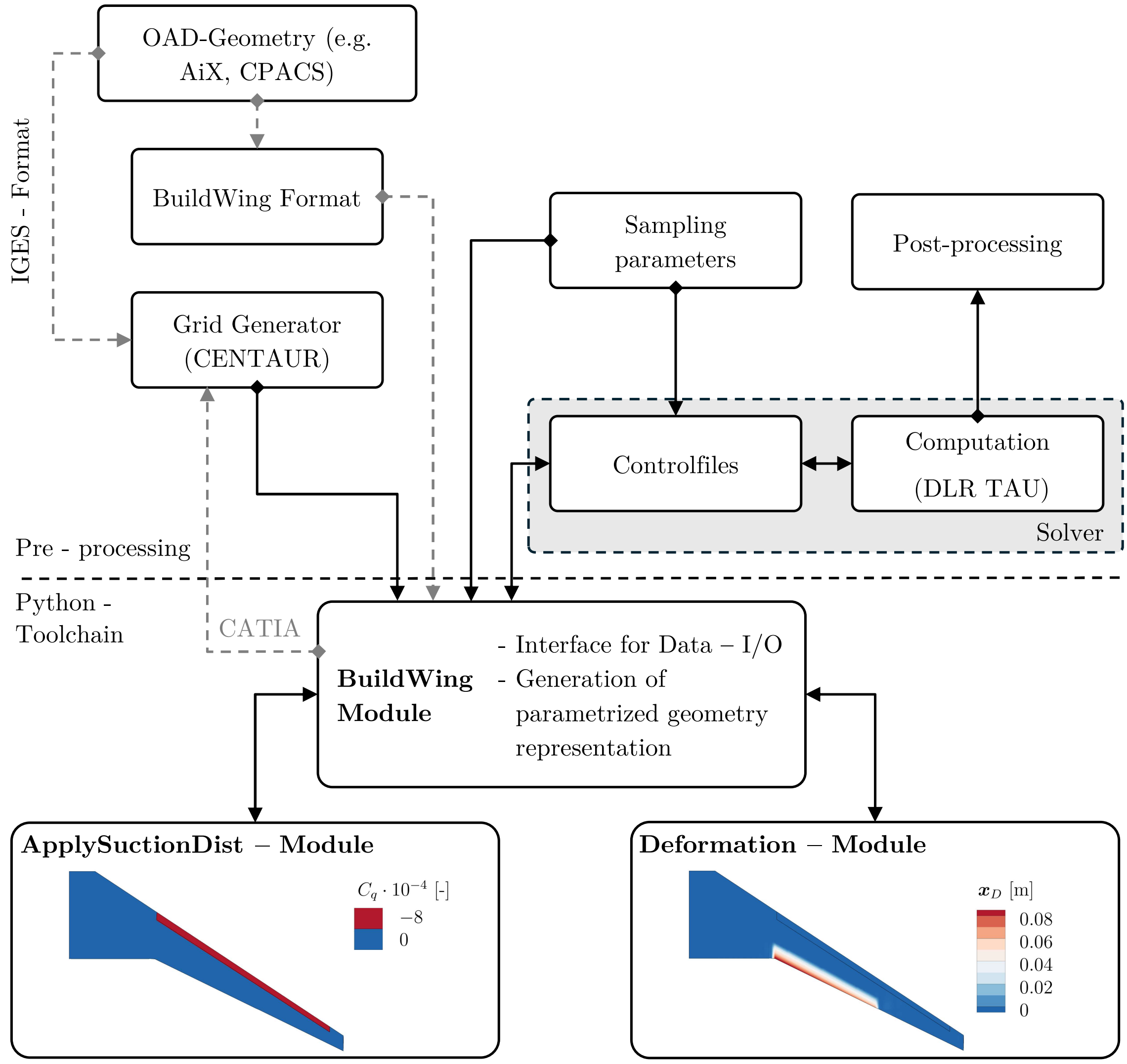


Figure 2.10: Python toolchain implemented and employed for data set generation for assessment of the technology coupling in the course of the thesis. The toolchain consists of three main modules, the BuildWing, ApplySuctionDist, and Deformation modules. These modules interact with OAD geometry specifications on the one hand and the required pre-, post, and solution steps for high-fidelity CFD simulations on the other hand.

# 3 Application on Isolated Wing Level

Within this chapter, the technology coupling is initially assessed on wing level, with the main focus lying upon a retrofit application to the wing of the turbulent mid-range configuration CATeW-02. The reference geometry is presented in Sec. 3.1, alongside the generated numerical grids and a grid independence study. Section 3.2 focuses on the aerodynamic characterization of the reference geometry, whilst assessing the implications of VC integration realized through deflections of an ADHF and corresponding effects on the stability of the boundary layer in Sec. 3.2.2. Within Sec. 3.3.1, the coupled application of both HLFC and VC is assessed using LST coupled to the two-$N$-factor method for transition prediction, followed by the corresponding analyses using the LCTM alongside the framework for modeling of an active boundary layer suction system. The chapter is concluded by a brief synthesis in Sec. 3.4. Large parts of this chapter are based on the peer-reviewed publication "Aerodynamic drag reduction through a hybrid laminar flow control and variable camber coupled wing" published in *Aerospace Science and Technology* [54], as well as the final technical report of the research project CATeW (cf. Sec. 1.3) [55].

## 3.1 Reference Geometry and Computational Grids

The central geometry analyzed within this thesis is the turbulent reference configuration CATeW-02, the wing planform of which is depicted in Fig. 3.1. As previously indicated, the reference configuration has been set up at the Institute of Aerospace Systems of RWTH Aachen University using the toolchain MICADO. The reference configuration CATeW itself is based on the OAD version of the AVACON Research Baseline 2028 [138].

The wing comprises four sections (S1-S4), which are limited by airfoils A1-A4 in in- and outboard direction. The root airfoil A1 is an adapted version of the NASA SC(2)-0614 airfoil [44], while the outboard airfoils A2-A4 are adapted from the NASA Common Research Model [131]. The wing planform is characterized by a swept leading edge with a constant sweep angle of $\varphi_{LE} = 33.43°$ and a trailing edge sweep angle of $\varphi_{TE} = 26.01°$ in the outboard segments S3 and S4. The reference area of the full-span configuration is $S_{ref} = 220.2\ \text{m}^2$, with a wing span of $b = 52$ m at an aspect ratio of $\Lambda = 12.28$. This results in a mean aerodynamic chord length of $c_{ref} = 5.29$ m, which together with the design cruise Mach number of $Ma_{cr} = 0.83$ results in the operating envelope being characterized by the Reynolds number range $Re_{cr} = [34.5; 29.2] \cdot 10^6$ for the cruise altitudes $H = [35\ 000\ \text{ft}; 39\ 000\ \text{ft}]$.

As displayed in Fig. 3.1, VC-integration is achieved through deflections of an adaptive dropped hinge flap (ADHF), extending from $\eta_{IB} = 0.31$ to $\eta_{OB} = 0.68$ in spanwise direction, while possessing a constant local chord length of $c_{ADHF}/c_{loc} = 0.3$. As mentioned in Sec. 1.2, the ADHF foresees a Fowler-type motion of the flap, achieved through rotation of the flap about a dropped hinge point at $[x_H/c_{loc}, z_H/c_{loc}] = [0.747, -0.097]_{IB}$ and $[0.708, -0.112]_{OB}$, while the chordwise flap gap is sealed by deflecting the spoiler accordingly, see also Fig. 2.9 top right panel for a schematic overview. The HLFC suction panel is placed in the spanwise region $\eta = 0.32 - 0.95$, while extending from the leading edge up to the local front spar position, $x/c_{loc,IB} = 0.16$ and $x/c_{loc,OB} = 0.3$, in downstream direction.

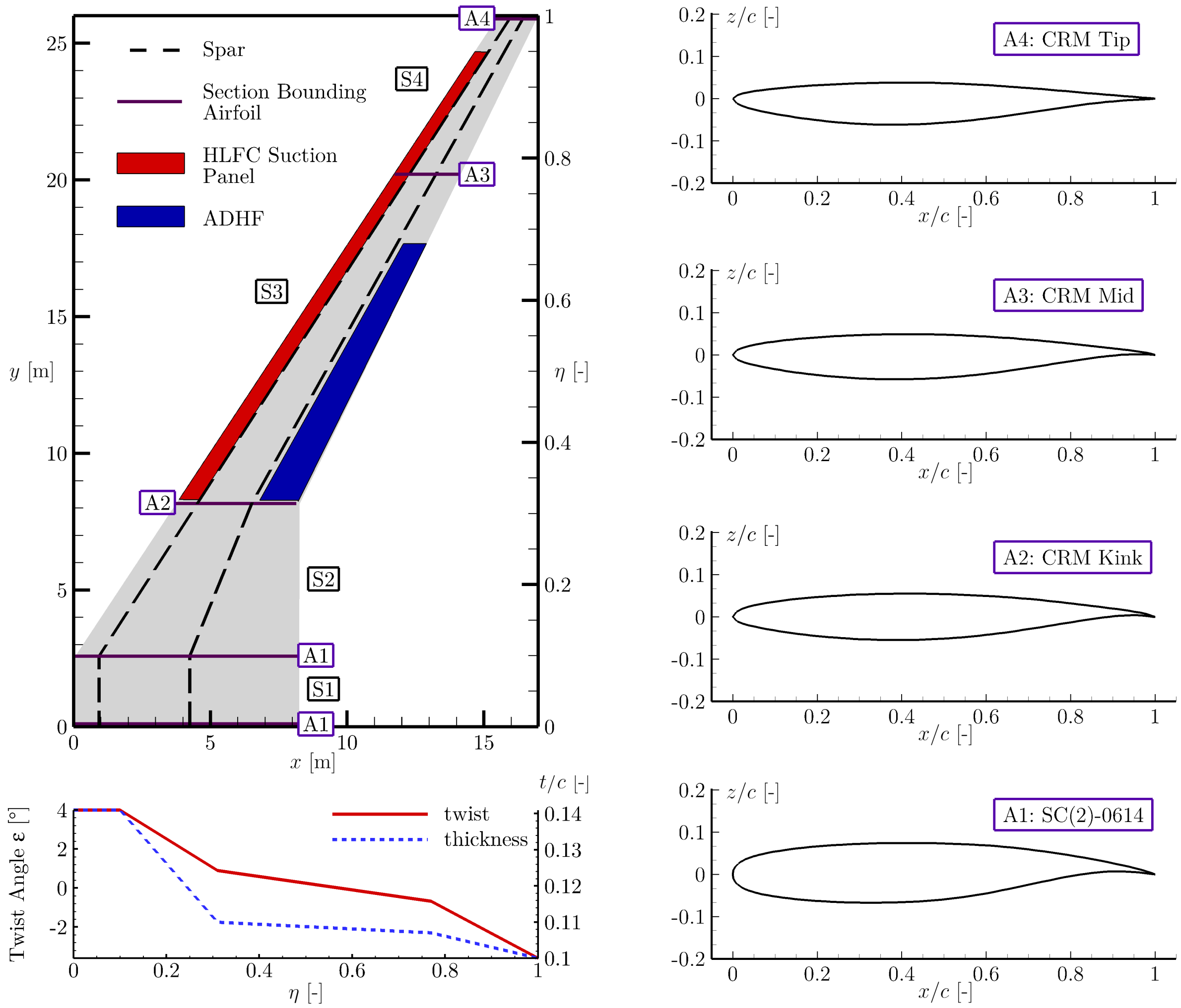


Figure 3.1: Left panels: Planform plot of the reference configuration CATeW-02, with indication of the HLFC suction panel and ADHF extent and twist and thickness distributions. Right panels: Airfoils at stations A1-A4.

Numerical gridding activities were performed with the commercial mesh generator CENTAUR by CentaurSoft [16], in a hybrid manner. Surface discretization is predominantly based on triangles, which are grown as prisms in wall-normal direction for the discretization of the boundary layer. The hemispherical computational domain is then filled with tetrahedra, up to the respective symmetry and farfield boundaries, see Fig.3.2.

Mesh independence is assessed by the generation of a grid family consisting of four grids $\mathcal{L}_1$ - $\mathcal{L}_4$, possessing increasing refinement levels with respect to surface and near-field domain resolution. A series of parameters are held constant throughout the grid study, especially considering the resolution of the boundary layer in wall-normal direction by using a prism layer stack of 60 cells in wall-normal direction, with an expansion ratio of 1.1 and a first prism layer height satisfying $y^+ < 1$. These parameters result from a series of best practice guidelines published in [83] and in the course of the 1st AIAA CFD Transition Modeling and Prediction Workshop [17], when applying LCTMs for transition prediction. Furthermore, the streamwise direction should be discretized by at least 200 grid points along the contour, which is achieved for the grids $\mathcal{L}_2$ - $\mathcal{L}_4$ within this study. The size of the hemispherical domain is chosen as $100 \cdot c_{ref} = 529$ m, confining a farfield boundary condition, while the $y$-plane is set to a symmetric boundary condition[1].

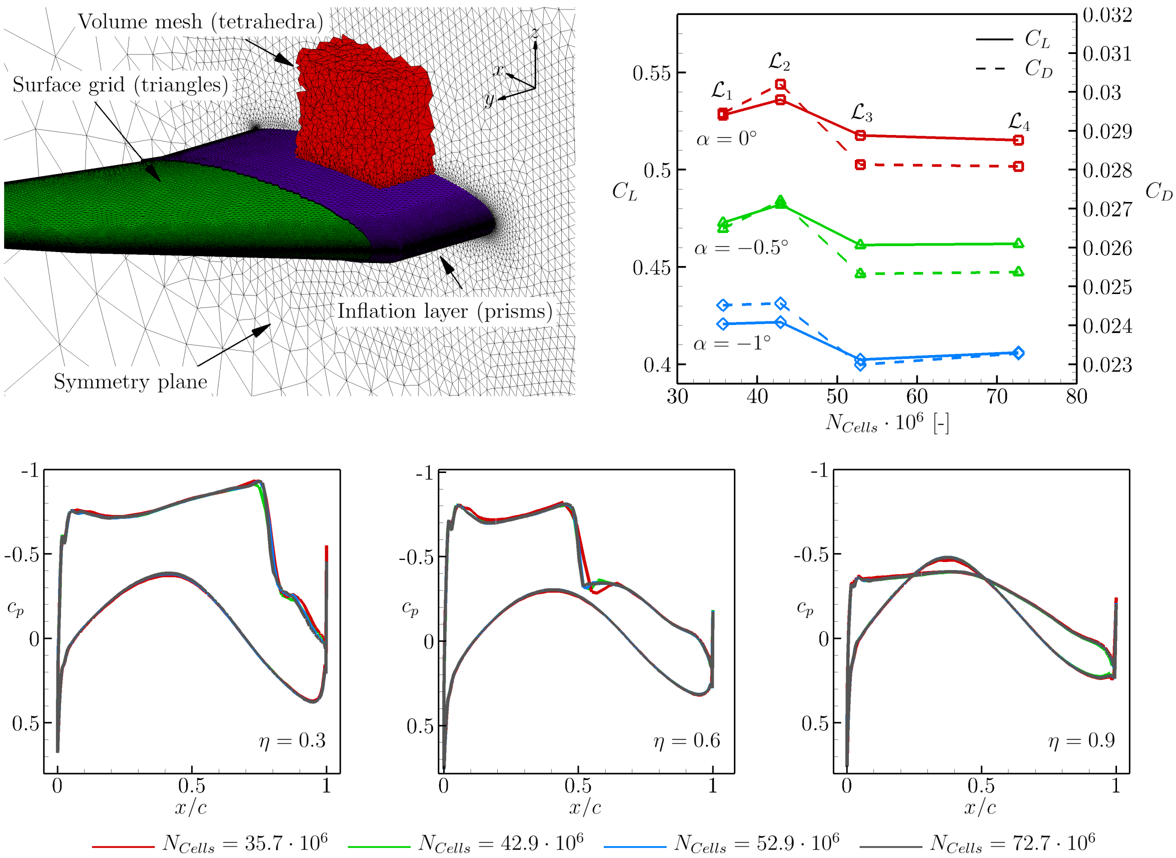


Figure 3.2: Top left panel: Overview of hybrid grid structure using triangles (surface), prisms (inflation layer), and tetrahedra (volume mesh) for representation of the numerical domain. Top right panel: Assessment of integral force coefficients $C_L$ and $C_D$ with varying mesh refinement levels, for three different angles of attack $\alpha$. Bottom panels: Pressure coefficient distributions for varying mesh refinement levels at three spanwise stations of CATeW-02, $\alpha = 0°$, from [54].

[1] For an overview of the computational domain and the wing surface grid, the reader may refer to the accordingly constructed mesh for CATeW-02-WB presented in Fig. 4.3.

Grid independence is achieved for grid refinement level $\mathcal{L}_3$. Considering integral force coefficients, further refinement only leads to marginal variation, while the computational expense in terms of CPU wall clock-h approximately doubles using a parallel computation on 768 domains. Referring to local aerodynamic effects of varying mesh resolution, differences arise mainly in the resolution of the shock. When comparing $c_p$ distributions computed with mesh $\mathcal{L}_3$ to the finest mesh $\mathcal{L}_4$, see Fig. 3.2 bottom, differences are correspondingly little, i.e. the shock matches in location and strength. Apart from the shock, grids $\mathcal{L}_3$ and $\mathcal{L}_4$ result in nearly identical $c_p$ distributions, for which the remaining numerical assessments are performed using grid $\mathcal{L}_3$.

## 3.2 Aerodynamic Characterization

### 3.2.1 General Flow Field

An initial aerodynamic assessment of the flow field occurring for the no-suction baseline case is presented in Fig. 3.3. The left-hand panels show the pressure coefficient distributions for both the suction side and the pressure side of the wing, alongside indications of relevant flow topological phenomena. The panels on the right are devoted to streamwise $c_p$ distributions at three spanwise stations along the wing. The depicted pressure distributions are extracted for the baseline cruise case at $C_L = 0.5$, $Ma = 0.83$ and altitude $H = 35\ 000$ ft, resulting in a Reynolds number of $34.4 \cdot 10^6$. As indicated in Sec. 2.3.1, the cruise flight envelope is sampled by prescription of lift coefficient $C_L$ values rather than the angle of attack $\alpha$, the latter being iteratively set by means of a target-$C_L$ algorithm during runtime of a numerical simulation.
The pressure coefficient distribution shows typical characteristics linked to the transonic operation regime. With reference to the surface distributions of the pressure coefficient $c_p$ on the suction side of the wing, a lambda shock structure emerges in the inboard sections of the wing. The shock system is marked by a weak shock wave, reducing in strength in the spanwise direction, upstream of a strong recompression shock in the rear stations of the wing. The shockwaves merge into a single front at approx. $\eta = 0.3$ (kink station of the wing), outboard of which a single shock propagates in outboard direction, successively diminishing in strength in wing tip direction and ultimately leading to a shock-free recompression outboard of $\eta \gtrapprox 0.8$. This behavior is connected to the aerodynamic washout incorporated in the three-dimensional geometry. The isobars on the wing suction side are slightly unswept with respect to the wing planform, when considering the upstream shift in shock position with increasing spanwise stations. This is primarily connected to the geometry being based on the OAD version of the wing, thus opening room for optimization for a final three-dimensional wing shape, especially in the kink region of the wing. In the recompression zone of the wing suction side, however, the sweep angle of the isobars agrees with the trailing edge sweep angle of the wing.
The same is true for the pressure side of the wing, where the isobar sweep angle agrees

with the geometrical sweep angle. A minor region of negative $c_p$ is observable, recompression takes place shock-free except for the limited inboard region $\eta \lessapprox 0.2$ (denoted by "secondary shock" in Fig. 3.3).

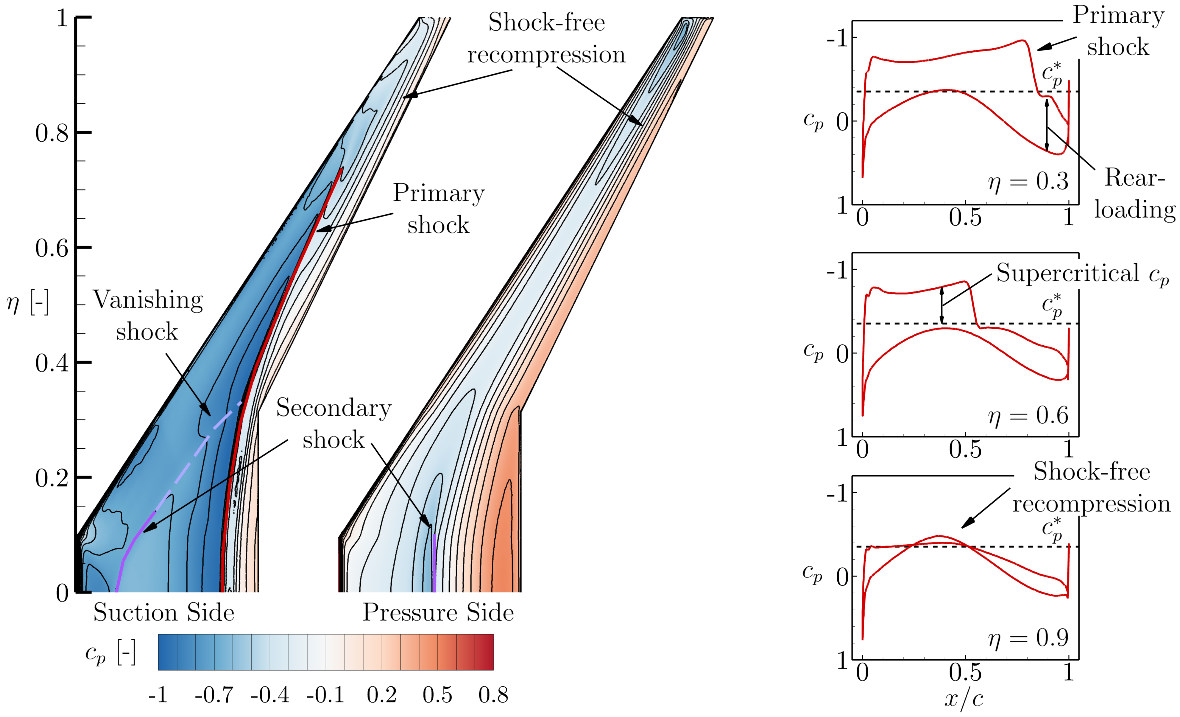


Figure 3.3: Left panels: Contour plots and isobars of the pressure coefficient $c_p$ on the wing suction and pressure sides, $C_L = 0.5$, $Ma = 0.83$, $H = 35\,000$ ft. Right panels: Streamwise $c_p$ distributions extracted at three spanwise stations.

The streamwise $c_p$ distribution (c.f. Fig. 3.3, right panels) correspondingly reflects the above-mentioned shock topology. Quantification of the supercritical loading is indicated by the corresponding critical pressure coefficient $c_p^*$ [21]:

$$c_p^* = \frac{2}{\kappa Ma^2} \cdot \left[ \left( \frac{1 + \frac{\kappa-1}{2} \cdot Ma^2}{1 + \frac{\kappa-1}{2}} \right)^{\frac{\kappa}{\kappa-1}} - 1 \right] \tag{3.1}$$

where $\kappa$ denotes the heat capacity ratio[2].

The pressure distributions are marked by large areas of supersonic flow, i.e., $c_p < c_p^*$ for spanwise stations along the shock front. Outboard sections, e.g. $\eta = 0.9$, still show the emergence of locally supersonic flow regions. As indicated above, however, recompression takes place without the development of a shock wave. The airfoils are furthermore linked to a marker rear loading characteristic, manifesting itself through a corresponding pressure coefficient difference $\Delta c_p$ in the trailing edge region of the wing. The rear-loading occurs over the entire span of the wing, with reducing loads being associated with further outboard spanwise stations.

To further assess the three-dimensional boundary layer characteristics associated with

[2] $\kappa = 1.4$ for dry air

the wing of CATeW-02, the right panel of Fig. 3.4 shows a general overview of the skin friction lines (black), alongside the streamlines based upon the boundary layer edge velocity $\boldsymbol{u}_e$. The contour plot is dedicated to the maximal flow angle within the three-dimensional boundary layer compared to the boundary layer edge velocity $\boldsymbol{u}_e$. As for the theoretical background presented in Sec. 2.1.1 in the context of ALT and CFI, the wing possesses a marked three-dimensional boundary layer velocity profile in the leading edge region of the wing, accompanied by high streamline distortion. Between the leading edge of the wing and the shock foot, the boundary layer velocity profile aligns with the inviscid streamlines, whereas the shock boundary layer interaction leads to two distinct separation phenomena, as typically encountered on transonic aircraft wings [74]. In the inboard stations of the wing, the flow locally separates at the shock foot, while reattaching further downstream to form a closed separation bubble up to $\eta \approx 0.25$. Outboard of $\eta = 0.25$, the shock wave correspondingly leads to flow separation, without subsequent turbulent reattachment. Both types of separation induce high deflection angles $\beta_{max}$, as the flow field within the separated regions of flow is dominated by spanwise velocity components within the boundary layer. Further outboard the separation bubble is again closed, and finally, no flow separation is encountered outboard of $\eta \approx 0.6$ due to the shock strength diminishing in the respective direction.

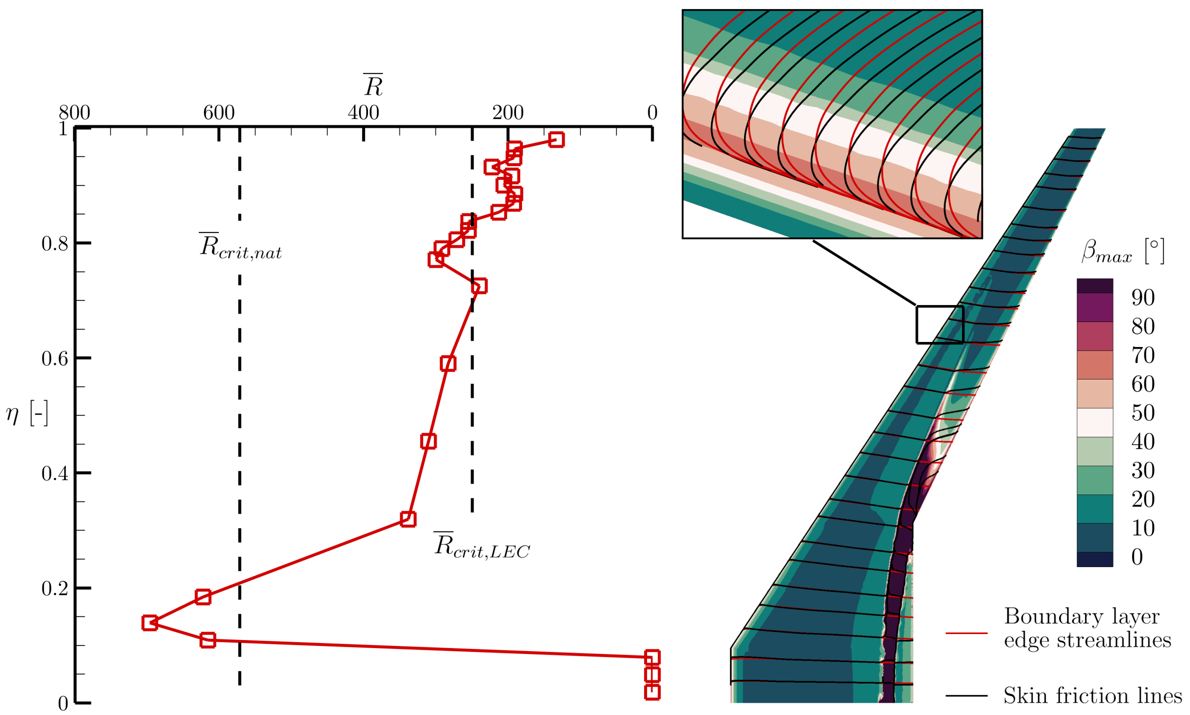


Figure 3.4: Left panel: $\overline{R}$ computed with the subroutine LEA [112] used for evaluation of the Pfenninger-Poll criterion. Right panel: Contour plot of the maximal flow direction angle $\beta$ between the boundary layer edge velocity direction and the three-dimensional boundary layer velocity profile, cf. Fig. 2.3 a).

For completeness, the left panel of Fig. 3.4 features an additional assessment of the attachment line momentum thickness Reynolds number $Re_{\theta,AL}$ used in the Pfenninger-Poll criterion, see Sec. 2.1.1. The Reynolds number $Re_{\theta,AL} = 0.4042\overline{R}$ is computed in the course of a transition prediction process with LST using the subroutine LEA [112]. As depicted in Fig. 3.4, the wing surpasses both critical levels for natural attachment line transition as well as LEC in the inboard station ($\eta < 0.2$) of the wing. In an operational scenario, this would require either reshaping the wing geometry in the critical region, e.g., by locally reducing the leading edge sweep angle $\phi_{LE}$, or the airfoil leading edge radius. Furthermore, flow control by applying boundary layer suction has also been shown to be an effective means of increasing the critical value of $\overline{R}$ [8, 74]. Transition at the attachment line is generally a show-stopper for laminar wings in operation. Nevertheless, as the HLFC/VC coupling is not intended to interact with the attachment line flow, this aspect is set aside at the analysis stage of the technology coupling considered within the remainder of the thesis, opening the opportunity to be envisaged in future work, e.g., when deriving an optimized three-dimensional wing geometry.

## 3.2.2 Implications of Variable Camber Integration

To assess the implications of VC-integration to the reference wing CATeW-02, initially the aerodynamic load case $C_L = 0.5$, $Ma = 0.83$, at the initial cruise altitude of $H = 35\ 000$ ft for varying ADHF deflection angles is considered in Fig. 3.5.

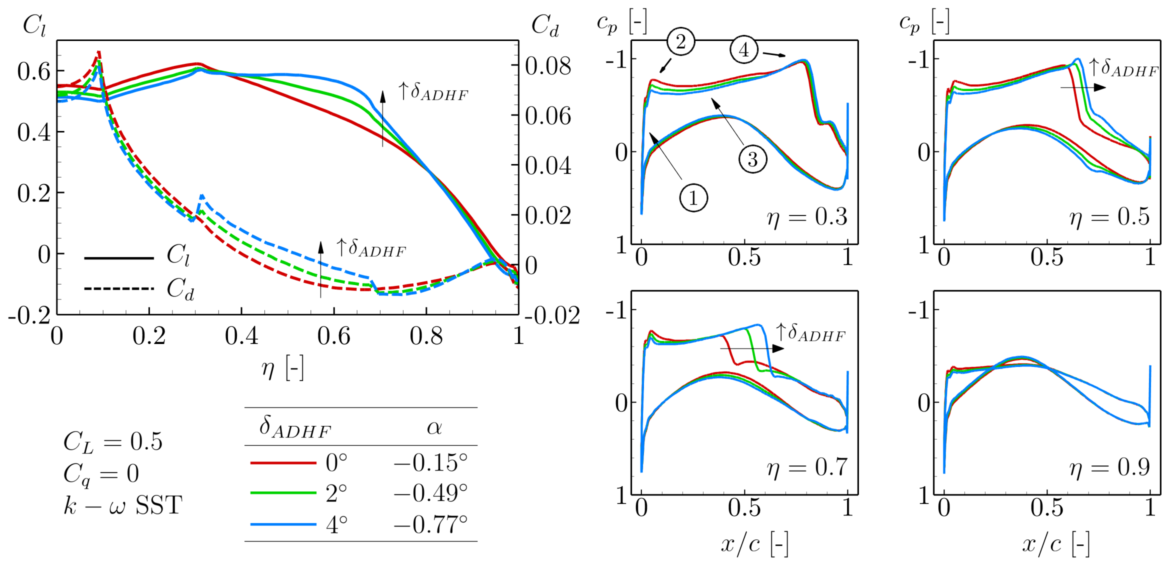


Figure 3.5: Left panel: Spanwise distribution of local lift $C_l$ and drag coefficients $C_d$ for varying ADHF deflection angles $\delta_{ADHF}$. Right panels: Pressure coefficient distributions at four spanwise slices along the wing, with varying $\delta_{ADHF}$. All extractions are performed for $C_L = 0.5$, $Ma = 0.83$ at $H = 35\ 000$ ft.

Concerning the distribution of local lift and drag coefficients $C_l$ and $C_d$, a positive (downward) deflection of the ADHF flap results in a local increase in load within the ADHF region located at $\eta = 0.31 - 0.68$, see left panel of Fig. 3.5. This is connected to the downward deflection of the ADHF acting in increasing the wing camber, as well as the wing area in the corresponding spanwise section. This ultimately leads to a reduction in the required angle of attack $\alpha$ to reach the prescribed $C_L$ values, and connected to this a corresponding reduction in local $C_l$ and $C_d$ values in the inboard section of the wing, i.e. $\eta \lessapprox 0.32$.

The implications discussed above for the spanwise load distributions correspondingly manifest themselves when considering the streamwise distribution of the pressure coefficient $c_p$, see right panels of Fig. 3.5. The reduction in the required angle of attack with increasing $\delta_{ADHF}$ initially leads to a reduction of the suction peak in the nose region of the wing. The increase in local aerodynamic loads is connected to a downstream shift of the shock position, which is accompanied by an increase in shock strength.

When targeting HLFC application to an aircraft wing, there exists a series of requirements towards the streamwise $c_p$ distribution, which are satisfied in the case of CATeW-02 [12]. Taking the sectional cut at $\eta = 0.3$ from Fig. 3.5 as a reference, the $c_p$ distribution initially shows a marked acceleration zone 1 in the leading edge region of the wing. In connection with the highly three-dimensional character of the boundary layer at this airfoil station, this region usually requires the highest suction rates in order to suppress critical amplification of CFI. To reduce the spanwise pressure gradient driving the development of cross-flow velocity profiles (cf. Sec. 2.1.1), the $c_p$ distribution should possess no or a mildly adverse pressure gradient in the following downstream section 2. This region is concluded by a preferably long region of negative pressure gradient 3, typically commencing downstream of the HLFC suction panel. As discussed in Secs. 2.1.1 and 2.1.2, a negative pressure gradient is decisive when it comes to stabilizing the boundary layer towards Tollmien-Schlichting instabilities, thus forming the central aspect of the NLF component of the HLFC system. In connection with the latter characteristic, the emergence of the recompression shock 4 is desirable to be as aft as possible concerning the streamwise coordinate $x/c$. Opposing this is the typically larger shock strength connected to a long flow acceleration zone with $dp/dx < 0$, which needs to be balanced with the above in order to avoid laminar separation of the boundary layer.

Based on the phenomena discussed above (reduction of the suction peak, downstream shift of the shock location), ADHF deflection, therefore, leads to a prolongation of negative pressure gradient flow, as well as an increase in the magnitude of the negative pressure gradient up to the shock position. Both effects are desirable when it comes to coupling VC with an HLFC system, in terms of stabilizing TS-waves in the mid-chord region of the airfoil. To quantify the corresponding effects, a set of no-suction reference computations employing the LST workflow with the two-$N$-factor integration method are presented in Fig. 3.6.

The stability calculations are presented in the form of $N_{TS}$- and $N_{CF}$-factor envelopes at three line-in-flight cuts within the ADHF span, see top panel of Fig. 3.6. For reference, the corresponding panel depicts contour plots of the $c_p$ distributions on the wing suction side for the above-presented ADHF deflection angles. The characteristics of a downstream shift in shock location are observable along the entirety of the ADHF span, i.e. regarding the three-dimensional flow field about CATeW-02, ADHF deflection tends to counteract the unsweeping of the isobars encountered for the baseline at $\delta_{ADHF} = 0°$. Returning to the bottom panels of Fig. 3.6, the stabilizing effect of ADHF deflection on TSI is reflected through a marked reduction in TS-wave amplification rates $N_{TS}$. Furthermore, the point of laminar separation, in this case the shock position, is shifted further downstream at $\eta = 0.45$ and 0.58, reflected in the higher streamwise extent of $N$-factors resulting from the stability computations for the respective ADHF settings.

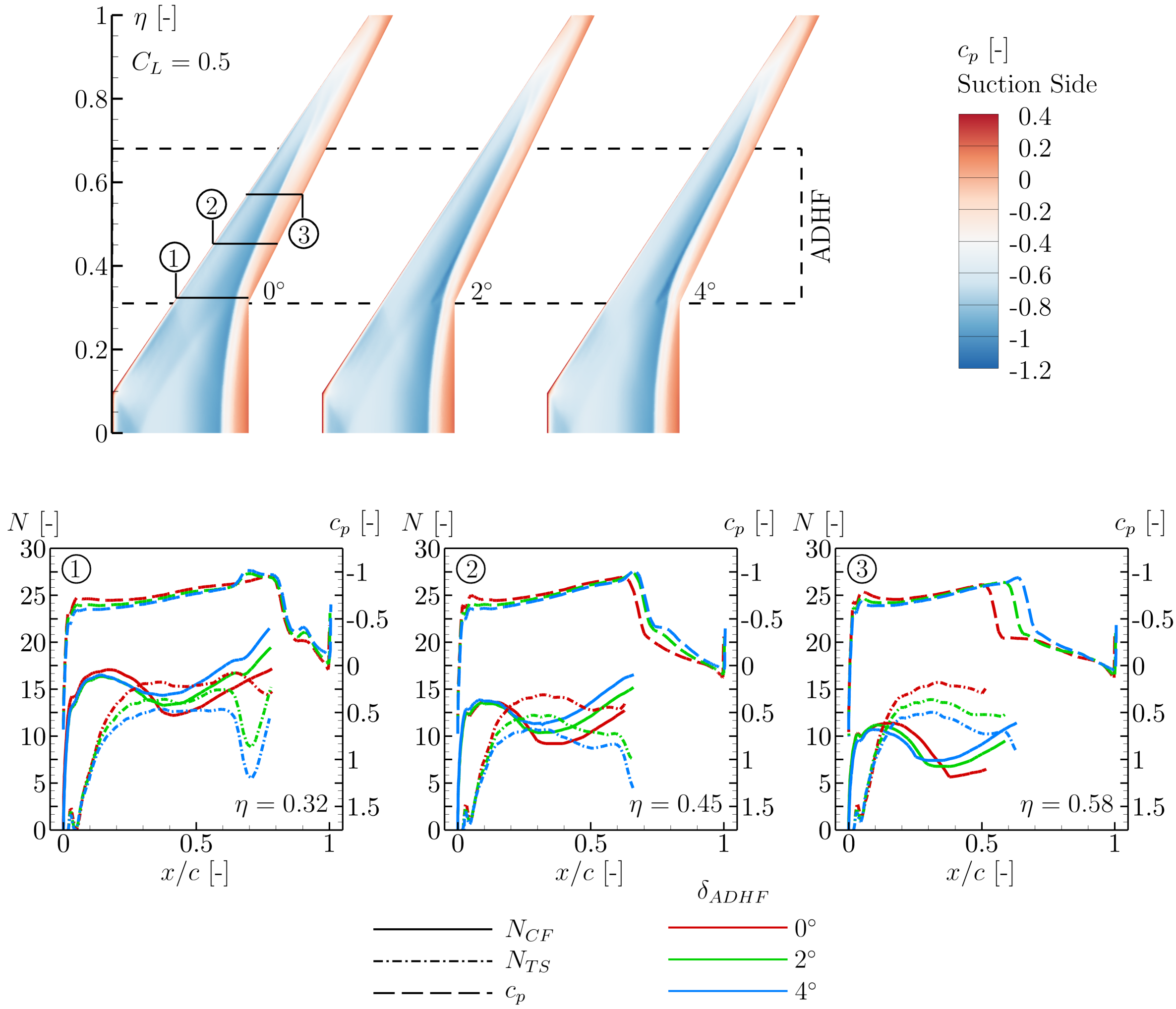


Figure 3.6: Top panel: Contour plot of $c_p$ distribution on the suction side of the wing for varying ADHF deflection angles $\delta_{ADHF}$. The bottom panel shows $N$-factors calculated with LST at three spanwise line-in-flight cuts within the extent of the ADHF, alongside the $c_p$ distributions on the wing suction side used for the corresponding analyses.

Considering the amplification of CF-waves, the $N_{CF}$-envelopes surpass the critical levels directly downstream of the leading edge, see Sec. 3.3.1 for an associated discussion on the transition position. Furthermore, the increase in pressure gradient magnitude in the mid-chord region of the wing is connected to an increase in corresponding $N_{CF}$-factors, therefore opposing the effect of VC integration on TSI. This behavior is connected to a pressure gradient always destabilizing a boundary layer concerning its cross-flow velocity profile, independent of its sign. While the VC system is naturally not targeted at the suppression of CFI, this opposing behavior needs to be considered in the suction strength requirement of the HLFC system. The suction strength needs to be sufficiently strong so that the synergistic potential of VC on TSI is not neutralized by the effects of VC on CFI.

## 3.3 Technology Coupling

To assess the technology coupling on wing level, the results of numerical simulations comprising the cruise Mach number $Ma = 0.83$ at initial cruise altitude $H = 35\ 000$ ft, for varying lift coefficients $C_L = 0.45-0.55$, ADHF deflection angles $\delta_{ADHF} = [0°; 2°; 4°]$, and suction coefficients $C_q = [0; -4; -8; -12] \cdot 10^{-4}$ are presented in the following. The suction coefficients are chosen based on studies performed by Effing et al. [29] on the AVACON Research Baseline 2028 [138] (see Sec. 3.1). It has to be noted, however, that the suction coefficients in this thesis are not optimized and feature a constant suction profile, as the main requirement of this study lies in reflecting the interactions of laminar flow with the VC system.
As pointed out in the introductory part of Chap. 3, a central differentiation point of the analyses consists in the application of both the LST framework coupled to the two-$N$-factor method for transition prediction (Sec. 3.3.1) and the $\gamma - Re_\theta$+CF (Sec. 3.3.2) model. The first approach presents state-of-the-art when it comes to transition prediction for HLFC design activities, and for assessment of the technology coupling from a flow physical viewpoint offers the decisive advantage of inherently differentiating between critical transition mechanisms. The LCTM approach is a current research area, especially when it comes to coupling with boundary layer suction. Therefore, next to purely aerodynamic analyses, an assessment comprising critical ratios and the influence of boundary layer suction by means of the effusion mass flux boundary condition on the latter is presented in Sec. 3.3.2.2.

### 3.3.1 Analysis with Linear Stability Theory

For the application of the automatic transition prediction framework, a set of 24 line-in-flight cuts is chosen along the span of the CATeW-02 wing, resulting in a corresponding evaluation of boundary layer profiles via COCO and subsequent stability analysis through LILO for 48 streamlines (24 per suction/pressure side). The critical $N$-factor correlation for transition prediction with the two-$N$-factor method is presented in Fig. 2.6, axes-intersection $N$-factors resulting in $N_{TS,crit} = 9.5$ and $N_{CF,crit} = 7.5$. The correlation curve is convex-shaped, which is intended to model weak interaction effects between TS- and CF-waves [95], otherwise not included in the present framework built upon LST.

Transition lines for varying suction coefficients $C_q$ and ADHF deflection angles $\delta_{ADHF}$ at the design $C_L = 0.5$ are presented in Fig. 3.7. The contour plot of the $c_p$ distribution shows the configuration $C_q = 0$ and $\delta_{ADHF} = 0°$ in all cases, while the color coding in the background of the figure intends to indicate the mechanism triggering transition in the corresponding spanwise stations.

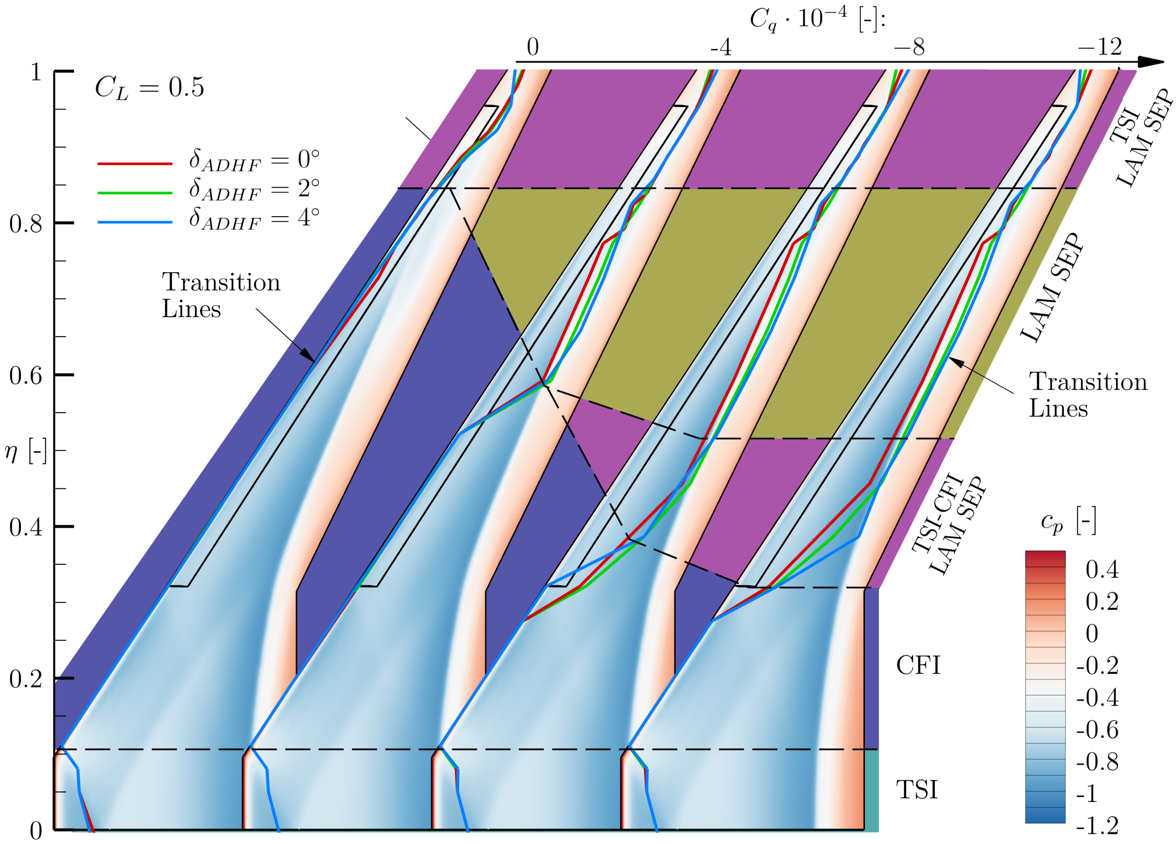


Figure 3.7: Predicted transition lines by means of linear stability with two-$N$-factor transition prediction method for varying suction coefficients $C_q$ and ADHF deflection angles $\delta_{ADHF}$ at $C_L = 0.5$, $Ma = 0.83$, $H = 35\,000$ ft. Additionally, the critical transition mechanisms are indicated along the wing span. The $c_p$ contour is extracted for the wing suction side at $\delta_{ADHF} = 0°$ and $C_q = 0$. Adapted from [54].

Focusing on the no suction case (leftmost wing in Fig. 3.7) first, the dominating transition mechanism is connected to CFI. Transition is therefore predicted to occur in direct vicinity of the wing leading edge along the majority of the wing span. A shift in transition mechanism is observable for $\eta \gtrapprox 0.85$, where transition is partially caused by TSI or, given the $N$-factors not surpassing the critical limit, the point of laminar separation is prescribed as transition position, indicated by LAM SEP in Fig. 3.7. The same is true for the wing root section ($\eta \leq 0.1$), where TSI presents the sole transition mechanism. When increasing the suction strength, i.e. $C_q \downarrow$, the LST framework predicts a pronounced shift in transition mechanism inboard of the stations $\eta \approx 0.85$. The previously CFI-dominated section $0.6 < \eta < 0.85$ exhibits subcritical amplification of both TSI and CFI, for which the transition position is set to the laminar separation point coinciding with the shock front. Inboard of $\eta \approx 0.6$, the suction strength $C_q = -4 \cdot 10^{-4}$ does not suffice to suppress transition due to CFI. Emphasizing the spanwise section $0.6 \lessapprox \eta \lessapprox 0.85$, the implications of VC integration to the wing (see Sec. 3.2.2) are therefore directly reflected in the predicted transition positions for varying ADHF deflection angles $\delta_{ADHF}$.

Further increasing the suction strength to $C_q \leq -8 \cdot 10^{-4}$ affirms the above-discussed phenomena. An expansion of the area with subcritical amplification of both CFI and TSI is predicted (ochre region in Fig. 3.7) up to $\eta \approx 0.5$, allowing for effective control of the transition position by means of ADHF deflection. The farthest downstream shift in transition position is connected to $\delta_{ADHF} = 4°$, with the mid-setting $\delta_{ADHF} = 2°$ leading to a comparable shift in transition position.

For both suction coefficients $C_q \leq -8 \cdot 10^{-4}$, an additional region of either coupled TSI-CFI transition or LAM SEP transition arises in the spanwise section $0.3 \lessapprox \eta \lessapprox 0.5$, for which the corresponding region is highly sensitive to the ADHF deflection angle. Considering the highest suction coefficient magnitude $C_q = -12 \cdot 10^{-4}$, the setting of the ADHF flap not only dictates the position of the transition front as for the LAM SEP area, but is also capable of switching the transition mechanism from TSI-CFI coupled transition to the latter. This effect is observable for the case $\delta_{ADHF} = 4°$, where the ADHF deflection leads to subcritical amplification of both transition mechanisms and thus a distinct downstream shift in transition position.

The impact of the technology coupling on the development of the aerodynamic drag coefficient is depicted in Fig. 3.8, for the design lift coefficient of $C_L = 0.5$. Considering the overall drag coefficient $C_D$, Fig. 3.12 a), an increase in suction strength, alongside an adequate setting of the ADHF deflection angle, in this case $\delta_{ADHF} = 2°$, both lead to a reduction in $C_D$.

When considering a split into pressure $C_{D,p}$ and friction $C_{D,f}$ parts of the overall drag coefficient[3], see Fig. 3.8 b) and c), the pressure drag component correspondingly reflects the trends connected to the overall drag coefficient $C_D$. With respect to the parameter variations in ADHF deflection, this is the intended mechanism of drag reduction, i.e. integrating VC to the wing is targeted at reducing the pressure drag component. The pressure drag reduction connected to an increase in suction strength $C_q$ may be classified as a secondary means of drag reduction through HLFC application. For the present case, the pressure drag reduction induced by laminarization of the boundary layer is not only of comparable magnitude to the VC effects, but surpasses the latter. This secondary effect is connected to the laminar boundary being thinner than its turbulent counterpart, leading to a reduction of associated viscous decambering. This is in line with the pressure drag component reaching a plateau at $C_q \leq -8 \cdot 10^{-4}$, as the transition front converges to its most downstream position at the corresponding suction coefficient, see

[3] That is, integrating the components of the wall-normal force for the pressure and tangential force components for the friction drag in free-stream direction.

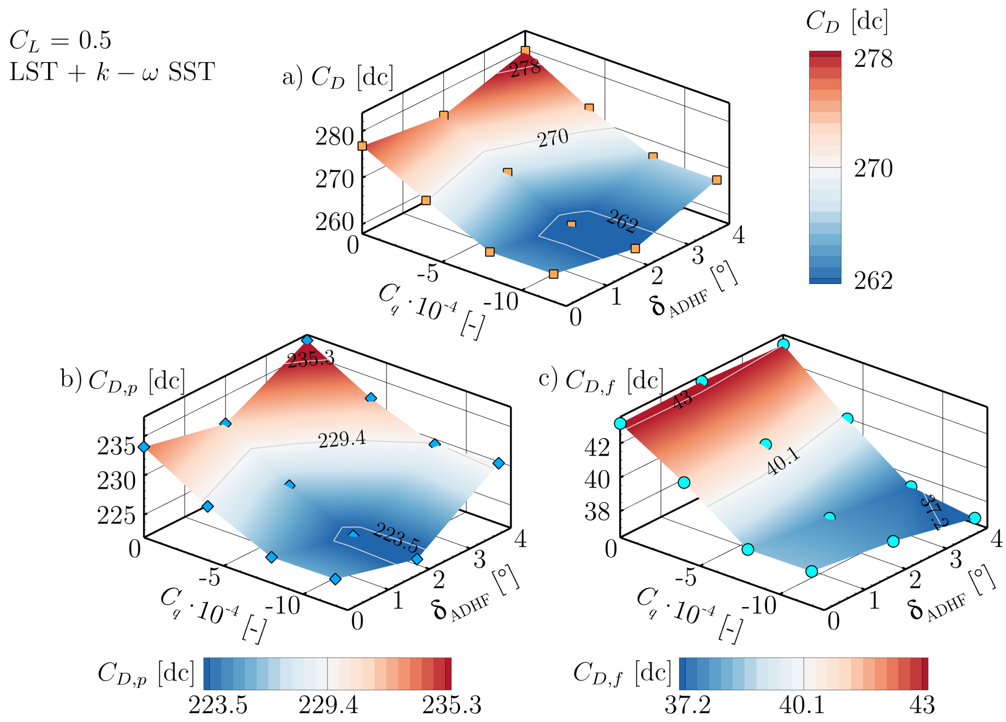


Figure 3.8: Development of the overall (a), pressure (b) and friction (c) drag coefficients for variations in $\delta_{ADHF}$ and $C_q$. Extracted for $C_L = 0.5$, transition prediction by means of LST and two-$N$-factor method. Adapted from [54].

Fig. 3.7. The increase in laminar flow through HLFC therefore acts similarly to a VC system, i.e. reducing the effect of viscous decambering ultimately alters the aerodynamically relevant camberline of the airfoils [23]. Associated with this are corresponding implications on boundary layer thickening via shock-boundary layer interactions, and a reduction in necessary angles of attack to reach the target $C_L$ values.

For the friction drag component $C_{D,f}$ (Fig. 3.8 c), a clear reduction with increasing suction strength, connected to the downstream shift of the transition position, is observable. Based on the course of the $C_{D,f}$ isolines, the most pronounced synergistic effects arise for a coupling of high suction coefficients with high ADHF deflection angles. Again, for suction coefficients $C_q \geq -4 \cdot 10^{-4}$, this is connected to transition being primarily driven by CFI, for which VC integration cannot be expected to yield distinct synergistic effects. These arise when assuring sufficient suction to suppress CFI, in this case, $C_q \leq -8 \cdot 10^{-4}$.

In connection with the above, Fig. 3.9 is dedicated to the development of the skin friction coefficient $c_f$ with increasing suction strength at $C_L = 0.5$, in this case for $\delta_{ADHF} = 2°$ and limited to $C_q = -8 \cdot 10^{-4}$.

The generally thinner boundary layer developing with larger extents of laminar flow not only manifests itself in higher local skin friction coefficients downstream of the shock (c.f. right panels of Fig. 3.9), but also impacts the topology of the skin friction lines in the spanwise extent from $\eta = 0.3$ (kink) to $\eta = 0.6$. This behavior is distinctively marked when the transition front moves closer to the shock front in the corresponding spanwise

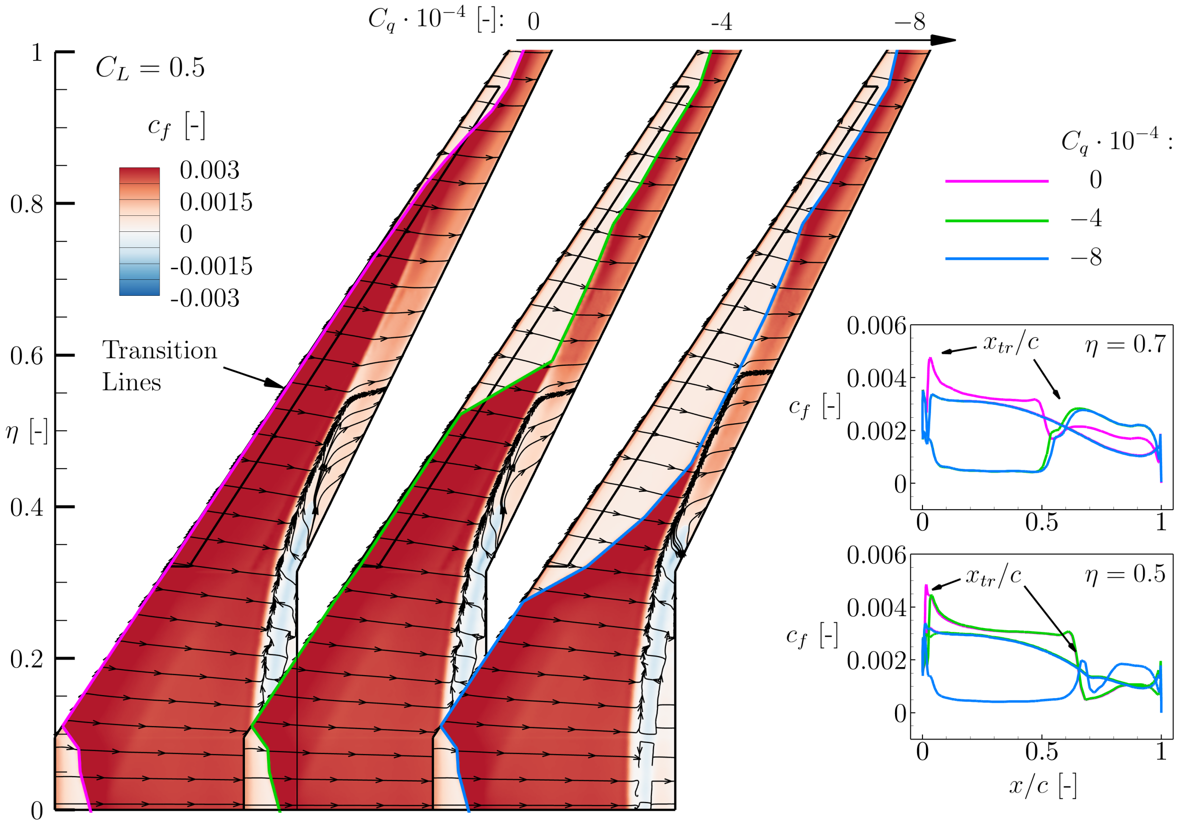


Figure 3.9: Skin friction coefficient $c_f$ distribution for varying $C_q$ at $\delta_{ADHF} = 2°$, $C_L = 0.5$, $Ma = 0.83$, $H = 35\ 000$ ft, alongside predicted transition line. Additionally, skin friction lines on the wing surface and two streamwise $c_f$ distributions at $\eta = 0.5$ and $\eta = 0.7$ are displayed.

region, i.e. when increasing the suction strength from $C_q = -4 \cdot 10^{-4}$ to $C_q = -8 \cdot 10^{-4}$. The region of spanwise flow emanating from the shock-induced recirculation zone separating from the wing surface at the kink position is reduced, for which the skin friction lines are more aligned with the boundary-layer edge streamlines (c.f. Fig. 3.4). This reduces the three-dimensional topology associated with the boundary layer in the corresponding region, positively impacting the reduction in viscous decambering mentioned above.

To further quantify the primary synergy potential of the HLFC/VC coupling, a series of $N_{CF}$- and $N_{TS}$-factors computed for the line-in-flight cut $\eta = 0.59$ are presented in Fig. 3.10. The rows of Fig. 3.10 present the lift coefficients $C_L = 0.45$, 0.5 and 0.55 from top to bottom, while the columns incorporate the suction coefficients $C_q = 0$, $-4 \cdot 10^{-4}$ to $-8 \cdot 10^{-4}$ from left to right.

Strong CF-wave amplification characterizes the no suction cases, Fig. 3.10 panels 1-3, for all parameter combinations of $\delta_{ADHF}$ and $C_L$. Connected to this is a transition location directly downstream of the wing leading edge. This has been discussed and graphically presented previously for $C_L = 0.5$, and correspondingly develops for the other two lift coefficients. With respect to streamwise transition modes, apart from the already described case $C_L = 0.5$ a significant reduction in $N_{TS}$-factors is achievable through ADHF deflections for $C_L = 0.45$. For the higher lift coefficient of $C_L = 0.55$, $N_{TS}$-factors are less sensitive to ADHF deflections.

Increasing the suction rate to $C_q = -4 \cdot 10^{-4}$ leads to sub-critical amplification of CF-waves in the leading edge region of the wing for $C_L = 0.45$ (Fig. 3.10 panel 4) and $C_L = 0.5$ (Fig. 3.10 panel 5), nevertheless, the amplification rates $N_{CF}$ are only little beneath the critical limit for cross-flow driven transition for which an increase in lift coefficient to $C_L = 0.55$ (Fig. 3.10 panel 6) is again characterized by transition due to CFI directly downstream of the attachment line.

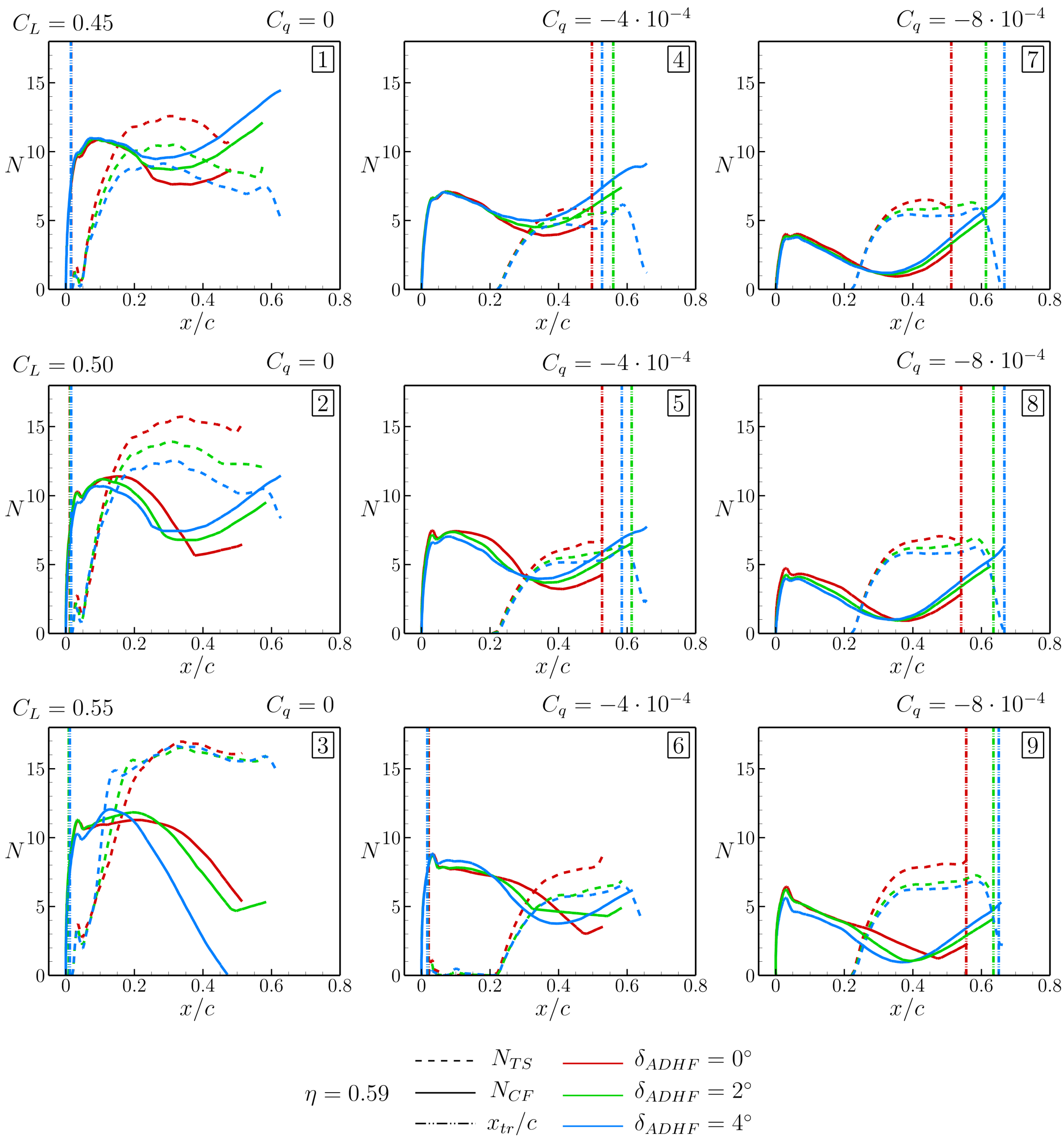


Figure 3.10: $N_{TS}$- and $N_{CF}$-factor envelopes and associated transition positions $x_{tr}/c$ extracted at the line-in-flight cut at $\eta = 0.59$ for varying ADHF deflection angles $\delta_{ADHF}$. Variation of $C_L = [0.45; 0.50; 0.55]$ from top to bottom, $C_q = [0; -4; -8] \cdot 10^{-4}$ from left to right. Adapted from [54].

For the cases $C_L = 0.45$ and $C_L = 0.5$, the farthest downstream shift in $x_{tr}/c$ is achieved by a flap setting of $\delta_{ADHF} = 2°$. This is connected to the intended reduction of $N_{TS}$-factors and the downstream shift in shock location due to VC integration, which, albeit the $N_{CF}$-factors increasing in comparable magnitude in the mid-chord region of the wing, leads to sub-critical amplification of both primary instability modes. The latter aspect is critical for the higher ADHF deflection angle $\delta_{ADHF} = 4°$, where it is possible to further reduce $N_{TS}$-factors, but the opposing behavior on $N_{CF}$-factors leads to an upstream shift of the transition position due to the $N_{TS}$-$N_{CF}$-factor combination exceeding the critical correlation curve. This aspect would aggravate if the correlation curve shows a strong interaction between CFI and TSI. This underlines the aspect, that for the technology coupling to develop synergy effects provision of sufficient suction is of key importance. Application of the highest suction strength $C_q = -8 \cdot 10^{-4}$ considered in Fig. 3.10, panels 7-9, results in a downstream shift of transition position for all computed load cases. Both primary instability mechanisms are sufficiently suppressed by HLFC application alone ($\delta_{ADHF} = 0°$), while the transition position is successively shifted downstream when increasing the ADHF deflection angle. As the transition position is set to the theoretical laminar separation point, i.e. the shock location, the implications of VC integration on the development of the shock front are primarily responsible for the highest shift connected to $\delta_{ADHF} = 4°$. When comparing the $N$-factor envelopes to the cases $C_q = -4 \cdot 10^{-4}$, significant stabilization of the boundary layer towards TSI is observable again, while the counteracting effect of ADHF deflection on $N_{CF}$-factors is less pronounced for the increased suction coefficient $C_q = -8 \cdot 10^{-4}$.

Table 3.1: Isolated and combined potential for drag count reduction for the observed lift coefficients. The increments indicate the difference between the baseline case ($\delta_{ADHF} = 0°$, $C_q = 0$) and the maximal possible reduction.

| $C_L$ | ΔVC | ΔHLFC | ΔVC/HLFC |
|---|---|---|---|
| 0.45 | -3.0 dc | -11.6 dc | -16.5 dc |
| 0.50 | -2.3 dc | -13.1 dc | -16.2 dc |
| 0.55 | -2.1 dc | -14.5 dc | -16.8 dc |

Based on the LST calculations, the technology coupling shows synergistic effects from an aerodynamic viewpoint. The synergy driver is either the intended stabilization of TSI through VC integration while providing sufficient suction for suppression of CFI, or as a secondary synergistic effect, the implications of VC integration on the development of the shock position when suction alone suffices to suppress transition due to TSI and CFI. As an increasing ADHF deflection is also beneficial for the development of the pressure drag component, HLFC integration catalyzes the associated reduction in the respective drag component.

On an integration level, when defining synergy as the coupled application of both technologies reaping greater benefit than the sum of their isolated application, synergy is also mirrored in the respective drag count reductions, see Tab. 3.1.

## 3.3.2 Analysis with Local-Correlation Based Transition Model

### 3.3.2.1 Numerical Simulation Results

An overview of transition positions for $C_L = 0.5$ at $\delta_{ADHF} = 0°$ and varying suction coefficients, predicted by the $\gamma - Re_\theta$+CF model is presented in Fig. 3.11.

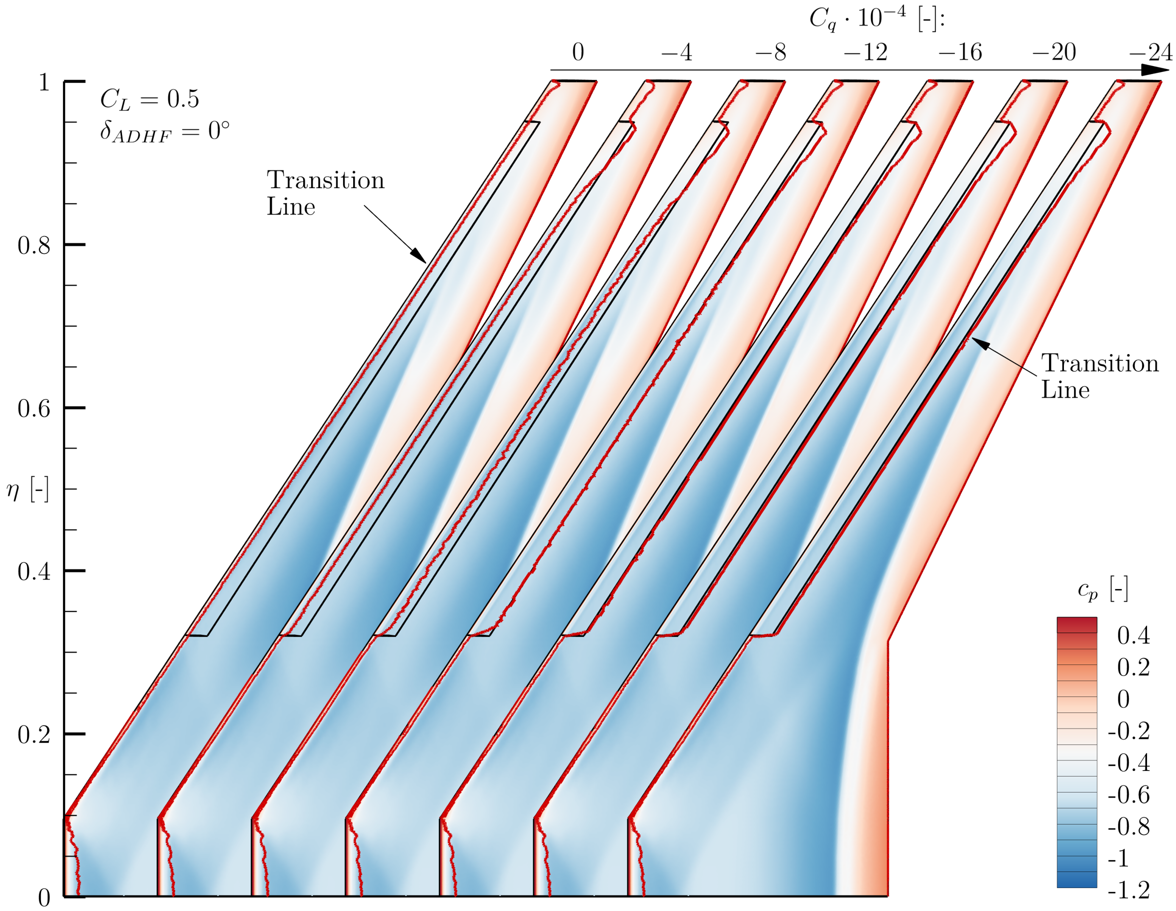


Figure 3.11: Predicted transition lines by means of the $\gamma - Re_\theta$+CF model for varying suction coefficients $C_q$ at $C_L = 0.5$ and $\delta_{ADHF} = 0°$, $Ma = 0.83$, $H = 35\ 000$ ft. The $c_p$ contour is extracted for the wing suction side at $\delta_{ADHF} = 0°$ and $C_q = 0$. Adapted from [54].

Suction, in this case, is implemented by the above-described framework using the effusion mass flux boundary condition (see Sec. 2.3.1), while the coefficients are chosen in line with the corresponding analyses based on LST. Turbulence intensity is set to $Tu = 0.1\%$ at the free-stream boundary of the computational domain, while a set of source terms, implemented in TAU, is activated to avoid the typical decay in turbulence intensity throughout the computational domain [83]. According to Mack's formula [70],

$Tu = 0.1\%$ results in a critical $N$-factor of $N_{crit,Mack} = 8.15$, which falls within the lower range of $N_{TS,crit}$-factors incorporated in the correlation curve used for the two-$N$-factor method, see Fig. 2.6. In the course of the thesis, a set of different turbulence intensities was tested, alongside the application of the Kato-Launder limiter function as studied by Langel et al. [66]. Nevertheless, the impact on the transition positions was found to be negligible.

In line with the previously discussed cases, the baseline case $C_q = 0$ is characterized by a highly upstream position of the transition front, in the direct vicinity of the wing leading edge. While the LCTM approach does not directly allow the identification of the driving transition mechanism, as the correlations for both TSI and CFI are abstracted into the same intermittency production term $P_\gamma$ (see Eq. 2.27), based on the transition position the critical mechanism can be attributed to CFI.

With increasing suction strength, the model reflects a successive downstream shift in transition position, converging to a maximum extent of laminar flow for $C_q = -12 \cdot 10^{-4}$. For the largest spanwise portion, the transition front coincides with the streamwise limit of the suction panel, except for the section $\eta \approx 0.85 - 0.95$ where locally a maximal downstream shift of transition position to $x_{tr}/c \approx 0.5$ is observable at $\eta = 0.94$.

Inclusion of VC into the analysis parameter space leads to the development of the drag coefficient and its corresponding components as depicted in Fig. 3.12.

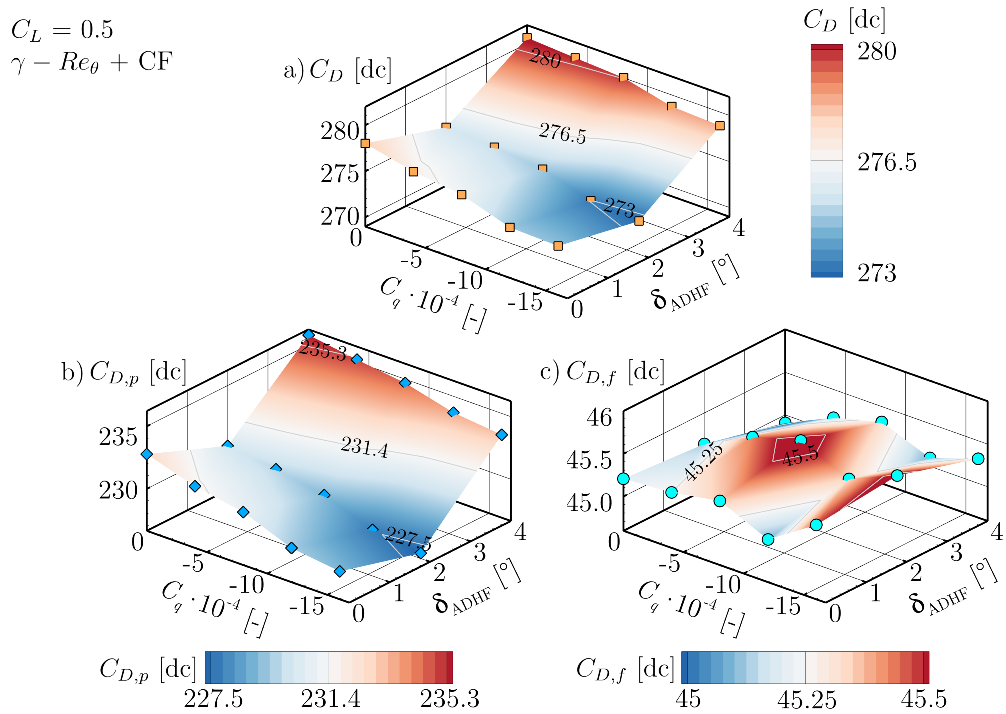


Figure 3.12: Development of the overall (a), pressure (b) and friction (c) drag coefficients for variations in $\delta_{ADHF}$ and $C_q$. Extracted for $C_L = 0.5$, transition prediction by means of $\gamma - Re_\theta$+CF model. Adapted from [54].

As for the analyses based on LST, the overall drag coefficient $C_D$ shows a successive decrease with increasing suction strength, as well as a minimum for $\delta_{ADHF} = 2°$. Considering the pressure drag component (Fig. 3.12, panel b) the trends of the overall drag coefficient are correspondingly reflected. As discussed previously, VC integration is intended to reduce the respective component, while the reduction of viscous decambering connected to boundary layer suction further synergizes with VC integration. Even though the transition front is not markedly shifted downstream by increasing the suction strength $C_q$ from $C_q = -12 \cdot 10^{-4}$ to $C_q = -16 \cdot 10^{-4}$, application of the suction system modeling framework incorporates suction effectively thinning the boundary layer. Therefore, in contrast to the LST-based analyses no plateau is reached in the development of the pressure drag component $C_{D,p}$, even though the magnitude of drag reduction is predicted to be lower overall.

The friction drag component predicted by the $\gamma - Re_\theta$+CF model shows only small sensitivity to parameter variations in $\delta_{ADHF}$ and $C_q$. Concerning the suction coefficient $C_q$, this behavior is connected to the limited extent of laminar flow predicted within the corresponding set of computations. The lowest values in $C_{D,f}$ are achieved for $C_q = -12 \cdot 10^{-4}$, while further increasing the suction strength leads to the friction drag component rising again. This behavior is connected to a higher suction strength ($C_q \leq -12 \cdot 10^{-4}$) leading to an increase in the gradient of the boundary layer velocity profile at the wall $(\frac{du}{dy})_w$, thus compensating the beneficial effect of laminar flow on the skin friction coefficient $c_f$ when the transition front is not further shifted downstream with increasing suction strength, see Eq. 2.6.

#### 3.3.2.2 Assessment of Model Sensitivities towards Boundary Layer Suction

Given the observations discussed above, the application of an LCTM-based approach in connection with the proposed framework for modeling boundary layer suction is able to reflect synergistic effects to a limited extent. While transition is successively shifted downstream with increasing suction strength, transition is predicted to occur further upstream in comparison to the LST-based approach, for which the main potential of transition control in the mid-chord region of the wing is not reproduced in the computations employing the $\gamma - Re_\theta$+CF model.

Transition occurring in upstream stations for high Reynolds number flows is a phenomenon commonly encountered when applying the original $\gamma - Re_\theta$ model with the formulation of the intermittency transport equation proposed by Langtry and Menter [67]. As discussed by Ströer [126], this behavior is connected to the eddy-viscosity production inducing an upstream effect on the production and destruction terms of the intermittency transport equation Eq. 2.22, alongside the momentum thickness Reynolds number $Re_\theta$ used within the correlation for transition prediction. The upstream effect correspondingly shifts the predicted transition position $x_{tr}$ upstream, resulting in a transition location lying ahead of the actual point $x'_{tr}$, where the transition criterion theoretically predicts the onset of transition, i.e. $F_{onset} \approx 1$. Furthermore, the (empirical) transition criterion used within the original model for streamwise transition, as already indicated above based upon the criterion by Abu-Ghannam and Shaw [1], is derived based on experimental data for relatively high turbulence intensities, and has been shown to differ to low turbulence analytical and experimental results in the extent of stabilization or destabilization predicted by the criterion concerning favorable or adverse pressure gradients, respectively [126].

Even though the $\gamma - Re_\theta$ and the hereon based $\gamma - Re_\theta$+CF model is associated with this series of limitations, the model opens the opportunity to assess implications connected to modeling boundary layer suction by means of the framework built around the effusion mass flux boundary condition. Models stemming from the domain of LCTM always incorporate a series of correlations for transition prediction, based on analytical or empirical analysis.

To extract the corresponding effects from a numerical simulation, a set of laminar reference computations is used in the following. Laminar in this case means, the numerical simulation still employs the four-equation $\gamma - Re_\theta$+CF model, but by setting the scale factor $\zeta$ to excessively high values in Eq. 2.25, while turning off the correlation for cross-flow induced transition, Eq. 2.26. Therefore, the transport equations are still solved throughout the reference computations, allowing for assessment of the transition position $x'_{tr}$ predicted by the corresponding correlations and the influence of the suction boundary condition on the latter, but the intermittency production is effectively suppressed due to $F_{onset} = F_{onset,CF} = 0$. The transition criterion connected to separated-flow transition is left unaltered, to avoid laminar separation at the shock foot and ensure stability of the numerical simulations.

Contour plots of $F_{onset}$ and $F_{onset,CF}$, reflecting the criteria for streamwise and cross-flow transition, respectively, are presented in Figs. 3.13 and 3.14. The contours are extracted for the suction coefficients $C_q = [0; -4; -8, -12] \cdot 10^{-4}$, at a spanwise station of $\eta = 0.5$. As indicated above, the onset functions $F_{onset}$ or $F_{onset,CF}$ act as a switch initiating the intermittency production for the ratios $Re_\theta / Re_{\theta c}$ or $Re_{He}/Re^+_{He,t} > 1$. Considering Fig. 3.13 for the streamwise transition mechanisms first, the corresponding downstream shift in $F_{onset} = 1$ is reflected with increasing suction strength. While the no-suction case is marked by a highly upstream position of transition onset, the application of suction with $C_q \leq -4 \cdot 10^{-4}$ sufficiently stabilizes the boundary layer to induce a marked shift in transition onset position, reaching a maximal extent of $x'_{tr}/c \approx 0.3$ for $C_q = -12 \cdot 10^{-4}$. When compared to linear stability theory, the transition onset positions are still predicted to lie further upstream, in the region of favorable pressure gradient, which can be primarily attributed to the limitations of the empirical transition criterion implemented in the $\gamma - Re_\theta$-model.

With respect to the onset function for cross-flow transition $F_{onset,CF}$, corresponding effects are observable when assessing the contour plots for increasing suction strength depicted in Fig. 3.14. The onset function $F_{onset,CF}$ switches directly downstream of the leading edge for the no-suction case, at $x'_{tr}/c \approx 0.007$. This behavior is in line with the

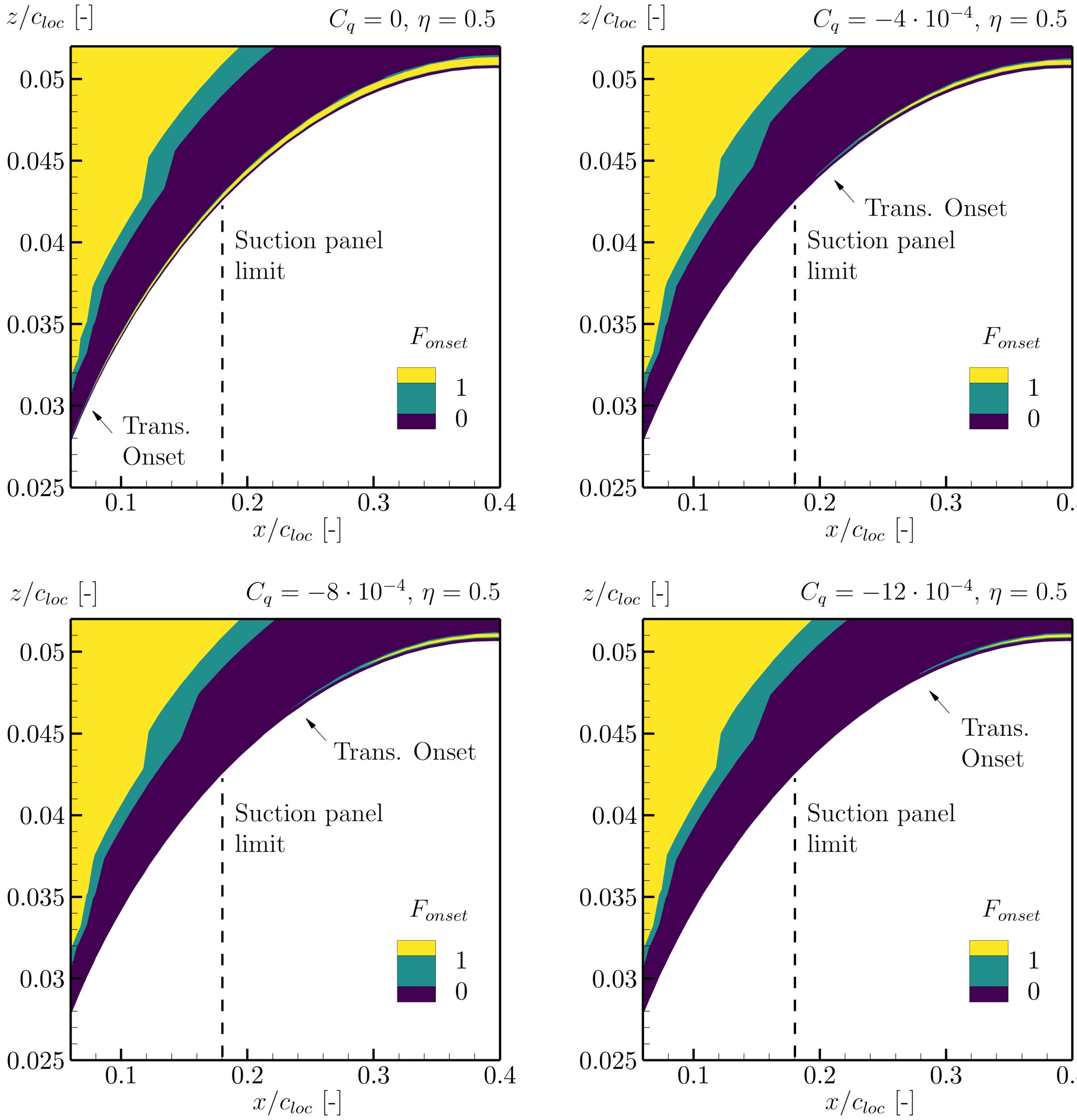


Figure 3.13: Contour plot of the onset function for streamwise transition $F_{onset}$, extracted for varying suction coefficients $C_q$ at $\eta = 0.5$ from laminar reference computations. Adapted from [55].

results of LST and the two-$N$-factor method, showing a comparable transition position at $\eta = 0.5$ due to CFI. With increasing suction strength the predicted transition onset position shifts to $x'_{tr}/c \approx 0.05$ for $C_q = -4 \cdot 10^{-4}$, while significantly shifting downstream to $x'_{tr}/c \approx 0.38$ and $x'_{tr}/c \approx 0.40$ for $C_q = -8 \cdot 10^{-4}$ and $C_q = -12 \cdot 10^{-4}$, respectively. When comparing the cross-flow related criterion embedded in $F_{onset,CF}$ to linear stability results for the cases with suction, the qualitative trends match the behavior reflected in LST-based calculations. Referring to the overview of transition positions computed with LST presented in Fig. 3.7, a suction coefficient of $C_q = -4 \cdot 10^{-4}$ does not suffice to suppress transition due to CFI, correspondingly leading to a comparable transition position predicted by the helicity based transition criterion. Subcritical amplification of

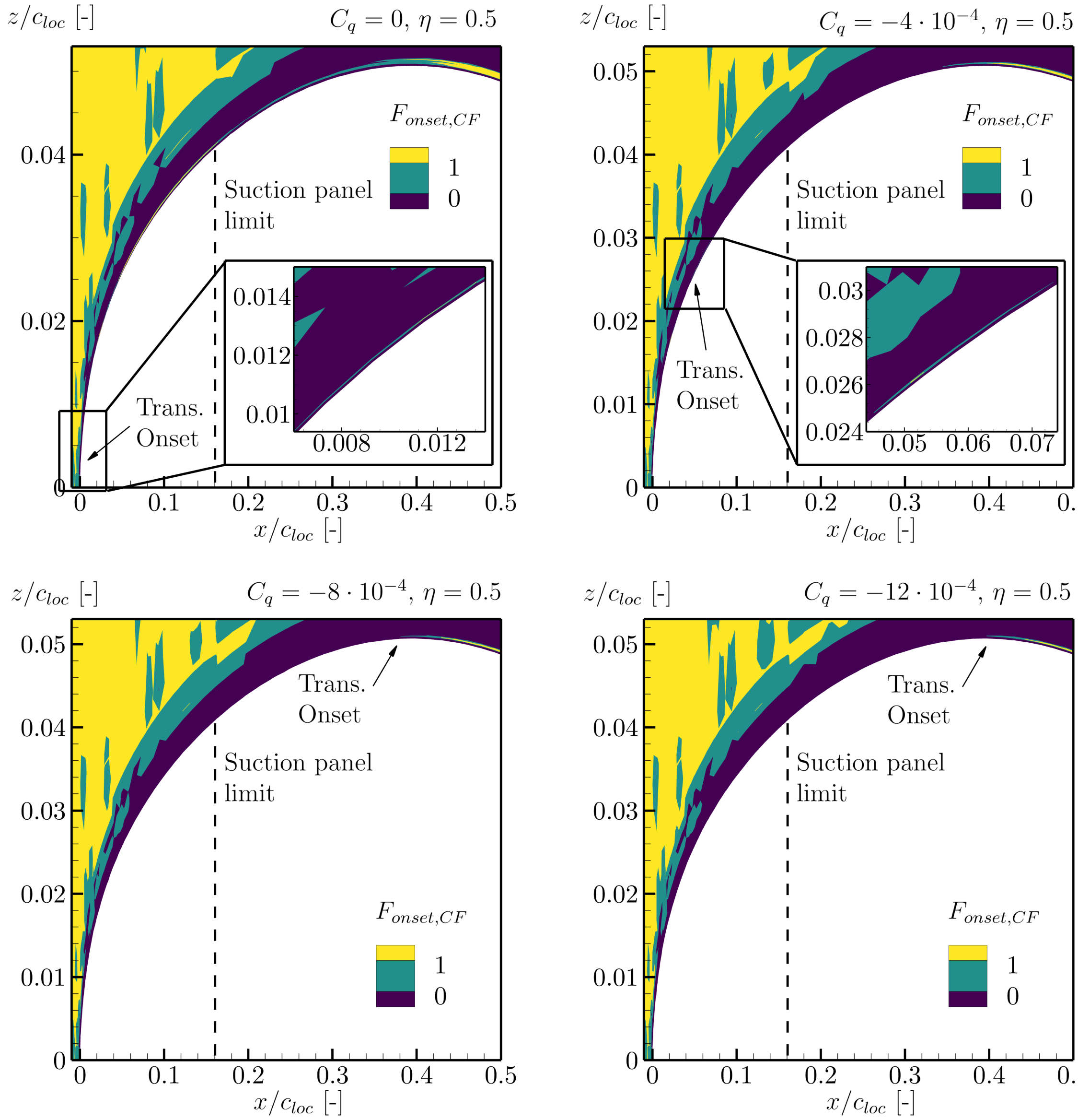


Figure 3.14: Contour plot of the onset function for cross-flow transition $F_{onset,CF}$, extracted for varying suction coefficients $C_q$ at $\eta = 0.5$ from laminar reference computations. Adapted from [55].

cross-flow waves is predicted by means of LST for $C_q \leq -8 \cdot 10^{-4}$ at $\eta = 0.5$, correspondingly leading to a pronounced shift in $x'_{tr}/c$ predicted by the helicity based transition criterion. Furthermore, the transition onset position $x'_{tr}/c$ and the actual transition position $x_{tr}/c$ resulting in the CFD simulation (Fig. 3.11) highly agree for $C_q = 0$ and $C_q = -4 \cdot 10^{-4}$. Even though the comparisons are exploratory, it can be concluded that the helicity-based criterion for the prediction of transition due to CFI is suitable for usage in connection with the boundary condition and can reflect the trends predicted by LST.

To further assess the model sensitivities towards boundary layer suction, Fig. 3.15 shows a series of boundary layer velocity profiles for varying suction coefficients, extracted from the laminar reference computation at $\eta = 0.59$ at six streamwise stations along the wing suction side. Figures 3.16 and 3.17 are dedicated to the same stations, but feature the profile of the Reynolds numbers driving the transition onset correlations Eqs. 2.25 and 2.26, i.e. $F_{onset,1}$ and $F_{onset,1,CF}$. To provide for the corresponding extraction coordinate system, $\boldsymbol{x}_i$ is initially set by the direction of the velocity vector at the boundary layer edge $\boldsymbol{u}_e$ tangentially projected onto the grid surface at the extraction point. From this, the cross-flow direction $\boldsymbol{z}_i$ directly follows by taking the cross-product of $\boldsymbol{x}_i$ with the wall-normal vector $\boldsymbol{y}_i$ at the corresponding extraction point, cf. Fig. 2.3 c).

Considering the laminar boundary layer velocity profiles first (Fig. 3.15), exposing the boundary layer to an increasing suction strength $C_q$ displays a reduction in boundary layer thickness, alongside a decrease in shape factor. Linked to this is an increase in wall-normal velocity gradient $(\frac{du}{dy})_w$ when considering the streamwise velocity profiles $u$. The associated cross-flow velocity profiles show a reduction in their velocity maxima with increasing suction strength, while the thinning of the boundary layer connected to the increasing suction strength draws the maxima in $v_c$ closer to the surface of the wing. As discussed in the context of transition due to TSI in Sec. 2.1.1, a decreasing shape factor generally tends to stabilize the boundary layer towards streamwise instability. This effect is correctly reflected when referring to the development of the vorticity Reynolds number $Re_\nu$ depicted in Fig. 3.16 (dashed lines). The vorticity Reynolds number is used as an auxiliary, locally available variable to model the momentum thickness Reynolds number $Re_\theta$ within the correlation driving the activation of $F_{onset}$. Therefore, the stabilizing effect of boundary layer suction is expressed in the maximum of $Re_\nu$ decreasing with increasing suction strength, while the wall-normal distance of the maxima follows the thinning of the boundary layer. Applying boundary layer suction also impacts the denominator of the correlation for transition onset $2.193 \cdot Re_{\theta c}$ (Eq. 2.25). The biggest impact is observable in stations close to the wall, where a marked increase in the critical Reynolds number for transition onset can be noted. The value of $Re_{\theta c}$ at the boundary layer edge is left unaltered with increasing suction strength. This behavior is connected to the model formulation, as $Re_{\theta c} = f(\widehat{Re}_{\theta t})$ is set according to the above-discussed empirical criterion at the edge of the boundary layer while being transported within the boundary layer by the corresponding transport equation for $\widehat{Re}_{\theta t}$ (Eq. 2.21). Therefore, the suction boundary condition does not alter the transition criterion itself but impacts the transport rates of $\widehat{Re}_{\theta t}$ within the boundary layer, therefore locally reducing the value of the onset function $F_{onset,1} = Re_\nu/(2.193 \cdot Re_{\theta c})$ throughout the boundary layer. This results in the previously shown downstream shift of $F_{onset} = 1$, where based on the profiles shown in Fig. 3.16 the critical ratio driving $F_{onset}$ is already satisfied at $x'_{tr}/c = 0.06$, while the implications on $Re_\nu$ and $Re_{\theta c}$ connected to the suction boundary condition shift $F_{onset} > 1$ to approx. $x'_{tr}/c = 0.28$.

The corresponding plots for assessing the influence of the suction boundary condition on central modeling quantities connected to the cross-flow transition criterion are depicted in Fig. 3.17. The helicity Reynolds number $Re_{He}$ (dashed lines) is compared to the critical helicity Reynolds number $Re^+_{He,t}$ at transition onset, using the original scale factor

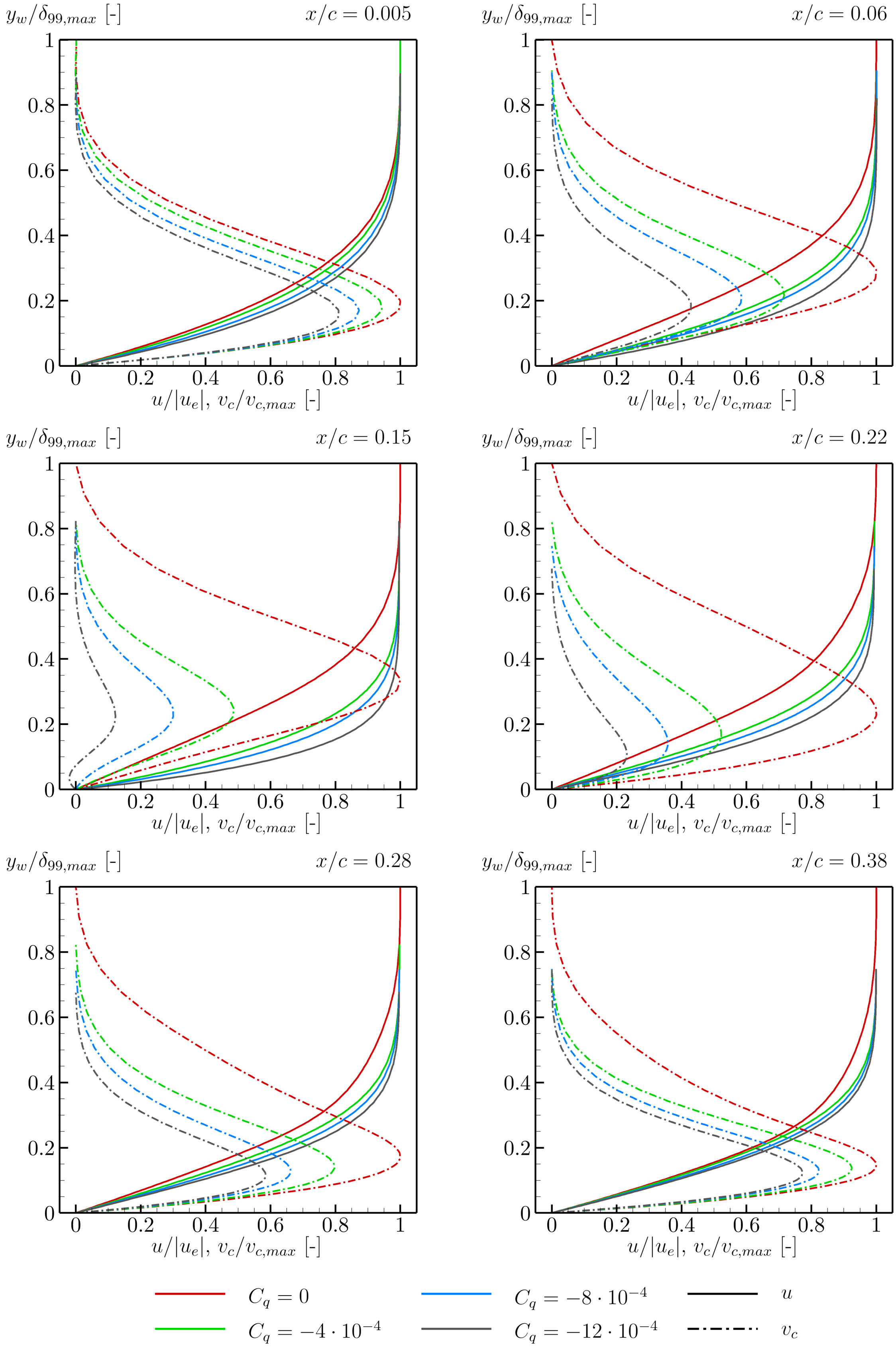


Figure 3.15: Development of laminar boundary layer velocity profiles with increasing suction strength, extracted from laminar reference computations at $\eta = 0.59$ and $C_L = 0.5$. Adapted from [55].

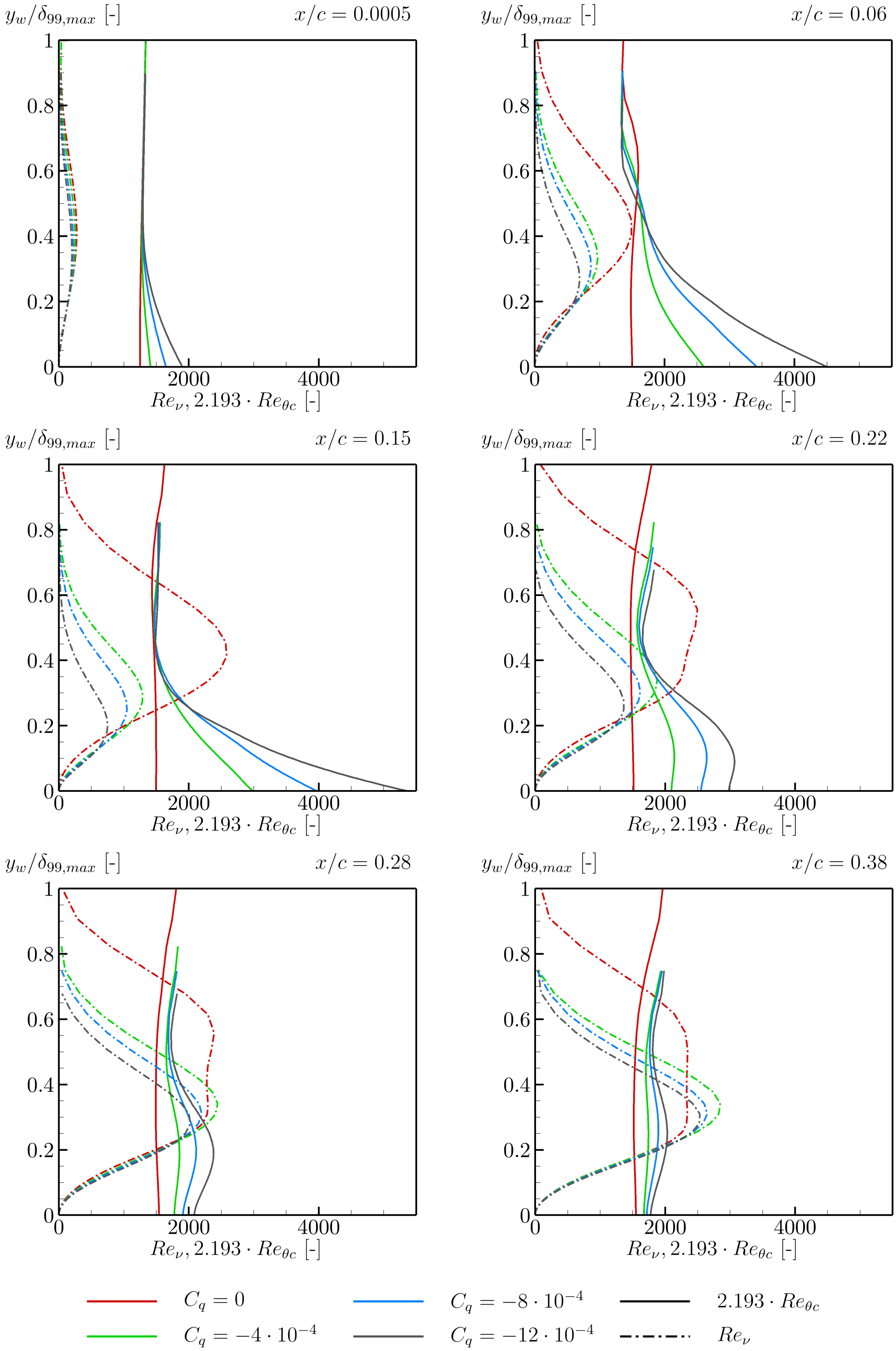


Figure 3.16: Development of vorticity Reynolds number $Re_\nu$ and associated transition criterion $2.193 \cdot Re_{\theta c}$ throughout the laminar boundary layer with increasing suction strength, extracted from laminar reference computations at $\eta = 0.59$ and $C_L = 0.5$. Adapted from [55].

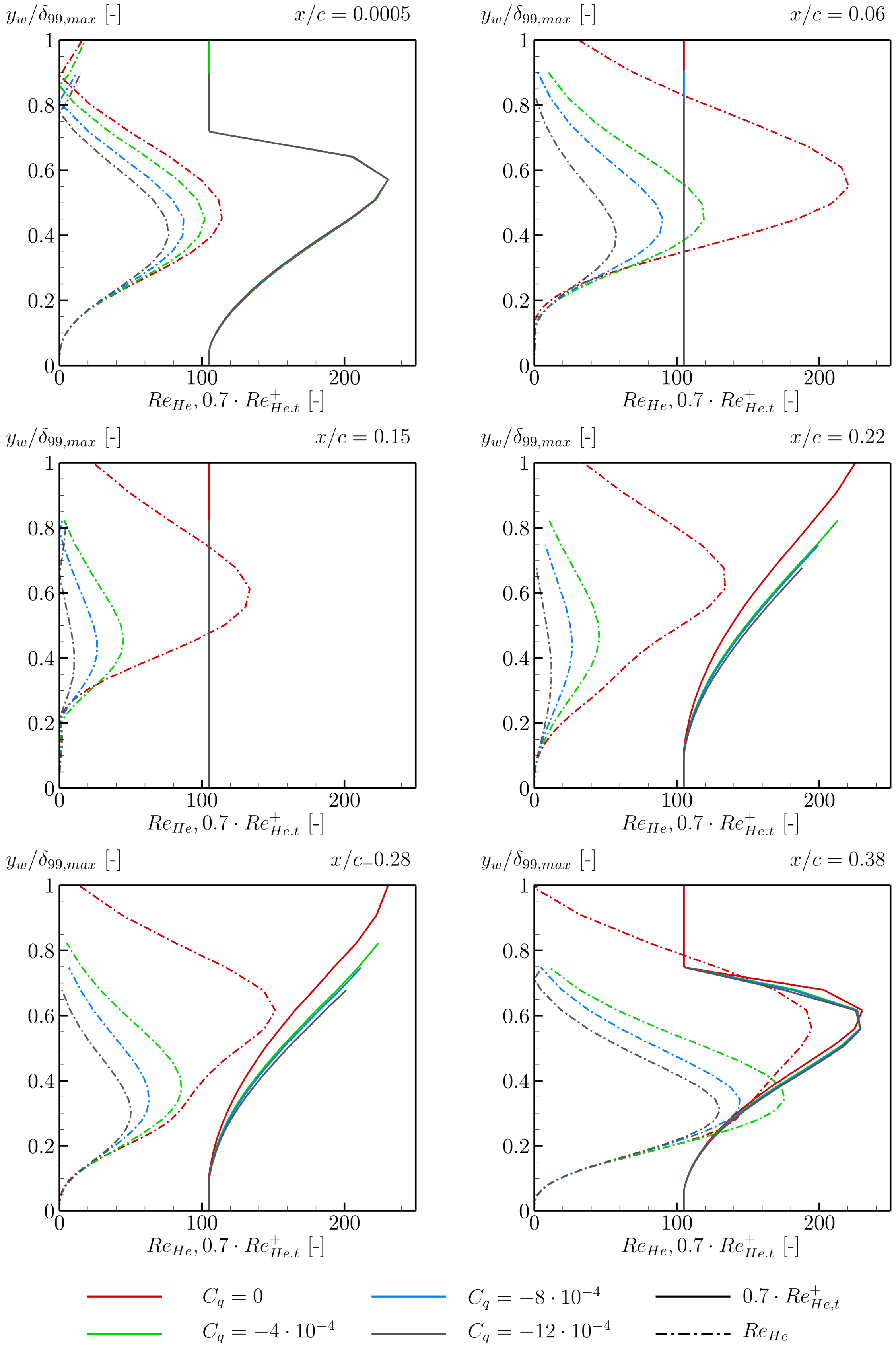


Figure 3.17: Development of helicity Reynolds number $Re_{He}$ and associated transition criterion $0.7 \cdot Re^+_{He,t}$ throughout the laminar boundary layer with increasing suction strength, extracted from laminar reference computations at $\eta = 0.59$ and $C_L = 0.5$. Adapted from [55].

$C = 0.7$ incorporated in the $\gamma - Re_\theta$+CF model. As for the streamwise transition mechanisms, the suction boundary condition leads to the desired (in terms of LFC) effects in the development of $Re_{He}$ throughout the boundary layer. These consist of a reduction in the $Re_{He}$ maxima, while the corresponding wall-normal distance of the maxima follows the reduction in boundary layer thickness imposed through the application of suction. In contrast to the development of $Re_{\theta c}$, however, the transition criterion formulated based on $Re^+_{He,t}$ is less sensitive to boundary layer suction. This is to be expected, as $Re^+_{He,t}$ is primarily based upon grid point local velocity and pressure values, calibrated by a curve fit of experimental data for known transition onset positions [39]. Therefore, the transition criterion expressed in $Re^+_{He,t}$ can only account for suction based on the effect the latter has on the velocity and pressure field. Nevertheless, a pronounced downstream shift of the transition onset point predicted by $F_{onset,1,CF} = Re_{He}/(0.7Re^+_{He,t}) > 1$ is observable through the application of the suction boundary condition, moving from $x'_{tr}/c = 0.006$ for $C_q = 0$ to $x'_{tr}/c \approx 0.38$ for $C_q = -12 \cdot 10^{-4}$.
The assessments presented above underline the applicability of the suction boundary condition in the framework of a LCTM-based computational approach. Nevertheless, difficulties remain in the above-mentioned behavior of the specific model applied here, where it has been shown that the correlations embedded in the model predict the onset of transition $x'_{tr}/c$ downstream of the actual transition position $x_{tr}/c$ resulting in the numerical simulation. Alongside this, the correlations embedded in the baseline $\gamma - Re_\theta$ model for streamwise transition show deficiencies for high Reynolds number, compressible flows, predicting the onset of transition in positions lying to far upstream. Remedies are being proposed in the latest research activities devoted to the matter, e.g. by Menter et al. [76] and Ströer [126] for streamwise transition modes or extended on the basis of Fehrs [31] by François et al. [36] to include cross-flow effects as presented in the thesis at hand. Coupling the approaches with the framework for modeling an active suction system boundary condition therefore presents a promising approach for the automatic numerical assessment of such aerodynamic technology couplings as envisaged within this thesis.

## 3.4 Synthesis

In the present chapter, the HLFC/VC technology coupling as well as isolated integration effects of VC and HLFC were analyzed when applied to the wing of the transonic reference aircraft CATeW-02. The analyses made use of the automated modeling toolchain presented in Chap. 2, using both transition prediction approaches presented in the respective chapter. The latter also constitutes the main differentiation aspect for the herein-presented analyses. The LST approach coupled with the two-$N$-factor transition prediction method reflects synergy-driven aspects of the technology coupling in an associated drag count reduction. These synergy effects are split into primary synergy effects, which are the encompassed reduction in TS-wave amplification rates through load adaptation via VC suppressing otherwise critical amplification, and secondary effects, which are connected to the possibility of controlling the shock wave position by means of VC, thus prolonging the extent of favorable pressure gradient flow and shifting the transition position downstream. A secondary effect when it comes to overall drag reduction, consists of the thinner laminar boundary layer also providing a reduction in pressure drag. This is caused by the reduction of the effect of viscous decambering.

Analyses with the framework built around the effusion mass flux boundary condition and the LCTM-based transition prediction approach also reflected synergistic trends, however, the achievable drag count reduction is predicted to be lower than for the LST-based analyses. This is connected to the main driver for drag count reduction predicted by the LCTM-based framework consists of VC and secondary synergy effects, i.e. the thinning of the boundary layer being reflected by incorporating boundary layer suction to the computations. Transition positions are successively shifted downstream with increasing suction strength, nevertheless are predicted to lie further upstream when compared to the LST-based computations for which the NLF part of HLFC is not reflected in this case.

Therefore, the chapter concluded with an analysis of driving correlations used in the transition prediction framework implemented in the $\gamma - Re_\theta$+CF model, which based on a set of laminar reference computations, assessed possibilities and limitations of incorporating the suction boundary condition to an LCTM-based framework. The analyses in this context are exploratory and belong to the area of turbulence modeling research, rather than the scope of aerodynamics intended within this thesis.

# 4 Application on Wing-Body Level

In the previous chapter, the technology coupling has been assessed on wing level, using different transition prediction frameworks. Within the present chapter, the corresponding analyses are expanded to a higher integration level, i.e., (next to the wing) the fuselage and horizontal tailplane of the CATeW-02 configuration is included in the analyses. The analyses are based upon linear stability and the two-$N$-factor transition prediction method. At the same time, the off-design parameter space is expanded by including off-design Mach numbers $Ma$ and a change in cruise altitude $H$, resulting in a corresponding Reynolds number variation at the previously envisaged lift coefficient of $C_L = 0.5$.

The reference geometry, consisting of wing, fuselage and HTP is termed CATeW-02-WB in the following, an overview of which is presented in Sec. 4.1. Within the same section, geometry adaptations concerning the wing-body junction are discussed, followed by a presentation of the general grid topology and an evaluation of spatial grid resolution in terms of a grid independence study.

For a consistent aerodynamic assessment, it is necessary to simulate the aircraft in a trimmed flight state, for which Sec. 4.2.1 is dedicated to the framework used for the inclusion of aircraft trim in the numerical simulations. Based upon the trimmed state, an overview of the general flow field in terms of surface pressure distributions is presented in Sec. 4.2.2, while Sec. 4.2.3 is dedicated to effects of VC integration to CATeW-02-WB. Results of the coupled system application to CATeW-02-WB are presented in Sec. 4.3, as previously mentioned based on the LST framework for transition prediction. Additionally to variations in lift coefficient $C_L$ and ADHF deflection angle, the system is analyzed for variations in Mach and Reynolds number in Secs. 4.3.2 and 4.3.3, respectively.

## 4.1 Reference Geometry and Computational Grids

The present chapter deals with the reference configuration CATeW-02-WB. In addition to the wing analyzed in Chap. 3, CATeW-02-WB includes the fuselage and the horizontal tailplane (HTP) of the reference configuration CATeW-02. As for the wing, the additional aircraft components included in CATeW-02-WB have been derived at the Institute of Aerospace Systems of RWTH Aachen University in the course of the likewise named research project CATeW, c.f. Secs 1.3 and 3.1.

A three-view drawing of CATeW-02-WB, alongside an isometric projection of the (mirrored) full-span geometry is presented in Fig. 4.1. As previously indicated, the wing of CATeW-02-WB corresponds to the geometry treated within Chap.3, for which geometrical parameters considering planform, airfoils and twist/thickness distributions can be extracted from Sec. 3.1. The same applies to the dimensions and position of the HLFC suction panel and the ADHF, respectively marked in red and blue in the top panel of Fig. 4.1.

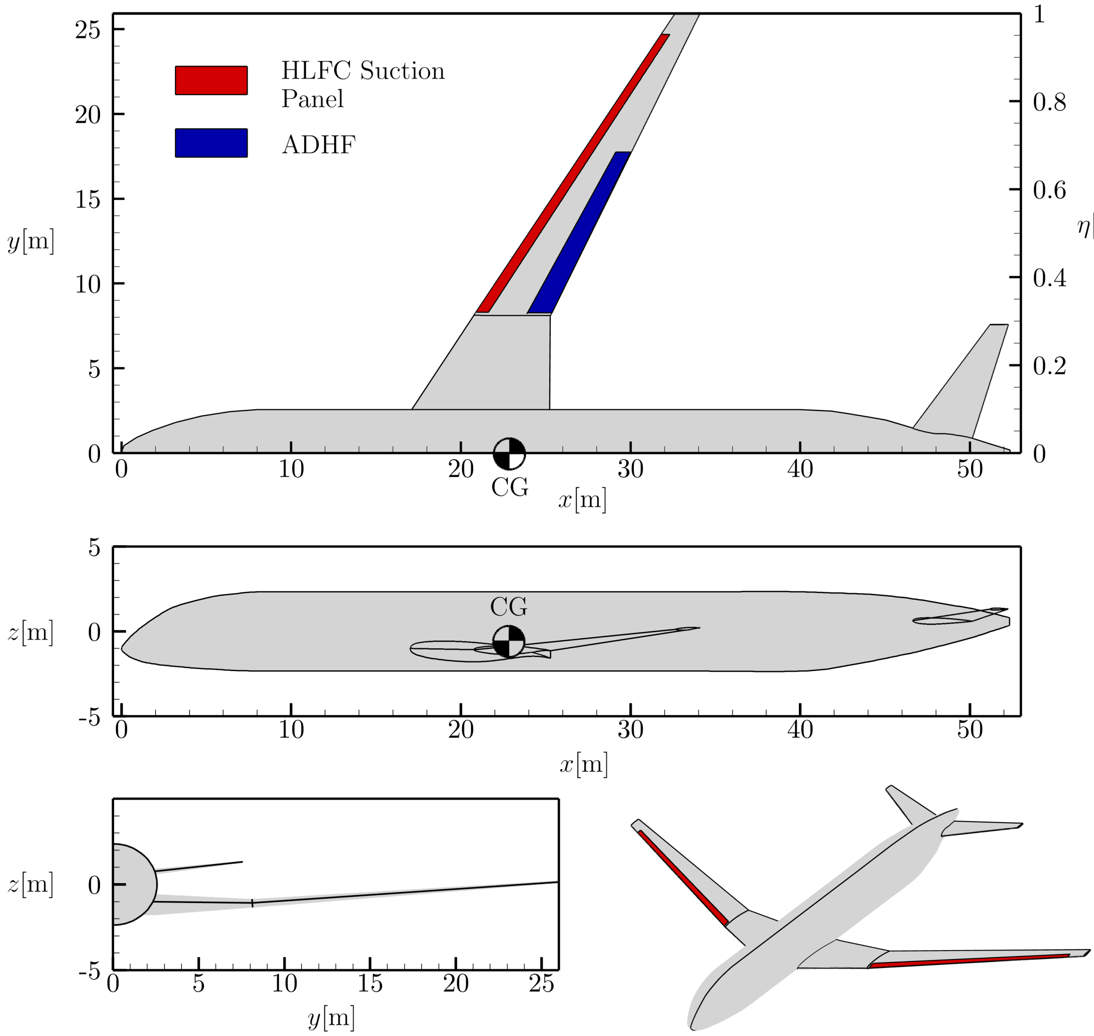


Figure 4.1: Three-view drawing of the reference configuration CATeW-02-WB, alongside isometric view mirrored at the $y$ symmetry plane.

The fuselage of CATeW-02-WB possesses a total length of 52.3 m, and consists of an elliptical cross-section with maximal major and minor axis lengths of 5.2 m ($y$-direction) and 4.71 m ($z$-direction). The nose cone of the fuselage is drooped downwards, as encountered in modern aircraft such as those of the Airbus A350 or Boeing 787. The aircraft center of gravity (CG), used as moment reference point for subsequent analyses, is fixed at $\boldsymbol{x}_{CG} = [22.85, 0, -0.58]$ m, with reference to the coordinate system depicted in Fig. 4.1. It should be noted, however, that the CG possesses a range of possible positions of approx. $\Delta\boldsymbol{x}_{CG} = [-0.2/+0.05, 0, -0.2/+0.02]$ m, limiting the CG position for trimming different mass configurations.

The HTP possesses a half-span of 7.6 m, with no twist and a constant dihedral of 6°. The HTP leading edge sweep angle measures $\varphi_{LE,HTP} = 36.75°$. As the HTP consists of only one section, a symmetrical NACA 0009 airfoil is adopted along the entire HTP span.

**Adaptation of Wing-Body Junction.** The geometry presented above is derived from an OAD geometry definition file, for which the different aircraft components are combined without special treatment of their respective interfaces. While this presents no difficulties concerning the application of an OAD toolchain, running three-dimensional RANS simulations requires local geometry adaptation. This requirement is primarily connected to the LST-based transition prediction framework being implemented for steady-state simulations only, i.e., it is not applicable when the RANS simulation does not converge to a steady-state solution due to the development of transient flow phenomena.

A typical zone faced with this challenge when being left untreated is the trailing edge region of the wing-body junction. As depicted in Fig. 4.2 a) and d), small included-angles between the surfaces of the wing upper side and fuselage lead to a pronounced side-of-body (SOB) separation, and thus stalling convergence of the RANS simulation. This phenomenon is described in detail in a large number of publications, one of the most prominent examples stemming from numerical analyses of NASA's Common Research Model in the course of the AIAA Drag Predicition Workshop series, see [120].

To prepare CATeW-02-WB for subsequent grid generation, the wing-body junction has been adapted following the procedure outlined by Vassberg et al. [132]. In a first step, a wing belly fairing has been added to the fuselage of the geometry, while the intersection line of the wing and the fuselage is rounded off to form a fillet, see Fig. 4.2 b). The addition of the wing belly fairing increases the included-angle between fuselage and wing surfaces to 90°, leading to a pronounced reduction in SOB separation, depicted in Fig. 4.2 e) in terms of the skin friction coefficient $c_f$ distribution and associated skin friction lines.

To entirely suppress the formation of the SOB separation bubble, a bump has been added to the intersection region of the wing trailing edge and the wing belly fairing in a second step, see Fig. 4.2 c). The bump is constructed to be tangential to the surface of the belly fairing, while the normal vector of its peak is aligned with the wing trailing edge. The addition of the bump to CATeW-02-WB entirely suppresses SOB separation, i.e., as depicted in Fig. 4.2 f), the flow remains attached in the respective region. The updated geometry furthermore improves the mesh quality due to the continuous surface transition achieved by the incorporation of the fillet, leading to the desired convergence behavior of the RANS simulation to a steady state flow solution.

**Grid Generation and Independence Study.** As for the analyses on wing level presented in Chap. 3, grid generation was performed in a hybrid manner utilizing the commercial mesh generator CENTAUR by CentaurSoft [16], utilizing the adapted CATeW-02-WB geometry. The set of requirements for the computational grid has been correspondingly adapted from the grids generated for the CATeW-02 wing, especially considering the spatial resolution as well as the prism layer structure on the surface of the wing (cf. Sec. 3.1). The same is true for the extent and the boundary conditions

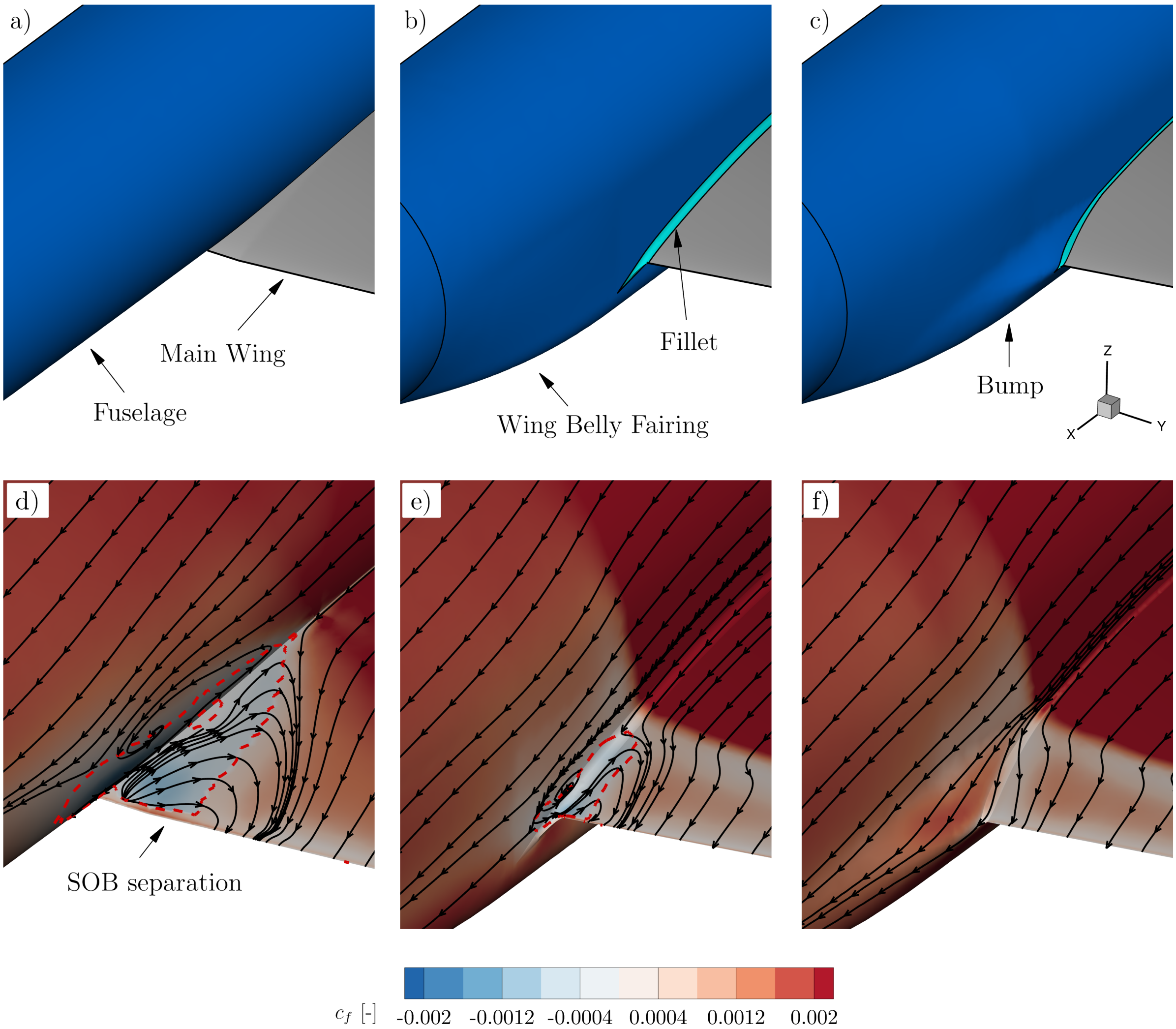


Figure 4.2: Top panels: Overview of geometry adaptation at wing-fuselage junction for CATeW-02. Bottom panels: Skin friction lines and contour of skin friction coefficient at wing-body junction, with indication of side-of-body separation bubble.

limiting the computational domain, forming a hemispherical domain with a radius of $100 \cdot c_{ref} = 529$ m. Different refinement zones encompassing the overall aircraft near-field, wing upper and lower surface near-field as well as the wake of the wing, HTP and fuselage are included in the surface and volume grids. An overview of the general grid topology is presented in Fig. 4.3.

Grid independence of the numerical results is assessed based on drag $C_D$ and pitching moment coefficients $C_m$. The grid study encompasses four grids $\mathcal{L}_1 - \mathcal{L}_4$ with increasing resolution levels, while the resulting drag and pitching moment coefficients are computed for the later analyzed set of lift coefficients $C_L = [0.45; 0.50; 0.55]$. The corresponding results are depicted in Fig 4.4, alongside an indication of computational expense connected to the different grid levels in terms of CPU wall-clock time $t_{CPU}$ per timestep.

Refining the grid from $\mathcal{L}_1$ to $\mathcal{L}_4$ results in a reduction of integral force and moment coefficients. Convergence in $C_D$ starts to be observable at $\mathcal{L}_3$, while $C_m$ is still subject

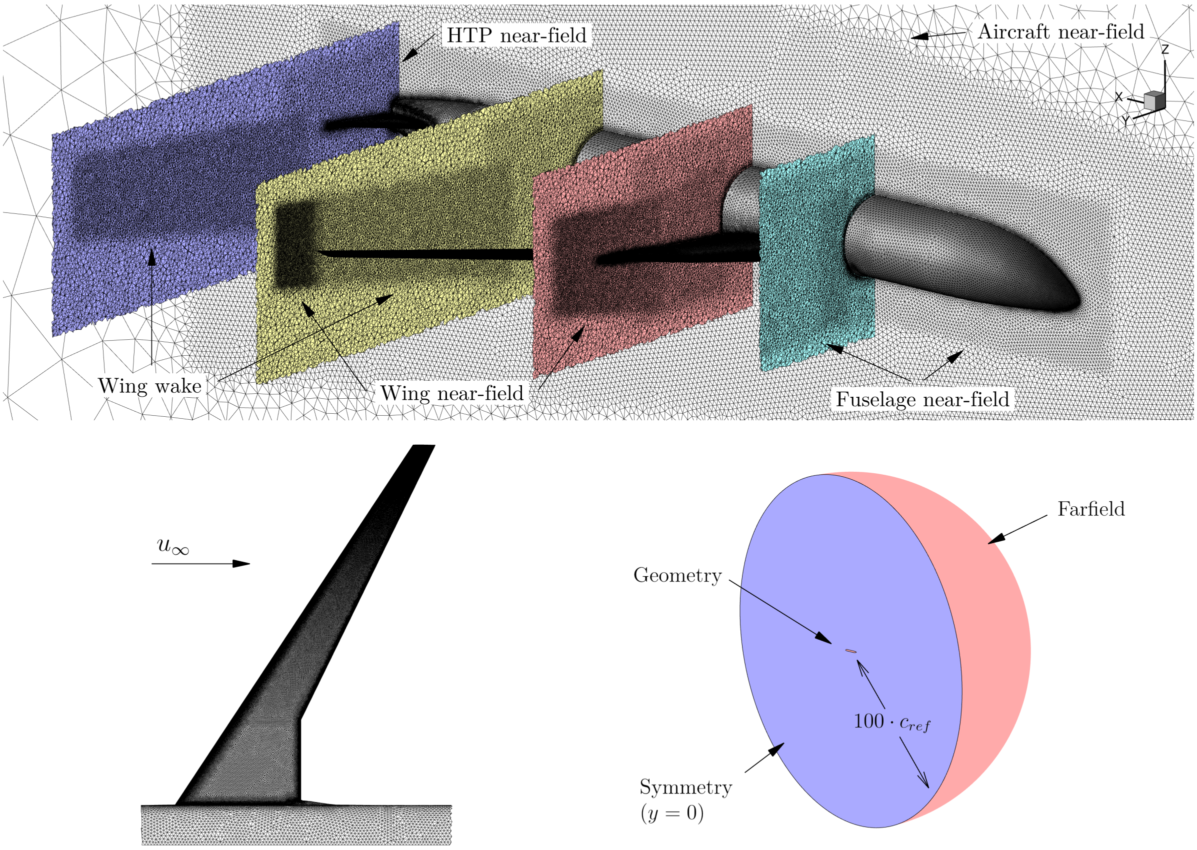


Figure 4.3: Overview of CATeW-02-WB numerical grid. Top panel: Surface mesh alongside four slices through the volume grid, alongside indication of volume mesh refinement regions. Bottom left panel: Wing surface grid on upper surface. Bottom right panel: Computational domain and associated boundary conditions.

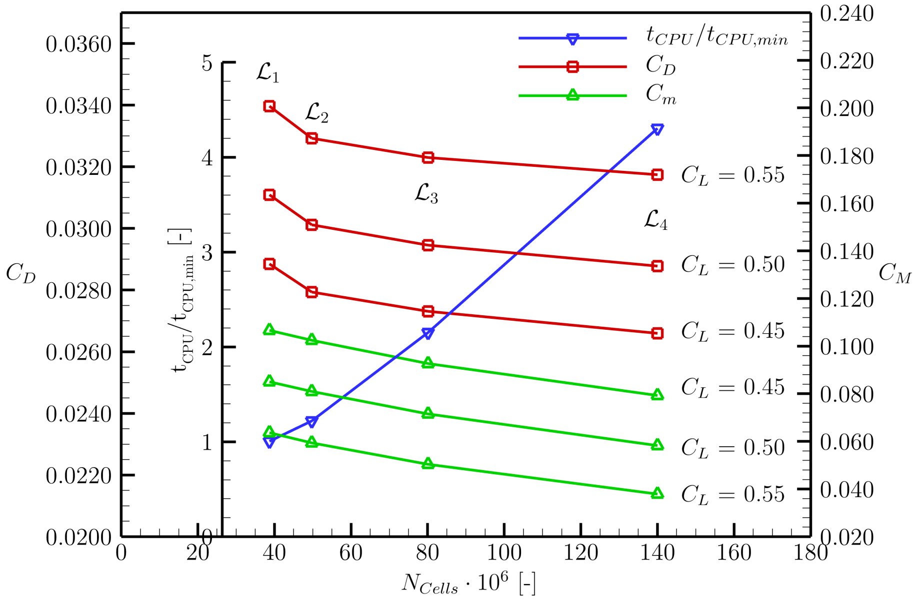


Figure 4.4: Integral force and moment coefficients resulting for grid levels $\mathcal{L}_1$ - $\mathcal{L}_4$, at the lift coefficients $C_L = [0.45; 0.50; 0.55]$. Additionally, the normalized computational time per timestep is indicated.

to variations for all observed grid refinement levels. For the present study, however, the latter can be considered looser when it comes to grid convergence, as the pitching moment coefficient is highly sensitive to the flow solution at the HTP of CATeW-02-WB. Therefore, minor differences in pressure and shear force distributions at the HTP are amplified in terms of $C_m$.
Considering the computational expense, changing from grid $\mathcal{L}_3$ to $\mathcal{L}_4$ approx. doubles the necessary computational time per CPU core. The expense is further aggravated when considering grid level $\mathcal{L}_4$ requiring a larger number of time steps to converge to a steady state solution, not directly reflected in $t_{CPU}$. Therefore, all further numerical analyses are based on grid $\mathcal{L}_3$.

## 4.2 Aerodynamic Characterization

### 4.2.1 Inclusion of Aircraft Trim

To allow for a consistent evaluation and comparison of different load cases or operating points in the following analyses, a central prerequisite consists of simulating the aircraft in a trimmed flight state. The latter is especially relevant when considering VC integration, as a deflection of the ADHF leads to substantial variations in pitching moment about the aircraft center of gravity $x_{CG}$. The additional pitching moments need to be trimmed during cruise flight, the trim effects ultimately affecting the wing pressure distribution for the different operating points due to aerodynamic loads shifted to the HTP itself, alongside the resulting change in necessary angle of attack $\alpha$.
Transonic transport aircraft are usually equipped with a trimmable horizontal stabilizer, i.e. the incidence angle of the HTP is changed to generate the required pitching moments for trimmed flight. To incorporate HTP rotations into the numerical simulation, the above-introduced deformation module of the automated simulation framework (cf. Fig. 2.10) implemented within the course of the thesis is used. The module builds around the RBF mesh deformation tool implemented in TAU. Therefore, deflection fields of the HTP considering rigid body rotation are computed within the toolchain, which are subsequently redirected to the mesh deformation tool. Special consideration has to be directed towards the fuselage surface in the empennage region, as the deformation applied to the surface grid of the HTP propagates to the fuselage in the respective zone. When left untreated, this leads to a deformation of the fuselage surface alongside the HTP, or, when setting the allowable deformation of the fuselage surface mesh to zero, a mesh deterioration prohibiting numerical simulation due to negative volume cells in the mesh confining the fuselage HTP junction. Therefore, CATeW-02-WB is further adapted to incorporate a planar fuselage-HTP junction, allowing for in-plane movement of the fuselage surface grid points in the respective region and ultimately blending to zero deformation at the boundaries of the junction, see Fig. 4.5 a). An overview of the resulting surface grid point translation in the trailing edge region of the HTP is depicted

in Fig. 4.5 b), while 4.5 c) is dedicated to the magnitude of the resulting deformation field $|\boldsymbol{x}_D|$ for $i_H = -2°$. The rotation axis for the HTP is chosen normal to the planar fuselage-HTP junction, whilst intersecting the plane at the HTP front spar position.

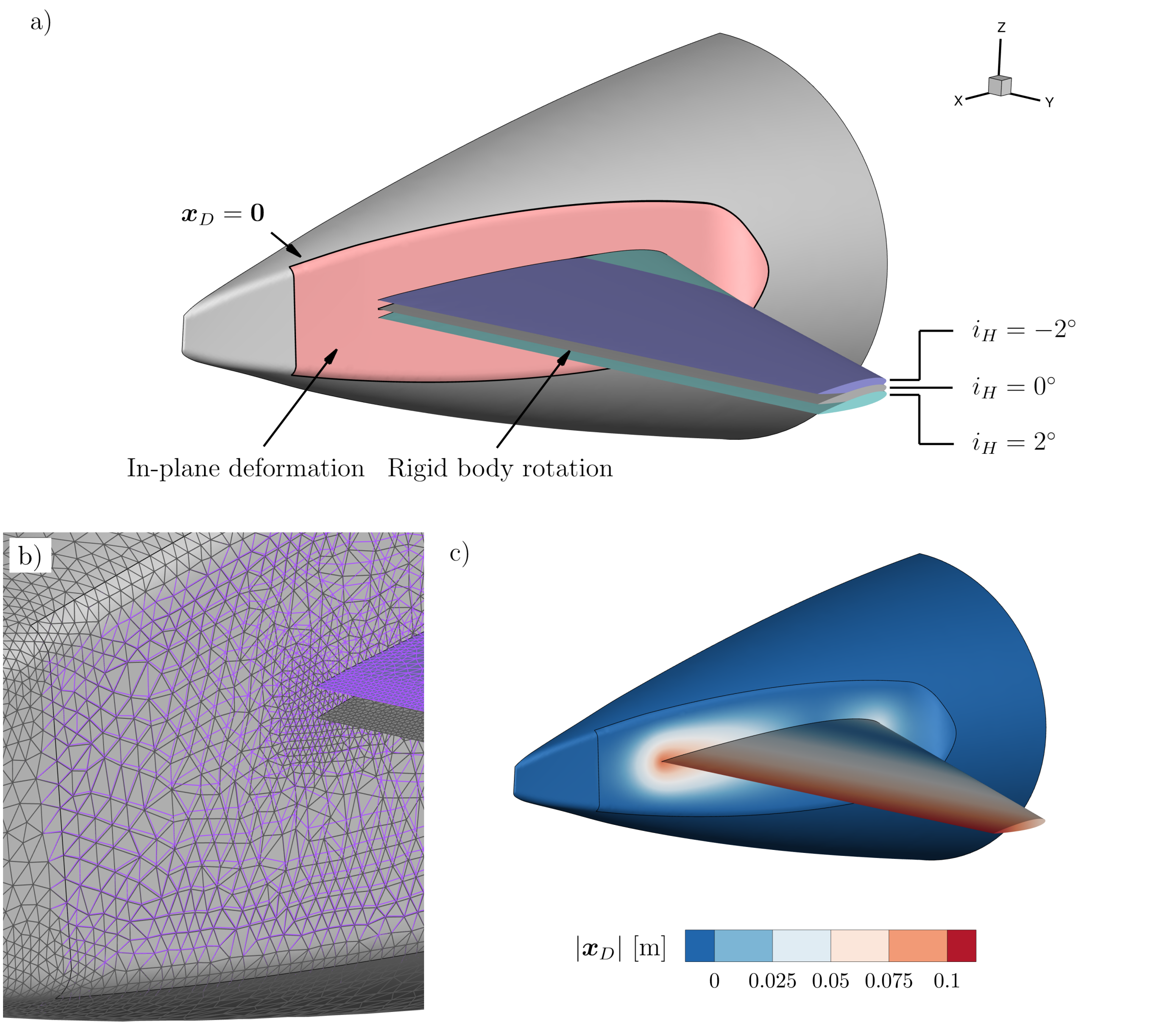


Figure 4.5: Panel a): Overview of different HTP incidence angle $i_H$ settings, realized via mesh deformations utilizing the Deformation module of the Python toolchain. Panel b): Close-up view of base and deformed grids for $i_H = -2°$. Panel c): Magnitude of deformation vector for $i_H = -2°$.

To determine the necessary incidence angle $i_H$ for a trimmed flight state, i.e. $C_L = C_{L,cruise}$ and $C_M = 0$, the linearized trim problem is solved [78]:

$$\begin{bmatrix} C_L \\ C_M \end{bmatrix} - \begin{bmatrix} C_{L,ref} \\ C_{M,ref} \end{bmatrix} = \overbrace{\begin{bmatrix} \frac{\partial C_L}{\partial \alpha} & \frac{\partial C_L}{\partial i_H} \\ \frac{\partial C_M}{\partial \alpha} & \frac{\partial C_M}{\partial i_H} \end{bmatrix}}^{J} \begin{bmatrix} \Delta\alpha \\ \Delta i_H \end{bmatrix} \tag{4.1}$$

The entries on the left-hand side of Eq. 4.1 are, as already mentioned, set by the envisaged, trimmed flight condition. The missing link is reflected by the entries of the Jacobian matrix $J$ on the right-hand side of Eq. 4.1, namely the values of the derivatives with respect to $\alpha$ and $i_H$, which again depend on the operating point of the aircraft.

To determine the entries of $J$ two approaches are applicable. First, approaches based upon finite differences or solutions of the adjoint embedded in an iterative optimization problem can be applied during the runtime of a simulation, see e.g. [78] or [103].
These methods, however, require several trim iterations accompanied by mesh deformation in each coupling step to determine the values of the trim variables. This is of limited concern for the above-mentioned references, as they also include elastic effects, requiring mesh deformations in any case. Nevertheless, for the comprehensive operating points encompassed within the present thesis, including several mesh deformation iterations to each numerical simulation leads to prohibitive computational costs.
Therefore, the second commonly adopted approach builds upon the generation of a look-up table for the derivative values and subsequent interpolation for the envisaged operating point during runtime of the simulation, see e.g. [96]. Before the bulk data set generation, a set of simulations with varying input parameters $\boldsymbol{p} = [C_L, \delta_{ADHF}, i_H, Ma, Re]$ are run, which results in the corresponding sensitivities of the pitching moment coefficient with respect to the parameters $\boldsymbol{p}$, see left panel of Fig. 4.6. Recalling the linear formulation underlying Eq. 4.1, the necessary perturbation $\Delta\alpha$ is solved for during runtime by the above-mentioned target $C_L$ algorithm implemented in TAU, whilst $\Delta i_H$ is linearly interpolated from the given sensitivities within the bulk data set. The resulting incidence angles $i_H$ are exemplarily depicted in the mid panel of Fig. 4.6, considering varying ADHF deflection angles and lift coefficients. The right panel of Fig. 4.6 shows the resulting pitching moment coefficients about the center of gravity using the interpolated incidence angles $i_{H,trim}$, resulting in a trim or close trim condition when applying the implemented framework.

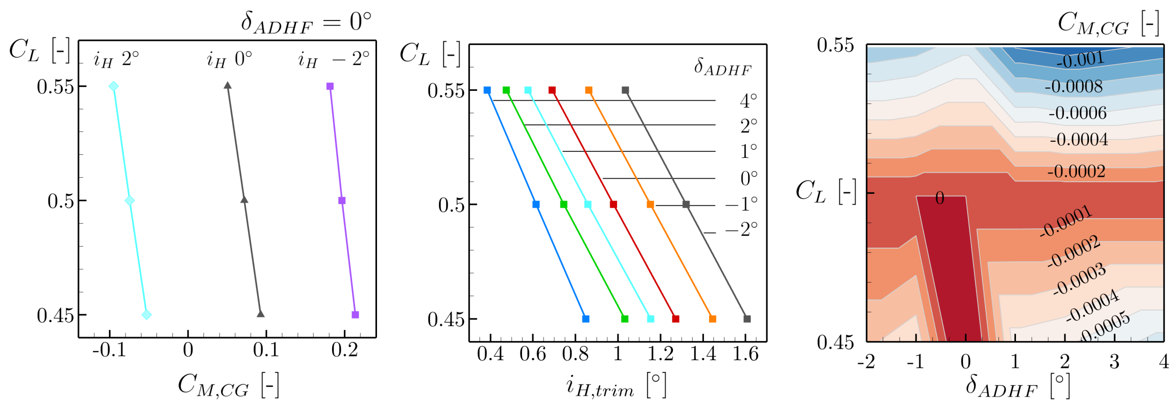


Figure 4.6: Left panel: Pitching moment coefficient $C_{M,CG}$ about the aircraft CG for varying lift coefficients $C_L$ and incidence angles $i_H$ at $\delta_{ADHF} = 0°$. Mid panel: Interpolated incidence angles $i_{H,trim}$ for trimmed flight state for varying ADHF deflection angles. Right panel: Resulting pitching moment coefficient $C_{M,CG}$ for varying lift coefficients $C_L$ and ADHF deflection angles $\delta_{ADHF}$ using $i_H = i_{H,trim}$. All panels refer to $Ma = 0.83$, $H = 35\ 000$ ft ($Re \approx 34.5 \cdot 10^6$).

### 4.2.2 General Flow Field

A general characterization of the flow field considering the surface pressure coefficient $c_p$ distribution on the lower (pressure) and upper (suction) side of CATeW-02-WB is presented in Fig. 4.7. As indicated earlier the analyses from hereon include the adapted wing-body junction and are all performed for a trimmed flight state.
Figure 4.7 shows the pressure distribution at the design point of CATeW-02-WB ($C_L = 0.50$, $Ma = 0.83$) in its clean configuration ($\delta_{ADHF} = 0°$), while $c_p$ slices are extracted for inclusion of the later treated (cf. Sec. 4.3, Fig. 4.9) off-design lift coefficients $C_L = [0.45; 0.55]$ and Mach numbers $Ma = 0.81$ and $Ma = 0.78$ at $H = 35\ 000$ ft. Similar to the isolated wing case, the flow on the suction side of the wing is characterized by a pronounced shock front in rearward chordwise positions, consequently leading to a marked region of favorable pressure gradient flow up to the shock position. In outboard direction, the shock front is shifted upstream with respect to its chordwise position while the shock decreases in strength, i.e. the associated recompression jump reduces in magnitude until shock-free recompression is obtained for $\eta \gtrapprox 0.95$.
Varying the lift coefficient $C_L$ shows its largest effects considering the outboard stations of the wing. This is connected to a larger reduction in shock strength for lower lift coefficients, for which the spanwise limit of shock-free recompression is moved inboard towards $\eta \gtrapprox 0.8$. While $C_L = 0.5$ is already marked by the development of an adverse pressure gradient flow in the respective spanwise positions, the pressure distribution resulting for $C_L = 0.45$ shows a further increase in the magnitude of adverse pressure gradient.
The opposite behavior is connected to an increase in lift coefficient to $C_L = 0.55$, where the shock extends further outboard in comparison to $C_L = 0.5$. Considering the section $\eta = 0.8$ depicted in Fig. 4.7, the comparison between $C_L = 0.5$ and $C_L = 0.55$ attributes a more downstream shock position to $C_L = 0.55$, resulting in a higher isobar sweep in the corresponding spanwise region. Therefore, the adverse pressure gradient in the leading edge region of the wing is reduced or vanishes, while downstream of $x/c = 0.28$, a favorable pressure gradient develops.
Inboard of $\eta \approx 0.8$, shock position and shock strength lose sensitivity to $C_L$ variations in the inboard direction. For the $c_p$ distributions included in Fig. 4.7, the shock topology coincides for $\eta = 0.2$ and $\eta = 0.4$, while $\eta = 0.6$ is still marked by the effects discussed above. More dominant effects are observable in the leading edge region of the wing, as with increasing $C_L$ a more pronounced suction peak develops in the respective region. The resulting pressure gradients in the mid-chord region are, however, less impacted by the increase in suction peak, as the load-bearing region, i.e. negative $c_p$ regions on the suction side of the wing, is shifted to the mid-chord region of the wing.
The off-design Mach numbers $Ma = 0.81$ and $Ma = 0.78$, in comparison to the design Mach number $Ma = 0.83$ at $C_L = 0.5$, are treated in the bottom panels of Fig. 4.7. Lowering the Mach number is generally characterized by an upstream shift of the shock

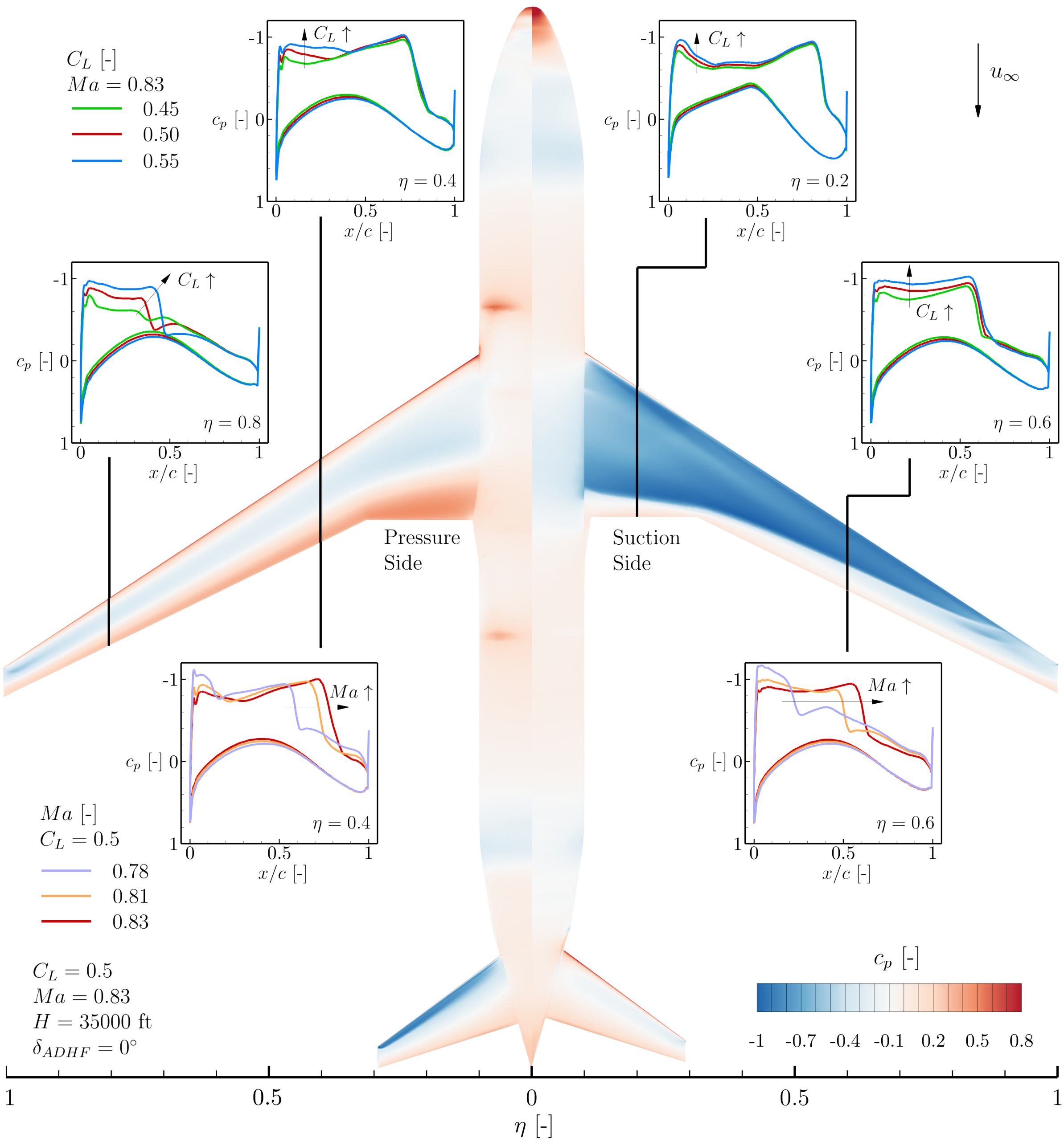


Figure 4.7: Contour plot of surface $c_p$ on the pressure (left) and suction side (right) of CATeW-02-WB at the design point. The $c_p$ slices on the top show corresponding extractions for varying lift coefficients $C_L$ at $Ma = 0.83$, while the bottom panels are dedicated to $c_p$ slices for varying $Ma$ at $C_L = 0.5$.

position, featuring a more pronounced suction peak in comparison to $Ma = 0.83$. The shock strength is reduced with decreasing Mach number, for which in connection with the higher suction peak the extent of negative pressure gradient flow is reduced, or not achieved at all considering the depicted section cut at $\eta = 0.6$.
The general characteristics of the pressure distribution partially satisfy the requirements formulated in Sec. 3.2.2 for the application of HLFC. Nevertheless, especially off-design pressure distributions are characterized by a large potential for actively shaping the pressure distribution based on VC integration.

### 4.2.3 Implications of Variable Camber Integration

Within Sec. 3.2.2, implications of VC integration are described on isolated wing level. The corresponding effects are transferable to CATeW-02-WB, for which the reader may refer to the respective section for an overview of the development of $c_p$ distributions as well as spanwise loads with increasing ADHF deflection angle.
Within this section, the focus lies on the shift in increments of component-wise integral loads:

$$\Delta C_L = C_L(\delta_{ADHF} = 0°) - C_L(\delta_{ADHF,var}) \tag{4.2}$$

$$\Delta C_D = C_D(\delta_{ADHF} = 0°) - C_D(\delta_{ADHF,var}) \tag{4.3}$$

incurred by VC integration, an overview of which is depicted in Fig. 4.8. As stated above, the analysis is based on CATeW-02-WB cruising in a trimmed flight state, and encompasses the design point $C_L = 0.5$ and $Ma = 0.83$, alongside the off-design lift coefficients $C_L = [0.45, 0.55]$ and Mach numbers $Ma = [0.78, 0.81]$ (cf. left panel of Fig. 4.9), all at $H = 35\,000$ ft.
In general, the load shift accompanied by deflection of the ADHF acts in transferring lift and drag production between the different components of the aircraft. Deflecting the flap to negative deflection angles, i.e. decambering the wing, correspondingly reduces the lift production associated with the wing, while the corresponding forces are approximately equally shifted to the fuselage and HTP for the herein-considered cases. Vice versa, when increasing wing camber by setting the ADHF to positive deflection angles $\delta_{ADHF}$, leads to the lift production associated with the wing increasing while the share of the fuselage and HTP decrease.
Considering sensitivities with respect to $C_L$ variations (top panels of Fig. 4.8), the most pronounced load shift is associated with the lowest lift coefficient $C_L = 0.45$, while incrementally increasing $C_L$ reduces the sensitivity of the aircraft towards $\delta_{ADHF}$ variations. Mach number variations at constant $C_L = 0.5$ (bottom panels of Fig. 4.8), also show a corresponding trend between $Ma = 0.83$ and $Ma = 0.78$, however, the case $Ma = 0.81$ possesses the highest sensitivities with respect to $\Delta C_L$ for positive ADHF deflection

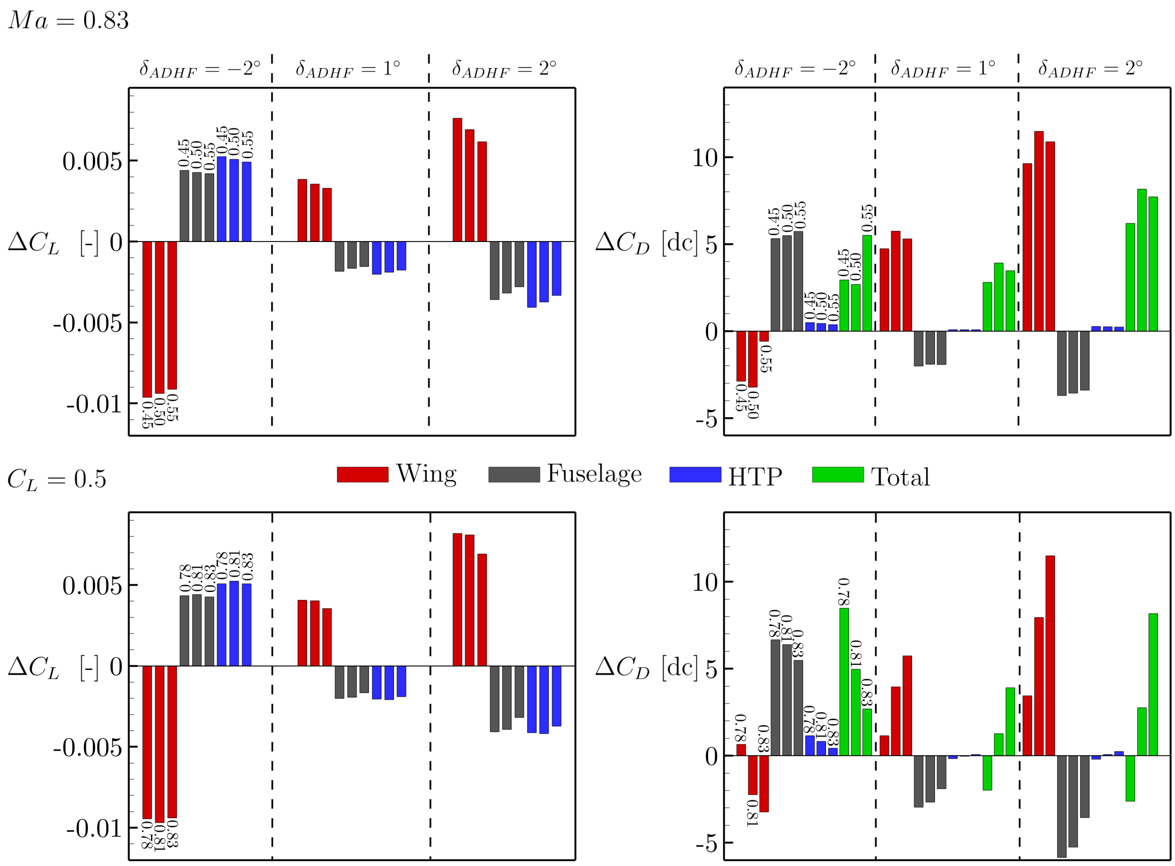


Figure 4.8: Bar chart of component-wise increments in lift $\Delta C_L$ (left panels) and drag $\Delta C_D$ (right panels) coefficients for different ADHF deflection angles. The top panels additionally consider variations in overall lift coefficient $C_L = [0.45, 0.50, 0.55]$, while the bottom panels are devoted to variations in cruise Mach number $Ma = [0.78, 0.81, 0.83]$. All computations performed for $H = 35\ 000$ ft.

angles $\delta_{ADHF}$. The latter is associated with the inclusion of trim, as the load shift connected to VC integration at $Ma = 0.81$ requires the highest loading of the HTP.

The increment in drag coefficients $\Delta C_D$ at $Ma = 0.83$ and varying $C_L$ (Fig. 4.8, top right), follows the general trends reflected in $\Delta C_L$. Decambering the wing ($\delta_{ADHF} < 0$) leads to a reduction in drag associated with the wing, whilst drag production associated with the fuselage is elevated. The latter surpasses the reduction connected to the wing, increasing total drag for all included lift coefficients $C_L$ in comparison to the baseline case $\delta_{ADHF} = 0°$. For positive ADHF deflection angles, the additional drag produced by the wing is higher than the drag reduction observable at the fuselage, correspondingly resulting in an increase in the total drag coefficient for all lift coefficients $C_L$. Whilst the above-described effects are correspondingly reflected for a Mach number variation to $Ma = 0.81$ (Fig. 4.8, bottom right panel) at $C_L = 0.5$, the lowest off-design Mach number $Ma = 0.78$ reflects a shift in optimum flap deflection angle to $\delta_{ADHF} = 2°$, leading to a total drag count reduction of 2.6 dc. Further ADHF deflection is not considered in Fig. 4.8, nevertheless leads to increasing $C_D$ again (cf. Fig. 4.13 for $\delta_{ADHF} > 2°$ at

$Ma = 0.78$).
In contrast to VC integration to the isolated wing, the analysis of the trimmed wing-body configuration attributes the lowest drag coefficient to $\delta_{ADHF} = 0°$ for the largest part of the envelope. Considering the primary design point, this behavior is desirable, as it confirms the aerodynamic design of CATeW-02-WB presenting an applicable baseline for assessment of the technology coupling. In other words, if deflecting the ADHF would lead to a drag reduction for CATeW-02-WB in its design point, the general design of CATeW-02-WB should be reconsidered instead of attributing this to a benefit of VC integration.
Furthermore, CATeW-02-WB is insensitive to off-design operation with regard to varying lift coefficients and, to a limited extent, Mach numbers. As indicated above, VC integration to CATeW-02-WB becomes beneficial for Mach numbers encompassing the lower limit of the off-design envelope, namely by reducing total drag when increasing the wing's camber. This behaviour is connected to the reduction in flow velocity associated with a reduction in Mach number at fixed altitude $H$, i.e. it is generally beneficial to increase wing camber when reducing flow speed at fixed $C_L$.
Considering the coupled application of VC with an HLFC system, the preliminary conclusion can be drawn, that the highest synergistic potential will be associated with off-design operation at reduced Mach numbers. As already shown on isolated wing level (cf. Sec. 3.3.1), synergy potential develops when VC is integrated to increase wing camber, i.e. stabilization of the boundary layer was shown to be connected to implications on the chordwise pressure distribution incurred by a downward deflection of the ADHF. In contrast, increasing the Mach number or, at constant Mach number, decreasing $C_L$, typically requires a decrease in wing camber, as shown for instance in [97], therefore limiting the synergy potential for such operating scenarios. Accordingly, next to the design point, the analyses of the coupling in the following are focused on the lower extent of the cruise flight envelope.

## 4.3 Technology Coupling

With the preliminary aspects for a consistent evaluation of the HLFC/VC coupling set in the preceding sections of this chapter, the synergistic potential of the technology coupling is assessed in this section. The assessment includes the operation of CATeW-02-WB at its design point ($C_L = 0.5$, $Ma = 0.83$) at $H = 35\ 000$ ft, considering the isolated effect of VC integration on the development of the transition position, as well as the development of the overall drag coefficient for the off-design lift coefficients $C_L = 0.45$ and 0.55. Following the implications derived from isolated VC-integration, the technology coupling is assessed with respect to off-design variation of the Mach number, i.e. $Ma = [0.78; 0.81]$ are considered at $C_L = 0.5$ and $H = 35\ 000$ ft. Additionally, the isolated influence of a Reynolds number variation is included in the assessment at the design point, by including cruise at $H = 39\ 000$ ft ($Re = 28.8 \cdot 10^6$) next to $Re = 34.5 \cdot 10^6$

at $H = 35\ 000$ ft at $C_L = 0.5$ and $Ma = 0.83$. For an overview of the considered design and off-design envelopes, the reader may refer to the left panel of Fig. 4.9.
The right panel of Fig. 4.9 reflects the line-of-flight cuts used for transition prediction by means of the LST-based framework (cf. Sec. 2.2.2.2) for transition prediction on the wing of CATeW-02-WB. A series of 40 cuts is placed along the wing suction side, with prescription of the corresponding suction coefficients to the line-in-flight cuts located within the spanwise section of the HLFC suction panel (red).

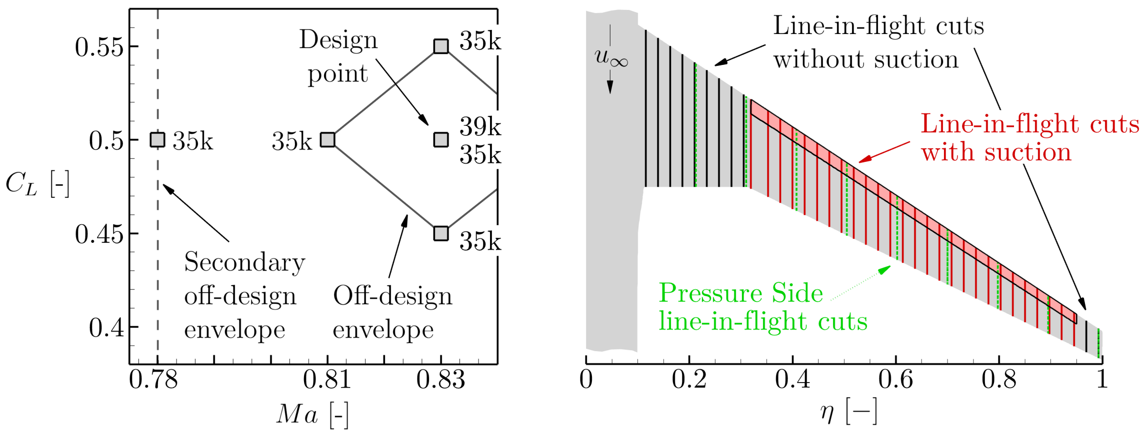


Figure 4.9: Left panel: Design and off-design points assessed for CATeW-02-WB. Right panel: Line-in-flight cuts utilized for application of LST and the two-$N$-factor method for transition prediction along the upper and lower side of the CATeW-02-WB wing.

The green dashed lines in the right panel of Fig. 4.9 show the line-in-flight cuts on the pressure side of the wing, where a series of nine cuts are equidistantly spaced along the wing span. The reduced number is chosen to save computational time, as laminar flow is not foreseen on the pressure side of the wing. Transition on the pressure side is accordingly predicted directly downstream of the leading edge for all cases observed in the following, triggered by amplification of CFI.
Transition prediction is based on the LST framework only for CATeW-02-WB, as the transition behavior predicted by the LCTM is comparable to the one observed for the isolated wing case, see Sec. 3.3.2.1. Thus, synergistic effects become masked by particularities of the transition prediction model, necessitating adaptations of the LCTM framework discussed in Sec. 3.3.2.2 for a corresponding analysis.

### 4.3.1 Sensitivity to Camber Variation

The transition fronts resulting from suction coefficients $C_q = 0$ - $-12 \cdot 10^{-4}$ and varying ADHF deflection angles ($\delta_{ADHF} = -2$ - $4°$), at the design point ($C_L = 0.5$, $Ma = 0.83$), for the initial cruise altitude (ICA) $H = 35\ 000$ ft are depicted in Fig. 4.10. As already discussed for the isolated wing case (cf. Sec. 3.3.1), the zero suction case $C_q = 0$ is characterized by immediate transition downstream of the wing leading edge due to CFI

up to $\eta \approx 0.85$ for all ADHF deflection angles. In the outboard segment $\eta = 0.85 - 1.0$, transition is predicted due to TSI-CFI interaction, nevertheless not resulting in a pronounced downstream shift when compared to the remainder of the wing.
Increasing the suction strength ($C_q \downarrow$) stabilizes the boundary layer towards both TSI and CFI for $\eta \gtrapprox 0.62$ in all observed cases, for which the transition position is driven by the predicted position of laminar separation (LAM SEP). To re-emphasize, laminar separation, in this case, does not refer to the flow separating at this position within the numerical simulation, but the point of laminar separation computed by COCO is used to switch on the turbulence model within the CFD run, for which no actual flow separation occurs downstream of the transition front marked by LAM SEP.

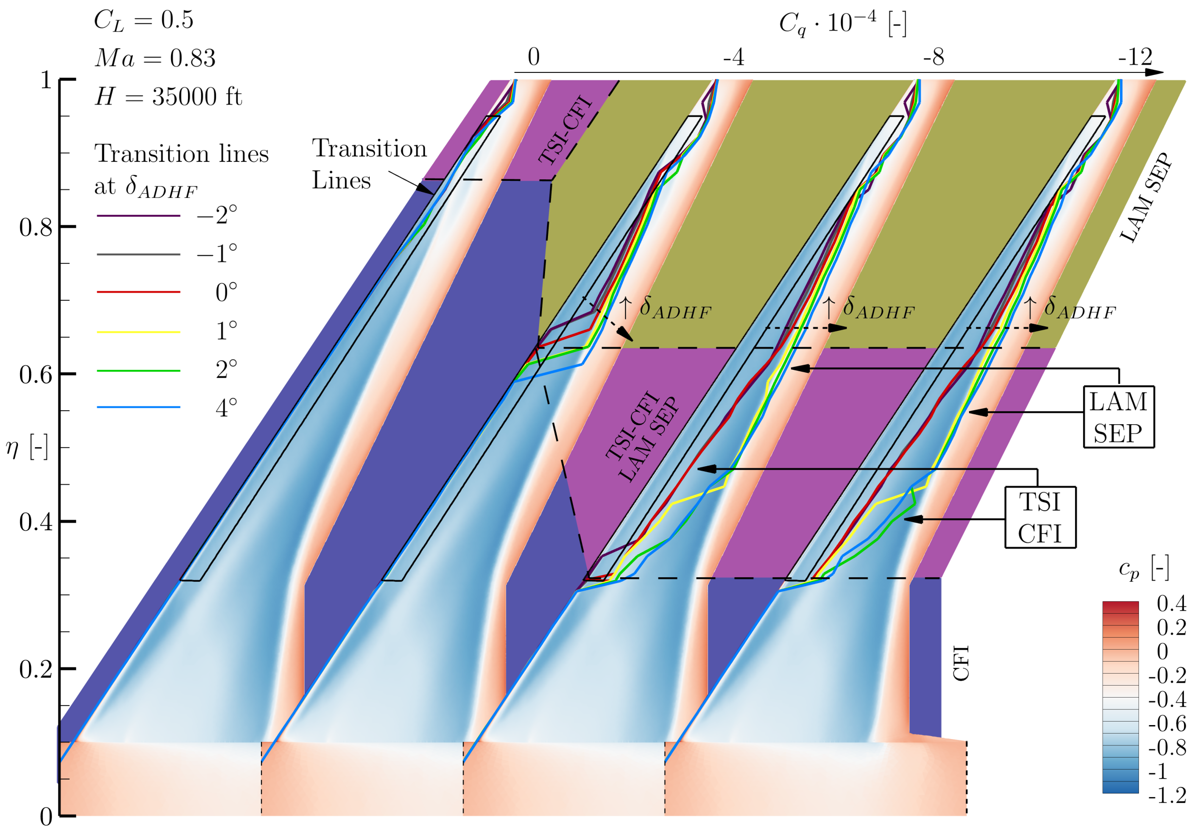


Figure 4.10: Predicted transition lines by means of linear stability with two-$N$-factor transition prediction method for varying suction coefficients $C_q$ and ADHF deflection angles $\delta_{ADHF}$ at $C_L = 0.5$, $Ma = 0.83$, $H = 35\ 000$ ft. Additionally, the critical transition mechanisms are indicated along the wing span. The $c_p$ contour is extracted for the wing suction side at $\delta_{ADHF} = 0°$ and $C_q = 0$.

Considering the case $C_q = -4 \cdot 10^{-4}$, the suction strength does not suffice to suppress transition due to CFI inboard of the limit $\eta \approx 0.62$. Sensitivity is predicted to the ADHF deflection angle in the spanwise region $\eta$ = 0.58 - 0.65, where increasing the ADHF deflection angle results in a switch in transition mechanism from CFI to laminar separation. In contrast to what has been described earlier (cf. Sec .3.3.1), this attributes potential for suppression of CFI to VC-integration, in this case, connected to the development of the pressure gradient in the leading edge region of the wing for increasing ADHF deflection angles. Deflecting the ADHF leads to a reduction in up to vanishing pressure gradients in the leading edge region, for which this effect may be classified as a tertiary synergistic effect[1]. Nevertheless, this effect is only of limited practical relevance, as it is highly sensitive to the operating condition, whilst arising at a suction strength that is not sufficient for a large extent of laminar flow on the wing suction side.

The secondary synergistic effect introduced in Sec. 3.3.1, however, is observable outboard of $\eta \approx 0.62$ for all suction coefficients $C_q \leq -4 \cdot 10^{-4}$. The downstream shift in shock position induced by a downward deflection of the ADHF is accompanied by a downstream shift in transition position for all observed cases. Decambering the wing by deflecting the ADHF upwards ($\delta_{ADHF} < 0°$) leads to the opposite behavior as the shock front moves upstream.

Inboard of $\eta \approx 0.62$, primary synergy effects develop markedly for $\delta_{ADHF} \geq 1°$ for both suction coefficients $C_q \leq -8 \cdot 10^{-4}$. Deflecting the ADHF leads to a shift in transition mechanism from amplification of the primary instability mechanisms TSI and CFI to laminar separation, connected to the reduction in TS-wave amplification by correspondingly adapting the pressure distribution through ADHF deflection. As the development of the transition front corresponds to the development of the shock front, the downstream shift in the shock position through ADHF deflection is additionally reflected in the transition position.

The resulting drag coefficients for variations in suction strength and ADHF deflection angles are presented in Fig. 4.11. Next to the total drag coefficient $C_D$ (left column) the mid column of Fig. 4.11 is dedicated to the pressure drag component $C_{D,p}$, while the right-most column shows the friction drag component $C_{D,f}$. Next to the design lift coefficient $C_L = 0.5$ discussed so far in this section, the off-design lift coefficients $C_L = 0.45$ and 0.55 are included in the top and bottom rows of Fig. 4.11, respectively.

Concerning an increase in suction strength, all presented cases are characterized by a reduction in drag coefficient $C_D$. In the case of CATeW-02-WB, the overall reduction in $C_D$ due to boundary layer suction is approx. equally split on $C_{D,p}$ and $C_{D,f}$, as discussed for the isolated wing case connected to the increase in laminar flow area reducing the effect of viscous decambering next to the associated skin friction of the flow.

In contrast to the isolated wing case, however, deflecting the ADHF at the design Mach number $Ma = 0.83$ is not beneficial for the development of the overall drag coefficient $C_D$ in the wing-body case CATeW-02-WB, neither at its design point $C_L = 0.5$ nor for off-design conditions $C_L = 0.45$ and 0.55 at $Ma = 0.83$. Even though the prior discussion assessed synergistic effects to the technology coupling in terms of a downward

[1] Next to the primary HLFC/VC synergy of camber variations stabilizing the boundary layer towards transition due to TSI (cf. Fig. 1.2) and the secondary synergy of VC-integration resulting in a downstream shift of the shock position while both CFI and TSI are suppressed due to suction (cf. Sec. 3.3.1).

deflection of the ADHF leading to a downstream shift in transition position and thus an increase in the extent of laminar flow, the associated reduction in friction drag (right columns of Fig. 4.11) does not suffice to counteract the increase in pressure drag induced by a camber variation.

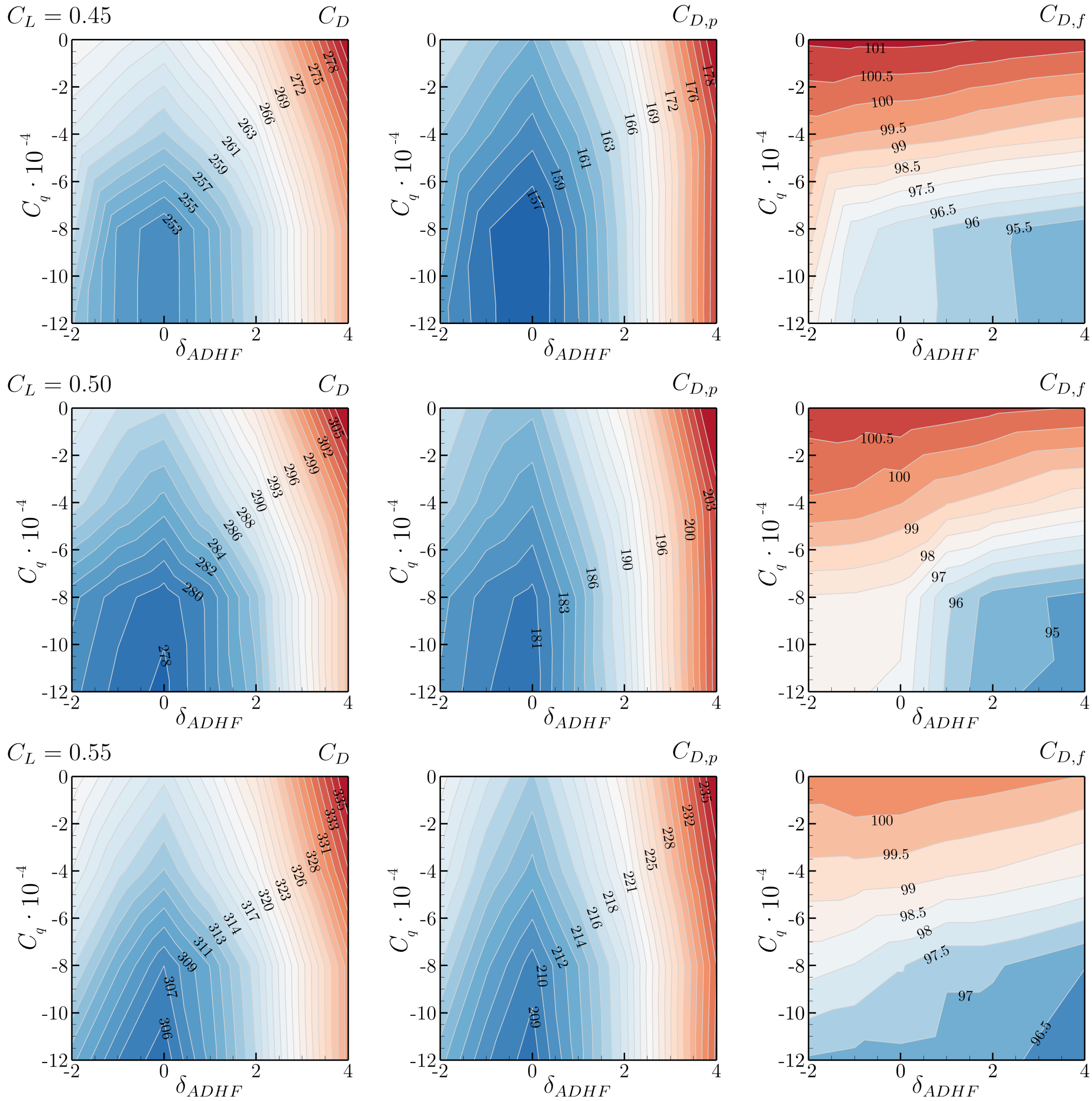


Figure 4.11: Overall drag coefficient, pressure and friction drag components (all in drag counts) for varying $\delta_{ADHF}$ and $C_q$ at $C_L = 0.45$ (top row), $C_L = 0.50$ (mid row) and $C_L = 0.55$ (bottom row). Mach number $Ma = 0.83$, Flight altitude $H = 35\,000$ ft.

This possible trade-off has already been indicated in the discussion considering isolated VC integration to CATeW-02-WB (cf. Sec. 4.2.3), and does not necessarily prohibit synergistically coupling VC and HLFC, but rather assesses design robustness to off-design operating conditions to CATeW-02-WB in terms of lift coefficient variations. Synergistic effects can therefore be expected when isolated VC integration (an increase in camber for the case CATeW-02-WB) already leads to a drag reduction. As discussed in Sec.

4.2.3, this is observable for off-design operation at a reduced Mach number, which will be discussed in the subsequent section.

### 4.3.2 Sensitivity to Mach Number Variation

The development of the transition front for the off-design Mach numbers $Ma = 0.78$ and $Ma = 0.81$, next to the design Mach number $Ma = 0.83$ at $C_L = 0.5$, ICA $H = 35\,000$ ft and for varying ADHF deflection angles $\delta_{ADHF} = [0°; 1°; 2°; 4°]$ is depicted in Fig. 4.12. The right-most contour has already been discussed above and is included for reference.

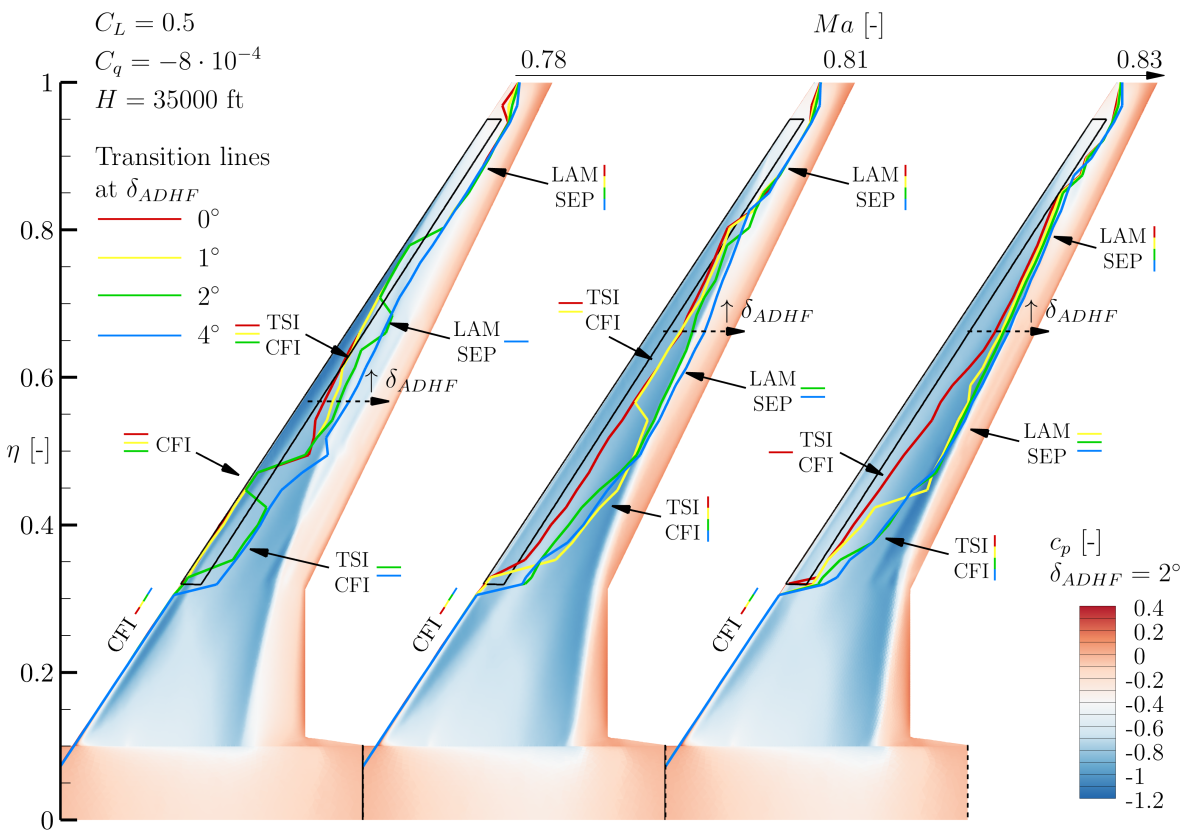


Figure 4.12: Predicted transition lines by means of linear stability with two-$N$-factor transition prediction method for varying Mach numbers $Ma$ and ADHF deflection angles $\delta_{ADHF}$ at $C_L = 0.5$, $H = 35\,000$ ft and $C_q = -8 \cdot 10^{-4}$. Additionally, the critical transition mechanisms are indicated along the wing span, the colored lines refer to the critical transition mechanism connected to the respective ADHF deflection angle. The $c_p$ contour is extracted for the wing suction side at $\delta_{ADHF} = 2°$ and $C_q = -8 \cdot 10^{-4}$.

Considering a Mach number variation without VC integration, i.e. $\delta_{ADHF} = 0°$ (red lines), a successive upstream shift in transition position is predicted with decreasing Mach number. This behavior is connected to the characteristics of the pressure distribution with decreasing Mach number discussed in Sec. 4.2.2, where a reduction in Mach number leads to a decrease up to a change in sign of the pressure gradient for $Ma = 0.81$ and $Ma = 0.78$, respectively, while a pronounced suction peak develops for

the here presented case $C_L = 0.5$. The first aspect is destabilizing when it comes to TS-waves, while the latter tends to amplify CFI in the leading edge region of the wing. Correspondingly, the mid-span region $\eta \approx 0.5 - 0.9$ is characterized by an upstream shift in transition front with decreasing Mach numbers, while for the case $Ma = 0.78$ the suction coefficient $C_q = -8 \cdot 10^{-4}$ does not suffice to suppress transition due to CFI for $\eta \lessapprox 0.5$ due to the strong suction peak.
As the shock front is accordingly shifted upstream with a decreasing Mach number, the transition front shows high sensitivity to VC integration. The synergy effects discussed in the previous section (cf. Sec. 4.3.1) are directly transferable to the off-design Mach numbers $Ma = 0.78$ and $0.81$, where according to the intended benefit of VC integration sensitivity rises when operating the aircraft at lower Mach numbers. Focusing on the operating point at $Ma = 0.81$, for instance, the depicted increments in ADHF deflection angle initially lead to the boundary layer being stabilized in the inboard region of the wing $\delta_{ADHF} \geq 1°$ up to the point $\eta \approx 0.55$, outboard of which further ADHF deflection to $\delta_{ADHF} \geq 2°$ is necessary to maintain subcritical amplification of both TSI and CFI.
A further decrease in the freestream Mach number to $Ma = 0.78$ reinforces this behavior, i.e. for a marked downstream shift in transition position, it is necessary to set the ADHF to the highest considered deflection angle of $\delta_{ADHF} = 4°$. For $\delta_{ADHF} = 2°$, abrupt switches in transition mechanisms and thus transition positions are observable, as the $N$-factors of both CFI and TSI are close to the respective limiting curve.
In contrast to the design Mach number $Ma = 0.83$, for reduced Mach numbers synergy does not only express itself in a downstream shift of the transition front when applying the HLFC/VC coupling but, in line with the aspects indicated above, translates to a synergy-driven drag reduction when applying both technologies together, see Fig. 4.13. This means, that deflecting the ADHF to $\delta_{ADHF} = 2°$ for the case $Ma = 0.78$, leads to both a maximal[2] reduction in the pressure drag component of CATeW-02-WB while setting $C_q \leq -8 \cdot 10^{-4}$ beneficially couples to the adapted pressure distribution induced by VC integration to foster the lowest overall drag coefficient $C_D$.
This aspect is further reaffirmed when observing the case $Ma = 0.81$, as the lowest drag coefficient $C_D$ is not connected to a constant ADHF deflection angle throughout a variation of the suction coefficient $C_q$, but varies accordingly. That is, for $C_q = 0$, the lowest drag coefficient occurs at $\delta_{ADHF} = 0°$, reflecting the results discussed in terms of VC implications in Sec. 4.2.3. With increasing suction strength, however, the ADHF deflection angle leading to the lowest drag coefficients switches to $\delta_{ADHF} = 1°$ for $C_q \leq -8 \cdot 10^{-4}$, connected to both technologies influencing each other beneficially, by making use of the synergistic effects derived in the discussions above.

[2] "Maximal" considering the individual datapoints upon which this analysis is based.

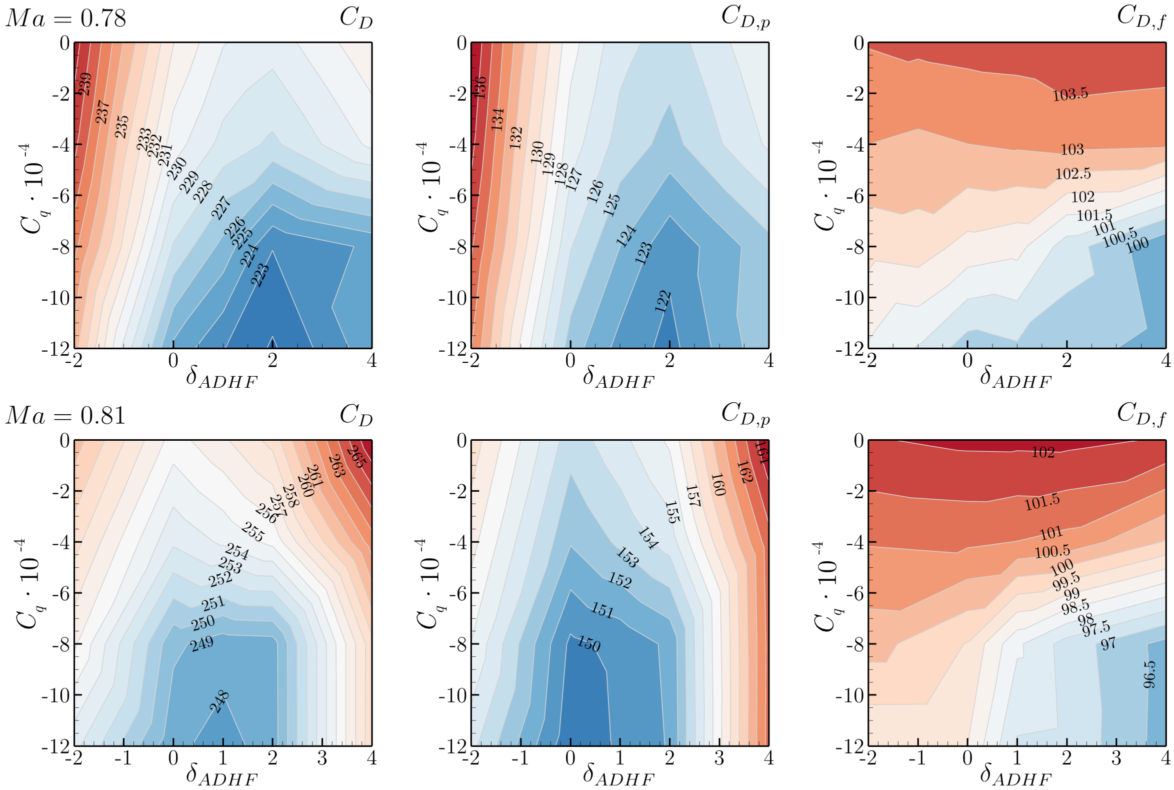


Figure 4.13: Overall drag coefficient, pressure and friction drag components (all in drag counts) for varying $\delta_{ADHF}$ and $C_q$ at $Ma = 0.78$ (top row) and $Ma = 0.81$ (bottom row). Lift coefficient $C_L = 0.5$, flight altitude $H = 35\ 000$ ft.

### 4.3.3 Sensitivity to Reynolds Number Variation

To conclude the analyses of CATeW-02-WB throughout its flight envelope, the parameter space proposed in Fig. 4.9 foresees a variation in Reynolds number at fixed lift coefficient $C_L = 0.5$ and Mach number $Ma = 0.83$ from $Re = 34.5 \cdot 10^6$ to $28.8 \cdot 10^6$. The corresponding Reynolds numbers result from considering a step climb from ICA $H = 35\ 000$ ft to a higher flight level at $H = 39\ 000$ ft, the underlying thermodynamic properties being set automatically by the simulation toolchain according to the International Standard Atmosphere (ISA) [52] model. It should be noted, that, due to the latter aspect, the Mach number variation analyzed in the previous section is naturally accompanied by a Reynolds number variation as well, since by using the flight altitude as an input parameter for the ISA model a Mach number variation is achieved by changing the freestream velocity $u_\infty$, which linearly scales with the Reynolds number of the flow considered in the analysis (cf. Eq. 2.1). Therefore, the goal of this section also consists of the validation of the previously discussed effects being primarily driven by a Mach number variation, and not by a coupling of both similarity parameters $Ma$ and $Re$.
Therefore, the corresponding development of the drag coefficient $C_D$ and its pressure $C_{D,p}$ and friction components $C_{D,f}$ are depicted in Fig. 4.14. In general, the transition positions underlying the drag coefficients presented in Fig. 4.14 do not significantly vary with different ADHF deflection angles or suction coefficients when considering the

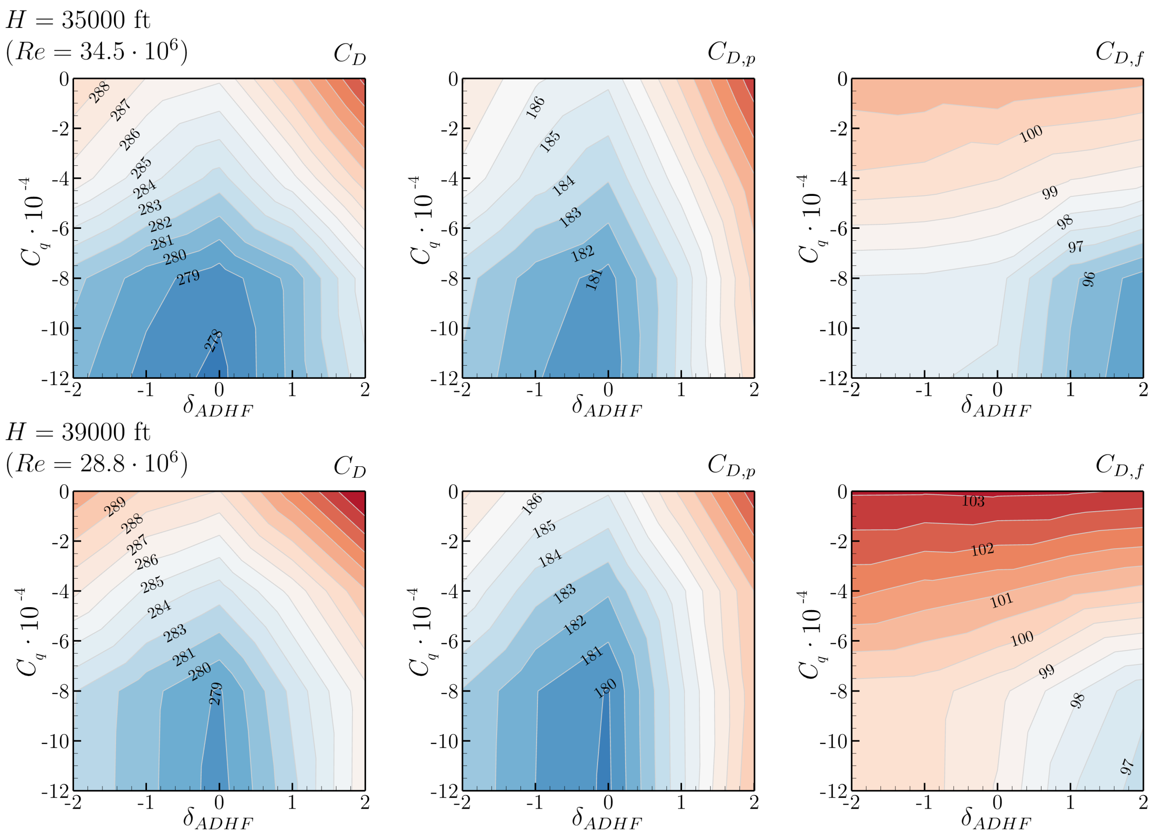


Figure 4.14: Overall drag coefficient, pressure and friction drag components (all in drag counts) for varying $\delta_{ADHF}$ and $C_q$ at $H$ = 35 000 ft (top row) and $H$ = 39 000 ft (bottom row). Lift coefficient $C_L = 0.5$, Mach number $Ma = 0.83$.

Reynolds numbers associated with $H$ = 35 000 ft and $H$ = 39 000 ft. This expresses itself in the development of the drag coefficients showing high qualitative agreement concerning their sensitivities, as well as deviations of approx. ±1 dc in their magnitude for the same parameter combinations $\boldsymbol{p} = [C_q, \delta_{ADHF}]$.

## 4.4 Synthesis

Within this chapter, the analyses previously presented for the isolated wing of CATeW-02 were expanded to wing-body plus horizontal tailplane (HTP) level CATeW-02-WB. To reach convergence to a steady state flow solution in the numerical simulation a geometry adaptation was introduced, namely the addition of a wing-belly fairing and bump to suppress side-of-body separation. Furthermore, the framework used for the inclusion of trim effects in the numerical simulations was presented, realized via mesh deformations in the form of rigid body rotation of the HTP and interpolation from a bulk data set for the determination of the corresponding stability derivatives. The inclusion of trim is necessary for a consistent evaluation and comparison of the technology coupling considering sensitivity to different operating parameters within the flight envelope, as it imposes a boundary condition on the pressure distribution obtainable during cruise flight, especially considering the additional pitching moments generated through camber variation in form of deflecting the ADHF.

Based on this framework, an analysis considering the development of the flow field for different operating parameters ($C_L$, $Ma$) was presented, the focus lying upon the pressure distributions arising in design and off-design conditions. Especially operation in off-design connected to a lower Mach number ($Ma = 0.78$) leads to an unfavorable development of the pressure distribution when foreseeing HLFC integration, for which this case optimally lends itself for actively controlling the pressure distribution employing VC.

Before analyzing the coupled HLFC/VC system, isolated effects of VC integration were discussed on component level of CATeW-02-WB for variations in lift coefficient and Mach number. As for the isolated wing case, deflecting the ADHF leads to a corresponding shift of aerodynamic loads from the wing to the other components of CATeW-02-WB. Neither for the design point ($C_L = 0.5$, $Ma = 0.83$), nor for the off-design lift coefficients $C_L = 0.45$ and 0.55 does VC integration benefit the development of the overall drag coefficient $C_D$, the lowest drag coefficients are obtained for $\delta_{ADHF} = 0°$ considering the envisaged $C_L$ variations. Operating the aircraft in off-design Mach numbers, however, attributed a benefit of VC integration to CATeW-02-WB. When reducing the Mach number to $Ma = 0.78$, the lowest drag coefficients are predicted for $\delta_{ADHF} = 2°$. This behavior is not only favorable when it comes to isolated VC integration, but as shown in the analysis considering the isolated wing case, the boundary layer is stabilized when the ADHF is positively (downwards) deflected. Therefore, the preliminary conclusion can be drawn, that on wing-body + HTP level the highest synergistic potential of the HLFC/VC coupling will be connected to off-design operation at reduced Mach numbers, yielding both a benefit in pressure drag as well as in the development of the chordwise pressure distribution through ADHF deflection.

This is correspondingly reflected when incorporating transition prediction and boundary layer suction into the analysis parameter space. Variable camber integration on one hand either stabilizes the boundary layer towards transition due to primary instabilities or suffices to suppress transition due to TSI or CFI given enough suction. Alongside this primary synergy effect, is the shock front being shifted downstream with positive ADHF deflection, for which the chordwise extent of negative pressure gradient flow is prolonged and the point of transition is further shifted downstream, in this work denoted as a secondary synergistic effect. In line with the isolated VC analysis on CATeW-02-WB, the benefit in drag reduction through VC integration is nevertheless outweighed by the increase in pressure drag for the design point $C_L = 0.5$ and off-design operation at $C_L = 0.45$ and 0.55, for which the lowest drag coefficient is still connected to the maximum amount of boundary layer suction at $\delta_{ADHF} = 0°$.

In contrast, the synergistic potential develops when reducing the cruise Mach number to $Ma = 0.81$ and 0.78 from the design Mach number $Ma = 0.83$. The downstream shift of transition position accompanied by the beneficial development of the pressure drag due to VC integration leads to a synergy-driven increase in the potential for drag reduction at both Mach numbers. Especially the case $Ma = 0.81$ shows high synergistic potential, as the ADHF deflection angle associated with the lowest drag coefficient is directly influenced by the addition of suction to the operating point, switching from $\delta_{ADHF} = 0°$ to $\delta_{ADHF} = 1°$ for $C_q \leq -8 \cdot 10^{-4}$.

# 5 Formulation of Reduced Order Models

## 5.1 Motivation

While the aerodynamic design and performance are central aspects to be considered during aircraft development, further requirements need to be satisfied for the derivation and optimization of the final product. This has already been mentioned in the context of the Breguet range equation (Eq. 1.1) in Chap. 1, connecting the cruise range of an aircraft to three factors based on aerodynamics, engine performance and structural weight. As these requirements oftentimes oppose each other, designing and optimizing an aircraft for its entire operational envelope and a multitude of mission scenarios solely based on high-fidelity (HiFi) methods is connected to prohibitively high computational expenses. Therefore, overall aircraft design (OAD) methods typically build upon Low-fidelity (LowFi) methods, which are computationally cheap to evaluate while offering sufficient accuracy to either approach HiFi results, or more decisively, correctly reflect design sensitivities and optima.

Up to this point, the central objective of the thesis consists of analyzing a VC/HLFC technology coupling from a purely aerodynamic viewpoint. To do so, comprehensive HiFi aerodynamic data sets have been created, alongside automated modeling and data generation routines. The latter aspects perfectly lend themselves to the creation of data-driven reduced order models (ROMs), based upon which HiFi-aerodynamic data can be efficiently incorporated into LowFi-OAD workflows.

A lot of research effort is currently directed toward the formulation and implementation of ROM approaches. The goal of this chapter consists in the application and the result assessment of two of the most efficient ROM algorithms, namely Gaussian Process regression (GPR) and the Proper Orthogonal Decomposition (POD), given the coupled HLFC/VC aerodynamic data set derived for the isolated wing analysis in Chap. 3. This concludes the thesis with an indication of possibilities of exploiting HiFi aerodynamic data sets for enhancing the results of LowFi toolchains, already early in an OAD process. The theoretical background of GPR and POD for the application case at hand is described in Sec. 5.2, while Sec. 5.3 deals with model conditioning aspects, i.e. sampling plan and training data set generation. The application case of the CATeW-02 wing and ROM results in comparison to CFD results are discussed in Sec. 5.4. To conclude the chapter, a comparison of results stemming from the LowFi aerodynamic toolchain employed in the project partner's OAD framework MICADO [102, 116] (cf. Sec. 2.3.3) to results using the ROM approaches discussed in the present chapter is presented.

The content of this chapter is closely reproduced from two conference contributions [57,58][1], both first-authored by the author of this thesis.

## 5.2 Theoretical Background

Two models are applied in the course of this chapter. On the one hand, a surrogate (SG) model based on Gaussian process regression (GPR-SG) is utilized to predict the total drag coefficient of the configuration, on the other a ROM based on Proper Orthogonal Decomposition (POD-ROM) is presented for the prediction of surface quantities on the reference wing. This differentiation results from the intended coupling framework to a LowFi aerodynamic toolchain and their respective abstraction levels, the main interest for OAD being centered around parametrically predicting the total drag coefficient $C_{D,total}$ of a vehicle.
To further address the above-mentioned aspect, an overview of different paths for prediction of $C_{D,total}$, based upon a series of input parameters stemming, for instance, from a prescribed mission profile ($C_L$, $Ma$, $Re$), or being part of an optimization problem (wing geometry), is depicted in Fig. 5.1.

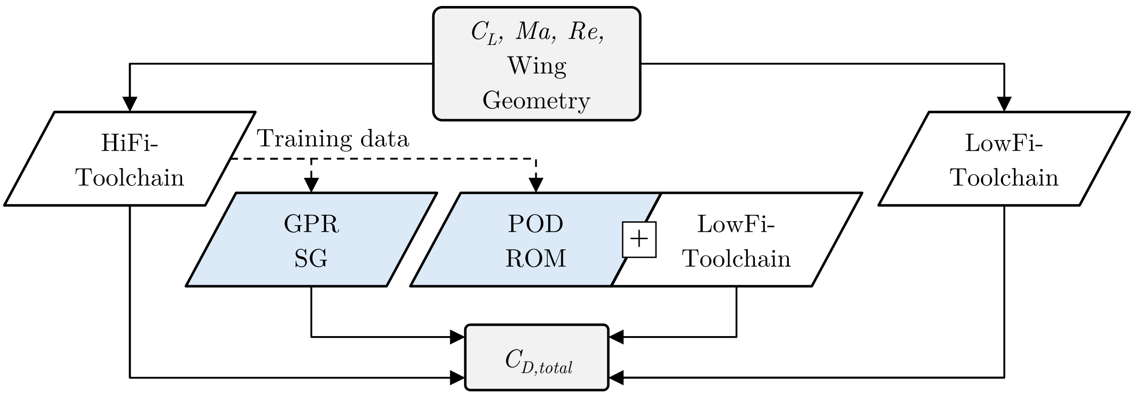


Figure 5.1: Integration of SG and ROM approaches to the top-level architecture of an OAD aerodynamic workflow.

As already mentioned, the left path (HiFi-Toolchain) offers the highest result accuracy at (oftentimes) prohibitive computational costs for OAD, whilst the right path (LowFi-Toolchain) is marked by low computational cost but typically highly restrictive modeling assumptions and, thus, lower accuracy of the aerodynamic results. The models mentioned earlier are intended to offer a trade-off between computational cost and accuracy, in the sense that they still require a set of expensive HiFi-simulations to be trained upon, nevertheless generalizing the results through model application allows to parametrically infer highly accurate data for unknown parameter combinations $\boldsymbol{p}^*$ in near real-time.

[1] The articles were published with copyright remaining with the authors, under exclusive license to the EUCASS association and Springer Nature Switzerland AG 2024, respectively. The co-authors have consented to publication in the present thesis.

Returning to the differentiation in the respective abstraction levels indicated above, the GPR-SG acts as a surrogate model, i.e., it is intended to entirely or partially replace a LowFi aerodynamic toolchain in the context of an OAD framework. Partially, in this case, does not refer to the replacement of parts of the LowFi aerodynamic toolchain, but to replacing results[2] of the latter. Interaction with the LowFi-toolchain is foreseen through the application of the POD-ROM in this work, namely using the POD framework to predict HiFi surface data, e.g. $c_p$ distributions at unknown parameter combinations $\boldsymbol{p}^*$, required during runtime of the LowFi-toolchain. The advantage of the latter is the possibility to further generalize the results for future applications, e.g. by derivation of a correction function for the methods utilized within the LowFi aerodynamic framework. For a detailed overview of the interaction points with a typical LowFi aerodynamic workflow the reader may refer to [57].
Within the following Secs. 5.2.1 and 5.2.2, a short overview of the theoretical foundation of both modeling approaches is presented.

### 5.2.1 Gaussian Process Regression

Gaussian Process regression belongs to the category of supervised machine learning techniques. The goal of GP application in the present context is to construct a surrogate model for parametric prediction of aerodynamic characteristics for unknown parameter combinations $\boldsymbol{p}^*$, based upon a limited set of training data points or observations at parameter combinations $\boldsymbol{p}$ stemming from HiFi aerodynamic simulations.
Numerous recent publications deal with surrogate models built upon GPR in an aerodynamic context. In [33], the authors apply GPR-based models for multi-fidelity aerodynamic data fusion, utilizing the herewith constructed SG to assess the properties of a blended wing body aircraft at its stability and control limits. Within [117], GPR is used to enhance linearized flight dynamics models, reflecting aerodynamic and propulsive characteristics at different points within the flight envelope. The application case for the enhanced model is an electric quad-rotor air-taxi concept vehicle. Next to the regression or data-fusion of aerodynamic data, GPR spans application fields from measuring probe calibration [45] to geostatistics [34] (commonly termed Kriging-interpolation in this context), proving the broad applicability and oftentimes advantageous generalization properties connected to GPR in otherwise data and thus time-intensive tasks.
To expand on this, the latter point is one of the key advantages of a GPR-SG when it comes to application for the regression task at hand. Good generalization properties with little training data reduce the cost associated with constructing the HiFi training data set, whilst the probabilistic nature of GPR provides an inherent uncertainty quantification and includes an automatic trade-off between the model fitting the data and the associated model complexity [91].

[2] For instance, using a drag decomposition of $C_{D,total} = C_{D,wing} + C_{D,rest}$, the term $C_{D,wing}$ may result from the SG, while $C_{D,rest}$ is still computed within the LowFi-toolchain.

In general, a GP is defined as a probabilistic distribution over functions, where the corresponding function values $f(\boldsymbol{p}_i)$ are jointly Gaussian distributed. Therefore, a GP can be characterized by its mean $\mu(\boldsymbol{p}_i)$ and covariance $k(\boldsymbol{p}_i,\boldsymbol{p}_j)$ functions [26]:

$$f(\boldsymbol{p}) = \begin{bmatrix} f(\boldsymbol{p}_1) \\ \vdots \\ f(\boldsymbol{p}_n) \end{bmatrix} \sim \mathcal{N}\left( \begin{bmatrix} \mu(\boldsymbol{p}_1) \\ \vdots \\ \mu(\boldsymbol{p}_n) \end{bmatrix}, \begin{bmatrix} k(\boldsymbol{p}_1,\boldsymbol{p}_1) & \dots & k(\boldsymbol{p}_1,\boldsymbol{p}_n) \\ \vdots & \ddots & \vdots \\ k(\boldsymbol{p}_1,\boldsymbol{p}_n) & \dots & k(\boldsymbol{p}_n,\boldsymbol{p}_n) \end{bmatrix} \right) \tag{5.1}$$

Without providing any observations to the GP, i.e. values of $f(\boldsymbol{p}_i)$, one speaks of the GP prior, which encapsulates the prior knowledge about the function $f(\boldsymbol{p}_i)$ to be regressed solely in the structure of the chosen covariance function $k$ and the input parameter vectors $\boldsymbol{p}_i$. The mean of the prior is typically set to be zero $\mu(\boldsymbol{p}_i) = 0$, while the covariance function, also referred to as the kernel of a GP, determines which type of functions are used within the GP.

To illustrate this, the prior of a GP considering a one-dimensional test case is depicted in the upper panel of Fig. 5.2, where 20 function realizations (light red lines) are randomly drawn from the prior of the GP. The samples depicted in Fig. 5.2 are constructed using a squared-exponential kernel [26]:

$$k(\boldsymbol{p}_i,\boldsymbol{p}_i') = \sigma_f^2 \exp\left( -\frac{1}{2} \sum_{i=1}^{d} \frac{(p_i - p_i')^2}{\ell_i^2} \right) \tag{5.2}$$

where the hyper-parameters $\ell_i$ are termed the length-scales for each input parameter dimension and $\sigma_f^2$ denotes the signal variance of the GP.

As mentioned above, the GP prior does not yet include any information on the underlying function to be regressed. To do so, one needs to incorporate observations drawn from the underlying function $f : \mathbb{R}^d \to \mathbb{R}$ into the GP, an observation at $\boldsymbol{p}_i$ resulting in $f(\boldsymbol{p}_i)$ at a discrete set of observation or training points $\{(\boldsymbol{p}_i, f(\boldsymbol{p}_i))|i = 1,\dots,n_{SP}\}$. The observations in the present case are considered noise-free, as commonly assumed when considering observations stemming from a computer experiment. Combination of known observations at points $\boldsymbol{p}_i$ with responses of the function to be regressed at point $\boldsymbol{p}_i^*$ is achieved by the so-called joint prior [91]:

$$\begin{bmatrix} f(P) \\ f(P^*) \end{bmatrix} \sim \mathcal{N}\left( \mathbf{0}, \begin{bmatrix} K(P,P) & K(P,P^*) \\ K(P^*,P) & K(P^*,P^*) \end{bmatrix} \right) \tag{5.3}$$

$P$, $P^*$ and $K$ respectively representing observation, prediction and covariance matrices, concatenating $\boldsymbol{p}_i$, $\boldsymbol{p}_i^*$ and the corresponding elementwise evaluation of the covariance functions $k(\cdot,\cdot)$ in their entries.

The joint prior builds upon the definition of a GP mentioned above, namely the known observations $f(P)$ and the unknown function values $f(P^*)$ being jointly Gaussian distributed (see Eq. 5.1). Note that the mean of the GP $\mu(P)$ and $\mu(P^*)$ is explicitly set

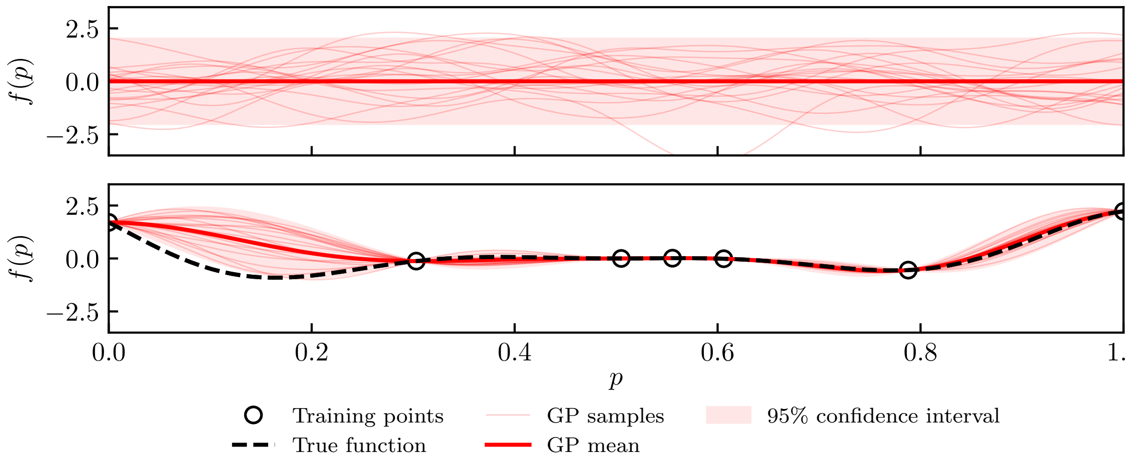


Figure 5.2: Upper panel: GP prior mean (red line) and 95% confidence interval (red shaded area), alongside 20 random samples from the prior (light red lines). Lower panel: GP posterior mean (red line) and 95% confidence interval (red shaded area), alongside 20 random samples from the posterior (light red lines), conditioned upon seven samples (black circles) from $f(p) = (3p - 1.5)^2 \sin 12p - 4$ (black dashed line). Adapted from [58].

to zero in Eq. 5.3, which is not strictly necessary but simplifies the notation.
To ultimately infer $f(P^*)$ from Eq. 5.3, one utilizes the standard GP predictive equations, resulting from conditioning the GP upon the given training outputs $f(P)$ and observation parameters $P$ and $P^*$ [91]:

$$\begin{aligned}(f(P^*)|P^*,P,f(P)) \sim \mathcal{N}\big(&K(P^*,P)K(P,P)^{-1}f(P),\\ &K(P^*,P^*) - K(P^*,P)K(P,P)^{-1}K(P,P^*)\big)\end{aligned} \tag{5.4}$$

The terms on the right-hand side of Eq. 5.4 are all known, the unknown function values $f(P^*)$ and the associated (co)variances of the GP at points $P^*$ can be directly extracted to read:

$$f(P^*) = \mathbb{E}(f(P^*)|P^*,P,f(P)) = K(P^*,P)K(P,P)^{-1}f(P) \tag{5.5}$$

$$\mathrm{cov}(f(P^*)) = K(P^*,P^*) - K(P^*,P)K(P,P)^{-1}K(P,P^*) \tag{5.6}$$

The conditioned distribution presented in Eq. 5.4 is referred to as the posterior of a GP. An example is depicted in the lower panel of Fig. 5.2, where the previously used prior is conditioned upon seven observations $f(p)$ (black circles) from the arbitrary function $f(p) = (3p - 1.5)^2 \sin(12p - 4)$. Alongside the mean function of the posterior, used for inferring $f(p^*)$ (red line, Eq. 5.5), again twenty samples drawn from the GP posterior are depicted (light red lines). This graphically reflects the intuition connected to conditioning a GP, which consists of only retaining functions from the prior passing exactly through the observation points for the formulation of the posterior distribution. Additionally, the above-mentioned point-wise uncertainty quantification (red shaded area) inherent to GPR is included in terms of the 95% confidence region ($\widehat{=} 2\sigma = 2\sqrt{\text{diag(cov)}}$, Eq. 5.6) in the graphical representations of the prior/posterior, where high uncertainty is associated to prediction points $p^*$ parametrically distant from the observations $p$ and, consequently to the graphical intuition discussed above, low uncertainty in vicinity of observation points.

The last building block required for the application of GPs within regression tasks is connected to "training" the GP. Training in the context of GPR refers to optimizing the hyper-parameters $\boldsymbol{\theta}$, in the case of the herein applied SE-kernel (Eq. 5.2) confining the terms $\boldsymbol{\theta} = [\sigma_f^2, \ell_i]$. This step is crucial for the generalization properties of a GP-based surrogate, as the values of the hyper-parameters significantly influence the structure of the response function predicted by means of GPR. To illustrate this aspect, Fig. 5.3 shows the influence of hyper-parameter variations on the structure of samples drawn from the prior of a GP.

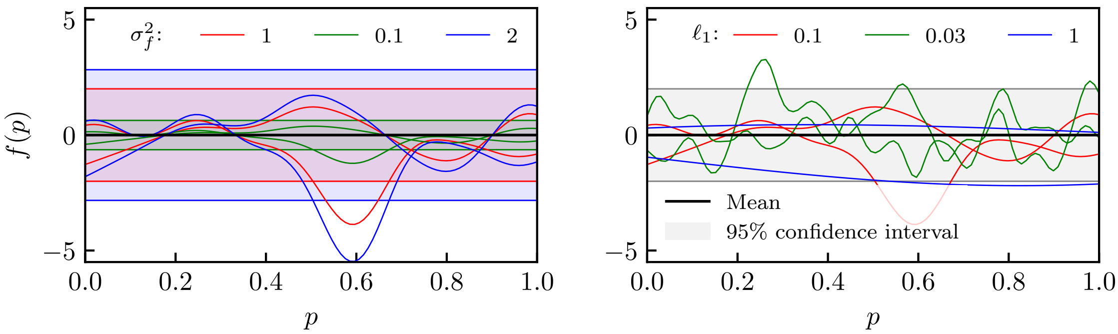


Figure 5.3: Samples from a GP prior (SE-kernel) for varying hyper-parameter values $\sigma_f^2 = [1{,}0.1{,}2]$ at $\ell_1 = 0.1$ (left panel) and $\ell_1 = [0.1{,}0.03{,}1]$ at $\sigma_f^2 = 1$ (right panel).

The left panel is dedicated to variations of the signal variance $\sigma_f^2$ contained within the formulation of the SE-kernel (Eq. 5.2), while the right panel shows the influence of varying the length scale $\ell_1$ for a one-dimensional test case. Variation of $\sigma_f^2$ sets the vertical extent of the functions to be considered within the GP, while $\ell_1$ controls the correlation rate of two points $p_1$ and $p_2$ depending on their respective parametric distance, i.e. how smooth the functions considered in the GP are. In other words, while inferring $f(P^*)$ from the posterior distribution Eq. 5.5 guarantees the predictions exactly passing through the observations $f(P)$, the structure of the function between the observations is highly dependent on the values of $\boldsymbol{\theta}$.

To set the values of $\boldsymbol{\theta}$ different methods exist. The most common approach is maximizing the log marginal likelihood [91]:

$$\log p(f(P)|P,\boldsymbol{\theta}) = -\frac{1}{2} f(P)^{\mathrm{T}} K(P,P)^{-1} f(P) - \frac{1}{2} \log |K(P,P)| - \frac{n_{SP}}{2} \log 2\pi \qquad (5.7)$$

In simplified terms, the log marginal likelihood presents the probability of the observations $f(P)$ given a specific set of hyper-parameters $\theta$. Maximizing the log marginal likelihood thereby leads to the above-mentioned automatic trade-off between data fit and the model complexity, i.e. it inherently includes a penalty term for over-fitting, namely $\log|K(P,P)|$, which is counteracted by the term $-f(P)^{\mathrm{T}}K(P,P)^{-1}f(P)$ specifying how well the observations are fitted by the model. As previously mentioned, the latter aspect is redundant for a set of noise-free observations, since in this case, GPR will fit the data exactly for parameter combinations included in the training data set. Therefore, maximizing the log marginal likelihood results in choosing the hyper-parameters according to the least complex model being able to explain the included training data for the present application case.

### 5.2.2 Proper Orthogonal Decomposition

In complement to parameter-wise regression of scalar outputs utilizing GPR, a framework built around the POD is applied for the parametric prediction of (vectorial) surface data.
The POD is one of the most commonly applied methods used in the context of dimensionality reduction, excelling through the simplicity associated with the POD being a linear autoencoder. For parametric predictions in an aerodynamic context, the method has been introduced by Bui-Tanh et al. [14], where it is termed POD with interpolation (POD+I) for the prediction of pressure coefficient distributions around airfoils. Ripepi et al. [100] also applied the POD+I method in the context of multidisciplinary design optimization for a transport aircraft, next to further approaches building about the POD as an efficient tool for dimensionality reduction when used in conjunction with the residual matrix of the underlying flow solver.
A flowchart presenting the required steps for surface data prediction or reconstruction utilizing the POD+I method is depicted in Fig. 5.4. As for GPR, the POD framework is based upon a parametric training data set, in the context of the herein applied POD snapshot method [122] commonly termed the snapshot matrix. As depicted in Fig. 5.4, the snapshot matrix might consist of $c_p$ distributions on the surface grid points of the wing, stacked in columns alongside the associated parameter vectors $\boldsymbol{p}_i$. The resulting snapshot matrix $W = (\boldsymbol{W}^1, \ldots, \boldsymbol{W}^{n_{sp}}) \in \mathbb{R}^{n_{GP} \times n_{SP}}$, $n_{GP}$ reflecting the number of grid points contained in the CFD surface mesh and $n_{SP}$ the number of sampling parameter combinations, is decomposed using a singular value decomposition (SVD):

$$W = U \Sigma V^T \tag{5.8}$$

the matrices $U \in \mathbb{R}^{n_{GP} \times n_{GP}}$ and $V \in \mathbb{R}^{n_{SP} \times n_{SP}}$ reflecting orthogonal bases of $W$, $\Sigma \in \mathbb{R}^{n_{GP} \times n_{SP}}$ containing the singular values $\sigma_1, \ldots, \sigma_{n_{SP}}$ in the diagonal of the first $n_{SP}$ rows of $\Sigma$ (for the typical case of $n_{SP} << n_{GP}$).

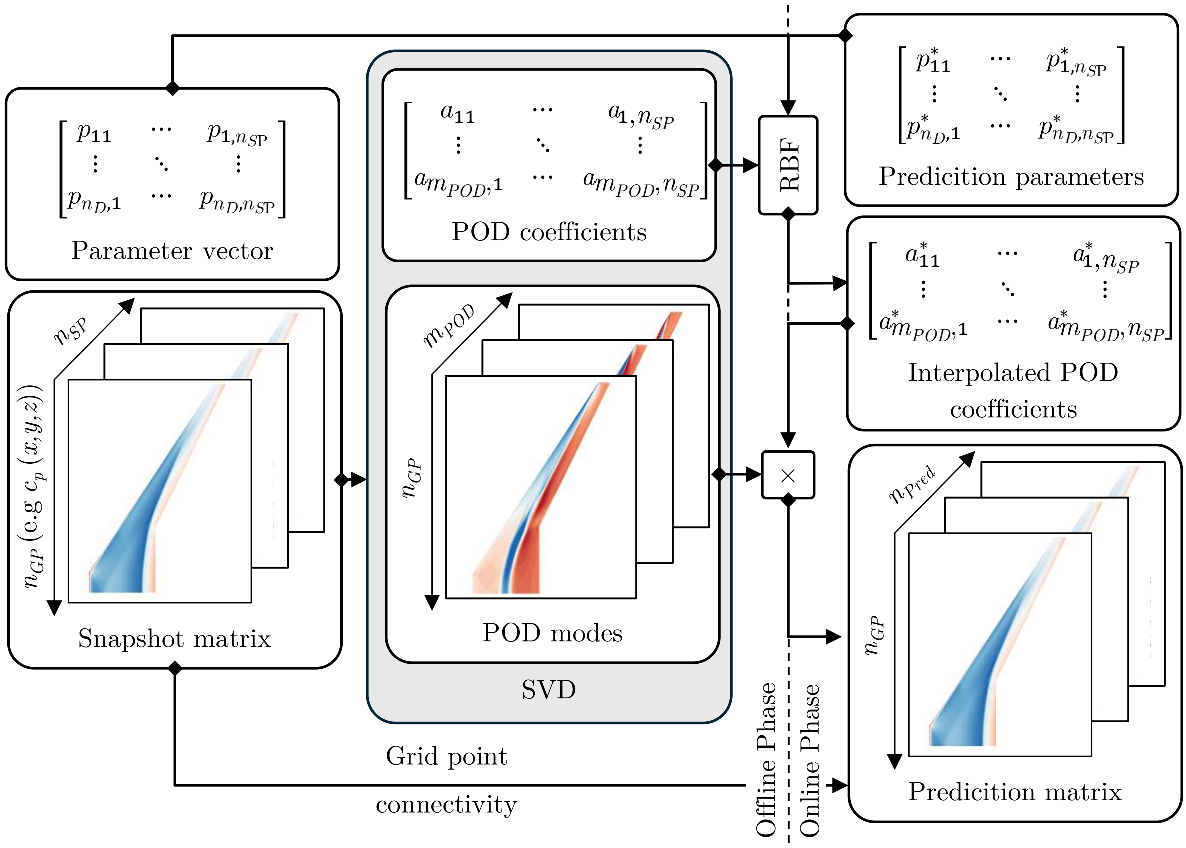


Figure 5.4: General overview of a POD-based data prediction workflow.

The columns of $U$ are termed the POD modes, while the resulting singular values are concatenated with the entries of $V$ to $a^i_j = \sigma_j V^j_i$ forming the POD coefficients. Model order reduction is now performed by retaining only the first $m_{POD}$ columns of $U$, $m_{POD}$ being determined according to the relative information content criterion (RIC) surpassing a threshold of $RIC \geq 0.99$ [137]:

$$RIC = \frac{\Sigma_{i=1}^{m_{POD}} \sigma_i^2}{\Sigma_{j=1}^{n_{SP}} \sigma_j^2}. \tag{5.9}$$

The RIC criterion is based upon the singular values $\sigma_i$ in $\Sigma$ automatically being ordered with decreasing magnitude, therefore reflecting the significance of the different POD modes contained in the modal basis $U$ for rebuilding the snapshot matrix $W$.
Back-mapping from the modal basis to the snapshot matrix is straightforward, utilizing a linear combination of the POD modes $\boldsymbol{U}^1, \ldots, \boldsymbol{U}^{m_{POD}}$ with the POD coefficients $\boldsymbol{a}^1, \ldots, \boldsymbol{a}^{n_{SP}}$:

$$\boldsymbol{W}^i \approx \sum_{j=1}^{m_{POD}} a^i_j \boldsymbol{U}^j \tag{5.10}$$

which, due to the reduced basis $U$ retaining the most relevant flow features in its $m_{POD}$ columns, results in a highly accurate reconstruction of the snapshot matrix $W$.
As mentioned before, the columns of the snapshot matrix $W$ represent, for instance, $c_p$ distributions at the corresponding sample parameter combinations $\boldsymbol{p}_i$. Therefore, the $i$-th column of the POD coefficient matrix $a$ can be comprehended as a function of $\boldsymbol{p}_i$, indicating the scaling of the invariant POD modes (columns of $U$, Eq. 5.10) necessary to reconstruct the corresponding column of $W$, i.e. $\boldsymbol{W}(\boldsymbol{p}_i)$. Therefore, given the reduced basis $U$, a surface solution $\boldsymbol{W}^*$ at an unknown parameter combination $\boldsymbol{p}^*$ can be inferred by interpolation in the POD coefficient space, namely by determination of $\boldsymbol{a}^* = \boldsymbol{a}(\boldsymbol{p}^*)$ and subsequent back-mapping to the original space using Eq. 5.10. Considering the aspect of model order reduction, the reconstruction problem is therefore shifted to the determination of the corresponding POD coefficient vectors $\boldsymbol{a}(\boldsymbol{p}^*)$ [35].
The interpolation of $\boldsymbol{a}(\boldsymbol{p}^*)$ is computationally very cheap given the predefined bases $U$ and $a$, making the POD+I method especially relevant for the intended real-time application in a LowFi aerodynamic toolchain. This results from the POD+I, as well as the GPR methods being of non-intrusive character, that is, they do not interact with the solution process itself but are applied in a stand-alone manner based on a previously deducted training data set. As indicated in Fig. 5.4 this allows for splitting the steps connected to the derivation of the models into an offline and an online phase, where the computationally expensive training data sets are formed a priori, while during the application of the models, i.e. the online phase, only the reduced representations of the data sets are queried for data at $\boldsymbol{p}^*$. Therefore, an important aspect consists of the formation of the data sets the models are conditioned on, which will be described in the following section.

## 5.3 Model Conditioning

Generating the underlying data sets for the derivation and training of the models requires the formulation of a sampling plan. Different approaches exist for the formulation of sampling plans, within the present work, a two-step approach is implemented, building on the above-described properties of uncertainty quantification inherent to GPR.
Based upon a predefined number of prediction parameter dimensions, a set of initial sampling parameters $P$ is derived using a Latin Hypercube sampling (LHS) strategy. Latin Hypercube sampling is chosen to build the base sampling plan due to its optimal space-filling properties, which is highly advantageous due to the predictions of both GPR as well as POD+I possessing higher accuracy, the closer the queried parameter combinations $P^*$ are to a training parameter combinations $P$ [34].
Based on the base sampling plan an initial version of the GPR-SG is trained, the prediction accuracy of which is subsequently assessed through the normalized root mean square (RMS) prediction error $\epsilon_{RMS}$ with respect to a dedicated test data set $\mathcal{P}_{Test}$. In the present context, no dedicated validation data set is utilized, due to the automatic

regularization properties of GPR.

The second step of the sampling strategy consists of adaptively adding sampling points to the training data set $P$ until $\epsilon_{RMS}$ falls below a user-specified threshold. To do so, an adaptive sampling strategy built upon the estimated mean squared error (MSE) of the GP is utilized, as described e.g. in [62]. Given the training parameters $P$, the estimated MSE $\hat{s}^2(\boldsymbol{p}^*)$ at parameter combination $\boldsymbol{p}^*$ reads [34]:

$$\hat{s}^2(\boldsymbol{p}^*) = \sigma^2 \left(1 - \boldsymbol{\psi}^{\mathrm{T}} \Psi^{-1} \boldsymbol{\psi} + \frac{1 - \mathbf{1}^{\mathrm{T}} \Psi^{-1} \boldsymbol{\psi}}{\mathbf{1}^{\mathrm{T}} \Psi^{-1} \mathbf{1}}\right) \tag{5.11}$$

where the training point parameters $P$ and the entries of $\boldsymbol{\theta}$ are contained in the correlation matrix $\Psi$ and correlation vector $\boldsymbol{\psi}$:

$$\Psi = \frac{\mathrm{cov}(P,P)}{\sigma^2} \in \mathbb{R}^{n_{SP} \times n_{SP}} \qquad \text{and} \qquad \boldsymbol{\psi} = \frac{\mathrm{cov}(P,\boldsymbol{p}^*)}{\sigma^2} \in \mathbb{R}^{n_{SP} \times 1} \tag{5.12}$$

Utilizing Eq. 5.11, the parameter combination $\boldsymbol{p}^*$ with the largest estimated MSE is chosen as the next sampling point $\boldsymbol{p}_{adapt}$ to be added to $P$, that is, a corresponding numerical simulation is run for $\boldsymbol{p}_{adapt} = \arg\max(\hat{s}^2(P^*))$. To run simulations for multiple sampling points in parallel, batches of ten parameter combinations $\boldsymbol{p}_{adapt}$ are successively computed from Eq. 5.11, by assuming the output of the GPR-SG at the parameter combination $\boldsymbol{p}_{adapt}$, still to be computed, forming part of the training data set and recomputing the corresponding maximum estimated MSE.

From a practical viewpoint, the implementation of the GPR-SG is performed in Python, making use of the GPR implemented in the Python module scikit-learn [84]. Attention should be paid when computing the inverse of the correlation matrix $\Psi$ in Eq. 5.11, which becomes computationally expensive when considering a large number of sampling points $n_{SP}$. For this purpose, the Cholesky decomposition implemented in the Python module SciPy [133] is employed.

Within the present work, the cut-off condition for adding adaptive sampling points is set to $\epsilon_{RMS} < 5 \cdot 10^{-3}$. As depicted in the left panel of Fig. 5.5 for the later used prediction parameter space $\mathcal{P} = C_L \times \delta_{ADHF} \times H = [0.4,0.6] \times [-2°,4°] \times [33000\text{ ft},39000\text{ ft}]$, the adaptive sampling strategy tends to fill the gaps contained within the LHS, especially orientating itself towards the borders of $\mathcal{P}$. This behavior is typical for a mainly explorative sampling strategy, and similar results could be achieved by just employing a larger initial sampling plan. Nevertheless, the method employed here is computationally more efficient, since it is difficult to estimate a priori which number of samples suffices to reach a specific $\epsilon_{RMS}$ threshold.

This is reflected in the development of the associated RMSE with increasing sample size, depicted in the mid panel of Fig. 5.5. Starting with a sample size of $n_{SP} = 50$ determined via LHS, the addition of four samples is sufficient to achieve $\epsilon_{RMS} < 5 \cdot 10^{-3}$. To link to the above-mentioned aspect considering the base sampling plan size, already the inclusion of $n_{SP} = 20$ leads to $\epsilon_{RMS}$ falling below $10^{-2}$, regardless of the fact that extracting a subset of sampling points from an LHS plan does not mean the subset is also optimally space-filling. This becomes clear when considering the right panel of Fig. 5.5, where the error distribution at $n_{SP} = 20$ is marked by the influence of outliers, naturally depending on the position of the sampling parameters with respect to the test set parameters. This indicates that the size of the initial sampling plan could be reduced, nevertheless, this depends on the problem at hand, as well as the structure of the test set (in this case full factorial) and the distance of the test set sampling points to the training points, for which utilization of an adaptive strategy in connection with a base strategy is more advantageous than simply increasing the base sample size. In the present case, the inclusion of the full training set of $n_{SP} = 54$ results in a zero-centered error density distribution concerning a full factorial test data set.

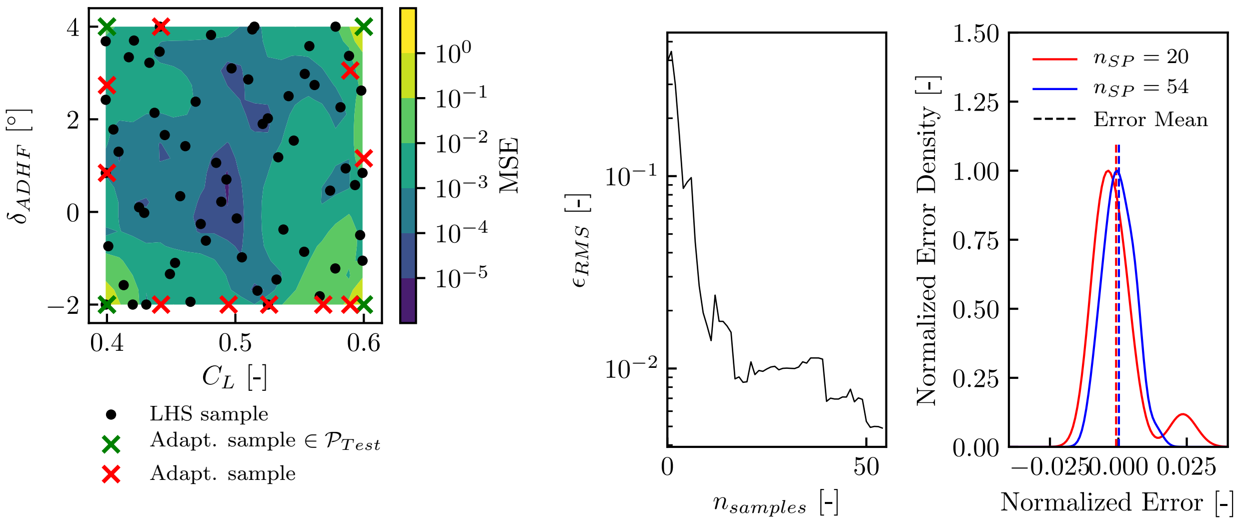


Figure 5.5: Left panel: Contour plot of the estimated MSE for a $C_L$ - $\delta_{ADHF}$ parameter plane, with additional projection of the base sampling points from the LHS strategy (black). Red crosses mark the positions of adaptively added samples, green crosses the positions of adaptively added samples that are part of the test data set and are therefore excluded from the adaptively added training points. Mid panel: Development of the normalized root mean square error $\epsilon_{RMS}$ of the predictions of the GPR-SG at the test points with respect to increasing sample size $n_{SP}$. Right panel: Error density distribution of model predictions with two different sample sizes of $n_{SP} = 20$ and $n_{SP} = 54$, alongside the corresponding prediction error mean. Adapted from [58].

The training data set of the GPR-SG optimally lends itself to the construction of the POD-ROM. An advantage inherent in the successive construction of both models is the surface data required to perform the POD being readily available from the computations to determine the training data (e.g. $C_D$) for construction of the GPR-SG. In addition, the LHS with an adaptive sampling strategy guarantees the sampled surface solutions possessing optimal space-filling properties concerning the envisaged prediction parameter space $\mathcal{P}$. One might also opt to exchange the sampling strategy underlying the

GPR-SG, for which performing an abstraction step upstream of the POD-ROM is advantageous in any case considering the formulation of a training data set.
The implementation of the POD-ROM is again performed in Python, utilizing standard linear algebra functions included in the Python module SciPy [133]. Utilizing the above-mentioned training data set used for conditioning the GPR-SG, the inclusion of $m_{POD} = 47$ POD modes suffices to fulfill the RIC criterion introduced in Eq. 5.9, see Fig. 5.6 for a corresponding overview.

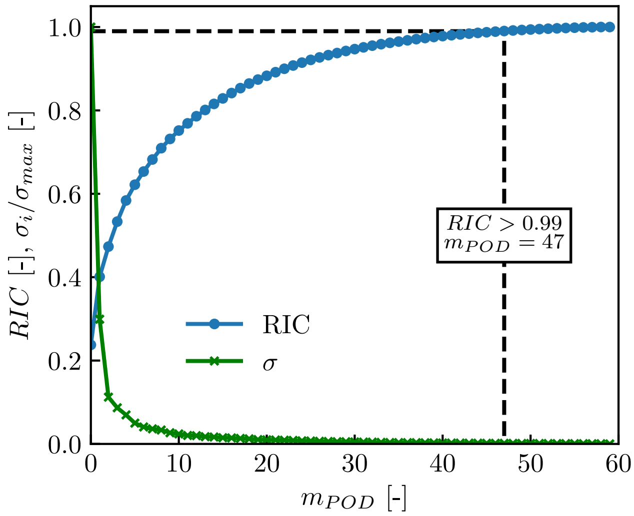


Figure 5.6: Relative information content of POD basis with an increasing number of modes $m_{POD}$, alongside the development of the normalized singular values $\sigma_i$. Adapted from [57].

## 5.4 Application Case

As already outlined in the previous sections, the main application case of the GPR-SG foresees parametrical prediction of the drag coefficient $C_D$, while the POD-ROM is used in the context of parametric predictions for surface pressure coefficient distributions, alongside associated aerodynamic loads. Model results are presented for the isolated wing case CATeW-02 in the following, a summary of the foreseen input parameters and prediction parameter spaces $\mathcal{P}$ is presented in Tab. 5.1. For generation of the training data sets, the automated Python toolchain presented in Sec. 2.3 is used. As indicated in Tab. 5.1, the results presented in the following use the LCTM-based transition prediction method at a constant suction coefficient. Due to the modularity of the toolchain, as well as the GPR-SG and POD-ROM, training data sets can be constructed with any of the transition prediction frameworks utilized so far within this thesis, just as expansion to wing-body + HTP level for future applications.

Table 5.1: Input parameter space for the GPR-SG and POD-ROM.

| Parameter | Value | Comment |
|---|---|---|
| $C_L$ | $[0.4; 0.6]$ | Cruise $C_L = 0.5 \pm 0.1$ |
| $\delta_{ADHF}$ | $[-2°; 4°]$ | Flap-gap free deflection angles of the ADHF |
| $H$ | $[33\ 000\ \text{ft}; 39\ 000\ \text{ft}]$ | Resulting in $\text{Re} \approx [36.9; 28.8] \cdot 10^6$ at $Ma_{cr}$ |
| $C_q$ | $-12 \cdot 10^{-4}$ | Maximum extent of laminar flow predicted with $\gamma - \text{Re}_\theta$+CF model (cf. Sec. 3.3.2.1) |
| Ma | 0.83 | Design cruise Mach number |

### 5.4.1 Surrogate Model Results

A drag coefficient response surface predicted through the GPR-SG, extracted for an altitude of $H = 35\ 000$ ft under variation of the lift coefficient $C_L$ and ADHF deflection angle $\delta_{ADHF}$ is shown in Fig. 5.7. As described in the context of Sec. 5.3, the high quantitative agreement of the predicted drag coefficients is qualitatively reflected in the response surface predicted by the model when comparing it to the test data set, marked by the black circles in Fig. 5.7.

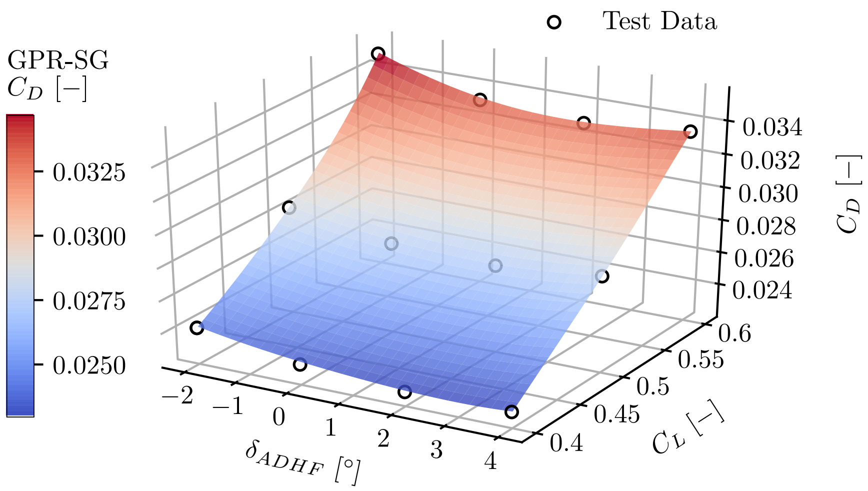


Figure 5.7: Predicted drag coefficients $C_D$ at $H = 35\ 000$ ft for varying ADHF deflection angles $\delta_{ADHF}$ and lift coefficients $C_L$, alongside corresponding results of the test set. Adapted from [58].

Using the log marginal likelihood approach sketched in Eq. 5.7, results in an optimized hyper-parameter set of $\boldsymbol{\theta} = [\sigma_f^2, \ell_i] = [0.00551^2, 0.459, 0.872, 60.6]$, regarding normalized model outputs. From the entries of $\boldsymbol{\theta}$ the predictive behavior of the model can be directly interpreted. As introduced in the context of hyper-parameter variations (cf. Fig. 5.3), the signal variance $\sigma_f^2$ is connected to the standard deviation of the function $\sigma_f$,

determining the amplitude of the predicted response surface. The length-scale parameters $\ell_1$ to $\ell_3$ determine the rate of correlation in the respective parameter dimension, i.e. a short length-scale is connected to rapid changes in the corresponding parameter dimension, as opposed to a long length-scale indicating little or slow changes in the corresponding parameter dimension. In line with the analyses presented in Chaps. 3 and 4, the model therefore correctly associates the highest sensitivity of $C_D$ to variations in $C_L$ ($\ell_1$), a reduced influence of the ADHF deflection angle $\delta_{ADHF}$ ($\ell_2$) on $C_D$, while the flight altitude $H$ shows only small effects upon the predicted drag coefficient $C_D$.
Next to the physical interpretability of the hyper-parameters, the SE-Kernel offers the advantage of being infinitely differentiable. Therefore, the trained GPR-SG, in addition to the regression of unknown function values $C_D$, can also be used in closed form for regressing partial derivatives of the response surface. The latter are of high importance when it comes to sensitivity analyses in an aerodynamic context, or embedding the GPR-SG into an optimization task.
For this purpose, it is convenient to rewrite the predictive equation (Eq. 5.5) of the GP in the form of the linear combination [91]:

$$f(P^*) = \mathbb{E}(f(P^*)|P^*,P,f(P)) = \sum_{i=1}^{n_{SP}} \alpha_i k(\boldsymbol{p}_i,\boldsymbol{p}^*) \tag{5.13}$$

where $\boldsymbol{\alpha} = K(P,P)^{-1}f(P)$.
As differentiation is a linear operator, the expected value of the gradient of $f(\boldsymbol{p}^*)$ can be written as [73]:

$$\mathbb{E}(\nabla f(\boldsymbol{p}^*)|\boldsymbol{p}^*,P,f(P)) = \nabla\mathbb{E}(f(\boldsymbol{p}^*)|\boldsymbol{p}^*,P,f(P)) = \sum_{i=1}^{n_{SP}} \alpha_i \nabla k(\boldsymbol{p}_i,\boldsymbol{p}^*) \tag{5.14}$$

Therefore, only the gradient of the SE-Kernel is required, as $\alpha_i$ does not depend on $\boldsymbol{p}^*$. Predicted derivatives for the response surface presented in Fig. 5.7 are displayed in Fig. 5.8, considering $\frac{\partial C_D}{\partial C_L}$ in the left panel, while $\frac{\partial C_D}{\partial \delta_{ADHF}}$ is shown on the right hand side.
With respect to $\frac{\partial C_D}{\partial C_L}$, the typical course of the Lilienthal-polar is reflected in the corresponding derivative values, i.e. the value of the gradient increases with increasing $C_L$. A variation in the parameter dimension $\delta_{ADHF}$ attributes a diminishing sensitivity of $C_D$ to $C_L$ variations, the lowest sensitivity connected to an ADHF deflection angle of $\delta_{ADHF} = 4°$.
The predicted optimal flap deflection angle $\delta_{ADHF}$ connected to the lowest drag coefficient $C_D$ can be directly extracted from the zero iso-line contained in the $C_{D\delta}$ derivative plot (right panel Fig. 5.8). In line with the results presented in Sec. 3.3.2.1, the optimal flap deflection angle for the isolated wing case lies within the range of $\delta_{ADHF} \approx 2°$, for the here presented variation in $C_L$ possessing the limit values $\delta_{ADHF} = [1.4°; 2.7°]$ with regard to the optimal flap deflection angle.

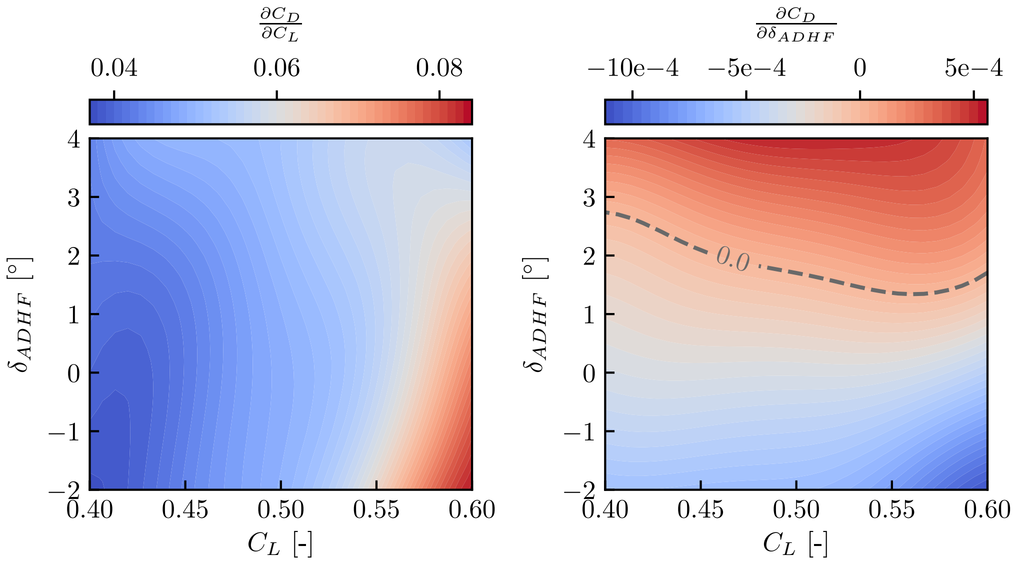


Figure 5.8: Predicted partial derivatives by means of the trained GPR-SG. Adapted from [58].

### 5.4.2 Reduced Order Model Results

Building upon the data set derived for training the GPR-SG, an exemplary result of the POD-based ROM in terms of predicted pressure coefficient $c_p$ distributions at the test set parameter combination $\boldsymbol{p}^* = [0.5, 0°, 35\ 000\ \text{ft}]$ compared to the CFD (surface) solution is presented in Fig. 5.9.

Focusing on the contour plots first, both qualitative as well as quantitative agreement between CFD solution and ROM prediction is observable. This aspect is especially challenging when considering non-linear aerodynamic phenomena, in this case the structure and position of the shock wave, as well as the weak lambda shock structure developing in inboard stations of CATeW-02. Consequently, these regions are also associated with the largest prediction errors, as displayed by means of the squared-error $\epsilon_{SE}$ contour on the right hand side of Fig. 5.9.

The assessment is expanded for consideration of different ADHF deflection angles in the $c_p$ slices extracted for three spanwise stations in the bottom panels of Fig. 5.9. Solid lines depict the streamwise $c_p$ distributions for three ADHF deflection angles computed via CFD, whereas the dashed lines are extracted from the corresponding ROM predictions. Near-perfect agreement between simulation and prediction is obtained on the pressure side of the wing, as well as on the suction side when considering chordwise stations out of the shock region. With respect to the latter, VC implications on the development of the pressure coefficient distribution and especially the shock (cf. Sec. 3.2.2) are correctly reflected. To summarize, these consist of a downstream shift of the shock position with increasing ADHF deflection angle, while due to the increasing shock strength at constant $C_L$ the suction peak at the wing leading edge decreases and, consequently, a prolongation of negative pressure gradient flow is achieved. To connect to

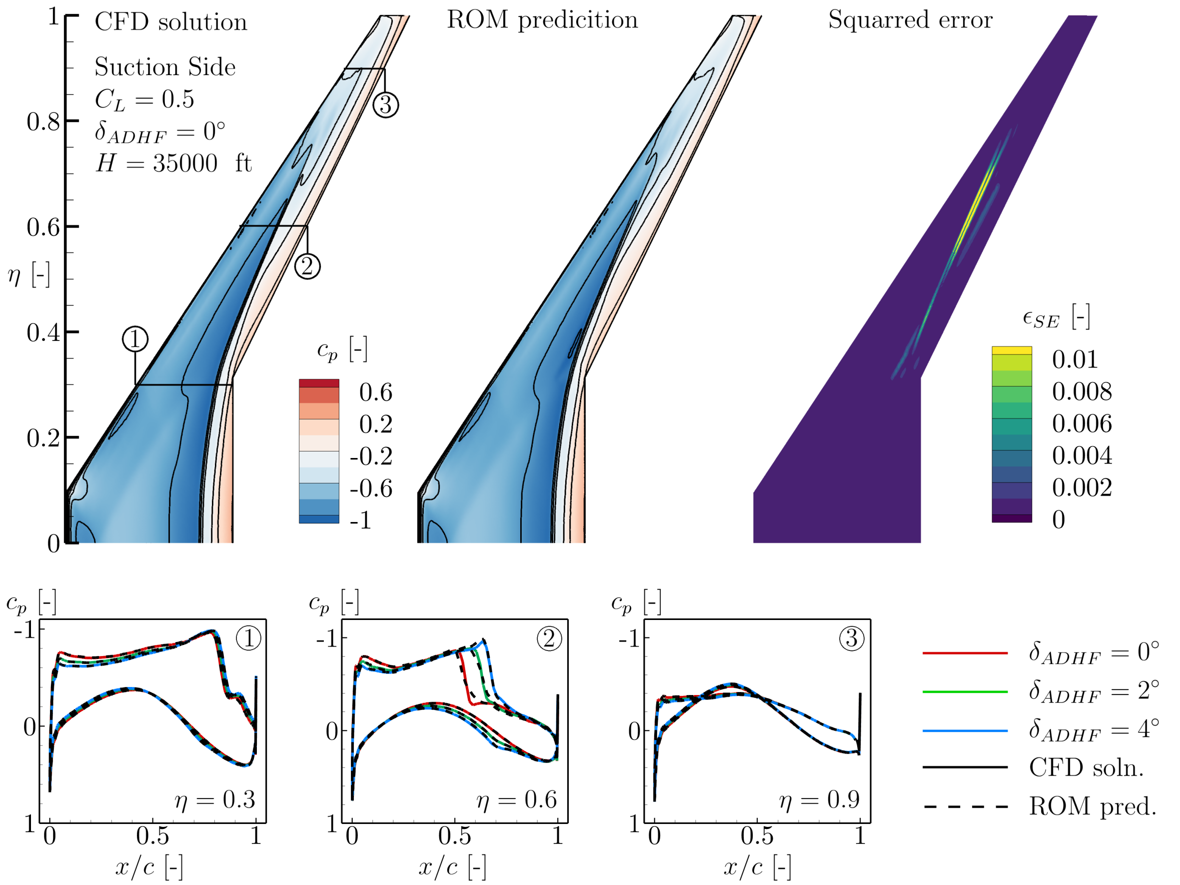


Figure 5.9: Predicted partial derivatives by means of the trained GPR-SG. Adapted from [57].

the above-mentioned discrepancies in predicted pressure coefficient distributions in the region of the shock, these differences are mainly attributed to the length of the shock. The POD-ROM acts in diffusing the shock over a larger extent of the chord, i.e. the shock appears to be stretched when compared to the CFD solution. This behavior is connected to the assumption of linearity inherent to the POD. It is hardly possible to exactly predict highly non-linear aerodynamic phenomena by linear superposition of the POD modes according to interpolated POD coefficients. Nevertheless, regarding the possibility for near real-time applicability of the method and the accuracy requirements connected to application within a LowFi-toolchain, the results are satisfactory.
The pressure loads readily available through the predicted $c_p$ distributions can be further expanded by their tangential complements to determine the spanwise aerodynamic loads acting upon the reference wing CATeW-02, as exemplarily depicted for the courses of the normalized aerodynamic lift loads $C_l \cdot c_{loc}/c_{ref}$ and local lift coefficients $C_l$ in Fig. 5.10. To determine the corresponding courses, the pressure coefficient distributions are expanded for the shear force components on the surface of the wing and correspondingly integrated in $x$- and $z$-directions of the body-fixed coordinate system. Transferring the components from the body-fixed coordinate system to the aerodynamic coordinate

system requires prediction of the corresponding angle of attack as a function of the sweep/prediction parameters $\alpha(\boldsymbol{p})$ with $\boldsymbol{p} = [C_L, \delta_{ADHF}, H]$. For this purpose, before application of the POD-ROM in load prediction mode an intermediate GPR-SG step is taken based upon the training data set, used for parametric prediction of the corresponding angles of attack $\alpha$ for the queried parameter combination $\boldsymbol{p}^*$.

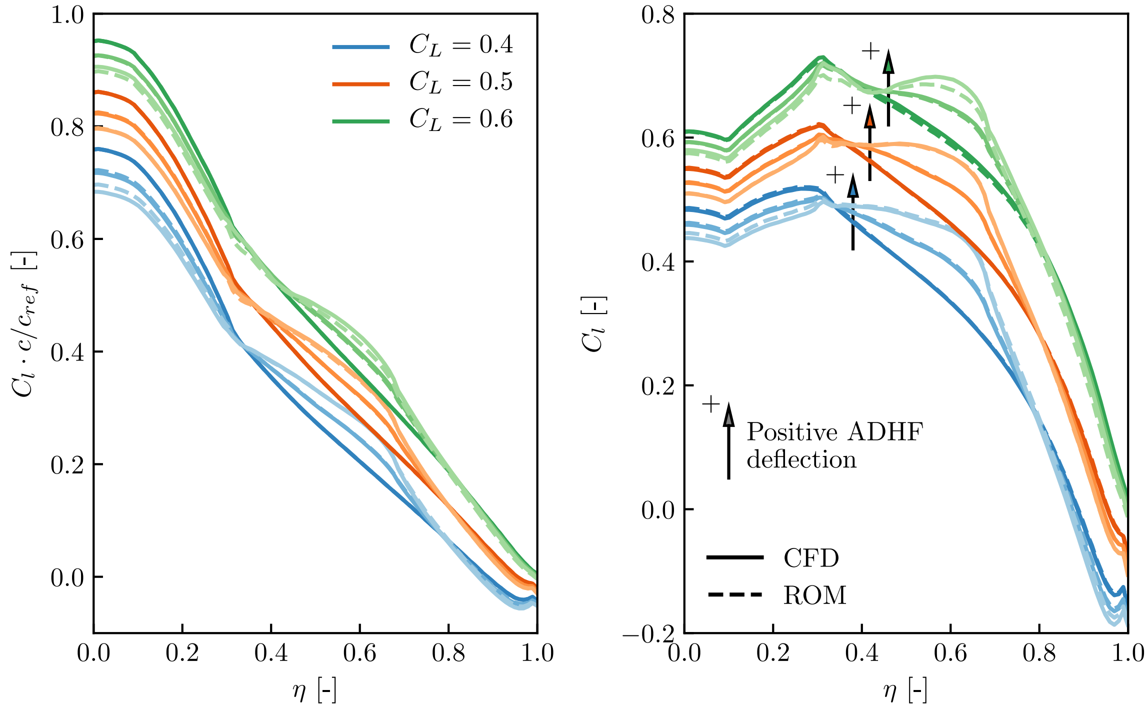


Figure 5.10: Aerodynamic loads (left panel) and local lift coefficients (right panel) predicted by the POD-ROM (dashed lines) in comparison to CFD solutions (solid lines) for test set parameter combinations. The distributions are extracted for varying ADHF deflection angles, per lift coefficient comprising $\delta_{ADHF} = 0°$ as the baseline case, increasing to $\delta_{ADHF} = 2°$ and $4°$ in the direction of the arrow $\uparrow$. Extracted at $H = 35\,000$ ft for $C_L = [0.4; 0.5; 0.6]$. Adapted from [57].

In line with the potential and limitations of the POD-ROM indicated above, the load and $C_l$ distributions depicted in Fig. 5.10 show corresponding sensitivities to the locations of the queried prediction parameters $\boldsymbol{p}^*$ with respect to the parameter space $\mathcal{P}$. High agreement between load distributions extracted from the CFD test data set (solid lines) to the distributions predicted via the ROM (dashed lines) is especially attributed to the lower range of lift coefficients $C_L = 0.4$ and $0.5$, for all included ADHF deflection angles. The shift in loads due to ADHF deflection is present throughout all cases, nevertheless underestimated for the combination of $C_L = 0.6$ with the highest flap deflection angle of $\delta_{ADHF} = 4°$, which can again be attributed to non-linear phenomena playing a major role in cases of high local loads, next to the sampling point being drawn from the boundary of the envisaged sampling parameter space $\mathcal{P}$, requiring the POD-ROM to extrapolate from the training data set when predicting loads for such parameter combinations.

### 5.4.3 Comparison to Low-Fidelity Results

To return to the aspect described in Sec. 5.2, the goal of both GPR-SG and POD-ROM ultimately consists of enhancing the results of a lower fidelity method. Therefore, this section concludes the present chapter with an exemplary integration of both modeling approaches into a representative LowFi aerodynamic toolchain, i.e. outlining the potential of the modeling approaches when integrated as presented in Fig. 5.1.

As a representative LowFi toolchain, the previously mentioned aerodynamic module of the OAD framework MICADO is employed. In the present case, the LowFi method builds upon a pre-computed aerodynamic database, utilizing the multi-lifting-line code LIFTING_LINE [49] in connection with a 2.5D method built around the two-dimensional Euler-solver MSES [22]. For the integration of HLFC and corresponding transition prediction, the same approach used in the HiFi analyses is used within MICADO, i.e. linear stability theory in connection with the two-$N$-factor method implemented in the COCO/LILO framework (cf. Sec. 2.2.2.2). For a comprehensive overview of the workings of the corresponding toolchain the reader may refer to [102,116] or concerning the multi-fidelity analyses presented here to [57].

Total aircraft drag coefficients $C_{D,total}$ computed with the LowFi method are compared to drag predictions enhanced through the application of the GPR-SG in the right panel of Fig. 5.11. The GPR-SG acts to replace the drag contribution of the wetted wing surface, i.e. drag contributions of fuselage and empennage are summed to the prediction of the GPR-SG for determination of $C_{D,total}$.

The isolated LowFi method tends to predict lower overall drag coefficients when compared to the GPR-SG integrated version throughout the entire investigated parameter envelope. The (normalized) differences amount from 7% to 14%, increasing with higher ADHF deflection angles. For the present case, the difference shows its highest sensitivity in the direction of the ADHF deflection angle, that is, throughout $C_L$ variations, the differences between both modeling approaches are approximately constant. Thus, the enhancement of the LowFi toolchain with the CFD-based GPR-SG results, in this case, acts in correcting the isolated LowFi results with respect to their absolute values. Both methods agree well regarding the predicted sensitivities towards the development of the drag coefficient concerning ADHF deflection angles, deviations are only observable in the LowFi method predicting a higher variation range in $C_{D,total}$.

A decisive advantage of enhancing the LowFi toolchain with the GPR-SG is reflected when considering the $C_L$ range for which drag coefficients are predicted. The polars based solely on the LowFi method are all shorter in the direction of increasing $C_L$, thus not reaching the envisaged maximal lift coefficient of $C_L = 0.6$. This is connected to limitations of the 2.5D methodology, namely the maximum lift of the underlying two-dimensional airfoil not reaching the locally required magnitude requested by the spanwise $C_l$ distribution [56]. Whilst the LowFi methodology incorporates approaches for extrapolating local, two-dimensional polars above the maximum $C_L$ computed by

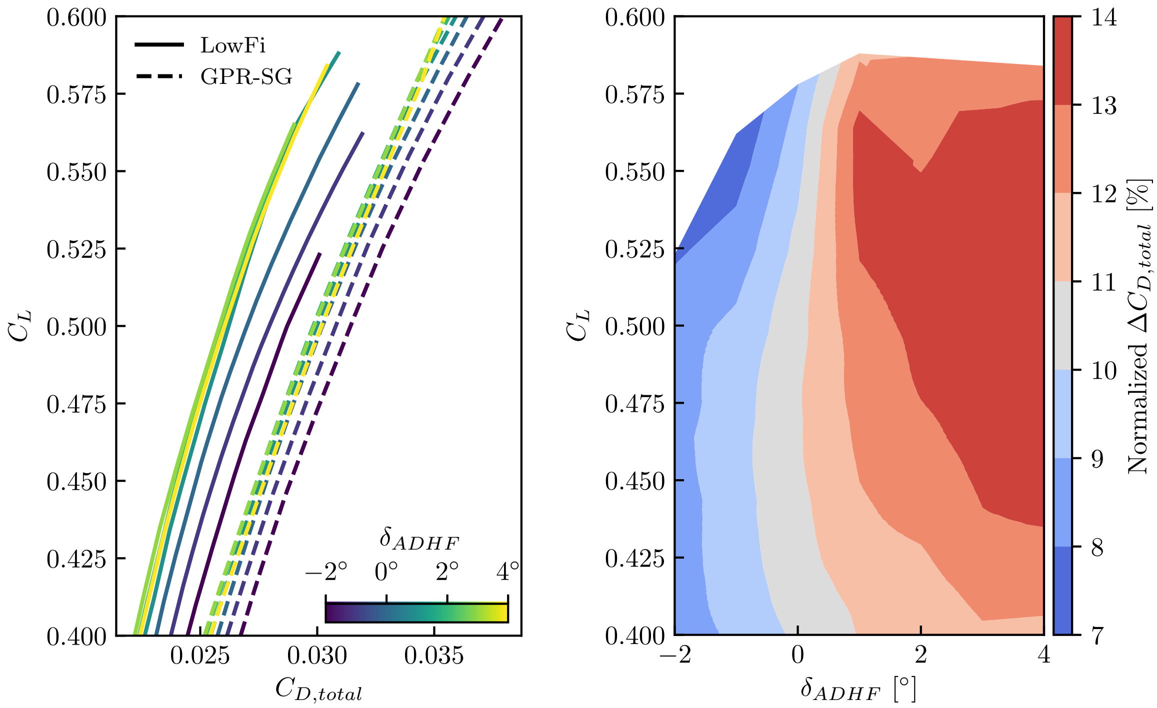


Figure 5.11: Left panel: Aircraft polars resulting from the LowFi method in comparison to predictions of the GPR-SG for varying ADHF deflection angles $\delta_{ADHF}$. Right panel: Normalized difference in GPR-SG and LowFi aircraft drag coefficients $\Delta C_{D,total}$ for varying $C_L$ and $\delta_{ADHF}$. Extracted for $Ma = 0.83$, $H = 35\ 000$ ft, adapted from [57].

MSES, the associated uncertainty is naturally high and effectively counteracted by the incorporation of the surrogate model.

The second integration example is directed towards the POD-ROM, and in this context, utilizing pressure coefficient distributions predicted by the latter for transition prediction. Pressure coefficient distributions utilized within the LowFi method in comparison to POD-ROM predictions on the suction side of the wing are depicted in Fig. 5.12, alongside the development of $N_{TS}$ and $N_{CF}$ and predicted transition positions. In line with the workings of the LowFi toolchain, the pressure coefficient distributions are extracted at two spanwise locations, $\eta = 0.313$ and 0.68, from the predicted surface distribution, incorporating the ADHF deflection angles $\delta_{ADHF} = 0°$ and 2°.

Considering the pressure coefficient distributions predicted by both methods first, deviations between the predicted pressure coefficient distributions are evident. Especially at the spanwise position $\eta = 0.313$ (inboard ADHF limit), marked differences arise in the magnitude of the suction peak as well as shock position, connected to which the pressure coefficient distributions and the associated gradients vary between both methods. However, considering the highly three-dimensional flow field at the near-kink station $\eta = 0.313$ (c.f. Fig. 3.3), discrepancies are to be expected. At the spanwise station $\eta = 0.68$ (outboard ADHF limit), the suction peak is comparably captured between

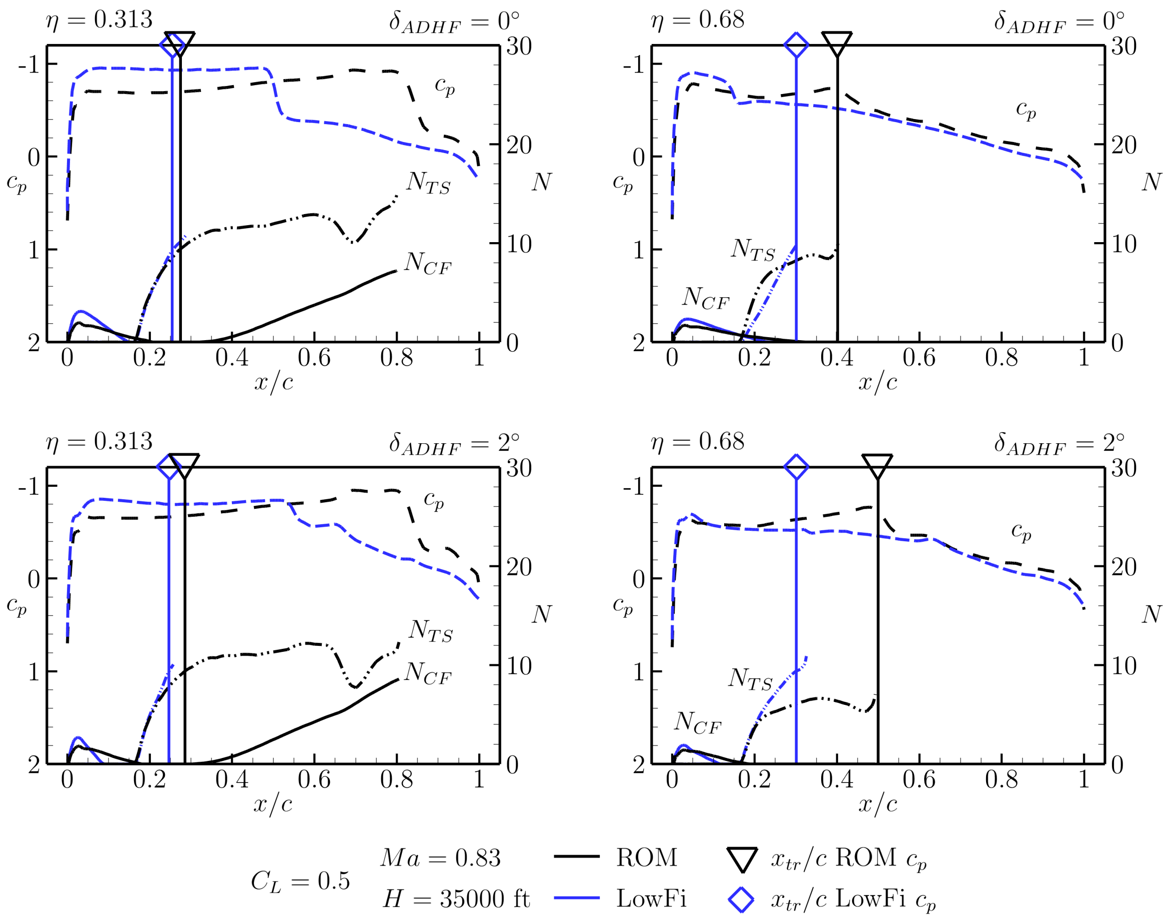


Figure 5.12: Pressure coefficient distributions, $N_{TS}$ and $N_{CF}$ factors alongside resulting transition positions computed with pressure coefficient distributions stemming from the LowFi toolchain and the POD-ROM at $\eta = 0.313$ and 0.68 for $\delta_{ADHF} = 0°$ and 2°. $C_L = 0.5$, $Ma = 0.83$, $H = 35\,000$ ft and $C_q = -12 \cdot 10^{-4}$, adapted from [57].

both methods, as well as the magnitude and gradient of the predicted pressure coefficient. Differences arise concerning the shock, the LowFi method predicting shock-free recompression, whereas the POD-ROM reflects the development of a weak shock in the mid-chord region. Correspondingly, the downstream shift and consequent increase in the extent of negative pressure gradient flow with downward deflection of the ADHF is not captured by the LowFi method.

Feeding the pressure coefficient distributions predicted by both methods into the two-$N$-factor transition prediction framework[3] formed by COCO/LILO (c.f. Sec. 2.2.2.2) showcases the enhancement potential connected to the POD-ROM for the present application case.

Whilst considerable differences in the pressure coefficient distributions arise at $\eta = 0.313$, the predicted transition positions coincide between both methods for both presented ADHF deflection angles. This is connected to the suction sufficiently damping CF-waves

[3] The present calculations use $C_q = -12 \cdot 10^{-4}$ and constant critical $N$-factors of $N_{CF,crit} = 7.5$ and $N_{TS,crit} = 9$, i.e. no interaction of TS- and CF-waves is modeled in this case.

upstream of the front spar, while the pressure gradient in the corresponding region leads to comparable amplification of TS-waves in both cases. As described earlier (c.f. Sec. 3.2.2), the implications of VC integration primarily manifest themselves in outboard wing stations, for which deflection of the ADHF does not majorly impact the development of the pressure coefficient distribution and therefore the extent of laminar flow at $\eta = 0.313$.

In contrast, the differences in $c_p$ distributions resulting at $\eta = 0.68$ result in larger variations concerning the predicted transition positions. Driven by the gradient of the $c_p$ distribution, $N_{TS}$ factors computed from the isolated LowFi method reach the critical boundary at $x_{tr}/c \approx 0.29$, both for the clean ($\delta_{ADHF} = 0°$) and the deflected case ($\delta_{ADHF} = 2°$). Utilizing the $c_p$ distribution predicted by the POD-ROM results in a more downstream transition position already for the baseline case $\delta_{ADHF} = 0°$ at $x_{tr}/c \approx 0.4$, whilst the reduction in $N_{TS}$ factors attributed to the implications of VC integration discussed in Sec. 3.3.1 are correctly reflected by the POD-ROM. This results in a downstream shift in transition position to $x_{tr}/c \approx 0.5$.

To conclude on the herein presented application and comparison case CATeW-02, the integration of a GPR-based surrogate as well as the POD for the derivation of a ROM are highly suitable for accuracy enhancement of an otherwise solely LowFi-based OAD toolchain. The potential especially manifests itself in case of high flow complexity, which is a natural limitation of a LowFi toolchain and the main motivation for the derivation of SG/ROM approaches in an aerodynamic context. Nevertheless, a substantial amount of computational effort is still required to train the models, for which initial design room screening and optimization is still most effectively performed on LowFi level. The SG and POD models are most effectively introduced as an intermediate step before detailed analysis only based on HiFi methods.

An attractive aspect not covered here is the possibility of employing SG/ROMs for the calibration of transformation rules typically incorporated in 2.5D LowFi aerodynamic toolchains. The advantage of the models lies in the reliable representation of complex flow phenomena for large parameter spaces, for which they are ideally suited for the generalization of correction techniques or recalibration of the above-mentioned transformation rules. This aspect is shown by Effing et al. [29], where transformation rules for $c_p$ distributions incorporated in the aerodynamic module of MICADO are recalibrated based on pointwise HiFi solutions. This approach can be further generalized in future work, when utilizing models such as the herein-presented GPR-SG or POD-ROM for efficient and highly accurate representation of aerodynamic data sets in large parameter spaces.

## 5.5 Synthesis

Within the present chapter, two different approaches for the derivation of a surrogate (SG) and a reduced order model (ROM) for efficient aerodynamic data set representation were presented and applied to the case CATeW-02 wing. The goal of deriving such models consists of efficiently integrating computationally expensive high-fidelity (HiFi) data sets (Chaps. 3 and 4) into lower fidelity toolchains, in the present case, the aerodynamic module of MICADO.

The main aerodynamic output required for mission analysis and overall aircraft design is the drag coefficient associated with a specific configuration, as a function of different input parameters stemming from the operating point and the geometry of the aircraft. In line with the previously presented parameter studies, an SG model based on Gaussian Process Regression (GPR) has been derived and applied for parametric drag coefficient prediction of the CATeW-02 wing based on the input parameters lift coefficient, flight altitude and ADHF deflection angle. A pictorial summary of the advantages associated with such a model approach is presented in Fig. 5.13. High-fidelity CFD data is typically only available on a coarse grid considering its parametric resolution. Therefore, a highly accurate representation of absolute values, in this case, the drag coefficient $C_D$, and sensitivities of the predicted values with respect to the parameter dimensions of interest enable analyses and optimizations on system level.

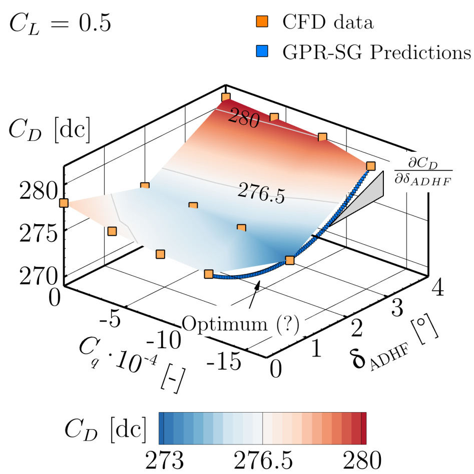


Figure 5.13: Comparison of solely CFD-based analysis (c.f. Fig. 3.12) with the potential opened by the surrogate model.

Furthermore, intended for later calibration of transformation rules present in a typical 2.5D aerodynamic low-fidelity (LowFi) toolchain and, in general, a lower abstraction of aerodynamic correlations within the model output, a ROM based on Proper Orthogonal Decomposition (POD) is additionally presented and applied for the corresponding input parameters with the goal of predicting surface distributions of e.g. the pressure coefficient $c_p$.

Comparison of both GPR-SG, as well as POD-ROM predictions to a dedicated HiFi test data set, assesses high prediction accuracy throughout the entire envisaged parameter space. The previously discussed synergistic behavior of the HLFC/VC technology coupling is correctly reflected in the model outputs. Furthermore, a comparison to representative results of a LowFi aerodynamic toolchain indicates the potential for accuracy enhancement and calibration offered by both the GPR-SG and the POD-ROM, making them attractive tools for efficient data exploitation towards the incorporation of HiFi data to LowFi computational frameworks.

# 6 Conclusions and Outlook

This thesis analyzed the coupled application of two of the most promising technologies for drag reduction of future transport aircraft, hybrid laminar flow control (HLFC) and the integration of variable camber (VC) to the aircraft wing. The primary motivation for coupling these technologies lies in their synergistic potential. Synergy is defined as the benefit of simultaneously employing HLFC and VC surpassing the drag reduction associated with both technologies applied in isolation (c.f. Chap. 1).
In the context of the theoretical background on which this thesis builds (Chap. 2), the driver for the synergistic potential was further specified. HLFC targets to suppress transition due to cross-flow instabilities (CFI) in the leading edge region of the wing through boundary layer suction, whilst the most dominant transition mechanism in the mid-chord region of the wing, Tollmien-Schlichting instabilities (TSI), can be effectively suppressed by ensuring an adequate pressure gradient in the corresponding wing section. The latter is highly sensitive to the employed airfoil geometry, which can be adjusted to meet the specific requirements of each mission segment using VC. A practical and robust solution for VC integration is achieved through the multi-functional use of already existing trailing edge devices, with an adaptive dropped hinge flap (ADHF) being selected for VC integration in this thesis.
Since the present investigations focus on assessing a laminar flow wing, a central requirement consists of predicting and incorporating transition to the computational fluid dynamics (CFD) framework. In this context, Chap. 2 introduces two different techniques. The first method is based on a linear stability analysis of boundary layer profiles in conjunction with a semi-empirical transition prediction method, the two-$N$-factor method. The second approach belongs to the domain of local-correlation based transition models, specifically the $\gamma - Re_\theta$+CF model. Both techniques are largely automated and integrated with the DLR TAU code, the state-of-the-art finite volume CFD solver used throughout this thesis. However, a framework for automated, parametrical studies of the technology coupling with both transition prediction tools was not available. Therefore, this framework was derived and implemented in the course of this thesis, foreseeing an efficient mapping of VC technology onto the wing through mesh deformations alongside an iterative routine to prescribe variable suction distributions to the surface grid of the wing.
To build a foundation for analyzing synergy and possible trade-offs when coupling HLFC and VC, Chap. 3 dealt with applying the technology coupling to the wing of the representative transonic transport configuration CATeW-02. Initially, implications of VC integration to the trailing edge considering the development of the pressure distribution were discussed. These analyses attributed beneficial (in the sense of HLFC) properties to a camber increase, i.e., deflecting the ADHF downwards ($\delta_{ADHF} \uparrow$). At fixed lift coefficient, the necessary angle of attack decreases, which in turn is connected to a decrease

in the suction peak at the wing leading edge and a downstream shift of the shock position. The latter two aspects are critical when it comes to the coupled application with an HLFC system since they lead to a prolongation of the flow extent with a negative pressure gradient, alongside a decrease in the magnitude of the gradient itself. Utilizing the linear stability theory (LST) based analysis framework, both aspects were shown to stabilize the flow concerning TSI. Considering CFI, however, the opposite behavior was reflected in the results. Therefore, to foster synergistic effects, it is essential to apply sufficient suction in the leading edge region of the wing to ensure the boundary layer is adequately stabilized with regard to CFI, so that the unfavorable effect of VC deployment on CFI is over-proportionally counteracted by the stabilization of TSI.
For the remainder of Chap. 3, the effect of suction was included into the analyses. For this purpose, four different suction strengths in combination with ADHF deflection angles ranging from $\delta_{ADHF} = -2°$ to $4°$ were investigated. Utilizing the LST-based transition prediction framework reflected the intended synergistic behavior of the technology coupling, where multiple synergistic effects could be deducted. Regarding the associated drag reduction, these effects were categorized to:

- Primary synergy effect: When assuring sufficient suction to suppress CFI, VC integration leads to an over-proportional reduction in TS-wave amplification, shifting the transition front downstream for otherwise TSI-triggered cases. Furthermore, when suction suffices to suppress both instability mechanisms and the transition position is determined by the shock position, the resulting downstream shift in shock position connected to an ADHF deployment consequently leads to a downstream shift in the transition position.

- Secondary synergy effect: Boundary layer suction itself and the downstream shift in transition position lead to a thinner boundary layer compared to its turbulent counterpart. Increasing suction, therefore, leads to a decrease in viscous decambering of the wing, for which in cases where a camber increase through VC is beneficial for the reduction of pressure drag, an increase in suction strength synergizes with the latter by effectively superimposing an additional camber increase to the wing.

An important aspect to note in an operational scenario regarding the technology coupling locally stabilizing the boundary layer up to the shock front (primary synergy effect) is the necessity to avoid laminar flow separation at the shock foot. The LST-based framework achieves this by setting the transition position to an upstream position of the predicted laminar separation point, ensuring the boundary layer is turbulent when the shock impinges. For future studies, an attractive approach to control and effectively reduce the shock strength is reflected through the integration of shock control bumps. This could also alleviate the increase in shock strength connected with the downstream shift through ADHF deflection, further boosting the potential for drag reduction of the

technology coupling by reducing the associated wave drag component.
Next to the analyses built around the LST-based transition prediction method, corresponding results were presented using the $\gamma - Re_\theta$+CF model for transition prediction. Therefore, the modeling framework for boundary layer suction presented in Chap. 2 was used. Coupling local-correlation based transition turbulence models to boundary layer suction is to be understood as explorative, considering that experimental data for validation is scarce, especially in conjunction with the complex three-dimensional boundary layer structure developing on swept aircraft wings. Including boundary layer suction to the numerical simulation via the suction boundary condition showed a corresponding downstream shift in transition position, however, confined to the chordwise limit of the HLFC suction panel for most of the wing span. While the secondary synergy potential defined above is reflected throughout the computations, the primary synergy potential is not predicted by this method. To further analyze the effect of the suction boundary condition on the transition turbulence model, driving correlations triggering the onset of transition were extracted from a laminar reference computation for varying suction strengths. This revealed the suction boundary condition being successful in delaying the first occurrence of transition onset further downstream. However, due to an upstream propagation of eddy viscosity production within the model transport equations, the transition position set in the CFD simulation is shifted upstream of this point. Current research in turbulence modeling is devoted to this effects, where new transition turbulence models are derived specifically for high Reynolds number, transonic wing flows, serving as a remedy for this behavior. The implemented boundary condition has shown to succeed in such local-correlation based framework, for which coupling with new models offers a promising approach for future analyses and optimizations.
The investigations performed on wing level were expanded to a higher integration level in Chap. 4 through the inclusion of the fuselage and the horizontal tailplane (HTP). A comprehensive cruise flight parameter space was covered, varying the prescribed lift coefficient, cruise Mach number and altitude. To allow for a consistent evaluation, the aircraft was simulated in a trimmed flight state, achieved by a bulk data approach for the computation of the required HTP incidence angle. The HTP was then set using the functions implemented in the automated analysis framework, namely by rigidly rotating the surface mesh of the HTP to the corresponding angle within the simulations.
In the isolated wing study conducted in Chap. 3, an ADHF deflection angle of $\delta_{ADHF} = 2°$ showed the lowest associated drag even for operation at the design point of the aircraft. This is not desirable, as a well-designed aircraft should not require geometry adaptations when flying at its design point. This finding underlines the importance of integrating the wing-only analyses into a full configuration to derive final conclusions. The integrated wing-body + HTP configuration CATeW-02-WB proved to be suitable for assessing the technology coupling, as computations without application of boundary layer suction not only showed the clean configuration operating at its lowest drag coefficient at its design point, but the configuration also exhibiting high robustness towards

operation at off-design lift coefficients. The benefit of VC integration arises when reducing the flight Mach number at a constant lift coefficient, where a downward (positive) ADHF deflection again results in an overall drag reduction. This behavior can be directly redirected toward the operating conditions where the technology coupling can be expected to yield the most significant benefit. Consistent with the wing-level analysis, VC integration positively impacts the chordwise pressure distribution towards HLFC when the ADHF is deflected downward, increasing the wing's camber. Therefore, operating points that benefit from a camber increase, in this case connected to a reduction in flight velocity or otherwise operation at higher lift coefficients, are optimally suited to exploit the synergistic effects of these technologies.

This conclusion was reinforced by including boundary layer suction into the parameter space. At the design cruise Mach number, the application of the technology coupling resulted in a downstream shift in transition position with increasing ADHF deflection angle. Nevertheless, the increase in pressure drag due to ADHF deflection outweighed the reduction in skin friction drag connected to the downstream shift in transition position. At reduced Mach numbers, both (primary and secondary) synergy effects became apparent again, for which VC integration showed to enhance the laminar performance achievable by a stand-alone HLFC system.

The results presented within this thesis provide a promising foundation for future investigations, clearly demonstrating the synergy potential inherent to an HLFC/VC coupled wing when integrated into a realistic configuration. Furthermore, necessary boundary conditions and operating scenarios in which to expect the highest benefit of the coupling were detailed. A further boost in drag reduction can be expected when developing a configuration specifically designed and optimized for the technology coupling. Within the present thesis, the HLFC/VC coupling was applied in a retrofit setting to a turbulent reference configuration. Further design and optimization variables are introduced when considering a larger number of VC integration devices, e.g. splitting the ADHF flap into multiple sub-flaps or foreseeing VC integration not only at the trailing edge of the wing but also in the leading edge or mid-chord region of the wing.

However, the extensive parameter space developing through the addition of such a manifold of design variables renders exploration and optimization tasks solely based on computationally expensive CFD simulations prohibitive. Therefore, the last chapter of this thesis (Chap. 5) is devoted to surrogate (SG) and reduced order modeling (ROM) approaches applicable for efficiently and accurately coupling results of high-fidelity CFD to an overall aircraft design (OAD) toolchain. An SG based upon Gaussian Process regression for parametric prediction of wing drag coefficients and a ROM based upon the Proper Orthogonal Decomposition were implemented and compared to the results of an OAD toolchain. Both approaches were able to accurately capture complex aerodynamic phenomena, relevant for the successful implementation of the technology coupling. Additionally, areas in which an SG or ROM enhancement to lower fidelity methods used in OAD is indispensable were shown. Integrating reliable models to highly efficient OAD toolchains will enable the resulting optimization task to be solved, ultimately advancing the development of highly fuel-efficient products of the next generation.

# Bibliography


[1] Abu-Ghannam, B.J. and Shaw, R. "Natural Transition of Boundary Layers—The Effects of Turbulence, Pressure Gradient, and Flow History." *Journal of Mechanical Engineering Science*, 22(5): pp. 213–228, 1980

[2] Alcaraz Capsada, L. and Heinrich, R. "Development of the DLR TAU Code for Modelling of Control Surfaces." In: Deutsche Gesellschaft für Luft- und Raumfahrt - Lilienthal - Oberth e.V., ed., *67. Deutscher Luft- und Raumfahrtkongress*. 2018

[3] Alder, M., Moerland, E., Jepsen, J. and Nagel, B. "Recent Advances in Establishing a Common Language for Aircraft Design with CPACS." In: *Aerospace Europe Conference 2020*. 2020

[4] Anderson, J. *Computational Fluid Dynamics: The basics with applications*. McGraw Hill, New York, NY, 1995

[5] Anderson, J. *Introduction to Flight*. McGraw Hill Education, New York, NY, 8 edn., 2016

[6] Anderson, J. *Fundamentals of Aerodynamics*. McGraw Hill Education, New York, NY, 6 edn., 2017

[7] Arnal, D. "Boundary layer transition: Predictions based on linear theory." In: *Special Course on Progress in Transition Modelling*, vol. AGARD-R-793, NATO AGARD. 1994

[8] Arnal, D., Juillen, J.C., Reneaux, J. and Gasparian, G. "Effect of Wall Suction on Leading Edge Contamination." *Aerospace Science and Technology*, 1(8): pp. 505–517, 1997

[9] Beck, N., Landa, T., Seitz, A., Boermans, L., Liu, Y. and Radespiel, R. "Drag Reduction by Laminar Flow Control." *Energies*, 11(252): pp. 1–28, 2018

[10] Bismark, A., Radestock, M., Wahlich, M., Menchel, K., Milot, M. and Cruz, D. "Hybrid Laminar Flow Control Activities within the Frame of Clean Sky 2." In: *AIAA Scitech 2024 Forum*. 2024

[11] Blazek, J. *Computational Fluid Dynamics: Principles and Applications*. Butterworth-Heinemann, 2015

[12] Boeing Commercial Airplane Group. "High Reynolds Number Hybrid Laminar Flight Experiment II. Aerodynamic Design.", 1999

[13] Braslow, A.L. *A History of Suction-Type Laminar-Flow Control with Emphasis on Flight Research.* Monographs in Aerospace History. Washington, D.C, 13 edn., 1999

[14] Bui-Thanh, T., Damodaran, M. and Willcox, K. "Proper Orthogonal Decomposition Extensions for Parametric Applications in Compressible Aerodynamics." In: *21st AIAA Applied Aerodynamics Conference.* 2003

[15] Bulgubure, C. and Arnal, D. "Dassault Falcon 50 Laminar Flow Flight Demonstrator." In: DGLR, ed., *First European Forum on Laminar Flow Technology.* 1992

[16] CentaurSoft™. *CENTAUR Grid Generator.* URL `http://www.centaursoft.com`

[17] Choudhari, M.M. "1st AIAA Transition Modeling and Prediction Workshop: CRM-NLF Grid Generation Guidelines.", 2020. URL `https://transitionmodeling.larc.nasa.gov/workshop_i/`

[18] Criminale, W.O., Jackson, T.L. and Joslin, R.D. *Theory and Computation of Hydrodynamic Stability.* Cambridge Monographs on Mechanics. Cambridge University Press, 2003

[19] Dagenhart, J.R. "Amplified crossflow disturbances in the laminar boundary layer on swept wings with suction." Tech. rep., NASA Technical Paper 1902, 1981

[20] Dargel, G. and Thiede, P. "Assessment of Shock and Boundary Layer Control Concepts for Hybrid Laminar Flow Wing Design." In: E. Stanewsky, J. Délery, J. Fulker and P. de Matteis, eds., *Drag Reduction by Shock and Boundary Layer Control*, pp. 383–414. Springer Berlin Heidelberg, Berlin, Heidelberg, 2002

[21] Dietz, M. *Aerodynamik des Fliegens.* Springer Vieweg, Berlin, 2024

[22] Drela, M. "A User's Guide to MSES 3.05: User Manual.", 2007

[23] Drela, M. *Flight Vehicle Aerodynamics.* MIT Press, Cambridge, MA, 2014

[24] Drela, M. and Giles, M. "Viscous-inviscid analysis of transonic and low Reynolds number airfoils." In: *4th Applied Aerodynamics Conference*, pp. 131–140. 1987

[25] van Driest, E.R. and Blumer, C.B. "Boundary Layer Transition: Freestream Turbulence and Pressure Gradient Effects." *AIAA Journal*, 1(6): pp. 1303–1306, 1963

[26] Duvenaud, D. *Automatic model construction with Gaussian processes.* Ph.D. thesis, 2014

[27] Edi, P. *Investigation of the application of hybrid laminar flow control and variable camber wing design for regional aircraft.* Ph.D. thesis, Cranfield University

[28] Edi, P. and Fielding, J.P. "Civil-Transport Wing Design Concept Exploiting New Technologies." *Journal of Aircraft*, 43(4): pp. 932–940, 2006

[29] Effing, T., Schültke, F. and Stumpf, E. "HLFC-optimized retrofit aircraft design of a medium-range reference configuration within the AVACON project." *CEAS Aeronautical Journal*, 12(2): pp. 441–456, 2021

[30] European Commission and Directorate-General for Mobility and Transport and Directorate-General for Research and Innovation. *Flightpath 2050: Europe's vision for aviation: maintaining global leadership and serving society's needs*. Publications Office (2011)

[31] Fehrs, M. "Boundary Layer Transition in External Aerodynamics and Dynamic Aeroelastic Stability." Tech. Rep. 2018-11, DLR-Institut für Aeroelastik, also Ph.D. thesis, Technische Universität Braunschweig, 2018

[32] Fehrs, M. "Boundary Layer Suction Modeling Based on the DLR TAU-Code Effusion Mass Flux Boundary Condition." In: A. Dillmann, G. Heller, E. Krämer, C. Wagner, C. Tropea and S. Jakirlić, eds., *New Results in Numerical and Experimental Fluid Mechanics XII*, pp. 175–184. Springer International Publishing, Cham, 2020

[33] Feldstein, A., Lazzara, D., Princen, N. and Willcox, K. "Multifidelity Data Fusion: Application to Blended-Wing-Body Multidisciplinary Analysis Under Uncertainty." *AIAA Journal*, 58(2): pp. 889–906, 2020

[34] Forrester, A.I.J., Sóbester, A. and Keane, A.J. *Engineering Design via Surrogate Modelling: A Practical Guide*. John Wiley & Sons, Ltd., 2008

[35] Franz, T. "Reduced-order modeling for steady transonic flows via manifold learning." Tech. Rep. 2016-14, DLR-Institut für Aerodynamik und Strömungstechnik, also Ph.D. thesis, Technische Universität Braunschweig, 2016

[36] François, D.G., Krumbein, A. and Krimmelbein, N. "Simplified Transition Transport Model for Three-Dimensional Aerodynamic Configurations." In: *AIAA AVIATION 2022 Forum*. 2022

[37] Gaster, M. "A simple device for preventing turbulent contamination on swept leading edges." *Journal of the Royal Aeronautical Society*, 142, 1965

[38] Gowree, E. *Influence of Attachment Line Flow on Form Drag*. Ph.D. thesis, City University London, 2014

[39] Grabe, C., Shengyang, N. and Krumbein, A. "Transport Modeling for the Prediction of Crossflow Transition." *AIAA Journal*, 56(8): pp. 3167–3178, 2018

[40] Greenshields, C. and Weller, H. *Notes on Computational Fluid Dynamics: General Principles.* CFD Direct Ltd, Reading, UK, 2022

[41] Greff, E. “Aerodynamic design and technology concepts for a new ultra-high capacity aircraft.” In: *20th Congress of the International Council of the Aeronautical Sciences.* Reston, Va., 1996

[42] Hain, R., Kähler, C.J. and Radespiel, R. “Dynamics of laminar separation bubbles at low-Reynolds-number aerofoils.” *Journal of Fluid Mechanics*, 630: p. 129–153, 2009

[43] Hall, P., Malik, M. and Poll, I. “On the Stability of an Infinite Swept Attachment Line Boundary Layer.” *Proceedings of The Royal Society A*, 395, 1984

[44] Harris, C.D. “NASA Supercritical Airfoils: A Matrix of Family-Related Airfoils.” Tech. Rep. NASA-TP-2969, NASA Langley Research Center, 1990

[45] Heckmeier, F.M. and Breitsamter, C. “Aerodynamic probe calibration using Gaussian process regression.” *Meas. Sci. Technol.*, 31: p. 125301, 2020

[46] Helm, S., Grabe, C., Krumbein, A., Soldenhoff, R., Luedeke, H., Thamm, K. and Scholz, P. “Wind-Tunnel Test with Boundary Layer Suction for the Validation of Transition Transport Models.” In: *AIAA SCITECH 2024 Forum.* 2024

[47] Henke, R. “’A 320 HLF Fin’ flight tests completed.” *Air & Space Europe*, 1(2): pp. 76–79, 1999

[48] Horstmann, K.-H. and Schrauf, G. and Sawyers, D.M. and Sturm, H. “A Simplified Suction System for an HLFC Leading Edge Box of an A320 Fin.” In: *CEAS Aerospace Aerodynamics Research Conference*, vol. 91, pp. 1–7. 2002

[49] Horstmann, K.-H., Engelbrecht, T. and Liersch, C. “LIFTING_LINE: Version 3.0 Revision: User Manual.”, 2019

[50] Iannelli, P., Wild, J., Minervino, M., Strüber, H., Moens, F. and Vervliet, A. “Design of a High-Lift System for a Laminar Wing.” In: EUCASS Association, ed., *5th European Conference for Aeronautics and Space Sciences.* 2013

[51] van Ingen, J. “A suggested semi-empirical method for the calculation of the boundary layer transition region.” Tech. Rep. Univ. of Technology, Rept. UTH1-74, Delft, 1956

[52] International Organization for Standardization (ISO). *ISO 2533:1975: Standard Atmosphere.* ISO, Geneva, Switzerland, 1975

[53] Iyer, V., Bertram, O. and Seibel, O. “Review of hybrid laminar flow control systems.” *Progress in Aerospace Sciences*, 93: pp. 24–52, 2017

[54] Jentys, M. and Breitsamter, C. “Aerodynamic drag reduction through a hybrid laminar flow control and variable camber coupled wing.” *Aerospace Science and Technology*, 142: p. 108652, 2023

[55] Jentys, M. and Breitsamter, C. “Strömungsanalysen zur Tragflügelaerodynamik bei variabler Wölbung und hybrider Laminarhaltung : Schlussbericht: CATeW-AER : Luftfahrtforschungsprogramm LuFo VI-1: CATeW - Coupled Aerodynamic Technologies for Aircraft Wings : Laufzeit: 11/2020-10/2023.” Tech. rep., Technische Universität München, Lehrstuhl für Aerodynamik und Strömungsmechanik, 2024

[56] Jentys, M., Effing, T., Breitsamter, C. and Stumpf, E. “Numerical analyses of a reference wing for combination of hybrid laminar flow control and variable camber.” *CEAS Aeronautical Journal*, 13(4): pp. 989–1002, 2022

[57] Jentys, M., Effing, T., Breitsamter, C. and Stumpf, E. “Multifidelity Aerodynamic Analyses of a Hybrid Laminar Flow Control and Variable Camber Coupled Wing.” In: *Aerospace Europe Conference 2023 - 10th EUCASS - 9th CEAS*. 2023

[58] Jentys, M., Breitsamter, C. “Surrogate Modeling of Hybrid Laminar Wing Aerodynamic Coefficients.” In: A. Dillmann, G. Heller, E. Krämer and C. Wagner, eds., *New Results in Numerical and Experimental Fluid Mechanics XIV*. Springer International Publishing, Cham, 2023

[59] Joo, J.J., Marks, C.R., Zientarski, L. and Culler, A.J. “Variable Camber Compliant Wing - Design.” In: *23rd AIAA/AHS Adaptive Structures Conference*. Reston, Virginia, 2015

[60] Joslin, R.D. “Overview of Laminar Flow Control: Technical Report.” Tech. Rep. NASA/TP-1998-208705, NASA Langley Research Center, 1998

[61] van de Kamp, B., Kleinberg, M. and Schröder, A. “Hybrid Laminar Flow Control ready for Series Application.” In: *Aerospace Europe Conference 2023 - 10th EUCASS - 9th CEAS*. 2023

[62] Karcher, N. and Franz, T. “Adaptive sampling strategies for reduced-order modeling.” *CEAS Aeronautical Journal*, 13: pp. 487–502, 2022

[63] Krimmelbein, N. and Krumbein, A. “Transition prediction for flows with suction using the $e^N$-method.” In: *AIAA Scitech 2021 Forum*. 2021

[64] Krumbein, A., Krimmelbein, N. and Schrauf, G. “Automatic Transition Prediction in Hybrid Flow Solver, Part 1: Methodology and Sensitivities.” *Journal of Aircraft*, 46(4): pp. 1176–1190, 2009

[65] Kudva, J., Lockyer, A. and Appa, K. "Adaptive aircraft wing." In: *AGARD SMP Lecture series 205, smart structures and materials: Implications for military aircraft of new generation*, vol. AGARD-LS-205. 1992

[66] Langel, C.M., Chow, R. and van Dam, C.P. "A Comparison of Transition Prediction Methodologies Applied to High Reynolds Number External Flows." In: *54th AIAA Aerospace Sciences Meeting*. 2016

[67] Langtry, R.B. and Menter, F.R. "Correlation-Based Transition Modeling for Unstructured Parallelized Computational Fluid Dynamics Codes." *AIAA Journal*, 47(12): pp. 2894–2906, 2009

[68] Leschziner, M. *Statistical Turbulence Modelling for Fluid Dynamics — Demystified*. Imperial College Press, 2015

[69] Lord Rayleigh, J. "On the Stability, or Instability, of certain Fluid Motions." In: *Proceedings of the London Mathematical Society*, vol. 11. 1880

[70] Mack, L.M. "Transition prediction and linear stability theory." Tech. Rep. AGARD-CP-224, NATO AGARD, 1977

[71] Mack, L.M. "Boundary-Layer Linear Stability Theory." Tech. Rep. AGARD Report No. 709, 1984

[72] Martins, J.R. *Fuel Burn Reduction Through Wing Morphing*. John Wiley & Sons, Ltd, 2016

[73] McHutchon, A. *Nonlinear Modelling and Control using Gaussian Processes*. Ph.D. thesis, University of Cambridge

[74] McLean, D. *Understanding aerodynamics*. Aerospace series. Wiley-Blackwell, Chichester, 2013

[75] Meerts, C., Steelant, J. and Hendrick, P. "Preliminary Design of the Low Speed Propulsion Air Intake of the LAPCAT-MR2 Aircraft." In: *Proceedings of the 7th European Symposium on Aerothermodynamics*. Brugge, Belgium, 2011

[76] Menter, F., Matyushenko, A., Lechner, R., Stabnikov, A. and Garbaruk, A. "An Algebraic LCTM Model for Laminar–Turbulent Transition Prediction." *Flow, Turbulence and Combustion*, 109(4): pp. 841–869, 2022

[77] Menter, F.R. "Two-equation eddy-viscosity turbulence models for engineering applications." *AIAA Journal*, 32(8): pp. 1598–1605, 1994

[78] Michler, A.K., Dwight, R.P. and Heinrich, R. "Trimmed Simulations of a Transport Aircraft Using Fluid-Structure Coupling." In: *Coupled Problems 2009: 3rd*

*International Conference on Computational Methods for Coupled Problems in Science and Engineering*. 2009

[79] Monner, H., Bein, T., Hanselka, H. and Breitbach, E. "Design aspects of the adaptive wing - the elastic trailing edge and the local spoiler bump." *The Aeronautical Journal*, 104, 2000

[80] Nelson, T. *787 Systems and Performance*. Tech. Presentation, The Boeing Company, 2005

[81] Nguyen, N., Kaul, U., Lebofsky, S., Ting, E., Chaparrp, D. and Urnes, J.M. "Development of Variable Camber Continuous Trailing Edge Flap for Performance Adaptive Aeroelastic Wing." In: SAE International, ed., *AeroTech Congress & Exhibition*. 2015

[82] Nguyen, N.T., Precup, N., Livne, E., Urnes, J.M., Dickey, E., Nelson, C., Chiew, J., Rodriguez, D.L., Ting, E. and Lebofsky, S. "Wind Tunnel Investigation of a Flexible Wing High-Lift Configuration with a Variable Camber Continuous Trailing Edge Flap Design." In: *33rd AIAA Applied Aerodynamics Conference*, vol. AIAA 2015-2417. 2015

[83] Nie, S. "Extension of Transition Modeling by a Transport Equation Approach." Tech. rep., DLR, 2017

[84] Pedregosa, F., Varoquaux, G., Gramfort, A., Michel, V., Thirion, B., Grisel, O., Blondel, M., Prettenhofer, P., Weiss, R., Dubourg, V., Vanderplas, J., Passos, A., Cournapeau, D., Brucher, M., Perrot, M. and Duchesnay, E. "Scikit-learn: Machine Learning in Python." *Journal of Machine Learning Research*, 12: pp. 2825–2830, 2011

[85] Peter, F.N., Risse, K., Schueltke, F. and Stumpf, E. "Variable Camber Impact on Aircraft Mission Planning." In: *53rd AIAA Aerospace Sciences Meeting 2015*, vol. AIAA 2015-1902. Curran, Red Hook, NY, 2015

[86] Pfenninger, W. "Some Results from the X-21A Programm. Part I: Flow Phenomena at the Leading Edge of Swept Wings." *Recent Developments in Boundary Layer Research, AGARDograph*, 97(4): pp. 1–41, 1965

[87] Poll, D. "Transition in the Infinite Swept Attachment Line Boundary Layer." *Aeronautical Quarterly*, 30(4): p. 607–629, 1979

[88] Prandtl, L. "Über die Flüssigkeitsbewegung bei sehr kleiner Reibung." In: *Verhandlungen des Dritten Internationalen Mathematiker-Kongresses*, pp. 485 – 491. B. G. Teubner, Leipzig, 1905

[89] Preliminary Design Department, Boeing Commercial Airplane Company. "Hybrid Laminar Flow Control Study, Final Technical Report." Tech. Rep. NASA/CR-165930, National Aeronautics and Space Administration, 1982

[90] Radespiel, R. "On the long-term needs of flight physics research." In: *Plenary talk 4, 22. DGLR-Fachsymposium der STAB*. Berlin, Germany, 2022

[91] Rasmussen, C.E. and Williams, C.K.I. *Gaussian Processes for Machine Learning*. The MIT Press, Cambridge, MA, 2006

[92] Raymer, D.P. *Aircraft Design: A Conceptional Approach: AIAA Education Series*. AIAA education series. American Institute of Aeronautics and Astronautics, Washington, DC, 6. edn., 2018

[93] Reckzeh, D. "Multifunctional Wing Moveables: Design of the A350XWB and the Way to Future Concepts." In: *29th Congress of the International Council of the Aeronautical Sciences*. St. Petersburg, Russia, 2014

[94] Reckzeh, D. "Technology Integration for Future Aircraft Configurations." In: *33rd Congress of the International Council of the Aeronautical Sciences*. Stockholm, Sweden, 2022

[95] Redeker, G., Horstmann, K.-H., Koester H., Thiede, P. and Szodruch, J. "Design for a natural laminar flow glove for a transport aircraft." In: *Flight Simulation Technologies Conference and Exhibit*. 1990

[96] Reinbold, C., Bantscheff, K., Sørensen, K. and Breitsamter, C. "Influence of structural elasticity on the aerodynamic characteristics of the common research model with deflected control surfaces." *Aerospace Science and Technology*, 149: p. 109154, 2024

[97] Reist, T.A., Koo, D. and Zingg, D.W. "Aircraft Cruise Drag Reduction Through Variable Camber Using Existing Control Surfaces." *Journal of Aircraft*, 59(6): pp. 1406–1415, 2022

[98] Reshotko, E. "Boundary layer instability, transition and control." In: *32nd Aerospace Sciences Meeting and Exhibit*. 1994

[99] Reynolds, O. "III. An experimental investigation of the circumstances which determine whether the motion of water shall be direct or sinuous, and of the law of resistance in parallel channels." *Proceedings of the Royal Society of London*, 35(224-226): pp. 84–99, 1883

[100] Ripepi, M., Verveld, M., Karcher, N., Franz, T., Abu-Zurayk, M., Görtz, S. and Kier, T. "Reduced-order models for aerodynamic applications, loads and MDO." *CEAS Aeronautical Journal*, 9, 2018

[101] Risse, K. *Preliminary Overall Aircraft Design with Hybrid Laminar Flow Control: Vorentwurf von Flugzeugen mit hybrider laminarer Strömungskontrolle*. Ph.D. thesis, RWTH Aachen University, 2016

[102] Risse, K., Anton, E., Lammering, T., Franz, K. and Hoernschemeyer, R. "An Integrated Environment for Preliminary Aircraft Design and Optimization." In: *53rd AIAA/ASME/ASCE/AHS/ASC Structures, Structural Dynamics and Materials Conference: SciTech 2012*, vol. AIAA 2012-1675. 2012

[103] Ruhao, H., Hao, C., Xianxu, Y., Zhigong, T. and Lin, B. "Trimming analysis of flexible aircrafts based on computational fluid dynamics/computational structural dynamics coupling methodology." *Proceedings of the Institution of Mechanical Engineers, Part G: Journal of Aerospace Engineering*, 235(2): pp. 219–237, 2021

[104] Rumsey, C. "Implementing Turbulence Models into the Compressible RANS Equations.", 2023. URL `https://turbmodels.larc.nasa.gov/implementrans.html`

[105] Saric, W.S., Reed, H.L. and White, E.B. "Stability and Transition of Three-Dimensional Boundary Layers." *Annual Review of Fluid Mechanics*, 35(1): pp. 413–440, 2003

[106] Schlichting, H. *Amplitudenverteilung und Energiebilanz der kleinen Störungen bei der Plattenströmung*. Nachrichten von der Gesellschaft der Wissenschaften zu Göttingen, Mathematisch-physikalische Klasse. Weidmann, 1935

[107] Schlichting, H. and Gersten, K. *Boundary-Layer Theory*. Springer Berlin Heidelberg, Berlin, Heidelberg, 2017

[108] Schrauf, G. "Transition prediction using different linear stability analysis strategies." In: *12th Applied Aerodynamics Conference*. 1994

[109] Schrauf, G. "COCO: A Program to Compute Velocity and Temperature Profiles for Local and Nonlocal Stability Analysis of Compressible, Conical Boundary Layers with Suction: Technical Report ZARM.", 1998

[110] Schrauf, G. "Status and perspectives of laminar flow." *The Aeronautical Journal*, 109(1102): p. 639–644, 2005

[111] Schrauf, G. "LILO 2.1: User's Guide and Tutorial: GSSC Technical Report 6.", 2006

[112] Schrauf, G. "LEA — A FORTRAN Subroutine to Compute the Effective Sweep Angle and the Attachment Line Reynolds Number." Tech. rep., GSSC TR 10, Airbus, Bremen, 2012

[113] Schrauf, G. and Frhr. von Geyr, H. "Simplified hybrid laminar flow control for transport aircraft." In: *ECCOMAS 2012 - European Congress on Computational Methods in Applied Sciences and Engineering*, pp. 3831–3842. 2012

[114] Schrauf, G. and Frhr. von Geyr, H. "Hybrid Laminar Flow Control on A320 Fin: Retrofit Design and Sample Results." *Journal of Aircraft*, 58: pp. 1–9, 2021

[115] Schrauf, G., Perraud, J., Vitiello, D. and Lam, F. "Comparison of Boundary-Layer Transition Predictions Using Flight Test Data." *Journal of Aircraft*, 35(6): pp. 891–897, 1998

[116] Schueltke, F., Aigner, B., Effing, T., Strathoff, P. and Stumpf, E. "MICADO: Overview of Recent Developments within the Conceptual Aircraft Design and Optimization Environment." In: Deutsche Gesellschaft für Luft- und Raumfahrt - Lilienthal - Oberth e.V., ed., *69. Deutscher Luft- und Raumfahrtkongress*. 2020

[117] Schuet, S., Malpica, C. and Aires, J. *A Gaussian Process Enhancement to Linear Parameter Varying Models*. 2021

[118] Schültke, F. and Stumpf, E. "UNICADO - Development and Establishment of a University Conceptual Aircraft Design Environment." In: Deutsche Gesellschaft für Luft- und Raumfahrt - Lilienthal - Oberth e.V., ed., *69. Deutscher Luft- und Raumfahrtkongress*. 2020

[119] Schwamborn, D., Gardner, A., von Geyer, H., Krumbein, A., Lüdeke, H. and Stürmer, A. "Development of the TAU-Code for aerospace applications." In: *50th NAL International Conference on Aerospace Science and Technology*. 2008

[120] Sclafani, A., Dehaan, M., Vassberg, J., Rumsey, C. and Pulliam, T. "Drag prediction for the common research model using CFL3D and OVERFLOW." *Journal of Aircraft*, 51: pp. 1101–1117, 2014

[121] Seitz, A. and Horstmann, K.-H. "Design Studies on NLF and HLFC Applications at DLR." In: *27th Congress of the International Council of the Aeronautical Sciences*. 2010

[122] Sirovich, L. "Turbulence and the dynamics of coherent structures. I - Coherent structures. II - Symmetries and transformations. III - Dynamics and scaling." *Quarterly of Applied Mathematics - QUART APPL MATH*, 45, 1987

[123] Smith, A. and Gamberoni, N. *Transition, Pressure Gradient and Stability Theory*. ARC-19322. Douglas Aircraft Company, El Segundo Division, 1956

[124] Smith, S.B. and Nelson, D.W. "Determination of the aerodynamic characteristics of the mission adaptive wing." *Journal of Aircraft*, 27(11): pp. 950–958, 1990

[125] Stanewsky, E. "Adaptive wing and flow control technology." *Progress in Aerospace Sciences*, 37(7): pp. 583–667, 2001

[126] Ströer, P. "Eine Familie stabilitätsbasierter Transitionstransportgleichungsmodelle für die numerische Strömungssimulation." Tech. Rep. 2022-12, DLR-Institut für Aerodynamik und Strömungstechnik, also Ph.D. thesis, Technische Universität Braunschweig, 2022

[127] Strüber, H. "The Aerodynamic Design of the A350 XWB-900 High Lift System." In: International Council of the Aeronautical Sciences, ed., *29th International Congress of the Aeronautical Sciences*. 2014

[128] Thornton, S.V. "Reduction of Structural Loads Using Maneuver Load Control on the Advanced Fighter Technology Integration (AFTI)/F-111 Mission Adaptive Wing." Tech. rep., NASA TM 4526, Edwards, California, 1993

[129] Tollmien, W. *Über die Entstehung der Turbulenz. 1. Mitteilung*. Nachrichten von der Gesellschaft der Wissenschaften zu Göttingen, Mathematisch-Physikalische Klasse. Weidmann, 1928

[130] Tollmien, W. *Ein allgemeines Kriterium der Instabilität laminarer Geschwindigkeitsverteilungen*. Nachrichten von der Gesellschaft der Wissenschaften zu Göttingen, Mathematisch-Physische Klasse. Weidmann, 1935

[131] Vassberg, J., Dehaan, M., Rivers, M. and Wahls, R. "Development of a Common Research Model for Applied CFD Validation Studies." In: *26th AIAA Applied Aerodynamics Conference*. 2008

[132] Vassberg, J., Sclafani, A. and DeHaan, M. "A Wing-Body Fairing Design for the DLR-F6 Model: A DPW-III Case Study." In: *23rd AIAA Applied Aerodynamics Conference*. 2005

[133] Virtanen, P., Gommers, R., Oliphant, T.E., Haberland, M., Reddy, T., Cournapeau, D., Burovski, E., Peterson, P., Weckesser, W., Bright, J., van der Walt, S.J., Brett, M., Wilson, J., Millman, K.J., Mayorov, N., Nelson, A.R.J., Jones, E., Kern, R., Larson, E., Carey, C.J., Polat, İ., Feng, Y., Moore, E.W., VanderPlas, J., Laxalde, D., Perktold, J., Cimrman, R., Henriksen, I., Quintero, E.A., Harris, C.R., Archibald, A.M., Ribeiro, A.H., Pedregosa, F., van Mulbregt, P. and SciPy 1.0 Contributors. "SciPy 1.0: Fundamental Algorithms for Scientific Computing in Python." *Nature Methods*, 17: pp. 261–272, 2020

[134] Voogt, V. "Flight Testing of a Fokker 100 Test Aircraft with Laminar Flow Glove." In: *2nd European Forum on Laminar Flow Technology*. 1996

[135] Wilcox, D.C. "Reassessment of the scale-determining equation for advanced turbulence models." *AIAA Journal*, 26(11): pp. 1299–1310, 1988

[136] Wilcox, D.C. *Turbulence Modeling for CFD (Third Edition)*. DCW Industries, 2006

[137] Winter, M. *Nonlinear Aerodynamic Reduced-Order Modeling Using Neuro-Fuzzy Approaches*. Ph.D. thesis, Technical University of Munich, 2021

[138] Woehler, S., Hartmann, J., Prenzel, E. and Kwik, H. "Preliminary aircraft design for a midrange reference aircraft taking advanced technologies into account as part of the AVACON project for an entry into service in 2028." In: Deutsche Gesellschaft für Luft- und Raumfahrt - Lilienthal - Oberth e.V., ed., *67. Deutscher Luft- und Raumfahrtkongress*. 2018

[139] Young, T.M. *Investigations into the Operational Effectiveness of Hybrid Laminar Flow Control Aircraft*. Ph.D. thesis, Cranfield University, 2002

# List of Publications

## Peer-Reviewed Publications


- M. Jentys and C. Breitsamter, "Aerodynamic Drag Reduction through a Hybrid Laminar Flow Control and Variable Camber Coupled Wing," *Aerospace Science and Technology*, Vol. 142, (2023). `doi:10.1016/j.ast.2023.108652`

- M. Jentys and C. Breitsamter, "Surrogate Modeling of Hybrid Laminar Wing Aerodynamic Coefficients," In: *Notes on Numerical Fluid Mechanics and Multidisciplinary Design*, Vol. 154, edited by Dillmann et al., New Results in Numerical and Experimental Fluid Mechanics XIV, Springer-Verlag, Cham, 2023. `doi:10.1007/978-3-031-40482-5_22`

- M. Jentys, T. Effing, C. Breitsamter and E. Stumpf, "Numerical analyses of a reference wing for combination of hybrid laminar flow control and variable camber," In: *CEAS Aeronautical Journal*, Vol. 13, (2022). `doi:10.1007/s13272-022-00598-y`


## Conference Contributions


- M. Jentys, T. Effing, C. Breitsamter and E. Stumpf, "Multifidelity aerodynamic analyses of a hybrid laminar flow control and variable camber coupled wing," In: Aerospace Europe Conference, Joint 10th EUCASS - 9th CEAS Conference, Lausanne, Switzerland, 2023. `doi:10.13009/EUCASS2023-384`

- M. Jentys, and C. Breitsamter, "Parametric Surrogate Modelling of Integral Aerodynamic Force Coefficients for a Transonic Transport Aircraft Wing," In: 22. DGLR-Fachsymposium der STAB, Berlin, Germany, 2022.

- M. Jentys, and C. Breitsamter, "Transitional flow modelling of a hybrid laminar flow control and variable camber transonic transport aircraft wing," In: 33rd Congress of the International Council of the Aeronautical Sciences, Stockholm, Sweden, 2022.

- M. Jentys, and C. Breitsamter, "Aerodynamic Analysis of Variable Camber and Hybrid Laminar Flow Control Coupling on a Transonic Transport Aircraft Wing," In: 20. STAB-Workshop, Göettingen, Germany, 2021.

- M. Jentys, T. Effing, C. Breitsamter and E. Stumpf, "Numerische Analysen eines Referenzflügels zur Kombination hybrider Laminarhaltung und variabler Wölbung," In: 70. Deutscher Luft- und Raumfahrtkongress, Bremen, Germany, Deutsche Gesellschaft für Luft- und Raumfahrt - Lilienthal-Oberth e.V., 2021.